ACCURATE DESCRIPTIONS OF THE ANISOTROPIC PLASTIC YIELDING BEHAVIOUR OF VARIOUS METALLIC SHEETS

by

Hamzah Abdulrahman Alharthi

A thesis submitted in partial fulfilment of the requirements for the degree of

Doctor of Philosophy in Engineering

University of Warwick, Warwick Manufacturing Group

September 2016

Contents

List of Figures

List of Tables

Abstract

This thesis focuses on two vital requirements - yield criterion and flow curve - to obtain reliable numerical results in sheet metal forming simulations.

First, this thesis generally aims to explore the potential accuracy of the Taylor models, namely the full constraint and pancake, for replacing complicated mechanical tests involved in the defining process of advanced yield functions for aluminium alloys. The exploration process resulted in a simple and efficient yield locus description denoted as CTF. This model correlates with the texture-based model (Taylor full constraint) and the phenomenological model (BBC2005) for the considered aluminium alloys. Based on this newly proposed model (CTF), a hybrid solution, denoted as Method II, is suggested. Consequently, the demands associated with the extensive and difficult tests required for calibrating the advanced yield function can be reduced. A remaining issue related with the identification procedure of the plastic anisotropy parameters associated with advanced yield criteria was addressed in this thesis by applying the trust region approach for identifying the material coefficients, and its performance was compared with the line-search approach. The applied algorithms were tested for various aluminium and steel alloys with different levels of anisotropy.

Second, this research sought to develop an accurate determination of the biaxial flow curve for various aluminium and steel alloys when a continuous and in-line thickness measurement system, such as the digital image correlation (DIC) system, is absent. In certain sheet metal forming processes, it is more appropriate to determine a flow curve using biaxial stress condition tests, such as the hydraulic bulge test, than a uniaxial test because hardening proceeds higher strains before necking occurs. In a uniaxial test, higher strains are extrapolated, which might lead to erroneous results. Usually, the bulge test coupled with the DIC system is used to obtain stress–strain data. In the absence of the DIC system, analytical methods are instead employed to estimate hardening. Typically, such models incorporate a correction factor to achieve correlation with the experimental data. An example is the Chakrabarty and Alexander method that utilises a correction factor based on the *n*-value. Here, the Chakrabarty and Alexander approach was modified with a correction factor based on normal anisotropy. When compared with DIC data, the modified model was found to be able to predict the hardening curves better for the materials examined in this study. Based on the fact that a biaxial flow curve is required to compute the biaxial yield stress, an essential input to advanced yield functions, the

effects of various approaches to biaxial stress–strain data on the shape of the BBC2005 yield loci were also investigated. The proposed method could accurately predict the magnitude of biaxial yield stress, when compared with DIC data, for all materials that were investigated in this study.

Declaration

This thesis is submitted to the University of Warwick in support of my application for the degree of Doctor of Philosophy. It has been composed by myself and has not been submitted in any previous application for any degree.

The work presented (including data generated and data analysis) was carried out by the author except in the cases outlined below:

List of data provided by collaborators.

- Tensile tests
- Bulge Tests
- Compression Tests
- Texture measurements

Parts of this thesis have been published by the author:

H. Alharthi, S. Hazra, D. Banabic, R. Dashwood, Analytical methodology for the determination of the flow curves of aluminium and steel alloys using the hydraulic bulge tests, in: AIP Conf. Proc. 19th ESAFORM Conf., 2016 (accepted).

H. Alharthi, S. Hazra, D. Banabic, R. Dashwood, Determination of the yield loci of four sheet materials (AA6111-T4, AC600, DX54D+Z, and H220BD+Z) by using uniaxial tensile and hydraulic bulge tests, Int. J. Mater. Form. (submitted).

Acknowledgments

First of all, I would like to thank the almighty God for allowing me to complete this thesis.

Second, I wish to express my sincere gratitude to my supervisors, Prof. Richard Dashwood and Dr. Sumit Hazra, for their continuous support and guidance.

I would like to extend my thanks to the following individuals who helped along the way: Dave Williams, Ian Masters, Richard Beaumont, Scott Taylor, Craig Carnegie, Elspeth Keating, Yogendra Joshi, Mario Carandente, Zachary Parkinson, Georgina Haslop, and Neil Small. To Khalid, Fahad, Amjed, Abdullah, and Abdulrahman, who motivated me endlessly.

I did enjoy many discussions with Prof. Dorel Banabic regarding the mechanical tests conducted at his lab at the Technical University of Cluj-Napoca. Also, I would like to thank Prof. Seefeldt, Prof. Van Bael, Dr. Philip Eyckens, and Louis Depre at the University of Leuven for their support and the discussions on texture and its measurement.

I wish to extend my appreciation to Umm Al-Qura University for sponsoring my studies. This journey would not have been possible without my family, beginning with the unconditional support, love, and prayers of my parents. I am particularly grateful for the ongoing encouragement that I received from my wonderful sisters (Areej, Amel, Asma, and Raghad) and brothers (Wael and Ahmed).

Here in the UK, my adorable wife Afaf and my lovely daughters Jalnar, Rifal, and Lauren are the pillars that supported me wholeheartedly during my study. Thanks to Afaf for bearing the unbearable. The Sunday swimming sessions with my daughters have always lessened the burdens that I carried as I worked toward this PhD. To all who gave me support throughout this journey, thank you.

Abbreviations and Symbols

Abbreviations

A	ARAMIS
A1	First anomalous behaviour
A2	Second anomalous behaviour
BBC	Banabic-Balan-Comsa (BBC)
BCC	Body-centred Cubic
Bs	Brass
CAD	Computer aided design
CPFEM	Crystal plasticity finite element method
CPFFT	Crystal plasticity fast Fourier transform
CTFP	Yield locus derived from Taylor models (TF & TP)
CTF	Yield locus derived from Taylor model (TF)
Cu	Copper
DIC	Digital image correlation
FC, TF, FC-Taylor	Taylor model (Full constraint)
FCC	Face-centred Cubic
FLD	Forming Limit Diagram
FEM	Finite Element Method
G	Goss
GA	Genetic Algorithm
HCP	Hexagonal Close-Packed
L	Levenberg
LM	Levenberg–Marquardt
LVDT	Linear Voltage Displacement Transducer
NR	Newton–Raphson algorithm

ND	Normal Direction
O	Origin
ODF	Orientation Distribution Function
P-C	Panknin-Chakrabarty & Alexander
P-C-M	Proposed model for flow curve determination
PCYS	Polycrystal yield surface
P-K	Panknin-Kruglov
RD	Rolling Direction
SD	Strength differential
TD	Transverse Direction
TBH	Taylor-Bishop-Hill
TP, RC	Relaxed version of Taylor model (Pancake)
TRD	Trust Region Dogleg
VPSC	Visco Plastic Self Consistent
3-D	3-Dimensional
2-D	2-Dimensional

Symbols

R	Lankford parameter
ε	Logarithmic strain
ε_{11}	Length strain
ε_{22}	Width strain
ε_{33}	Thickness strain
w	Final width
w_o	Initial width
t	Final thickness
t_o	Initial thickness
l	Final gage length
l_o	Initial gage length
$\overline{R}$	Normal plastic anisotropy
R_0	R-value along the RD
R_{45}	R-value determined at specimens cut along 45° to the RD
R_{90}	R-value along the TD
ΔR	Planar anisotropy
σ_{ij}, σ	Cauchy stress tensor
σ_{11}, σ_{22}	Membrane stresses
σ_{33}	Normal stress
σ_{12} , σ_{21}	Shear stress
σ_1	Principal stress component along the RD
σ_2	Principal stress component along the TD
$d\varepsilon^p$	Plastic strain-increment

λ_1	Scalar factor of proportionality
F	Yield function
Y_{ref}	Constant
$\overline{\sigma}$	Equivalent stress
R_b	Equibiaxial R-value
YS_0 , σ_0	Uniaxial yield stress for a specimen cut at the RD
YS_{45} , σ_{45}	Uniaxial yield stress for a specimen cut 45° to the RD
YS_{90} , σ_{90}	Uniaxial yield stress for a specimen cut at the TD
Y_b , σ_b	Equi-biaxial yield stress
τ	Maximum shear stress
U_d	Distortion energy per unit volume
υ	Poisson ratio
E	Modulus of elasticity
k_1, k_2	Stress tensor invariants
a_B, c, h, p	Material constants associated with Barlat 1989
M_B	Material parameter
ϕ	Plane stress yield function
ϕ' , ϕ''	Isotropic, convex functions
$\tilde{S}_1'$, $\tilde{S}_2'$	Two principal values of the transformed stress deviator $\tilde{S}'$
$\tilde{S}_1''$, $\tilde{S}_2''$	Two principal values of the transformed stress deviator $\tilde{S}''$
a	Constant
$\tilde{S}'$	Transformed stress deviator associated with ϕ'
$\tilde{S}''$	Transformed stress deviator associated with ϕ''
$\tilde{S}_{xx}'$, $\tilde{S}_{yy}'$, $\tilde{S}_{xy}'$	Components of $\tilde{S}'$

$\tilde{S}''_{xx}, \tilde{S}''_{yy}, \tilde{S}''_{xy}$	Components of $\tilde{S}''$
S_{xx}, S_{yy}, S_{xy}	Components of stress deviatoric stress tensor for plane stress state
C'_{ij} , C''_{kl}	Coefficients
α_k	Eight unknown coefficients associated with Yld2000
J	Index $J = 1,2,3$
$\gamma_J, \delta_J, \sigma_J, q_{xJ}, q_{yJ}$	Complementary information needed to calculate the α_k coefficients
F_J	Three equations associated with Yld2000
G_J	Three equations associated with Yld2000
F_4	Equation associated with Yld2000
G_4	Equation associated with Yld2000
x'_1, x'_2, x''_1, x''_2	Expressions used in F_4 and G_4
$\overline{V''}, \overline{V''}, \overline{W''}$	Expressions used in F_4 and G_4
$\bar{\eta}$	Accumulated equivalent plastic strain
$a_B, M_B, N_B, P_B, Q_B,$ R_B, S_B, T_B	Eight parameters associated with BBC2003
k	Exponent related to the crystal structure of the materials
Γ, Ψ , Λ	Terms related to the non-zero components of the stress tensor
φ	Orientation angle $\varphi \in \{0,45,90\}$
YS_φ	Uniaxial yield stress associated with the orientation φ
A	Function associated with BBC2003
$a_{B5}, b, L, M, N,$ P, Q, R_{B5}	Eight parameters associated with BBC2005
$F(x)$	System of nonlinear equations

x	Vector of unknowns
x^*	Solution vector
$F(x^*)$	Values of the objective functions at x^*
x_i	Current estimate
$J(x_i)$, J_i	Jacobian of the $F(x_i)$ at x_i
x_{i+1}	Update estimate
x_0	Initial estimate
d_i	Search direction
Δ	Trust region radius
d_C	Cauchy step
d_{GN}	Gauss–Newton step
ρ_{tr}	Parameter to update Δ
$\Delta_{\max}$	Maximum trusted radius
η_1	Constant to update Δ
η_2	Constant to update Δ
α_{tr1}	Constant to update Δ
α_{tr2}	Constant to update Δ
λ_s	Trail step associated with the steepest descent method
B_i	Approximation of Hessian
I	Identity matrix
g_i	Gradient
$diag$	Diagonal
dV	Volume of all grains with the orientation g

V	Sample volume
$f(g)$	Orientation distribution function
dg	Orientation range
$\varphi_1, \Phi, \varphi_2$	Euler angles
L_h	Maximal degree of the series expansion
α , γ	Texture fibres
M_T	Taylor factor
$\dot{E}_{ij}$	Strain rate tensor
$\dot{\gamma}_s$	Rate of slip on slip system s
z	Total slip number
$\dot{E}_{eq}$	Equivalent strain rate
$\dot{W}$	Plastic work rate per unit volume for that crystal
τ^c	Critical resolved shear stress of the crystal
$\overline{\dot{W}}$	Average plastic work rate of the entire polycrystal
$\overline{M}$	Average Taylor factor
$\dot{\varepsilon}_{13}$, $\dot{\varepsilon}_{23}$	Strain rate components
$M(g)$	Series expansion of M_T
$C_l^{\mu\nu}$	Series expansion coefficients of the material texture
$m_l^{\mu\nu}$	Coefficients which describe $M(g)$
S_1	Normalised yield stress in the RD
S_2	Normalised yield stress in the TD
f_b	Balanced biaxial stress factor on the yield loci for the CTFP model

f_b^{TF}	Balanced biaxial stress factor on the yield loci for the TF model
f_b^{TP}	Balanced biaxial stress factor on the yield loci for the TP model
f_{b1}, f_{b2}	Two stress factor components for the biaxial point.
f_1, f_2	Stress factors in the stretching regime of the CTFP.
f_1^{TF}, f_2^{TF}	Components of the stress factor on the yield loci derived from the TF model.
β^{TF}	Stress ratio for each point on the TF model.
H_b^{TF}	Hypotenuse of the biaxial point of the TF
f_b^{CTF}	Balanced biaxial stress factor on the yield loci for the CTF model
f_b^{TF}	Balanced biaxial stress factor on the yield loci for the TF model
H_b^{CTF}	Hypotenuse of the biaxial point of the CTF
$f_{b1}^{CTF}, f_{b2}^{CTF}$	Two stress factor components for the biaxial point of the CTF.
α	Angle where the stress factor is measured.
f_1^{CTF}, f_2^{CTF}	Major and minor stress factors in the stretching regime of the CTF.
p	Hydraulic pressure
ρ_1, ρ_2	Curvature radii
ε_b	Biaxial strain
d	Diameter of the die cavity
R	Die fillet radius
h	Height of the bulge
λ	Unknown parameter
n	Strain hardening exponent of the material
W_u	Plastic work per unit volume in the case of uniaxial loading

W_b	Plastic work per unit volume in the case of biaxial loading
a_0	Original diameter of the specimen parallel to the RD.
a_1	Diameter of the specimen after deformation parallel to the RD
b_0	Original diameter of the specimen perpendicular to the RD.
b_1	Diameter of the specimen after deformation perpendicular to RD.
ε_{RD}	True strain parallel to the RD.
ε_{TD}	True strain perpendicular to the RD.

Chapter 1

General Introduction

1.1 Sheet metal forming

To transform a material into a useful part with a relatively complex geometry, a manufacturing process must be used. Sheet metal forming processes such as deep drawing and stamping are employed for producing various products, some of which are automotive panels, military components, domestic appliances, and food cans [1]. In the sheet metal forming process, deformation can occur at a temperature below or above the recrystallization temperature. The process is referred to as cold or hot forming, respectively [2]. This thesis deals with aspects that are related mainly to the cold forming processes. However, concepts and methods described in this thesis could be applicable for hot forming as well.

Bending, stamping, deep drawing, and ironing are some of the basic industrial sheet metal forming processes. Figure **1.1** illustrates four common forming processes.

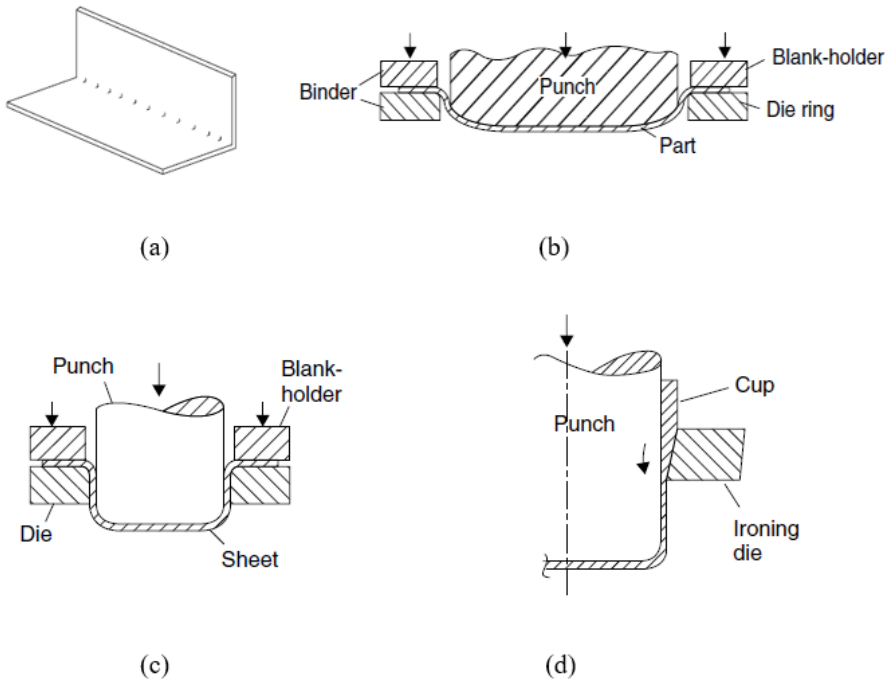

Figure 1.1. Various sheet metal forming processes [3].

1.2 Sheet metal forming simulation

Historically, the evaluation and improvement of sheet metal forming processes involved expensive trial and error iterations during the design phase [4,5]. Such trials were performed based on experience with the geometry and material of the part. The number of iterations has since been reduced by using modern numerical analysis techniques, including the finite element method (FEM) [5]. In other words, numerical simulation of sheet metal forming processes such as the stamping process is crucial in the design phase [6]. The utilization of such methods should be reliable, and that reliability partially depends on the constitutive material models (i.e. the mechanical/plastic characterization or description of the materials being used) [4,7].

A variety of finite element codes are employed in the sheet metal forming industry. These codes can be classified into five categories [5,8]:

- Dynamic explicit
- Static explicit
- Static implicit
- Static implicit large step
- Static implicit one step

More details about these categories can be found in [8,9]. Processes such as deep drawing, binder wrapping, and springback can be simulated with these codes [8]. Such codes might be able to predict defects such as wrinkle, thickness, and geometrical defects after springback [8].

When engineering simulation software was introduced decades ago, companies such as Toyota Motor had reservations about the usefulness of the software. However, with the advent of new materials and panel shapes, as well as the increasing sophistication of simulation software, these companies increasingly began to employ finite element codes such as LS-DYNA3D [8].

1.2.1 Simulation role

The utilisation of quick and reliable numerical techniques such as FEM is required and extremely helpful, particularly at the design phase [10]. Such powerful modelling techniques have minimised expensive and time-consuming experiments, including trials for the stamping process.

In the automotive industry, demand is continuous to reduce the weight of cars, so interest in lightweight alloys such as aluminium alloys [11] is growing. As a result, fuel efficiency will be improved, which in turn leads to a considerable reduction in vehicle emissions [12]. With the advent of new materials, simulation techniques can compensate for the lack of experience.

Another aspect of the car industry, time to market, is a critical aspect of the industry [4,8,13]. Car manufacturers are required to develop more new, reliable vehicles in a shorter period than has previously been the case. In other words, lead time in a competitive market, especially that of the automotive market, can be decisive [4]. Long lead times pose a risk to the business, because over that time consumer demand may have changed. In 1997, Schacher said, “In the past we introduced 3 new models every 10 years, now we introduce 10 new models every 3 years” [5].

This level of reduction in development time, as well as the demand to reduce the weight of the car, has taken the lead in rebuilding conventional design and manufacturing procedures [5]. Finite element simulation is a powerful modelling technique in the automotive industry, and its use will reduce the number of trials for the expensive and time-consuming stamping process significantly. Therefore, time to market will be shortened [7].

Industrial engineers are interested in computing numerically the following simulation outputs [5]:

- Distribution of the sheet thickness and strain.
- The indications of failure such as fracture, earing, and wrinkling [14]
- Residual stresses in the formed part
- Spring-back value
- Pressure of the blank holder
- Lubrication conditions
- Punch forces

To be more specific, one of the desired simulation outcomes is to inspect the geometry of the formed part. In other words, a conclusion is made from the outcomes whether or not the part is feasible. Part feasibility can be assured if the assumptions and inputs included in the simulation model are aligned more realistically with the reality of the stamping environment [6]. With a feasibility solution, the product function can be delivered by assessing the geometry of the part and specification of the material. A feasibility study

determines whether the product can be made safely, but it does not ensure that it can be manufactured [6]. However, the FEM techniques should be reliable, and that reliability depends on the numerical description of the problem and the description of the process parameters as well as the constitutive material model that will be used [7]. The minimum required inputs for a feasibility study are 3D CAD data and a material specification. A hardening curve, yield locus, and forming limit curve are required by the material model [6]. Various fundamental elements are required to develop sound constitutive equations for anisotropic materials. The most important concepts and issues are briefly discussed in section 1.3.

1.3 Ingredients of the classical plasticity

To describe the plastic "irreversible or permanent or inelastic" deformation at a macroscopic scale, three essential elements are required to be specified. These ingredients are the following [15,16]:

- **Yield surface "locus"**, determining the combinations of stresses for which yielding first occurs.
- **Flow rule,** describing the relation between the stress and the strain rate components.
- **Hardening law "rule",** specifying the strain hardening behaviour of the material as the plastic deformation continues.

Researchers in [17,18] mentioned other issues or subtasks that require separate and careful attention:

- **Plastic hardening curve**
- **Strain rate dependence**

1.4 Objectives

The motivation of this thesis is to contribute to the knowledge in the field of sheet metal plastic modelling. In particular, the contribution will advance two of the fundamental elements of classical plasticity, namely the yield locus description and plastic hardening curve, which are required to develop sound constitutive equations for anisotropic materials. First, this comprises a thorough and critical review of the anisotropic yielding approaches. It also includes the comprehensive details of the current mathematical models that are used to establish the plastic hardening curve when a continuous and in-line thickness measurement system, such as the Digital image correlation (DIC) system, is absent.

Two main goals are hoped to be reached within the scope of this manuscript:

- Accurate and cost-effective description of the yield locus
- Accurate determination of the biaxial flow curve when a continuous and in-line thickness measurement system, such as the DIC system, is absent

1.4.1 Accurate and cost-effective description of the yield locus

1.4.1.1 *Yield locus for aluminium alloys*

According to Mattiasson and Sigvant [18], the demands on the material models from the industrial viewpoint are the following:

- **Accuracy and reliability.** In other words, the models must describe accurately the plastic anisotropy or the yielding characteristics of the material. This requirement has been proved to be achieved by some of the recent advanced models such as Yld2000 [19] and BBC2008 [20].
- **Simplicity.** Some of the advanced models are complex and require advanced mathematical ability.
- **Efficiency.** A number of parameters are involved in the yield condition, and these parameters must be identified by conducting a certain number of experiments. The parameters have to be fitted to the experimental data. The greater the parameters are, the better the yield locus is determined. Therefore, a significant number of mechanical tests, which are time consuming and expensive, are required to identify the models' parameters. As a result, most sheet forming industry analysts believe that this would not be suitable for industrial applications.

The central ingredient in the material characterizations is the yield function, which has a vital impact on the accuracy of numerical results such as thinning and splitting [17,21–23].

The initial plastic anisotropy can be geometrically presented by a yield surface, while numerically it can be treated primarily through two approaches. The first approach is the phenomenological approach, which is a modelling of the macroscopic plasticity in which the average behaviour of all the grains is determined generally with experimental and mechanical tests. The second approach is the micro-macro or polycrystalline plasticity approach [24]; it is based on the crystal behaviour and averaging scheme used to determine the behaviour of the polycrystalline material. These two approaches will be described in detail in the literature review chapters (chapter 3 & chapter 4).

Today, the phenomenological approach is the only realistic approach to define the yield criteria [18,25,26]. However, some of the advanced models have a high number of parameters which must be computed by conducting more experimental work. Such mechanical tests that are involved in the identification process are costly and time consuming and must be conducted with care [7,27]; therefore, they are unrealistic for the sheet forming industry.

The main downside of the polycrystalline plasticity approach is the fact that the computational costs are still quite high. This hinders their applicability for industrial applications. Degree of complexity of the most accurate anisotropic yielding models- advanced polycrystalline plasticity models- increases analogously to the degree of their capabilities. However, the question remains whether models under this approach can replace experimental tests.

The trend in recent years is to combine the strengths of the physics-based models and phenomenological yield criteria. Consequently, the severity associated with the extensive and difficult tests that are required for calibrating advanced flexible yield functions can be reduced. These issues can be solved to some extent by combining the strengths of the polycrystalline and phenomenological approach (i.e. the possible accuracy of the polycrystal plasticity models and the computational efficiency of the phenomenological models) [25]. Crystal plasticity models can provide data points or "virtual points or experiments" that can be employed, in addition to experimental data, to calibrate advanced macroscopic yield functions. In other words, they can identify the anisotropy coefficients of the macroscopic yield functions [28].

The process of improving texture-based models and documenting knowledge about the performances of different polycrystalline models, as well as their performances in fitting advanced yield functions for different metallic sheets, is still in progress.

Yield locus derived from Taylor models (TP and TF) -CTFP

Pioneering previous work in the area of combining the strengths of the two approaches showed that the simple Taylor models, namely the full constraint model (TF) and its relaxed version (TP), were able to be useful tools to describe the behaviour of different considered steel alloys [7]. In their work, the correlation between the calculated texture-based yield loci and those measured from mechanical tests to define advanced yield functions efficiently and effectively for different steel grades was investigated. Based on the two texture-based yield loci calculated from the Taylor models, An et al. proposed a

new combined model referred to as CTFP [7]. The applicability of this model on the considered aluminium alloys is firstly examined.

Yield locus derived from Taylor model (TF) -CTF

Following a similar methodology to the CTFP model, a new yield loci description based on the simple (Full constraint) FC-Taylor model is proposed and compared with different macroscopic yield functions in chapter 7. One of the ultimate goals of this thesis is to develop and validate this new description using two aluminium alloys (Al-Mg-Si alloys). The new methodology focuses on calibrating the initial yield loci of the BBC2005 for two aluminium alloys. Simplicity and efficiency were put under consideration at the phase of proposing this new description for the anisotropic yielding behaviour.

1.4.1.2 *Optimization of the phenomenological constitutive models parameters*

Advanced yield criteria are used in academia and industry to describe the onset of plastic anisotropy for a material subject to given strain paths. Advanced yield criteria involve a certain number of plastic anisotropy parameters that have to be identified. The Newton–Raphson (NR) procedure has been widely used to identify these parameters. However, this procedure can fail to converge, especially for highly anisotropic materials such as AA2090-T3 or initial guesses far from the solution. Moreover, methods based on Newton iteration fail if the Jacobian of the system of nonlinear equations associated with yield function is singular. This research presents three solution methods for identifying material coefficients: the Levenberg (L), Levenberg–Marquardt (LM), and trust region dogleg (TRD) methods. These algorithms are hoped to overcome the problems encountered with the NR procedure. The constitutive models used to investigate the capability of these optimization methods are the BBC2003 and Yld2000-2d yield criteria, which are suitable for various materials. The applied algorithms are tested for various aluminium and steel alloys with different levels of anisotropy. The sensitivity of the yield functions to the initial guess is examined for the various applied solution methods and materials. The robustness and the effectiveness of the solution methods are investigated for the yield functions and materials. Finally, the performances of the yield functions are compared for the considered identification procedures for different materials.

1.4.2 Accurate and cost-effective description of the biaxial flow curve

In sheet metal forming simulation, flow curve and yield criterion are vital requirements for reliable numerical results. It is more appropriate to determine the flow curve using biaxial stress state tests such as the hydraulic bulge test instead of the uniaxial test because

hardening proceeds higher strains before necking occurs. With the uniaxial test, higher strains are extrapolated, which might lead to incorrect results. The bulge test, coupled with the digital image correlation (DIC) system, is utilized to determine the stress-strain data. In the absence of the DIC system, analytical methodologies are used to estimate hardening.

The hydraulic bulge test, in combination with a digital image correlation (DIC) system, is the state of the art to determine the biaxial stress-strain curves [29–31]. However, in the absence of continuous and in-line thickness measurement systems, such as the DIC system, researchers use simple analytical methods to determine the biaxial flow curves [30,32]. Furthermore, the usefulness of these analytical methodologies becomes apparent when deformation is reordered at high temperature [32,33]. It was reported by Koc et al. [33] that the results obtained with optical systems are inaccurate due to vapour and smoke occurring during deformation at high temperatures. These methods are concerned with identifying the bulge radius as well as the thickness at the dome apex.

Typically, such models incorporate a correction factor to achieve correlation to experimental data. An example is the Chakrabarty and Alexander method that uses a correction factor based on the n-value. Here, the Chakrabarty and Alexander approach is modified using a correction factor based on normal anisotropy.

Finally, because the biaxial flow curve is required to compute the biaxial yield stress, which is an essential input to define advanced yield functions, the effects of the different approaches of the biaxial stress-strain data determination on the shape of the BBC2005 yield loci is also investigated.

1.5 Structure of the thesis

This chapter has discussed the general framework of the thesis. Chapter 2 describes the basic concepts and aspects of plastic deformation involved in the sheet metal forming processes that are related in particular to phenomenological yield functions. The next two chapters are dedicated to modelling the initial plastic anisotropy. Chapter 3 presents the phenomenological approach, while chapter 4 is dedicated to the polycrystalline plasticity approach and the method of calculating the yield locus by combining the strengths of the two approaches. Chapter 5 describes the concept of the flow curve determination under the biaxial stress condition, in the absence of continuous and in-line thickness measurement systems. The literature review is included in these chapters where appropriate. Notably, chapters 3 to 5 discuss the original contributions of this thesis where

appropriate to each objective. In chapter 6, the methodology followed to reach the goals of this manuscript is described. Chapter 7 presents the results of the new yield loci, based on the FC-Taylor model, which are proposed for aluminium alloys. Chapter 8 presents and evaluates the reviewed solution methods: the TRD algorithm, Levenberg algorithm, and Levenberg-Marquardt algorithm. In chapter 9, the results of the new methodology proposed to determine the biaxial flow curves are presented. Finally, the conclusions of this project, including a proposal for future work in the field, are formulated in chapter 10.

Chapter 2

Concepts of Continuum Plasticity

2.1 Introduction

Sheet metal forming processes involve plastic deformation. Therefore, the materials properties, including the stress-strain relations, should be characterised accurately so they can be used in the numerical analysis of the sheet metal forming processes. This relation is derived principally from the yield surface, which is one of the fundamental elements necessary to develop sound constitutive equations for anisotropic materials in the field of sheet metal forming. This thesis is not concerned with the evolution of the yield surface but rather the definition of its initial shape (i.e. the initial plastic anisotropy).

The initial plastic anisotropy can be presented geometrically by a yield surface, while numerically it can be treated primarily through two approaches. The first method is the phenomenological approach, which models the macroscopic plasticity in which the average behaviour of all the grains is determined predominantly with experimental and mechanical tests. The second method is the micro-macro or polycrystalline plasticity approach [24], which is based on the crystal behaviour and averaging scheme utilised to deduce the behaviour of the polycrystalline material. The phenomenological approach is described in greater detail in chapter 3 and the polycrystalline approach is described in chapter 4.

This chapter presents a concise review of basic concepts that are related to phenomenological yield functions. These functions describe the behaviour of metallic sheets. The phenomenological approach is the most commonly used approach to describe the plasticity of polycrystalline metallic sheets. The phenomenological yield functions approximate the experimental data through analytical functions.

Before describing the anisotropic yielding models that relate to sheet materials (chapter 3), this thesis addresses in the current chapter key aspects of plastic deformation involved in the sheet metal forming processes.

The yield functions, loci, surface and condition definitions, and approaches for designing them are described in section 2.2. Section 2.3 relates yielding behaviour to the drawability

of sheet material, its failure and general formability. Finally, a summary of the chapter is given in section 2.4.

2.2 Formulation of the rate independent metal plasticity

Classically, the rate independent plasticity is formulated with the following ingredients:

- An equivalent stress and a yield function must be identified.
- A hypothesis such as the maximum plastic dissipation [34] must be applied to derive the associated flow rule (normality rule) and to prove convexity of the yield surface in the stress space.

In section 2.4.1, the concept of normality rule (associated flow rule) is discussed briefly. Section 2.4.2 introduces the concept of the yield surface. Finally, section 2.4.3 summarises the approaches that are used to develop phenomenological yield functions in general.

2.2.1 Normality rule, associated and non-associated

The normality rule hypothesis describes the relationship between the stresses and plastic strain increments [1]. This connection between yielding and plastic strain increments is required to form a sound constitutive equation [35]. This hypothesis is obtained from microstructural consideration [36]. In particular, Bishop [37] showed that the yield surface of a single crystal is convex and the plastic strain increment is normal to the surface. Most of the developed anisotropic yield functions are based on the associated flow rule hypothesis [38] which states that [39]

- The gradient of the yield function is normal to the yield locus and
- The plastic strain-increment $d\varepsilon^p$ is equal to the gradient $\frac{\partial F}{\partial \sigma}$ multiplied by a scalar factor of proportionality λ_1; i.e. $d\varepsilon^p = \lambda_1 \frac{\partial F}{\partial \sigma}$ where F is the yield function.

Figure **2.1** illustrates the principle of the normality rule. Knowing the yield locus expressed by F, the plastic strain-increment $d\varepsilon^p$ can be calculated, and the strain ratio $d\varepsilon_{yy} / d\varepsilon_{xx}$ can be obtained.

The equivalent stress is a representative expression that predicts the yielding of material for a multiaxial stress state [39]. The expressions of the **equivalent stress** as well as the **yield function** are specific to the yield criterion adopted in the plasticity model [6].

The maximum plastic dissipation hypothesis [34], Drucker's postulate of material stability [40], or the framework proposed by Aretz [39] are different hypotheses or frameworks that can be used to derive the associated flow rule and to prove the convexity of the yield surface. These hypotheses are considered necessary conditions for stability [41].

Convexity is an essential property of the yield functions. The yield surface with no vertex is represented by a convex yield function. Mathematically, convexity is provided if the Hessian matrix of the yield function is positive semi-definite (i.e. its eigenvalues are positive or zero) [38]. This property is the primary issue in the development of orthotropic yield functions [42]. If the normality rule is violated, then the convexity is not preserved [35]; therefore, stability in numerical simulations is not ensured [16].

It has been reported recently that the normality rule is invalid for application to porous, geological materials [43] and even aluminium and steel alloys [41]. However, experimental observations reveal that the normality hypothesis is assumed to hold true for dense materials such as aluminium and steel alloys [42].

2.2.2 Yield criterion "or condition", function, surface, and locus

A surface in the stress space that separates elastic from plastic deformation is called the yield surface [44]. Mathematically, this surface is expressed as

$$F(\sigma_{ij}) = Y_{ref} \tag{2.6}$$

where F is the yield function which operates on stress tensor components σ_{ij} while Y_{ref} is a constant, known as the yield condition, which is typically defined by the yield stress in the rolling direction [44]. It is a condition or criterion under which the material's state transits from the elastic region to the plastic region. This transition occurs when the stress reaches the yielding point of the material, which can be easily identified in the uniaxial tension stress state. However, defining the transition in a multi-axial stress state is more difficult. Therefore, the yield function (F), which specifies the condition under which yielding occurs, is required to express a relationship between the principal stresses [6].

The yield function F defines the transition boundary that separates the elastic region from the plastic stress state for a metallic sheet subjected to a cold forming process. This yield function is related to the equivalent stress, and the relationship is expressed mathematically as

$$F = \bar{\sigma} - Y_{ref} = 0 \tag{2.7}$$

One of the central elements used to describe the material's plastic behaviour is the yield criterion. It defines a relationship between the stress components at the moment when yielding occurs [6].

The yield surface is represented by a mathematical equation (2.7) in a three-dimensional space of the principal stresses. For the case of the plane stress state, the representation will be in 2-D. This surface/locus must be closed, smooth, and convex. All the points inside the surface/locus ($F < 0$) define the elastic region, while the points located outside the surface/locus ($F > 0$) have no physical meaning. However, the points belonging to the surface/locus ($F = 0$) define the plastic state (i.e. they describe the yield surface/locus) [42]. Figure **2.1** represents the von Mises [45] locus shape for a plane stress state. It also shows the principle of the normality rule discussed in the previous section.

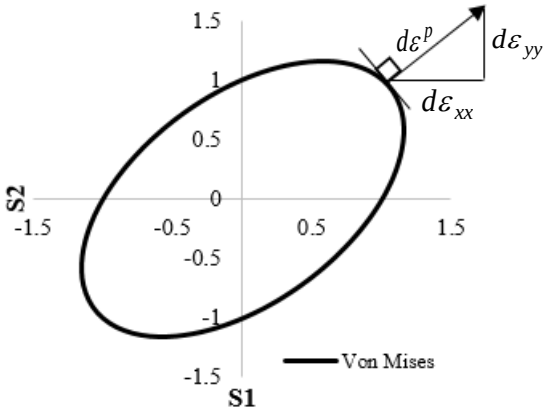

Figure 2.1. The von Mises and normality hypotheses.

2.2.2.1 *Approaches for designing yield functions for anisotropic metals*

Different methods can be used to develop anisotropic yield functions [46]. These methods are employed to transform isotropic formulations into anisotropic expressions. The approaches for designing anisotropic yield functions are described in [6,42] and summarized in the following paragraph.

The first approach is to include new parameters into an isotropic function [6]. The authors of Hill'48 [47] used the method of including new coefficients into von Mises [45], while the authors of BBC2003 and BBC2005 [48,49] included new plastic anisotropy parameters into Hershey's formulation [50]. A second approach is to use linear transformation. Examples of anisotropic yield functions that are based on linear

transformations are Barlat'91, Karafillis and Boyce and Yld200-2d [19,51,52]. Geometrical methods such as the Vegter model [53], which applies second-order Bezier interpolations, are the third approach. The anisotropy coefficients of this model are derived from four mechanical tests. Some of these tests have to be repeated for various directions. This greater number of parameters leads to a far more accurate description of the yield loci than other yield functions [53]. A fourth approach is based on the theory of tensor representations [54]. This approach can result in difficulty in ensuring convexity [36]. Finally, other yield functions introduce anisotropy by extending the functions outside the orthotropic axes by utilising coordinate transformations [6]. Examples of this approach are Barlat 1989 [55] and Hill 1990 [56].

2.2.2.2 *Mechanical parameters required for the identification procedure*

Each yield criterion has its own requirements. Particularly, each yield function has a certain number of mechanical parameters (Yield stresses, e.g. YS_0 ; and *R*-values, e.g. R_{90}) that must be obtained from experimental tests. These parameters work as inputs to the yield functions. The more advanced the yield function, the more tests required. As a large number of parameters are incorporated within the advanced yield functions, it is expected that these functions would describe the plastic behaviour of the materials more accurately. However, as illustrated in **Table 2.1**, yield criteria such asYld20004-18 [36] and Vegter [53] require 18 and 17 mechanical parameters, respectively. Therefore, their identification procedure is time consuming and expensive compared to the von Mises yield criterion that requires only one mechanical parameter, YS_0 .

Generally, these mechanical parameters/inputs obtained from the experimental tests are fed either to parameters of analytical yield function such as the case in Hill'48 [47] or a system of nonlinear equations associated with the yield function. In the latter case, the roots are used to calibrate the yield function shape to certain experimental points as in the case of advanced models such as BB2005 and Barlat 2000. The roots of such systems are called plastic anisotropy parameters (or coefficients or constants). These parameters are fed to the yield function in order to define the anisotropic locus. The roots can be identified using different numerical procedures such as Newton Raphson [19,48], minimisation of an error function [20,57], and genetic algorithm [58]. More discussion about the different numerical strategies that are used in the field will be held in chapter 3.

Table 2.1 shows the mechanical parameters required for the identification of various yield criteria, some of which will be used in this study and described in the next chapter. As

shown in **Table 2.1** some of the yield loci can be extended into full stress state (3-D), while most of them were developed only to account for the plane stress process (2-D). Each of the listed models has different levels of effectiveness in their capability to predict first anomalous behaviour denoted as A1 and second anomalous behaviour referred to as A2.

Table 2.1. Mechanical parameters required for the identification procedure. Table adopted from [6].

Model	YS_0	YS_{45}	YS_{90}	Y_b	R_0	R_{45}	R_{90}	R_b	$3D$	$A1$	$A2$	**More tests**
Von Mises-1	x								x			
Hill'48-4	x				x	x	x		x			
Hosford'79-4	x				x		x		x	x		
Barlat'89-4	x				x		x			x		
Barlat 2000-8	x	x	x	x	x	x	x	x		x	x	
BBC2003-8	x	x	x	x	x	x	x	x		x	x	
BBC2005-8	x	x	x	x	x	x	x	x		x	x	
Barlat 2004-18	x	x	x	x	x	x	x	x	x	x	x	x
Vegter-17	x	x	x	x	x	x	x	x		x	x	x

2.3 Importance of the yield function

In classical rate-independent plasticity, the yield surface is the central ingredient for modelling rate-independent materials because it separates between elastic and plastic domains [42]. Also, it serves as a potential for the plastic strain increments (i.e. it determines the direction of the plastic increment) [46].

The influence of different yield surface models on the quality of the computed predictions in the field of sheet metal forming processes was analysed extensively by different researchers. It has been proven that these yield surfaces have a critical influence on the accuracy of the numerical simulation results. A glimpse of the research on this effect is given in the following paragraphs.

2.3.1 Earing profile

Earing phenomenon is noticed when the height of the wall of the drawn cylindrical part have peaks and valleys [59] as shown in Figure **2.2** (on the left). It should be mentioned

that the classical isotropic von Mises yield function predicts that no ears appear when a cup is deep drawn [60,61]. The earing profile predicted by the classical anisotropic model, Hill'48 [47], is incorrect, as is shown in Figure **2.2** on the right, and four ears maximum can be predicted [24]. It has been shown that simulations based for instance in [62] agreed generally with the experimental results, as illustrated in Figure **2.2** on the right.

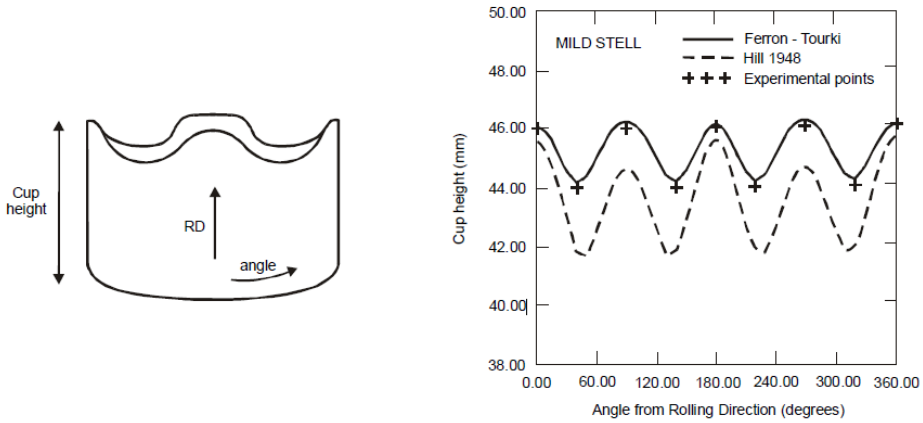

Figure 2.2. Deep drawing of a cylindrical cup with its predicted and calculated earing profiles [24].

In general, in round cup drawing simulations, materials exhibit four ears; however, this is not the case for highly anisotropic materials which could develop six or eight ears [63]. The earing profile of such materials can be predicted accurately using yield functions that use at least eight material parameters [63,64]. As a matter of fact, this kind of challenge was the main drive to develop more advanced yield functions that are capable of predicting the earing profile more precisely [63,65].

In [66], a simulation of a drawing process was conducted for the highly anisotropic material-AA2090-T3, utilising the analytical yield function YLD2004-18P, proposed by Barlat et al. [36]. The study concluded that the earing profile with six ears is well predicted provided that the anisotropy of the tensile properties is captured accurately. The same conclusions are drawn in [63] when the BBC2008 [20] yield function is utilised. This study proved that the BBC2008 model can predict the earing profile for highly textured materials provided that the materials characterization is done properly.

2.3.2 Forming limit diagrams -FLD

The forming limit diagram is an important tool in the sheet metal forming industries. Forming limit diagram or curve is used to predict limits of the in-plane strains that metallic sheets can resist before failure [1]. Extensive research efforts were performed to

study the influence of the different yield loci on theoretical forming limits. A few examples illustrating the importance of the advanced yield functions are given in the following paragraphs.

It has been reported by Banabic et al. [49,67] that the forming limit diagrams predicted well, for steel and aluminium alloys, by the BBC2005 [49].

Another investigation of the impact of the yield surface on the prediction of the FLD was reported by Vegter et al. [68]. In the case of aluminium alloy (5182), the prediction of the Vegter model [53], as illustrated in Figure **2.3**, shows that the part is critical (i.e. failure occurs during the deformation process), while Hill'48 holds the opposite.

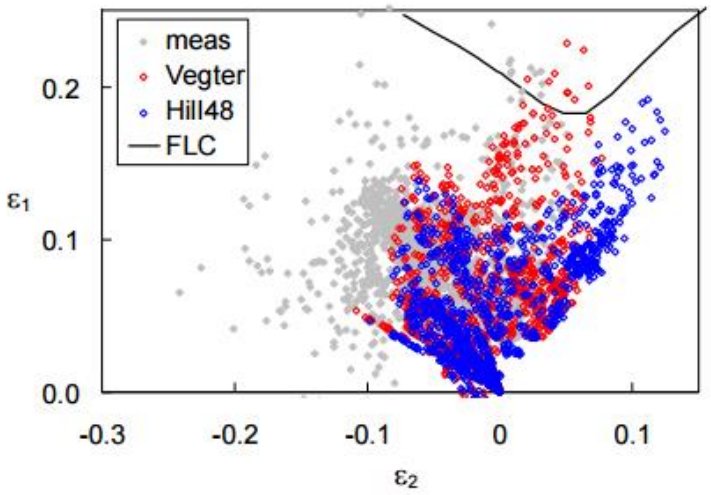

Figure 2.3. Comparison of simulations using Hill'48 yield locus and the Vegter yield criterion [68].

2.3.3 Thickness strain

In [69], the performance of the Hill'48 yield function fitted with two and four parameters [47], Barlat'89 fitted with four coefficients [55], and the BBC2005 yield function calibrated with six, seven, and eight mechanical parameters [49] was evaluated for the prediction of the thickness strain distribution, as shown in Figure **2.4**. The results shown in the figure were compared with experiments, and the conclusion that can be drawn is that the more advanced the material model, the better the accuracy of the prediction.

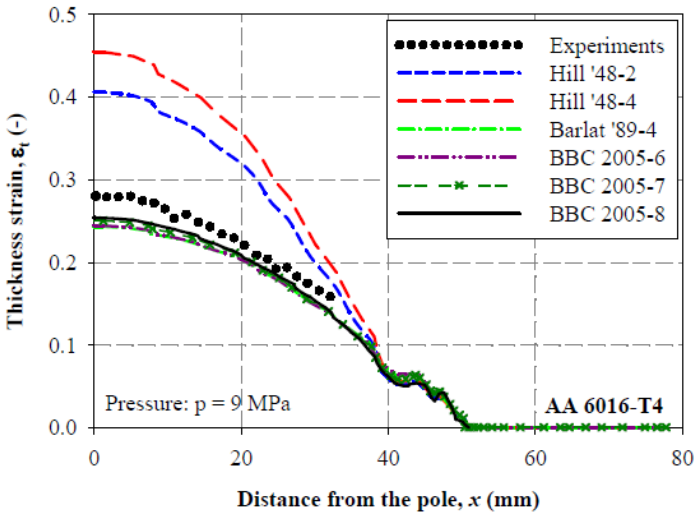

Figure 2.4. Comparison between prediction and experiment for thickness strain distribution [69].

2.3.4 Complex automotive part

An investigation was done on the effect of different yield surfaces on the accuracy of the forming simulations of a tailgate inner of the Renault Modus, which is a complex automotive part [70]. Horn et al. were able to demonstrate that the Corus-Vegter material model [68] could predict rupture risk, thinning, and strain distribution more accurately than the Hill'48 [47] and Hill'90 [56] yield functions.

2.4 Summary

When the change in the time scale does not influence the constitutive equations that describe the plastic deformation in cold forming processes, then rate independent plasticity is utilised [71]. In conventional sheet metal forming processes such as stamping, deep drawing, etc., the anisotropic metallic sheet deforms plastically under stretching, but not compression [72]. Therefore, the following assumptions are considered true for the yield functions used in this thesis:

- Effect of the perpendicular stress is negligible
- Plastic deformation is assumed to be pressure insensitive for aluminium and steels alloys; therefore, SD effect is neglected
- Utilised yield surface reveals symmetry around the origin
- Normality hypothesis is assumed to be true for the aluminium and steel alloys in this study

- Utilised yield functions can represent the anomalous behaviours that might be exhibited in some materials such as aluminium alloys

In this chapter, some of the basic principles and concepts of continuum plasticity are discussed. These principles are used frequently in the following chapters. In addition, this chapter shows that the yield surface has a vital impact on the quality of the numerical simulation results in the field of sheet metal forming. The next chapter describes different isotropic and anisotropic functions.

Chapter 3

Phenomenological Approach

3.1 Introduction

It is outside the scope of this thesis to cover and describe all the isotropic and anisotropic phenomenological yield functions proposed in the literature. This approach uses a yield function that employs an analytical expression such as the von Mises [45] and Tresca [73] criteria for isotropic materials. A brief outline of the history of the development of the isotropic models is given in section 3.2.1. It is followed by a description of the von Mises and Tresca criteria in section 3.2.2 and section 3.2.3.

However, anisotropy is an intrinsic feature of sheet materials. Therefore, for anisotropic materials, researchers developed numerous material models that have been able to describe the anisotropic material behaviour accurately. These include models related to Hill's family criteria, Hershey's family criteria, and many others. Section 3.3.1 illustrates the chronological enhancement in the anisotropic yield criteria. The remaining sections are devoted to describing succinctly the yield functions for anisotropy plasticity that are used in this thesis. From section 3.4 to section 3.6, the trust region technique for modelling in sheet metal forming is featured. In particular, this robust technique is introduced to the phenomenological approach for solving the systems of nonlinear equations associated with some of the advanced yield criteria. Finally, a summary of the chapter is provided in section 3.7.

3.2 Yield criteria for isotropic materials

3.2.1 Introduction

Tresca [73] and von Mises [45] proposed two of the oldest and most popular isotropic yield criteria. Subsequently, Hershey [50] and Hosford [74] independently introduced two identical isotropic non-quadratic yield functions. These two functions reproduced the yield surface calculated with a polycrystalline model [36]. Both of these non-quadratic criteria could be reduced to von Mises and Tresca as special cases [4]. A drawback of these criteria is that the shear stress is not accounted for; therefore, the prediction of the planar anisotropy of the *R*-values as well as uniaxial yield stresses are inaccurate [6].

Another earlier proposal was published by Drucker [75] who developed an isotropic function with a yield surface that is located between the Tresca and von Mises yield criteria. More examples of isotropic criteria are reviewed by Yu [76]. Tresca and von Mises are described briefly in the following sections.

3.2.2 Tresca, the maximum shear stress theory

Tresca criterion states that the plastic strains occur by crystallographic slip under acting shear stress [6,77]. The material transitions from an elastic to plastic region when the maximum shear stress attains a critical value.

It is known as the maximum shear stress theory. This theory states that yielding of the ductile materials occurs as a result of a slip along the crystalline planes after shear stress is applied. The material begins to yield when an absolute maximum shear stress in the material reaches the maximum shear stress in a specimen of the same material subjected to an axial test [77]. The maximum shear stress τ is equal to the uniaxial yield point σ_0 divided by 2. The value of the uniaxial yield point σ_0 is defined from a simple tension test. In the case of plane stress, the principal stress in the normal direction σ_3 is assumed to be zero. If $\sigma_1 > \sigma_2$, then

$$\tau = \frac{\sigma_0}{2} = \frac{|\sigma_1 - \sigma_2|}{2} \rightarrow \sigma_0 = |\sigma_1 - \sigma_2| \tag{3.1}$$

Figure **3.1** shows Tresca yield locus as a hexagonal locus represented by equation (3.1).

3.2.3 Von Mises theory

The von Mises theory is based on the observation that the hydrostatic pressure cannot yield the material. It concludes that only the elastic energy of distortion affects the material to be transitioned from the elastic region to the plastic stress state. This criterion will be referred to as the Mises criterion. This criterion is also known as the distortion energy theory or the shear energy theory; it is up to 15% more accurate than Tresca. It predicts that the yielding in a ductile material begins when the distortion energy per unit volume (U_d) becomes equal to the distortion energy per unit volume of the same material that is associated with yielding in a simple tensile test [$(U_d)_y$] [77]. In other words, $U_d = (U_d)_y$.

$$U_d = \frac{1+\nu}{6E}\left[(\sigma_1-\sigma_2)^2+(\sigma_2-\sigma_3)^2+(\sigma_3-\sigma_1)^2\right] \tag{3.2}$$

$$(U_d)_y = \frac{1+\nu}{3E}\sigma_0^2 \tag{3.3}$$

where υ and E are the Poisson ratio and modulus of elasticity, respectively. Then the equation that represents the theory for the triaxial state of stress is

$$2\sigma_0^2 = \left[(\sigma_1-\sigma_2)^2+(\sigma_2-\sigma_3)^2+(\sigma_3-\sigma_1)^2\right] \tag{3.4}$$

In the case of plane stress ($\sigma_3 = 0$), then the equation becomes

$$\sigma_0^2 = \sigma_1^2+\sigma_2^2-\sigma_1\sigma_2 \tag{3.5}$$

This equation represents an ellipse in the 2-D space, as illustrated in Figure 3.1.

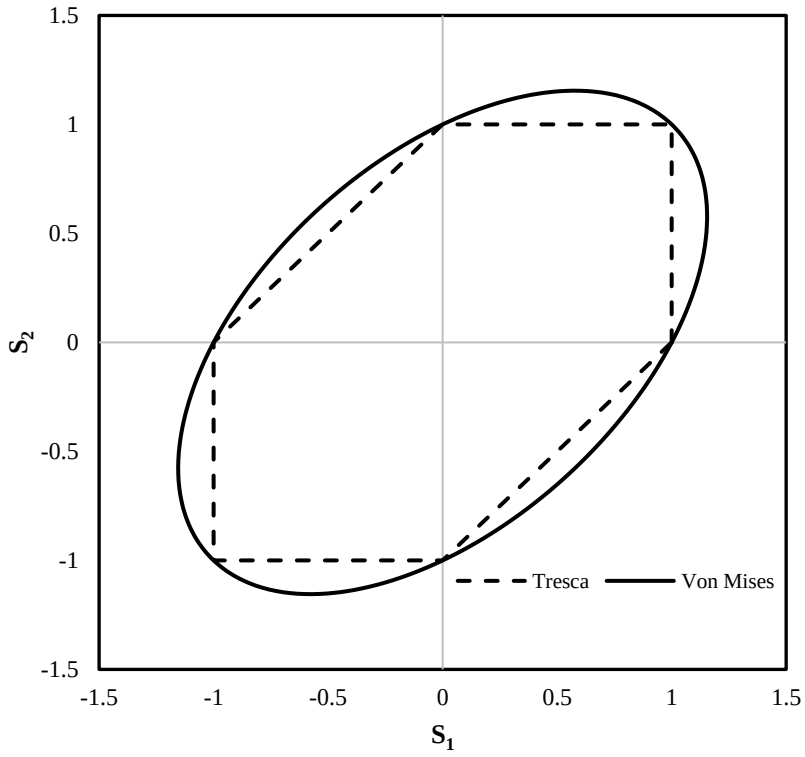

Figure 3.1. Tresca and von Mises yield loci.

3.3 Yield criteria for anisotropic materials based on the associated flow rule

This section covers a historical development of the anisotropic yield functions that are based on the associated flow rule.

3.3.1 Introduction

In reality, isotropic criteria are not able to predict the yielding properties of anisotropic materials since the properties of the metallic sheets in particular are directional [4]. The metallic sheets are orthotropic materials because the sheets experienced severe deformation during the rolling processes. Therefore, Hill [47] extended the von Mises theory in a quadratic form that suits orthotropic materials. Hill'48 is widely used in practice due its simplicity [18]. However, it is observed experimentally that this criterion cannot represent the first and second anomalous behaviours that are exhibited in some aluminium materials [6]. Additionally, this model can predict an inaccurate earing profile [63].

Non-quadratic yield functions were proposed to circumvent the weaknesses of the quadratic approach [42]. Therefore, Hill [78] proposed a non-quadratic yield function that can describe only the first-order anomalous behaviour. However, this yield function can be used when the directions of the principal stresses coincide with the orthotropic axes. Later on, Hill [56] generalised Hill'79 by expressing it in a general coordinate system. However, the formulation of this criterion is not user-friendly, and it also needs large CPU times when used in FEM. Hill [79] proposed simpler yield function that could overcome the two anomalous behaviours exhibited by aluminium alloys. However, the yield loci predicted by this function do not account for shear components, and the results obtained are far from the ones obtained from polycrystalline plasticity models (e.g. Taylor models) [6].

Independently from Hill, Hosford [74] proposed an important non-quadratic yield function based on Hershey's model [50], and the derived yield locus of this function was generally an accurate approximation to the computed yield loci from the Taylor model [4,6]. However, the function was not able to predict variation of the *R*-values with direction or the planar anisotropy of the uniaxial yield stresses because these criteria do not accommodate for shear stresses in their forms. It has to be mentioned that Hershey [50] and Hosford [74] are identical non-quadratic yield functions independently proposed.

Nonetheless, Hosford/Hershey's model served as the basis for more advanced yield functions that included the shear stresses in their forms in order to be able to predict the planar anisotropy of the *R*-values as well as uniaxial yield stresses [4,18,42].

Barlat and Lian [55] proposed an extended version of the Hosford's yield function to account for materials exhibiting planar anisotropy (i.e. the form involving shear stresses). However, the model cannot predict the yield stress at the biaxial stress state, especially for aluminium alloys with a pronounced anisotropy [6]. In practice, it is one of the most frequently used models due to its simplicity, although the model predicts unrealistic loci for highly anisotropic materials such as AA2090-T3 [18].

An isotropic yield function was proposed in [52] and then adopted for anisotropic materials based on linear transformation. Yield loci derived by this function agree well with experimental data as well as yield loci computed by the Bishop-Hill polycrystal plasticity theory. This function also agrees well with the experimental data for the variation of the *R*-value and the uniaxial yield stress in the plane of the sheet [6]. A deficiency of this model is that the identification procedure is complex. Furthermore, this criterion cannot account for more than four mechanical parameters.

To consider more mechanical parameters for plane stress state, Barlat et al. proposed a series of models [51,80] that extended the Hosford's criterion. Barlat'96 model provided in some cases good predictions of the *R*-values and uniaxial yield stress variations in the plane of the sheet [6]. However, it was reported that for aluminium-magnesium alloys the prediction was unreliable, especially in the pure shear regions [80]. Another disadvantage of such models is that convexity is not guaranteed; therefore, stability in numerical simulation cannot be ensured. Moreover, the CPU time is considerably larger for these models.

Of note, several non-quadratic yield criteria were proposed, including [81–83], but their use is limited [6]. Gotoh [81] proposed a yield function expressed in a polynomial form. Other proposed criteria [82,83] are expressed in polar coordinates.

3.3.1.1 *The need for more advanced criteria*

Sheet metal forming industries such as automotive and aerospace face a high level of competition, and time to market is a critical aspect of these industries. Weight reduction also is a priority across these industries to improve fuel efficiency and reduce gas emissions; therefore, more advanced materials were developed [4,6,42]. Because of this, the development of advanced yield functions that can model the anisotropic behaviour of these advanced materials accurately is encouraged [4,42]. With the advent of new materials, the necessity of developing more advanced yield criteria became apparent.

Several new yield functions have been proposed since 2000. Such models can predict the variations of the *R*-values and uniaxial yield stresses in materials exhibiting planar anisotropy [6]. Furthermore, these models can model materials with different crystallographic structures which are

- Body-centred Cubic (BCC),
- Face-centred Cubic (FCC), and
- Hexagonal Close-Packed (HCP).

These advanced models can describe the plastic behaviour of the materials more accurately because many parameters are incorporated in them. These models, which are considered to be advanced models, include Barlat yield criteria [19,36], Banabic-Balan-Comsa (BBC) yield criteria [48,57,84], Cazacu-Barlat yield criteria [54,85], polynomial yield criteria [46,86], and Vegter model [53].

Experimental observations showed that most of these advanced yield surfaces can accurately describe the biaxial stretching region which is the dominant deformation mode in sheet metal forming. Numerous researchers explored the validity of these yield criteria. For instance, Mattiasson and Sigvant [18] proved that two advanced yield criteria, referred to as Yld2000 and BBC2000, are suitable for industrial sheet forming applications. Researchers [65] proved that Yld2000 could capture the earing profile (number of ears as well as overall shape) of certain aluminium alloys. Researchers in [49] and [87] demonstrated that BBC2005 and BBC2003, respectively, can describe the effects of the plastic anisotropy of the metallic sheets (aluminium and steels) subjected to forming processes such as bulging and cross deep drawing.

Figure **3.2** shows the importance of the more advanced models in comparison with classical models such as Hill'48 and Barlat'89. It reveals the yield loci, calculated using different yield functions for the AA6016 T4 aluminium alloy, in comparison with the experimental data. The yield surface was determined using two versions of Hill'48, Barlat'89 and three versions of BBC2005 in comparison with the experimental points. Only the two versions of the BBC2005 model (BBC2005-7 & BBC2005-8) were able to predict the biaxial stress state well. This improved ability was because these versions include the biaxial yield stress in the identification process [69].

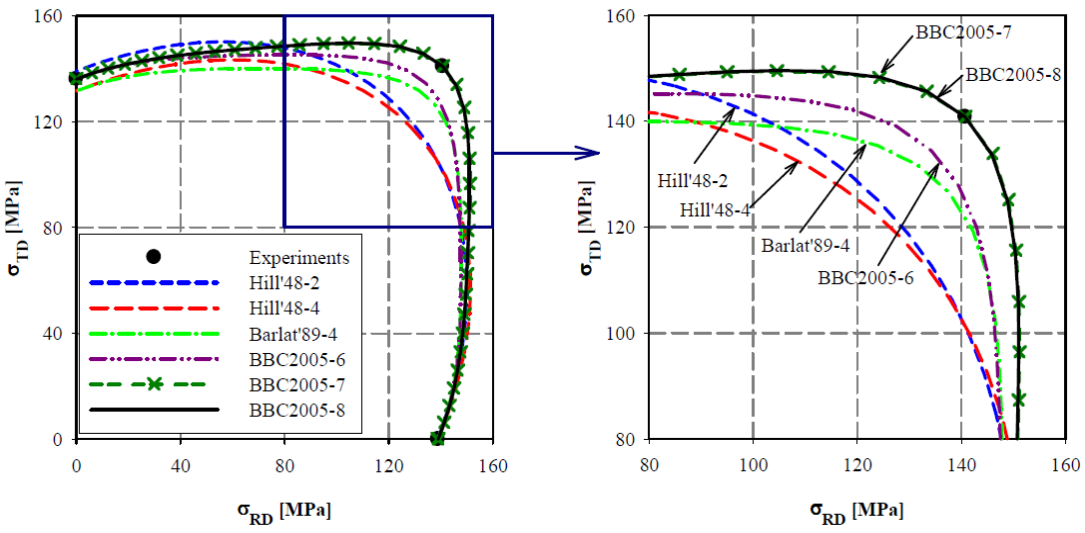

Figure 3.2. Comparison of different yield loci [69].

3.3.1.2 *Complex yield criteria*

Researchers realised that the description of the anisotropic behaviour of the metallic sheets can be improved further. Therefore, different complex yield criteria were proposed such as BBC2008 introduced by researchers in [20] with 16 experimental values. Another example of complex yield criteria is the function proposed by Barlat et al. [36], denoted as Yld2004-18. This yield function requires 18 and 13 experimental values for 3-D and 2-D cases, respectively. Some of these values are calculated using polycrystalline plasticity model. A further example is the Vegter model [53] which is based on interpolation by second-order Bezier curves. The anisotropy coefficients of this model are derived from four mechanical tests (uniaxial tension, biaxial tension, plane strain, and pure shearing). Some of these tests must be repeated for various directions. This number of parameters leads to a far more accurate description of the yield loci than other yield functions. However, the accuracy of these complex models is achieved at the expense of cost. Most of the anisotropic yield functions mentioned here are implemented in the commercial finite element software dedicated to numerical modelling of sheet metal forming. These kinds of complex criteria are recommended only when accuracy is desired (for example, when dealing with highly textured materials such as 2090-T3).

The models that are utilised in this thesis are described briefly in the following sections. The description will be limited to yield criteria that use a maximum of eight experimental values since, as shown in [63,64], phenomena such as earing can be predicted accurately using yield functions that employ at least eight material parameters.

3.3.2 HILL 1948 (Hill'48)

Hill'48 proposed in [47] the first anisotropic yield function, which is the most commonly used in practice due to its simplicity and effectiveness with weakly textured materials. Hill'48 is a generalisation of the von Mises yield function. The anisotropy is introduced analytically into the von Mises formulation. Its parameters are calibrated using either the *R*-values or yield stresses. The description here will be limited to the *R*-value based Hill'48. The yield function, for plane stress state, is expressed as

$$\sigma_1^2 - \frac{2R_0}{1+R_0}\sigma_1\sigma_2 + \frac{R_0(1+R_{90})}{R_{90}(1+R_0)}\sigma_2^2 = \sigma_0^2 \tag{3.6}$$

where σ_0 is the uniaxial yield stress in the RD; σ_1, σ_2 are the stress components; and R_0, R_{90} are the *R*-values of the RD and TD, respectively.

3.3.3 Barlat 1989 (Barlat'89)

To describe the planar anisotropy for full plane stress state (i.e. including the shear stress component), a yield function for materials exhibiting planar anisotropy was proposed by Barlat and Lian [55]. The yield function is written as follows:

$$\begin{aligned} F &= a_B\left|k_1 + k_2\right|^{M_B} + a_B\left|k_1 - k_2\right|^{M_B} + c\left|2k_2\right|^{M_B} = 2\bar{\sigma}^{M_B} \\ k_1 &= \frac{\sigma_{11} + h\sigma_{22}}{2} \\ k_2 &= \sqrt{\left(\frac{\sigma_{11} - h\sigma_{22}}{2}\right)^2 + p^2\sigma_{12}^2} \end{aligned} \tag{3.7}$$

where F is the yield function; k_1, k_2 are stress tensor invariants; $\sigma_{11}, \sigma_{22}, \sigma_{12}$ are the stress components; a_B, c, h, p are material constants; M_B is a material parameter; and $\bar{\sigma}$ is the effective stress identified with the uniaxial flow stress.

Using the *R*-values obtained from uniaxial tensile test in three directions is one of the methods for identifying *a*, *c*, and *h* parameters, as shown in equation (3.8).

$$\begin{aligned} a &= 2 - c = 2 - 2\sqrt{\left(\frac{R_0}{1+R_0}\right).\left(\frac{R_{90}}{1+R_{90}}\right)} \\ h &= \sqrt{\left(\frac{R_0}{1+R_0}\right).\left(\frac{1+R_{90}}{R_{90}}\right)} \end{aligned} \tag{3.8}$$

The coefficient p can be determined graphically or by using a numerical method, as described in [55].

3.3.4 Yld2000-2d

A yield function for the plane stress condition was proposed in [19]. It was developed to overcome the weaknesses of the yield criteria proposed by [51,80]. The function is based on two linear transformations of the stress deviator. It contains eight anisotropy parameters that are derived from flow stresses and *R*-values in uniaxial tension in three directions, as well as the flow stress and *R*-value in the biaxial regime [19].

Barlat et al. proposed a plane stress yield function ϕ that is found as the sum of two isotropic, convex functions ϕ' and ϕ'' [16,19]. It is defined as

$$\phi = \phi'(\tilde{S}_1', \tilde{S}_2') + \phi''(\tilde{S}_1'', \tilde{S}_2'') \tag{3.9}$$

or

$$\phi = \left|\tilde{S}_1' - \tilde{S}_2'\right|^a + \left|2\tilde{S}_2'' + \tilde{S}_1''\right|^a + \left|2\tilde{S}_1'' + \tilde{S}_2''\right|^a = 2\bar{\sigma}^a \tag{3.10}$$

where the coefficient a is constant (6 for steel alloys and 8 for aluminium alloys). This anisotropic yield function is associated with the effective stress:

$$\bar{\sigma} = \left\{\frac{1}{2}\left|\tilde{S}_1' - \tilde{S}_2'\right|^a + \left|2\tilde{S}_2'' + \tilde{S}_1''\right|^a + \left|2\tilde{S}_1'' + \tilde{S}_2''\right|^a\right\}^{1/a} \tag{3.11}$$

In equations (3.9), (3.10), and (3.11), $\tilde{S}_1'$, and $\tilde{S}_2'$, and $\tilde{S}_1''$ and $\tilde{S}_2''$ are the principal values of the two transformed stress deviators $\tilde{S}'$ and $\tilde{S}''$, respectively. For the plane stress state and orthotropic symmetry, these transformed stress deviators can be written in a matrix form as

$$\tilde{S}' = \begin{bmatrix} \tilde{S}'_{xx} \\ \tilde{S}'_{yy} \\ \tilde{S}'_{xy} \end{bmatrix} = \begin{bmatrix} C'_{11} & C'_{12} & 0 \\ C'_{21} & C'_{22} & 0 \\ 0 & 0 & C'_{66} \end{bmatrix} \begin{bmatrix} S_{xx} \\ S_{yy} \\ S_{xy} \end{bmatrix},$$
$$\tilde{S}'' = \begin{bmatrix} \tilde{S}''_{xx} \\ \tilde{S}''_{yy} \\ \tilde{S}''_{xy} \end{bmatrix} = \begin{bmatrix} C''_{11} & C''_{12} & 0 \\ C''_{21} & C''_{22} & 0 \\ 0 & 0 & C''_{66} \end{bmatrix} \begin{bmatrix} S_{xx} \\ S_{yy} \\ S_{xy} \end{bmatrix} \tag{3.12}$$

where, for the plane stress state, $S_{xx} = \frac{2\sigma_{11} - \sigma_{22}}{3}$ and $S_{yy} = \frac{2\sigma_{22} - \sigma_{11}}{3}$.

The three absolute values in equations (3.10) and (3.11) are

$$\begin{aligned} \left| \tilde{S}'_1 - \tilde{S}'_2 \right| &= 2\sqrt{\left(\frac{\tilde{S}'_{xx} - \tilde{S}'_{yy}}{2}\right)^2 + \tilde{S}'^{\,2}_{xy}} \\ \left| 2\tilde{S}''_2 + \tilde{S}''_1 \right| &= \left| \frac{3(\tilde{S}''_{xx} + \tilde{S}''_{yy})}{2} - \sqrt{\left(\frac{\tilde{S}''_{xx} - \tilde{S}''_{yy}}{2}\right)^2 + \tilde{S}''^{\,2}_{xy}} \right| \\ \left| 2\tilde{S}''_1 + \tilde{S}''_2 \right| &= \left| \frac{3(\tilde{S}''_{xx} + \tilde{S}''_{yy})}{2} + \sqrt{\left(\frac{\tilde{S}''_{xx} - \tilde{S}''_{yy}}{2}\right)^2 + \tilde{S}''^{\,2}_{xy}} \right| \end{aligned} \tag{3.13}$$

These three equations can be expressed as functions of the C'_{ij} and C''_{kl} coefficients. The following notations can be used to define another set of independent anisotropy parameters:

$$C' = \begin{bmatrix} \alpha_1 & 0 & 0 \\ 0 & \alpha_2 & 0 \\ 0 & 0 & \alpha_7 \end{bmatrix}$$
$$C'' = \begin{bmatrix} 4\alpha_5 - \alpha_3 & 2\alpha_6 - \alpha_4 & 0 \\ 2\alpha_3 - \alpha_5 & 4\alpha_4 - \alpha_6 & 0 \\ 0 & 0 & 3\alpha_8 \end{bmatrix} \tag{3.14}$$

Equations (3.10), (3.11), (3.12), (3.13), and (3.14) completely define the Yld2000-2d model. Using equation (3.14), equation (3.13) can be expressed as a function of the stress components as well as the α_k coefficients as

$$\left|\tilde{S}_1^{'}-\tilde{S}_2^{'}\right|=2\sqrt{\left[\frac{(2\alpha_1+\alpha_2)\sigma_{11}-(2\alpha_2+\alpha_1)\sigma_{22}}{6}\right]^2+\alpha_7^2\sigma_{12}^2}$$

$$\left|2\tilde{S}_2^{''}+\tilde{S}_1^{''}\right|=\left|\frac{(4\alpha_5+2\alpha_3-2\alpha_4-\alpha_6)\sigma_{11}+(4\alpha_4+2\alpha_6-2\alpha_5-\alpha_3)\sigma_{22}}{6}-\sqrt{\left(\frac{(4\alpha_5+2\alpha_3-2\alpha_4-\alpha_6)\sigma_{11}+(4\alpha_4+2\alpha_6-2\alpha_5-\alpha_3)\sigma_{22}}{6}\right)^2+(\alpha_8\sigma_{12})^2}\right| \quad (3.15)$$

$$\left|2\tilde{S}_1^{''}+\tilde{S}_2^{''}\right|=\left|\frac{(4\alpha_5+2\alpha_3-2\alpha_4-\alpha_6)\sigma_{11}+(4\alpha_4+2\alpha_6-2\alpha_5-\alpha_3)\sigma_{22}}{6}+\sqrt{\left(\frac{(4\alpha_5+2\alpha_3-2\alpha_4-\alpha_6)\sigma_{11}+(4\alpha_4+2\alpha_6-2\alpha_5-\alpha_3)\sigma_{22}}{6}\right)^2+(\alpha_8\sigma_{12})^2}\right|$$

The Yld2000-2d yield function requires the determination of eight mechanical parameters. Three uniaxial yield stresses and three *R*-values are obtained from three different directions (0°,45°,90°). These six parameters are obtained using a uniaxial tensile test that must be complemented by other tests such as a compression test to compute the biaxial *R*-value [19] and biaxial stress state test such as the hydraulic bulge test to determine the biaxial yield stress [31].

The input data are the same as those used with the BBC2003 yield function. The complementary information shown in Table **3.1** must be calculated to identify the eight α_k coefficients. The details of the system of nonlinear equations associated with Yld2000-2d will be discussed in the following section.

Table 3.1. Complementary information needed to calculate the α_k coefficients.

Mode	**Index** J	γ_J	δ_J	σ_J	q_{xJ}	q_{yJ}
0° tension	1	2/3	-1/3	σ_0	$1-R_0$	$2+R_0$
90° tension	2	-1/3	2/3	σ_{90}	$2+R_{90}$	$1-R_{90}$
Balanced biaxial tension	3	-1/3	-1/3	σ_b	$1+2R_b$	$2+R_b$

3.3.4.1 *The system of nonlinear equations*

The eight equations that must be solved numerically to identify the anisotropy coefficients α_k "roots" of Yld2000-2d are

$$
\begin{aligned}
&F_J = \left|\alpha_1\gamma_J - \alpha_2\delta_J\right|^a + \left|\alpha_3\gamma_J - 2\alpha_4\delta_J\right|^a + \left|2\alpha_5\gamma_J - \alpha_6\delta_J\right|^a - 2\left(\frac{\bar{\sigma}}{\sigma_J}\right)^a = 0\\
&F_4 = \left|\frac{\sqrt{x_2^{'2} + 4\alpha_7^2}}{2}\right|^a + \left|\frac{3x_1^{''} - \sqrt{x_2^{''2} + 4\alpha_8^2}}{4}\right|^a + \left|\frac{3x_1^{''} + \sqrt{x_2^{''2} + 4\alpha_8^2}}{4}\right|^a - 2\left(\frac{\bar{\sigma}}{\sigma_{45}}\right)^a = 0\\
&G_J = \left(\alpha_1 q_{xJ} + \alpha_2 q_{yJ}\right)\left(\alpha_1\gamma_J - \alpha_2\delta_J\right)\left|\alpha_1\gamma_J - \alpha_2\delta_J\right|^{a-2} + \left(\alpha_3 q_{xJ} + 2\alpha_4 q_{yJ}\right)\left(\alpha_3\gamma_J - 2\alpha_4\delta_J\right)\\
&\left|\alpha_3\gamma_J - 2\alpha_4\delta_J\right|^{a-2} + \left(2\alpha_5 q_{xJ} + \alpha_6 q_{yJ}\right)\left(2\alpha_5\gamma_J - \alpha_6\delta_J\right)\left|2\alpha_5\gamma_J - \alpha_6\delta_J\right|^{a-2} = 0\\
&G_4 = \overline{V^{'}}\,\frac{x_2^{'2}}{\sqrt{x_2^{'2} + 4\alpha_7^2}} + \frac{3}{2}x_1^{''}\left(\overline{V^{''}} + \overline{W^{''}}\right) + \frac{1}{2}\frac{x_2^{''2}}{\sqrt{x_2^{''2} + 4\alpha_8^2}}\left(\overline{W^{''}} - \overline{V^{''}}\right) - \frac{2a}{\left(1 + r_{45}\right)}\left(\frac{\bar{\sigma}}{\sigma_{45}}\right)^a = 0
\end{aligned}
\tag{3.16}
$$

Three equations for F_J correspond to $J = 1,2,3$. The same applies to G_J. In each equation, the values of γ_J, δ_J, q_{xJ}, and q_{yJ} are given in Table **3.1** for the corresponding J. The other expressions used in F_4 and G_4 are

$$
\begin{aligned}
x_1^{'} &= \frac{\alpha_1 + \alpha_2}{3}\\
x_2^{'} &= \frac{\alpha_1 - \alpha_2}{3}\\
x_1^{''} &= \frac{\alpha_3 + 2\alpha_4 + 2\alpha_5 + \alpha_6}{9}\\
x_2^{''} &= \frac{2\alpha_5 + \alpha_6 + \alpha_3 + 2\alpha_4}{3}
\end{aligned}
\tag{3.17}
$$

and

$$
\begin{aligned}
\overline{V^{'}} &= a\left(\frac{\sqrt{x_2^{'2} + 4\alpha_7^2}}{2}\right)^{a-1}\\
\overline{V^{''}} &= a\left(\frac{3x_1^{''} - \sqrt{x_2^{''2} + 4\alpha_8^2}}{4}\right)\left|\frac{3x_1^{''} - \sqrt{x_2^{''2} + 4\alpha_8^2}}{4}\right|^{a-2}\\
\overline{W^{''}} &= a\left(\frac{3x_1^{''} + \sqrt{x_2^{''2} + 4\alpha_8^2}}{4}\right)\left|\frac{3x_1^{''} + \sqrt{x_2^{''2} + 4\alpha_8^2}}{4}\right|^{a-2}
\end{aligned}
\tag{3.18}
$$

The roots of this system are the α_k coefficients, which will be used to define the shape of the yield locus of any given material. This system consists of eight equations with eight unknowns (α_k).

3.3.5 BBC2003

Several anisotropic yield functions have been developed by CERTETA researchers—they are known as the BBC yield criteria "family". One of these criteria, BBC2003, is an

advanced yield criterion that can match all experimental input data [48]; thus, this criterion will be used in this study. BBC2003 used the method of including new coefficients into Hershey's formulation [50]. This yield criterion can be seen as an extension of Barlat'89 [48,88]. Researchers [16] proved that the BBC2003 and Yld2000-2d are the same yet appear in different forms [6,48]. The authors of BBC2003 used the method of including new coefficients into Hershey's formulation, whereas the authors of Yld2000-2d used a linear transformation method.

In the phenomenological theory of plasticity, the elastic state is separated from the plastic state by utilizing a yield function. A yield function that accounts for plastic anisotropy can be written in the following form:

$$F(\sigma,\bar{\eta}) = \bar{\sigma}(c_i,\sigma) - Y_{ref}(\bar{\eta}) \le 0 \tag{3.19}$$

where F is the yield function, σ is the Cauchy stress, $\bar{\eta}$ is the accumulated equivalent plastic strain, $\bar{\sigma}$ is the equivalent stress, Y_{ref} is the instantaneous reference yield stress of material, and c_i are the anisotropy parameters.

One of the versions of the BBC criteria family developed by Banabic et al., BBC2003 criterion [48], can be written as

$$F(a_B,M_B,N_B,P_B,Q_B,R_B,S_B,T_B,k,\sigma,\bar{\eta}) = \bar{\sigma}(a_{B3},M_{B3},N_B,P_B,Q_B,R_B,S_B,T_B,k,\sigma) - Y_{ref} \le 0 \tag{3.20}$$

with

$$\bar{\sigma}(a_B,M_B,N_B,P_B,Q_B,R_B,S_B,T_B,k,\sigma) = \left[a_B(\Gamma+\Psi)^{2k} + a_B(\Gamma-\Psi)^{2k} + (1-a_B)(2\Lambda)^{2k}\right]^{\frac{1}{2k}} \tag{3.21}$$

The terms Γ, Ψ , and Λ are related to the non-zero components of the stress tensor and are defined as

$$\begin{aligned}
\Gamma &= \frac{\sigma_{11} + M_B\sigma_{22}}{2} \\
\Psi &= \sqrt{\frac{\left(N_B\sigma_{11} - P_B\sigma_{22}\right)^2}{4} + {Q_B}^2\sigma_{12}\sigma_{21}} \\
\Lambda &= \sqrt{\frac{\left(R_B\sigma_{11} - S_B\sigma_{22}\right)^2}{4} + {T_B}^2\sigma_{12}\sigma_{21}}
\end{aligned} \tag{3.22}$$

where $0 \le a_B \le 1$ to ensure convexity and k is the exponent related to the crystal structure of the materials (3 for steel sheets and 4 for aluminium sheets). The details of the system

of nonlinear equations associated with BBC2003 will be discussed in the following section.

3.3.5.1 *Determination of the plastic anisotropy parameters*

The BBC2003 yield function has eight equations with eight unknowns if all the mechanical parameters are provided. The experimental data which should be entered into the yield function includes eight mechanical parameters:

$YS_0, YS_{45}, YS_{90}, Y_b, R_0, R_{45}, R_{90}, R_b$.

- Three directional yield stresses are obtained from uniaxial tensile tests along a direction at 0°,45°, and 90° to the rolling direction of the sheet. The associated yield stresses are denoted here as YS_0, YS_{45}, YS_{90}.
- Three *R*-values correspond to 0°,45°, and 90° orientations (denoted here as R_0, R_{45}, R_{90}).
- The equibiaxial yield stress is obtained by cross tensile test or bulge test (denoted here as Y_b).
- The equibiaxial *R*-value (ratio of plastic strain in transverse direction to plastic strain in rolling direction) is denoted as R_b.

The eight parameters ($a_{B3}, M_{B3}, N, P, Q, R, S, T$) are determined by obtaining a set of eight equations that make up the following system:

$$\left.\begin{aligned}
&\bar{\sigma}(a_B, M_B, N_B, P_B, Q_B, R_B, S_B, T_B, \sigma_0) - Y_{ref} = 0\\
&\bar{\sigma}(a_B, M_B, N_B, P_B, Q_B, R_B, S_B, T_B, \sigma_{45}) - Y_{ref} = 0\\
&\bar{\sigma}(a_B, M_B, N_B, P_B, Q_B, R_B, S_B, T_B, \sigma_{90}) - Y_{ref} = 0\\
&\bar{\sigma}(a_B, M_B, N_B, P_B, Q_B, R_B, S_B, T_B, \sigma_b) - Y_{ref} = 0\\
&R_0(a_B, M_B, N_B, P_B, Q_B, R_B, S_B, T_B, \sigma_0) - R_0^{\exp} = 0\\
&R_{45}(a_B, M_B, N_B, P_B, Q_B, R_B, S_B, T_B, \sigma_{45}) - R_{45}^{\exp} = 0\\
&R_{90}(a_B, M_B, N_B, P_B, Q_B, R_B, S_B, T_B, \sigma_{90}) - R_{90}^{\exp} = 0\\
&R_b(a_B, M_B, N_B, P_B, Q_B, R_B, S_B, T_B, \sigma_b) - R_b^{\exp} = 0
\end{aligned}\right\} \qquad (3.23)$$

where $R_{(.)}$ are the calculated *R*-values while $R_{(.)}^{\exp}$ are the experimentally obtained *R*-values. To build this system of nonlinear equations, some quantities must be computed. First, the three stress tensors in the tensile tests, σ_0, σ_{45}, and σ_{90}, which are associated

with orientation angle $\varphi \in \{0,45,90\}$, should be computed using the following stress components in a tensile test specimen under uniaxial load:

$$\begin{aligned} &\sigma_{11} = YS_{\varphi} \cos^2 \varphi \\ &\sigma_{22} = YS_{\varphi} \sin^2 \varphi \\ &\sigma_{12} = \sigma_{21} = YS_{\varphi} \cos\varphi \sin\varphi \end{aligned} \quad \rightarrow \sigma_{\varphi} = \begin{bmatrix} \sigma_{11} & \sigma_{12} & 0 \\ \sigma_{12} & \sigma_{22} & 0 \\ 0 & 0 & 0 \end{bmatrix} \tag{3.24}$$

where YS_{φ} is the uniaxial yield stress associated with the orientation φ. Second, the equibiaxial stress tensor σ_b should be calculated using the following stress components to determine the fourth equation:

$$\begin{aligned} &\sigma_{11} = \sigma_{22} = Y_b \\ &\sigma_{12} = \sigma_{21} = 0 \end{aligned} \rightarrow \sigma_b = \begin{bmatrix} \sigma_{11} & 0 & 0 \\ 0 & \sigma_{22} & 0 \\ 0 & 0 & 0 \end{bmatrix} \tag{3.25}$$

Third, the *R*-values associated with the orientation angle $\varphi \in \{0,45,90\}$ can be computed using

$$R_{\varphi} = \frac{\sin^2 \varphi . \dfrac{\partial F}{\partial \sigma_{11}} - \sin 2\varphi . \dfrac{\partial F}{\partial \sigma_{12}} + \cos^2 \varphi . \dfrac{\partial F}{\partial \sigma_{22}}}{\dfrac{\partial F}{\partial \sigma_{11}} + \dfrac{\partial F}{\partial \sigma_{22}}} \tag{3.26}$$

Finally, to identify the last equation, the equibiaxial *R*-value can be calculated using

$$R_b = \frac{\dfrac{\partial F}{\partial \sigma_{22}}}{\dfrac{\partial F}{\partial \sigma_{11}}} \tag{3.27}$$

For the plane stress state (2-D), the non-zero gradient components are given by

$$\begin{aligned} \frac{\partial F}{\partial \sigma_{11}} &= \frac{\partial F}{\partial \Gamma}\frac{\partial \Gamma}{\partial \sigma_{11}} + \frac{\partial F}{\partial \Psi}\frac{\partial \Psi}{\partial \sigma_{11}} + \frac{\partial F}{\partial \Lambda}\frac{\partial \Lambda}{\partial \sigma_{11}} \\ \frac{\partial F}{\partial \sigma_{22}} &= \frac{\partial F}{\partial \Gamma}\frac{\partial \Gamma}{\partial \sigma_{22}} + \frac{\partial F}{\partial \Psi}\frac{\partial \Psi}{\partial \sigma_{22}} + \frac{\partial F}{\partial \Lambda}\frac{\partial \Lambda}{\partial \sigma_{22}} \\ \frac{\partial F}{\partial \sigma_{12}} &= \frac{\partial F}{\partial \Gamma}\frac{\partial \Gamma}{\partial \sigma_{12}} + \frac{\partial F}{\partial \Psi}\frac{\partial \Psi}{\partial \sigma_{12}} + \frac{\partial F}{\partial \Lambda}\frac{\partial \Lambda}{\partial \sigma_{12}} \\ \frac{\partial F}{\partial \sigma_{21}} &= \frac{\partial F}{\partial \Gamma}\frac{\partial \Gamma}{\partial \sigma_{21}} + \frac{\partial F}{\partial \Psi}\frac{\partial \Psi}{\partial \sigma_{21}} + \frac{\partial F}{\partial \Lambda}\frac{\partial \Lambda}{\partial \sigma_{21}} \end{aligned} \tag{3.28}$$

where the partial derivatives are given by

$$\frac{\partial F}{\partial \Gamma} = A.\{a_B.(\Gamma+\Psi)^{2k-1} + a._B(\Gamma-\Psi)^{2k-1}\}$$
$$\frac{\partial F}{\partial \Psi} = A.\{a_B.(\Gamma+\Psi)^{2k-1} - a_B.(\Gamma-\Psi)^{2k-1}\}$$
$$\frac{\partial F}{\partial \Lambda} = A.\{2.(1-a_B).(2\Lambda)^{2k-1}\} \quad (3.29)$$

with

$$A = [a_B.(\Gamma+\Psi)^{2k} + a_B.(\Gamma-\Psi)^{2k} + (1-a_B).(2\Lambda)^{2k}]^{(1/2k)-1}$$

The other partial derivatives are

$$\frac{\partial \Gamma}{\partial \sigma_{11}} = \frac{1}{2}, \frac{\partial \Gamma}{\partial \sigma_{22}} = \frac{M_B}{2}, \frac{\partial \Gamma}{\partial \sigma_{12}} = 0, \frac{\partial \Gamma}{\partial \sigma_{21}} = 0,$$
$$\frac{\partial \Psi}{\partial \sigma_{11}} = \frac{\frac{1}{4}.(N_B\sigma_{11} - P_B\sigma_{22}).N_B}{\sqrt{\frac{1}{4}.(N_B\sigma_{11} - P_B\sigma_{22})^2 + {Q_B}^2\sigma_{12}\sigma_{21}}}$$
$$\frac{\partial \Psi}{\partial \sigma_{22}} = \frac{\frac{1}{4}.(N_B\sigma_{11} - P_B\sigma_{22}).(-P_B)}{\sqrt{\frac{1}{4}.(N_B\sigma_{11} - P_B\sigma_{22})^2 + {Q_B}^2\sigma_{12}\sigma_{21}}} \quad (3.30)$$
$$\frac{\partial \Psi}{\partial \sigma_{12}} = \frac{{Q_B}^2\sigma_{12}}{2.\sqrt{\frac{1}{4}.(N_B\sigma_{11} - P_B\sigma_{22})^2 + {Q_B}^2\sigma_{12}\sigma_{21}}}$$
$$\frac{\partial \Psi}{\partial \sigma_{21}} = \frac{{Q_B}^2\sigma_{12}}{2.\sqrt{\frac{1}{4}.(N_B\sigma_{11} - P_B\sigma_{22})^2 + {Q_B}^2\sigma_{12}\sigma_{21}}}$$
$$\frac{\partial \Lambda}{\partial \sigma_{11}} = \frac{\frac{1}{4}.(R_B\sigma_{11} - S_B\sigma_{22}).R_B}{\sqrt{\frac{1}{4}.(R_B\sigma_{11} - S_B\sigma_{22})^2 + {T_B}^2\sigma_{12}\sigma_{21}}}$$
$$\frac{\partial \Lambda}{\partial \sigma_{22}} = \frac{\frac{1}{4}.(R_B\sigma_{11} - S_B\sigma_{22}).(-S_B)}{\sqrt{\frac{1}{4}.(R_B\sigma_{11} - S_B\sigma_{22})^2 + {T_B}^2\sigma_{12}\sigma_{21}}}$$
$$\frac{\partial \Lambda}{\partial \sigma_{12}} = \frac{{T_B}^2\sigma_{12}}{2.\sqrt{\frac{1}{4}.(R_B\sigma_{11} - S_B\sigma_{22})^2 + {T_B}^2\sigma_{12}\sigma_{21}}}$$
$$\frac{\partial \Lambda}{\partial \sigma_{21}} = \frac{{T_B}^2\sigma_{12}}{2.\sqrt{\frac{1}{4}.(R_B\sigma_{11} - S_B\sigma_{22})^2 + {T_B}^2\sigma_{12}\sigma_{21}}}$$

3.3.6 BBC2005

Banabic et al. [49] proposed a yield function denoted as BBC2005 that is implemented in the AUTOFORM 4.1 program. It is a modified version of the BBC2003, which is considered as an extension of the Barlat'89. The BBC2005 is considered to be one of 60

excellent inventions in metal forming [89]. This yield function can be written in the following form:

$$F = \overline{\sigma} - Y_{ref} = 0 \tag{3.31}$$

where F is the yield function, $\overline{\sigma}$ is the BBC2005 equivalent stress, and Y_{ref} is the instantaneous reference yield stress of the material. The BBC2005 equivalent stress can be written as

$$\overline{\sigma} = [a_{B5}(\Lambda+\Gamma)^{2k} + a(\Lambda-\Gamma)^{2k} + b(\Lambda+\Psi)^{2k} + b(\Lambda-\Psi)^{2k}]^{\frac{1}{2k}} \tag{3.32}$$

The terms Γ, Ψ, and Λ are defined as

$$\begin{aligned} \Gamma &= L\sigma_{11} + M\sigma_{22} \\ \Psi &= \sqrt{(N\sigma_{11} - P\sigma_{22})^2 + \sigma_{12}\sigma_{21}} \\ \Lambda &= \sqrt{(Q\sigma_{11} - R_{B5}\sigma_{22})^2 + \sigma_{12}\sigma_{21}} \end{aligned} \tag{3.33}$$

where a_{B5} and $b > 0$ are material parameters, and k is the exponent related to the crystal structure of the materials (3 for steel sheets and 4 for aluminium sheets). The coefficients L, M, N, P, Q, and R_{B5} in equation (3.33) are the remaining plastic anisotropy parameters. The details of the system of nonlinear equations associated with BBC2005 can be found in [6,49].

The BBC2005 yield function requires the determination of eight mechanical parameters. Three uniaxial yield stresses and three *R*-values are obtained from three different directions ($0^\circ, 45^\circ, 90^\circ$). These six parameters are obtained using a uniaxial tensile test that has to be complemented by other tests such as a compression test to compute the biaxial *R*-value [19] and a hydraulic bulge test to determine the biaxial yield stress [31].

3.4 Identification strategies

In sheet metal forming industries, the demand for quality enhancement and cost reduction is continuous [90]. Such demand has initiated intense research on the material constitutive models—specifically on the yield functions and on identification of the constitutive parameters.

In contrast to yield functions such as [47,56], for which the plastic anisotropy parameters are identified analytically, the “roots” of most of the advanced yield criteria are obtained

numerically. Mathematically, each of the advanced phenomenological models cited in this work results in a system of highly nonlinear equations that involve a certain number of parameters, called plastic anisotropic coefficients. These parameters work as weighting factors to improve the accuracy of the plastic behaviour description in different stress states [48].

3.5 Classification of algorithms

Different numerical methods can be used to solve any systems of nonlinear equations. These methods can be divided primarily into three groups [91]: gradient-based algorithms, derivative-free search algorithms, and evolutionary algorithms. From a mathematical viewpoint, solving a highly nonlinear system of equations can prove challenging [57,92].

The Newton–Raphson (NR) method [93,94], which is an example of a gradient-based algorithm—a group of algorithms that have the advantage of quick convergence—is the most widely used algorithm for solving any system of nonlinear equations. In particular, it is the most commonly used algorithm for identifying the plastic anisotropic coefficients of various yield criteria such as employed in [19,20,48,51,95].

However, with the NR method [18,96], if the Jacobian of the system of nonlinear equations function is singular, i.e., the Jacobian does not have an inverse (its determinant is zero), NR iteration can fail. Moreover, the NR method requires the calculation of the Jacobian of a function, which may be computationally expensive or impractical to evaluate. Furthermore, the NR method often fails in finding the roots of systems of nonlinear equations associated with one of the aforementioned advanced criteria, especially for materials with strong anisotropy [18]. Finally, Newton's method may fail to converge to a global minimum if the initial guess is far from the root [42]. This is a well-known disadvantage of the NR method [97–99]. Banabic et al. [48] and Barlat et al. [19] successfully used the NR method for the solution of the BBC2003 and Yld2000-2d models. The NR method is still used for such advanced models; however, it is difficult to select reliable starting points for the NR method (i.e. NR is strongly influenced by the initial guesses) [6,98,100].

The minimisation of an error function is an alternative identification procedure that has been used by [48,57,101] and many others. The steepest descent method, which is also an example of a gradient-based algorithm, was used to minimise such an error function. However, the method led to small deviations in the prediction of the planar distribution

of yield stresses and *R*-values [48]. The downhill simplex method is a derivative-free algorithm—simplicity is the main attribute of these algorithms—for minimizing error functions. It has been used for calculating the coefficients for various models, one of which is Yld2000-2d [18]. The downside of this alternative approach is that each yield criterion establishes a different form of the error function to ensure convergence. The resulting forms involve weighting factors for yield stress and *R*-value terms. These factors could be either equally distributed or not. Examples of the different forms of the error functions can be found in [42,48,102,103]. The error minimisation method is able to converge to a global minimum when the number of parameters to be identified equals the number of experimental data [18]. This type of approach was considered in [48,101] as an excellent engineering method for checking the flexibility of any newly proposed yield functions.

Another alternative to finding the roots of the system of nonlinear equations is the Genetic Algorithm (GA), which is the most popular type of evolutionary algorithm [91]. This type of approach has been used by Chaparro et al.[58,91]. Hybrid algorithms can be produced to combine the advantages of different algorithms: for instance, the advantages of the genetic algorithm and performance of the gradient-based algorithm [91]. Although this is a robust method, its convergence is slow, so it is very time consuming [91]. The results obtained by the genetic algorithms generally are not reproducible, which is a major drawback [102].

3.5.1 Trust region vs. line search

From another perspective, in continuous optimisation two fundamental search approaches can be employed for solving unconstrained optimisation problems [104]. To move from the current point to the next estimate, the line search strategy and the trust region strategy are the primary techniques. As an example, these strategies both guarantee global convergence of Newton's method [105]. Line search strategies choose the direction first, followed by the distance, whereas trust region strategies choose the maximum distance first, followed by the direction. The latter approach is a straightforward, yet robust, concept in optimisation [96]. Using the trust region approach reduces the objective value significantly and overcomes the difficulty caused by non-positive definite Hessian matrices in the line search [105].

3.6 Parameter identification algorithms

The following sections describe in details the solution methods that will be applied in this thesis.

3.6.1 Newton Raphson

Given a system of nonlinear equations $F(x) = 0$ where x is a vector of unknowns and F is a vector of eight functions in x:

$$F(x) = \begin{bmatrix} F_1(x) \\ F_2(x) \\ . \\ . \\ F_8(x) \end{bmatrix} \tag{3.34}$$

A solution of $F(x) = 0$ is a vector x^* such that $F(x^*) = 0$ for all $i \in \{1,...,8\}$ at the same time. The standard method of solving a system of nonlinear equations $F(x) = 0$ is Newton Raphson (NR), which is an iterative method [94]. The procedure starts with an initial guess of the solution, and then the NR algorithm will generate a sequence of iterates or estimates. To move from the current estimate x_i to the next x_{i+1}, NR algorithm uses the formula below, which is derived from the Taylor series expansion of the function $F(x_i)$ by using only the first two terms of the expansion:

$$x_{i+1} = x_i - F(x_i) / J(x_i) \tag{3.35}$$

and $J(x_i)$ represents the Jacobian of the function $F(x_i)$:

$$J(x_i) = \begin{bmatrix} \frac{\partial F_1}{\partial x_1} & \cdots & \frac{\partial F_1}{\partial x_8} \\ \vdots & \ddots & \vdots \\ \frac{\partial F_8}{\partial x_1} & \cdots & \frac{\partial F_8}{\partial x_8} \end{bmatrix} \tag{3.36}$$

where $F(x_i)$ is the function value at the current estimate and $J(x_i)$ is the Jacobian of the function at the current estimate. This procedure is repeated until a solution hopefully is obtained with sufficient accuracy. The process can be outlined as follows:

NR algorithm

1. Given initial estimate x_0

2. If no convergence occurs

3. Solve $-J(x_i)d_i = F(x_i)$, d_i is the search direction or Newton step.

4. Update estimate $x_{i+1} = x_i + d_i$

5. Estimate = estimate+1

6. End

NR is the most widely used algorithm in solving any system of nonlinear equations. However, the NR have certain shortcomings that can be encountered [96]:

- The Jacobian of the function might be singular; i.e., the Jacobian does not have an inverse (its determinant is zero), and therefore methods based on the Newton iteration fail.
- NR requires the calculation of the Jacobian of the function, which may be computationally expensive.
- NR may not converge if the initial guess is far from the solution.

3.6.2 Trust region dogleg (TRD) algorithm

The trust region strategy collects information about the system of nonlinear equations to construct a merit function such that the behaviour of the merit function resembles the behaviour of the actual objective function. The trust region strategy search is restricted to the neighbourhood around the current iterate. This neighbourhood is defined by the trust region radius, which can be adjusted; for instance, if there is no sufficient decrease in the function value then the radius has to be reduced [98]. The merit function $m(d_i)$ is required to decide if the next estimate is better or worse than the current estimate. A trail step d_i is computed by minimizing the merit function over the trusted region Δ.

The trust region sub-problem is stated mathematically as

$$\begin{aligned} & d_i = \arg\min m(d_i, x_i) \\ & s.t \\ & \|D.d\| \le \Delta \end{aligned} \tag{3.37}$$

where D is the diagonal scaling matrix, which could be taken from the diagonal of the approximate Hessian [94], Δ is a scalar positive, and $\|.\|$ is the two-norm operator.

The merit function in equation (3.37) is

$$m(d_i, x_i) = \frac{1}{2} F(x_i)^T F(x_i) + d_i^T J(x_i)^T F(x_i) + \frac{1}{2} d_i^T J(x_i)^T J(x_i) d_i \qquad (3.38)$$

where $F(x_i)$ is the function at the current iterate and $J(x_i)$ is the Jacobian of the function at the current iterate.

The Powell dogleg procedure is used to compute the step d_i by minimising the trust region sub-problem [106]. The step d_i is a linear combination of a Cauchy step d_C and a Gauss–Newton step d_{GN}:

$$d_i = (1 - \lambda_{tr}) d_C + \lambda_{tr} d_{GN} \qquad (3.39)$$

which can be calculated respectively as

$$d_C = -\alpha_{tr} J(x_i)^T F(x_i) \qquad (3.40)$$

and

$$d_{GN} J(x_i) = -F(x_i) \qquad (3.41)$$

where α_{tr} minimises the merit function $m(d_i, x_i)$ and λ_{tr} is the largest value in the interval $[0,1]$ such that $\|d_i\| \leq \Delta$. When the Jacobian is singular, $d_i = d_C$.

An important parameter in updating the trust region radius and selecting the new iterate is the ratio ρ_{tr}, which measures the agreement between the merit function and the objective function [105]:

$$\rho_{tr} = \frac{F(x_i) - F(x_i + d_i)}{m(x_i) - m(x_i + d_i)} \qquad (3.42)$$

Singularity of the Jacobian is the biggest concern using the NR solver, but another drawback of this procedure is that the NR method requires the evaluation of the Jacobian, which can be computationally expensive. In contrast, the TRD algorithm is able to overcome these shortcomings. This algorithm can handle the case of singularity by approximating the Jacobian using either the forward finite difference or central finite

difference methods; thus, solutions can be determined. Furthermore, the algorithm is more robust with respect to the initial guess [96]. The TRD process can be outlined as follows:

TRD algorithm

1. Give initial estimate x_0,

2. Initialization: $\Delta = 1, \Delta_{\max} = 10^{10}, \eta_1 = 0.05, \eta_2 = 0.9, \alpha_{tr1} = 2.5, \alpha_{tr2} = 0.25$

3. Compute $F(x)$

4. Define the model $m(x)$

5. Calculate the step d_i

6. Acceptance of the trail point: Define ρ_{tr}

If $\rho_{tr} \geq \eta_1$ then set $x_{i+1} = x_i + d_i$ otherwise $x_{i+1} = x_i$

7. Trust region update is based on ρ and the norm of the scaled step (nds).

Δ is updated as follows:

$$\Delta = \min\left(\frac{nds}{20}, \frac{\Delta}{20}\right)$$

$$\Delta_{i+1} = \begin{cases} \max(\Delta, \alpha_{tr1} * nds) & if \quad \rho_{tr} \geq \eta_2 \\ \alpha_{tr2} * nds & if \quad \rho_{tr} < \eta_1 \\ \min(\Delta, \Delta_{\max}) & otherwise \end{cases}$$

3.6.3 Levenberg and Levenberg-Marquardt algorithms

The L [107] and LM [108] algorithms are line search methods (i.e. the directions are first chosen, then the step sizes are defined). These algorithms can be put into the trust region framework [109]; however, in this study, the line search versions were used. They are used to fit parameterised functions to a set of experimental data points by minimising the sum of the squares of the error between the functions and the experimental data [110]. These algorithms are briefly reviewed here.

The steepest descent method is the simplest technique for finding minima, and the step is updated as follows [111].

$$x_{i+1} = x_i - \lambda_s g_i \qquad 3.43)$$

where λ_s is the step and g_i is the gradient.

However, a convergence issue related to the steepest descent method is taking small steps down the gradient at locations where the gradient is large [111]. To avoid such problems, the Gauss–Newton method uses the second derivatives in addition to the gradient information to expand the gradient around the current estimate using the Taylor series; this expanded gradient is then set to zero [111]. In addition, it neglects higher-order terms by assuming that the function is quadratic around the current estimate:

$$x_{i+1} = x_i - B_i^{-1} g_i \tag{3.44}$$

Levenberg [107] proposed an algorithm that provides the advantages of both the steepest method and the Gauss–Newton method. The algorithm uses an approximation of the Hessian method to enforce rapid convergence:

$$B_i = J_i^T J_i \tag{3.45}$$

This algorithm uses a direction d_i that is the solution of a linear set of equations for different values of i [96]:

$$(B_i + \lambda_s I) d_i = -g_i \tag{3.46}$$

where $g_i = J_i^T F_i$, $d_i = x_{i+1} - x_i$, and I identity matrix. This algorithm is identical to Gauss-Newton when λ_s is zero, whereas it follows the gradient when λ_s tends to infinity [96]. The parameter λ_s varies adaptively between these two methods.

The step will be accepted if the error decreases following an update, which implies that the Gauss–Newton method is working. Simultaneously, λ_s is reduced by a factor of ten to scale down the effect of the gradient descent method. In contrast, the step is rejected if the error increased. In this case, it is better to follow the gradient more, so λ_s is increased by a factor of ten [111].

The approximated Hessian is not utilised if the value of λ_s is large, and that is a well-known weakness of the L algorithm [111]. Therefore, the advantage of using the second derivatives is not realised. To confront this weakness, Marquardt [108] suggested scaling each component of the gradient with the approximated Hessian by replacing the identity matrix in the L update rule with the diagonal of the approximated Hessian. This ensures avoidance of the classic error valley [110,111]. The LM algorithm instead has the update rule,

$$\left(B_i + \lambda_s diag(B_i)\right) d_i = -g_i \tag{3.47}$$

As the LM algorithm has overtaken the L algorithm in frequency of use, the LM algorithm is generally thought of as a modification of the L algorithm. Thus, these algorithms are both described as LM algorithms.

3.7 Summary

In this chapter, several isotropic and anisotropic yield functions were presented. Two of the oldest and most popular isotropic yield criteria, namely von Mises and Tresca, were described. The most widely used anisotropic yield functions—the Hill'48 and Barlat'89—were described. Barlat2000 as well as two criteria of the BBC family were presented in detail; these advanced yield functions will be covered further in the findings chapters. To some extent, it can be concluded that the current advanced phenomenological models can meet the demand of the sheet metal forming industry in terms of accuracy but at the expense of cost and effort.

A discussion was devoted to the numerical methods used in this study for identifying the plastic anisotropy parameters that are involved in most of the advanced yield functions.

In the next chapter, the discussion will be shifted to the second approach for describing the plastic anisotropy of a polycrystalline material: from mechanical-based yield surface to texture-based yield locus.

Chapter 4

Polycrystalline Plasticity Approach

4.1 Introduction

The most common approach in describing the plastic anisotropy of a polycrystalline material is to use the phenomenological approach. The macroscopic analytical yield functions that lie under this approach were described previously in chapter 3. This approach neglects the microstructural effects such as texture and considers the global mechanical response of the metallic sheets [112]. Alternatively, the anisotropy can be treated numerically with the crystal plasticity approach. Its major benefit is the fact that the microstructural properties of the material, e.g. texture, can be considered when describing the material plastic anisotropy. The models that lie under the polycrystal plasticity approach can be used in the following two ways to calculate the macroscopic yield locus [28]:

- Calculate the yield locus using physics-based models (e.g. Taylor models)
- Calculate the yield locus by combining the strengths of the physics-based approach and phenomenological approach.

Thus, this chapter is dedicated to these two methods that can be used to describe the behaviour of polycrystal metals.

The chapter is structured as follows. In section 4.2, a description of anisotropy and its relation to texture is presented. In section 4.3, the logical approach to calculate the macroscopic yield locus is provided. The classification of the polycrystalline plasticity models is given in section 4.4. In section 4.5, the phenomenological and polycrystalline plasticity approaches are compared. In section 4.6, efforts made to combine the strength of the physics-based models and phenomenological yield criteria are presented. In section 4.7, a description of the main input for polycrystalline plasticity models is provided. In section 4.8, the Taylor polycrystal plasticity model and the Pancake model are described briefly. Section 4.9 illustrates the methodology of calculating the yield locus using texture data. In section 4.10, the CTFP developed by An et al. [7] is described. The CTF model, which is part of the contributions to knowledge is presented in section 4.11. Finally, a summary of the chapter is provided in section 4.12.

4.2 Anisotropy description

Metallic sheets are polycrystalline cold-rolled metals that are crystallographically textured [25]. Crystallographic textures can be developed as a result of the complex thermal and mechanical treatments that are used in the manufacture of these sheets [18]. The crystallographic texture is the primary cause of the plastic anisotropy in polycrystalline materials [26,113]. The plastic anisotropy induced by the thermo-mechanical processes causes the mechanical properties of the sheets to be directionally dependent (i.e. the mechanical properties of the sheet metals are anisotropic) [18,26]. This directionality should be taken into account when modelling sheet metal forming applications.

The macroscopic phenomenological approach discussed previously in chapter 3 is the most common for considering the effect of anisotropy. The other common approach to describe the plasticity and its anisotropy, i.e. to describe the anisotropic behaviour of polycrystalline materials, is to use crystal plasticity models, which can be referred to as "polycrystalline plasticity models, micro-macro models, or physic-based models" [24,26,114,115].

Polycrystalline plasticity models use the crystallographic texture as the primary input. These models are employed to approximate the physical mechanism that governs plasticity caused by dislocation glide [116]. For FCC and BCC materials, which deform at room temperature, slip or "dislocation glide" is the main physical microscopic mechanism that causes plastic deformation [112,117]. Therefore, our focus in the current study is limited to plasticity caused by slip.

Shear strains acting on a particular plane in a specific direction describe the dislocation slip [114,116]. The slip is easier along the most dense directions and planes that are material dependent [118]. In the case of FCC materials [24], slipping occurs on {111} crystallographic planes in <110> directions ({111} <110> is referred to as slip systems). However, in BCC materials, gliding takes on a different slip system—the planes and directions that are assumed to be the deformation mode are {110}+{112}<111> [7,24]. The primary slip systems for the FCC and BCC materials are indicated in Table **4.1** and Table **4.2** respectively [118,119].

Table 4.1. FCC slip systems {111} <110>.

Slip plane	Slip direction		
(111)	$[01\bar{1}]$	$[\bar{1}01]$	$[1\bar{1}0]$
$(\bar{1}\,\bar{1}\,1)$	$[0\bar{1}\,\bar{1}]$	$[101]$	$[\bar{1}10]$
$(1\bar{1}\,1)$	$[0\bar{1}\,\bar{1}]$	$[\bar{1}01]$	$[110]$
$(\bar{1}11)$	$[01\bar{1}]$	$[101]$	$[\bar{1}\,\bar{1}\,0]$

Table 4.2. BCC slip systems {110} + {112} <111>.

Slip direction	Slip planes					
$[111]$	$(01\bar{1})$	$(10\bar{1})$	$(1\bar{1}0)$	$(\bar{2}11)$	$(1\bar{2}1)$	$(11\bar{2})$
$[\bar{1}11]$	$(01\bar{1})$	(101)	(110)	(211)	$(\bar{1}\bar{2}1)$	$(\bar{1}1\bar{2})$
$[1\bar{1}1]$	(011)	$(10\bar{1})$	(110)	$(\bar{2}\,\bar{1}\,1)$	(121)	$(1\bar{1}\bar{2})$
$[11\bar{1}]$	(011)	(101)	$(1\bar{1}0)$	$(\bar{2}1\,\bar{1})$	$(1\bar{2}\,\bar{1})$	(112)

4.3 Usage of the polycrystalline plasticity models

The plastic behaviour of a polycrystalline material can be deduced from the behaviour of its constituent crystallites [120]. Generally, these models can be used to compute texture evolution and yield surfaces [121]. Our interest here is limited to the usage of polycrystal plasticity models in the calculation of the initial yield surface. The mechanical response of the metallic sheets can be examined numerically utilising

- Texture of the material obtained experimentally (e.g. X-ray).
- Single crystal plastic behaviour obtained theoretically (e.g. Taylor models).

To calculate the macroscopic yield locus of the polycrystalline material, micro-macro plasticity models are employed by averaging the microscopic values over all crystal orientations according to the texture of the polycrystal material [24,114,120,122,123]. With this logical approach, one can have:

$$\begin{aligned} \sigma^{macro} &= \int \sigma^{micro}(g)\, f(g) dg \\ \dot{\varepsilon}^{macro} &= \int \dot{\varepsilon}^{micro}(g)\, f(g) dg \end{aligned} \tag{4.1}$$

Where g is the orientation and $f(g)$ is the texture of the material (Orientation Distribution Function, ODF) and is described in section 4.7. Several crystal plasticity laws have been proposed over the last decades. These models and theories were developed to measure anisotropic yield locus for a polycrystalline material with a known texture. It is out of the scope of this thesis to describe in detail all the existing models. However, an overview of the current models is described briefly in the following section.

4.4 Polycrystalline plasticity model classifications

Crystal plasticity laws can be classified in full-field and statistical frameworks.

4.4.1 Full-field models

The full-field models include in their prediction most of the deformation mechanisms such as crystallographic slip, twinning, stress-induced phase transformation, etc. [7,116,124].

For particular loading, models under this class predict the average mechanical response of a representative volume element of the microstructure that corresponds to the behaviour of the material at a macroscopic scale [116]. At the local scale, models under this class ensure that the stress equilibrium and strain compatibility at grain boundaries are satisfied [25]. These models incorporate additional microstructural information such as grain shape and size.

The numerical methods/solvers that are employed to predict the nonlinear behaviour of the Representative Volume Element (RVE) are:

- Crystal Plasticity Finite Element Method (CPFEM)
- Crystal Plasticity Fast Fourier Transform (CPFFT)

The main shortcoming of the CFFEM models is the fact that the computational costs are still quite high, which hinders their usage in industrial applications. Additionally, issues related to the mesh calculations are encountered [7,125]. These intrinsic weaknesses have driven the development of the CPFFT models. These models were developed as an alternative to CPFEM to speed up the calculation time and to avoid the mesh issues since CPFFT is a meshless method [126,127]. However, fast Fourier transformation-based modelling is still computationally expensive. It is several orders of magnitude larger than the category of statistical models [116]. Nonetheless, researchers believe that these

numerical methods are valuable tools, particularly for virtual experiments in the future [7,116].

4.4.2 Statistical models

Models under this class assume that the plastic anisotropy is primarily caused by a limited deformation mechanism (e.g. crystallographic slip). As a consequence, these models are much faster than full-field models. The most significant microstructural factor included as the main input for this class of models is texture in the form of ODF. The Taylor-Bishop-Hill (TBH) is the classical and simplest statistical model [37,119,128]. This model can also be referred to as Taylor model or full constraint (FC) model. The TBH model assumes the iso-strain hypothesis (i.e. each grain experiences the same macroscopic strain or deformation) [26]. The model was used to validated old yield functions such as Barlat'89 and Hosford'72 [55,74]. Although the TBH model fulfils the compatibility condition, it violates equilibrium at grain boundaries; another factor is that grains have different orientations [24].

The downside of the Taylor model has driven the development of various classes of statistical crystal plasticity models. First, the homogeneity assumption is dropped to some extent in the relaxed Taylor models, such as the Pancake model [129], to increase the freedom of the single grains [26]. However, many researchers showed that the Taylor models are unable to calculate the macroscopic yield loci for several aluminium and steels alloys [7,26,116].

A comparison of the yield loci derived from Taylor models, namely the FC and Pancake models, for various aluminium alloys has been made. The results of this comparison indicate that the polycrystalline plastic models—Taylor models—give a good description of yield loci for materials with weak planer anisotropy. However, this is not the case for materials with strong planer anisotropy. The conclusion was made that further development of the micro-macro approach is required [130]. Recently, [131] showed that the TBH model could not predict the mechanical anisotropy of pure aluminium sheet. An et al. and Kuwabara et al. [7,132] showed that Taylor models cannot produce reliable initial yield locus, as tested on various steel alloys. More details of the TBH model are given in latter sections since it forms the basis of further investigation.

The Taylor models neglect the effect of the grain interaction with its nearest neighbours [112]. That factor led to the development of n-site models (a number of grain clusters) [25,116]. Several n-site formulations, including the Alamel model [133], study two grains

instantaneously with different types of relaxations. Zhang et al. [134] showed that the Alamel-type models [26,135] resulted in a slightly better prediction than the TBH model. These models assume that the average plastic deformation of the cluster equals the macroscopic deformation [112].

Another class of homogenisation scheme is the Visco-Plastic-Self-Consistent (VPSC) method, which treats a grain as an ellipsoidal inclusion surrounded by an effective medium. Among several self-consistent models, the one developed by [136] has been widely used [26]. Engler & An [137] compared two phenomenological yield functions [51,53] and the VPSC model [136], and they found that the polycrystal yield surface (PCYS) produces a good match with the experimental data with much less experimental work. However, the accuracy of their model was not as good as the accuracy of the advanced phenomenological models [137].

A recent study on AA3103 sheet was carried out by [134] in which five different crystal plasticity models were used to describe the plastic anisotropy of the aluminium alloy. The study utilised THB [37,119,128], ALAMEL [133], the Alamel type III model [135], VPSC [136], and the CPFEM [138]. It was concluded that none of the examined five physics-based models could accurately predict the plastic anisotropy of the tested material (e.g. the shape of the yield locus).

4.5 Values and limitations (phenomenological vs. polycrystalline models)

The key value of most of the phenomenological models lies in the ease of their use [27,51]. Therefore, this approach generally is easy to understand for mechanical engineers, although some of the advanced criteria are complex and difficult to comprehend [24]. Another advantage is the fast computation that can be obtained using the phenomenological approach; these models require low CPU time [6]. In addition, the parameters of such models can be identified easily, and some of these models, such as Hill'48 and Barlat'89, have a low number of parameters, which makes them effective models for materials having weak anisotropy [27].

Since advanced yield criteria require a large number of parameters to be identified to improve the fitting of experimental data, most of the phenomenological models are considered to be sufficiently accurate. This is the case for sheet forming when the level of strain is generally moderate [139]. Accordingly, models under this approach are better suited for industrial applications [18]. Therefore, most of the yield criteria mentioned in

this chapter are implemented in FEM codes that are mainly devoted to numerical simulation of sheet metal forming processes. To sum up, today, the phenomenological approach is the only realistic approach in defining the yield criteria [18,25,26].

However, some advanced criteria such as those of Barlat et al. [36] and Vegter and van den Boogaard [53] are complex and difficult to comprehend as well as limited for use in industrial practice [6,27]. Moreover, some advanced models have a high number of parameters that need to be identified by conducting more mechanical tests and/or polycrystalline plasticity models. The experiments that are involved in the identification process are costly and time consuming and must be conducted with care [7,27]. Thus, they are unrealistic for the sheet forming industry.

These issues can be resolved to some extent by combining the strengths of the polycrystalline and phenomenological approaches (i.e. the possible accuracy of the polycrystal plasticity models and the computational efficiency of the phenomenological models) [25]. Crystal plasticity models can provide data points or "virtual points or experiments" that can be employed, in addition to experimental data, to calibrate advanced macroscopic yield functions. In other words, they can identify the anisotropy coefficients of the macroscopic yield functions [28].

Combining the strengths of the two approaches would have the following advantages:

- Microstructure effect can be considered indirectly.
- Cost, time, and technical difficulty associated with the calibration procedures will be reduced since polycrystal plasticity models merely require the measurement of texture.

To conclude, this approach of combining the two methods can reduce the severity associated with the extensive and difficult tests that are required to calibrate advanced flexible yield functions. Further discussion is given in the next section regarding the combination of the two approaches.

4.6 CP models combined with phenomenological models

The trend in recent years is to combine the strengths of the physics-based models and phenomenological yield criteria. The most common polycrystalline plastic models used in the identification procedures are the FC, VPSC, Alamel and its variants, and CPFEM [112]. In particular, data points or "‘‘virtual points or experiments" provided by the polycrystal plasticity models are employed to calibrate advanced macroscopic yield functions. Consequently, the microstructural effects can be considered indirectly [28].

Grytten et al. [140] argued that polycrystalline plasticity theories, and particularly their usage in the calibration of advanced yield functions, is unreliable, and fitting them with mechanical tests is the only reliable approach. However, it is believed that combining virtual points provided by polycrystal plasticity models and mechanical tests can improve the calibration of advanced yield functions [7,25,26,141]. Therefore, it is believed that such combination could overcome the major downside of advanced yield function calibration, which is its requirement for experiments such as bulge, plane strain, shear tests, etc. that are time consuming and costly.

Several efforts were used with different phenomenological yield functions and polycrystalline plasticity models and various metallic sheets. As is demonstrated in the following paragraph, most of these attempts were devoted primarily to calibrating the initial yield surfaces. Because most of the existing polycrystalline plasticity models are still unable to predict the texture evolution accurately [121], the effects of texture evolution are neglected. [36] used the VPSC model developed by [136] to predict the out-of-plane material properties, which are some of the parameters required to define the Yld2004-18 developed by [36]. The out-of-plane properties cannot be probed; therefore, crystal plasticity models are used to measure virtual experimental values instead. [140] evaluated different calibration methods using the FC-Taylor model to calibrate the Yld2004-18, for AA5083-H116, which is a high-strength aluminium-magnesium alloy. The study concluded that Taylor models cannot provide reliable results. [142] calibrated successfully the Yld96 [80] with a Taylor-type polycrystal plasticity model. A demonstration of the capability of the CPFEM for the calibration of the Vegter model on two steel alloys was given in [125]. In their study, the results of the simulation with the predicted *R*-values were unrealistic. [143] demonstrated that the implemented CPFEM model could predict well the planar variation of the yield stresses as well as *R*-values. However, the CP model, when compared with CPB06ex2 yield function [85], was unable to predict the biaxial point of the yield surface used in the study for continuous cast AA5754 sheets. In 2011, a novel yield locus that combined the FC-Taylor and Pancake models was proposed for sheet steels [7]. Biaxial yield point using the CFTP model is well predicted. Thus, biaxial stress state tests such as bulge tests, which are needed to calibrate advanced yield functions such as BBC2005/Yld2000, can be skipped [7]. For two different aluminium alloys (AA7003-T6 and AA6063-T6), the application of two homogenization schemes, namely the CPFEM and FC-Taylor plasticity models, were investigated in a study conducted by [28] and it was concluded that the difference between the two predictions regarding the initial shape of the yield surfaces was small. However,

when these two predictions were compared with the mechanical-based yield function (Yld2004-18), the results were unsatisfactory. In particular, the planar variation of the yield stresses and *R*-value predictions was poor.

The process of improving texture-based models and documenting knowledge about the performances of different polycrystalline models as well as their performances in calibrating advanced yield functions for different metallic sheets is still in progress. In section 4.11, a new yield loci description based on the FC-Taylor model is proposed; it is compared with different macroscopic yield functions in chapter 7. The new methodology focuses on calibrating the initial yield loci of the BBC2005 for two aluminium alloys (Al-Mg-Si alloys).

4.7 Texture: the main input

Polycrystalline plasticity models use the crystallographic texture as the main input. Before describing the polycrystalline plasticity models, which are considered in this study for describing the plastic behaviour of the material, a description of some of the principles related to these models is given.

The crystallographic texture of polycrystalline materials, which is the primary source of plastic anisotropy in metals and thus affects the formability of their mechanical properties, is the main input of the polycrystalline plasticity models. A description of the texture and its measurements is given in section 4.7 of this chapter.

4.7.1 Definition

Texture, preferred crystallographic orientation, and lattice preferred orientation, are different names for this intrinsic feature of materials. Generally, each grain in aggregates of crystals has its own crystallographic orientation that is different from grain to grain [144]. Most of the human made materials display a preferred orientation of crystallite grains. Such alignment has a significant influence on the physical properties of the materials [145].

The crystallites' orientations in the whole aggregate may be either randomly or non-randomly distributed [145]. Texture, or preferred orientation, is a condition in which the orientations of the grains are non-randomly distributed [144]. Each grain orientation is described with a rotation, g, which describes the rotation of the sample coordinate with

respect to the crystal coordinate [146]. The use of Eulerian angles in describing the rotation, g, is the most common method of description [146].

In sheet metals this is a common condition due to the manufacturing process characteristics. In the forming process, preferred crystallographic orientation is called *deformation texture*. It is a result of the tendency of the grains to rotate during plastic deformation. In the annealing process of cold-rolled sheets a *re-crystallisation texture* is formed [147].

Texture must be controlled during the thermo-mechanical processes to satisfy the industrial requirements of these materials [12]. For instance, the {111} planes should be parallel to the sheet surface to reduce the probability of crack occurrence during deformation [147].

Materials can form many texture components, some of which are shown in Figure **4.1**. The Goss component in sheets made from aluminium alloys, where the {011} family of planes are parallel to the sheet surface and the <100> directions are parallel to the rolling direction, leads to poor formability. However, if the sheet possesses a weak, scattered cube texture component, then the formability of the sheet will be improved significantly [12].

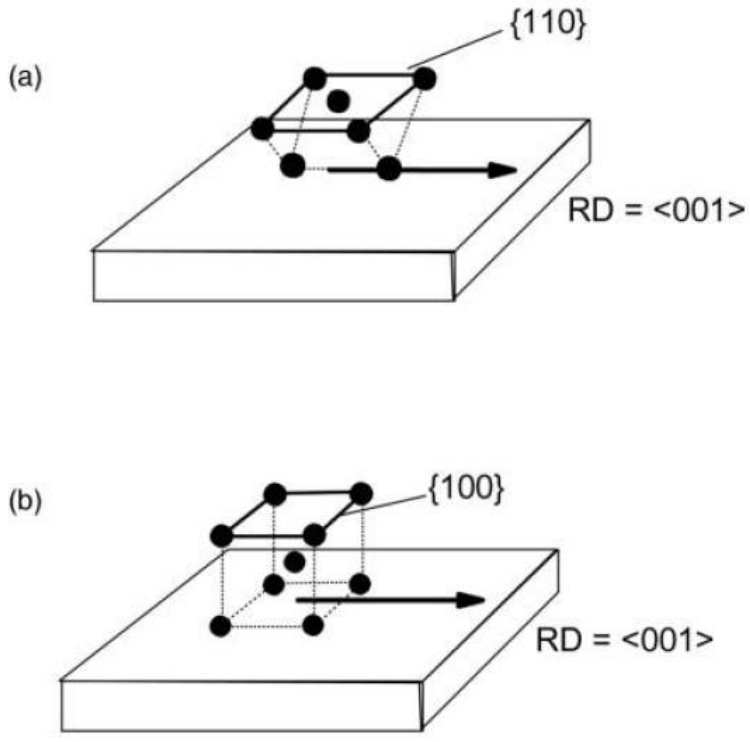

Figure 4.1. Texture components a Goss texture and b Cube texture [148].

4.7.2 Pole figures

The pole figures is a tool that is utilised to describe orientations of the grains in a 2-D space [146]. It is based on stereographic projection [145] and plots the positions and intensities of orientations of the grains in relation to the sample coordinate [149].

For instance, to construct the (100) pole figure for a single unit cell of FCC material, as illustrated in Figure **4.2**, the following steps are performed. First, the unit cell is transferred with the same orientation to the centre of the unit sphere, as shown in Figure **4.2**.

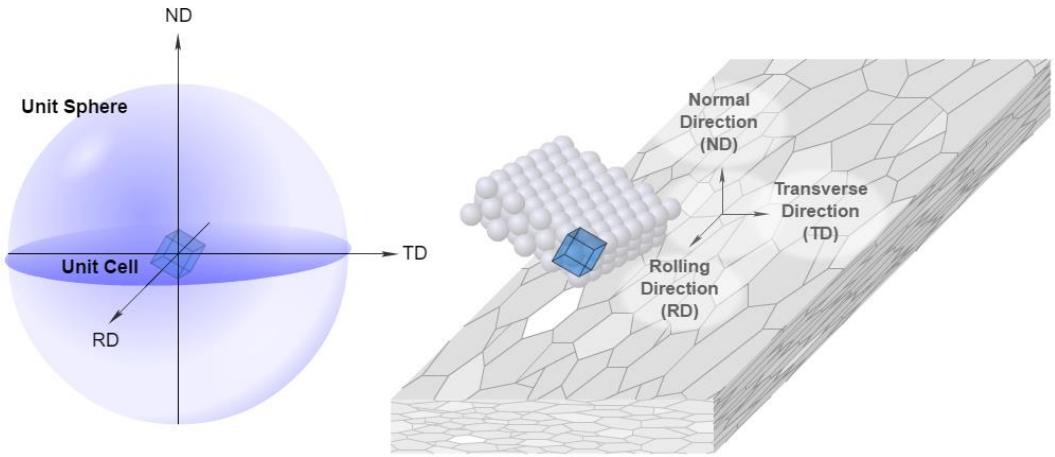

Figure 4.2. Transposing the unit cell with the same orientation to the centre of the unit sphere [150].

Then, the following steps are conducted in order, as illustrated in Figure 4.3.

- Step A: The intersections of the normal vectors that are perpendicular to the <100> faces are called poles.
- Step B: The points of intersection of the normal vectors with the unit sphere are numbered as 1, 2, and 3.
- Step C: Lines connecting the points (1, 2, and 3) with the south pole are drawn.
- Step D: The intersections of drawn lines in the previous step with the equatorial plane define 100 poles. These poles are labelled $1'$, $2'$, and $3'$.

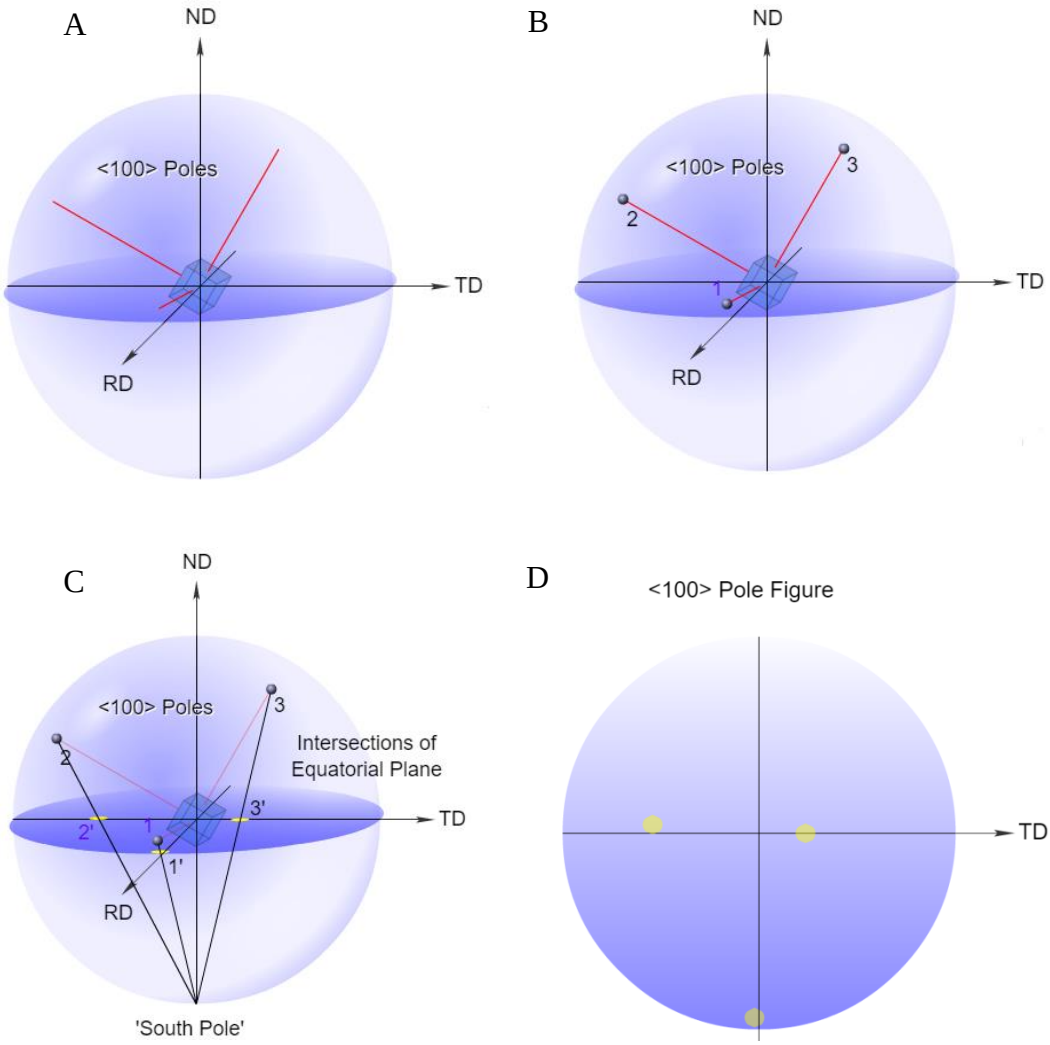

Figure 4.3. Construction of the (100) pole figure for a single unit cell of FCC material [150].

However, pole figures cannot record the whole range of the pole figures (i.e. an incomplete pole figure is formed) [151]. A 2-D projection plane results in a loss of information [152]. Moreover, some poles of different orientations may overlap [151]. Therefore, to overcome such ambiguities, a 3-D representation is used in the form of ODF, a 3-D space.

4.7.3 ODF

The orientation distribution function ODF is a probability density function of orientation g that is expressed in the form of Euler angles $\varphi_1, \Phi, \text{and } \varphi_2$. This describes the orientation density of crystallite grains in polycrystalline materials in a 3-D representation. It is used to represent the macro-texture data of the sample. The ODF $f(g)$ is defined by the following relationship:

$$\frac{dV}{V} = f(g)dg$$

with (4.2)

$$dg = \frac{1}{8\pi^2}\sin\Phi d\varphi_1 d\varphi_2$$

where V is the sample volume and dV is the volume of all grains with the orientation g in the angular element or an orientation range dg. This density function typically is projected parallel to the φ_2, as illustrated in Figure **4.4** [144].

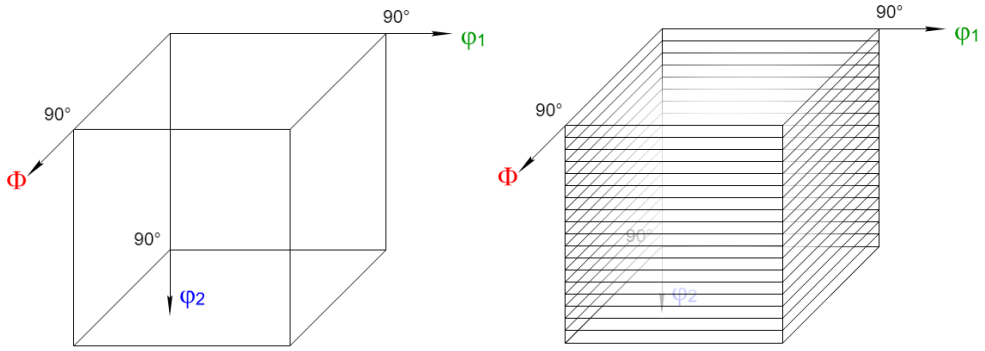

Figure 4.4. Slicing the Euler space to generate ODF in the direction [153].

The three Euler angles $(\varphi_1, \Phi, \varphi_2)$ are needed to represent an orientation g of a certain grain. The sequence of the three rotations of the Euler angles can also be illustrated in the Euler space to form the ODF. This is accomplished by slicing the space in the $\varphi_2$direction, as shown in Figure **4.4** for every $\varphi_2 = 5^\circ$. The following steps are performed to represent an orientation as a point on the ODF.

1. φ_1 about the normal direction ND to the Transverse direction TD into $TD'$and the rolling direction RD into RD' (Figure 4.5)

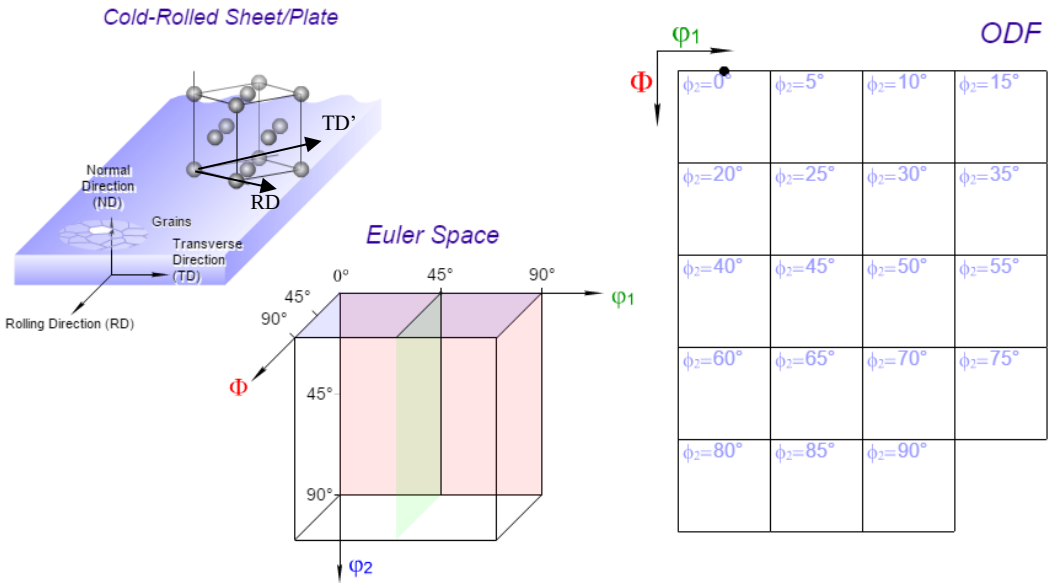

Figure 4.5. The first rotation of the first angle [153].

2. Φ about the axis RD' (in its new orientation, Figure **4.6**)

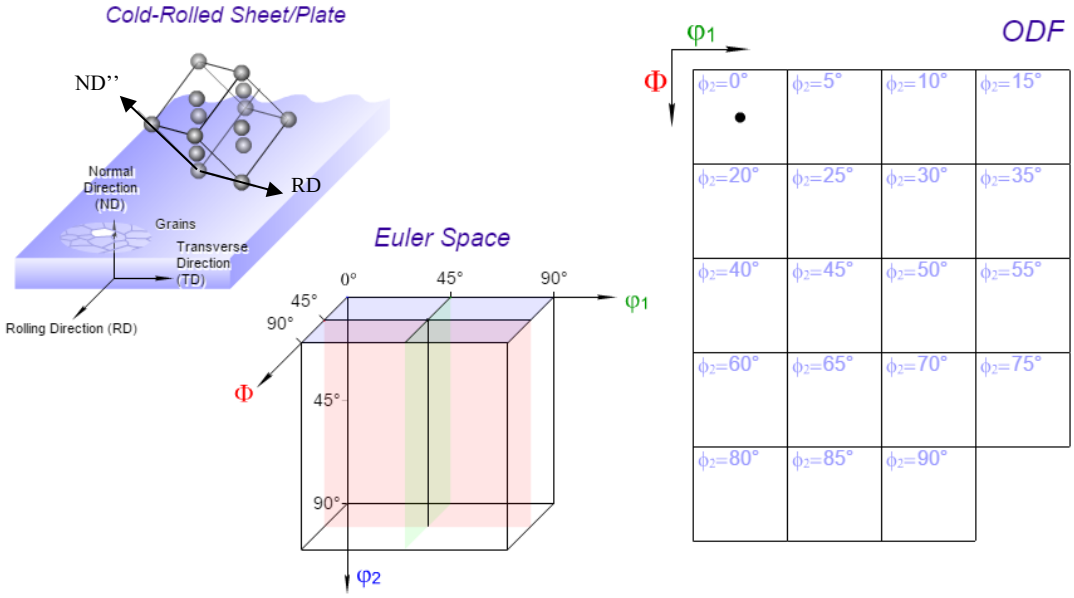

Figure 4.6. The second rotation of the second angle [153].

3. φ_2 about the ND'' (in its new orientation, Figure **4.7**)
4. The preferred crystallographic orientation 'texture' or 'ODF' is determined using the data from {111}, {200}, {220}, and {311} incomplete pole figures for the tested FCC

materials. With BCC materials, the {110}, {200}, {211}, and {301} incomplete pole figures are usually measured [154].

5. Next, the harmonic coefficients are determined from these data at truncation of L_h=22 and L_h=32 using the least square method for steel grades and aluminium alloys, respectively. The ODF, which is the main input for Taylor models, will be described in the following section.

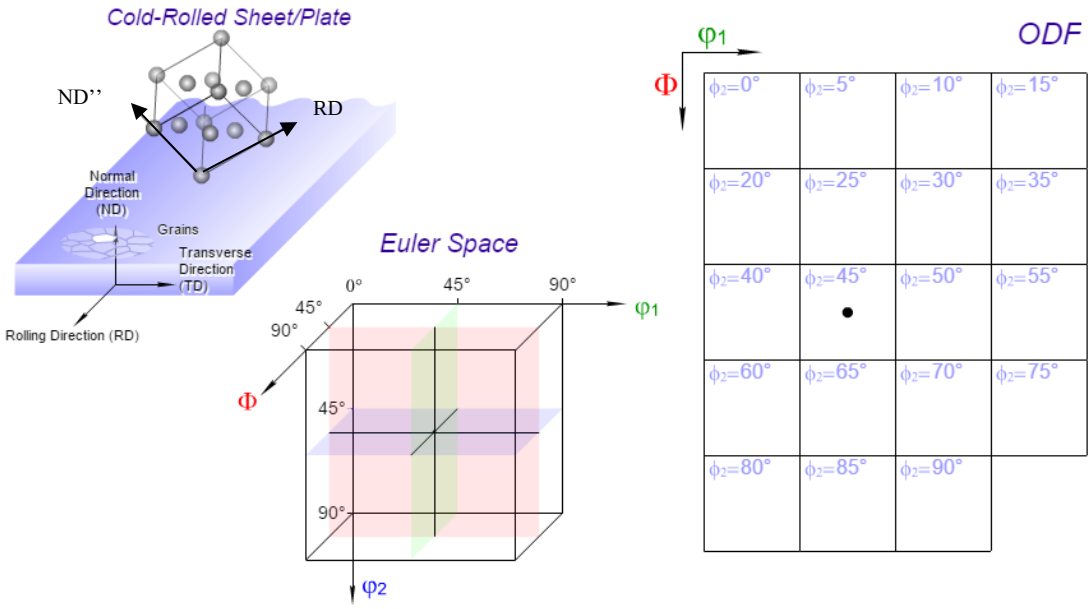

Figure 4.7. The third rotation of the third angle [153].

4.7.4 Texture components

The most important components of the deformation and recrystallization texture that can be found in aluminium alloys are the Copper (Cu), S, Brass (Bs), Goss(G), Cube, and P. [160]. In Table **4.3**, the Miller indices and Euler angles of these components are identified [32]. The typical positions of the texture components observed in FCC materials are illustrated in Figure **4.8**.

Table 4.3. The most important orientations of Al and Al alloys after rolling and after recrystallization [151].

Designation	Miller indices {hkl}<uvw>	Euler angles $\varphi_1, \Phi, \varphi_2$.
Copper (Cu)	{112}<111>	90°, 30°/35°, 45°
S	{123}<634>	59°, 34°, 65°or 60°, 32°, 65°
Brass (Bs)	{011}<211>	35°, 45°, 0°/90°
Goss (G)	{011}<100>	0°, 45°, 0°/ 90°
Cube	{001}<100>	0 °, 0 °, 0 °/ 90 °
P	{011}<122>	65 °,45 °,0 °/ 90 °

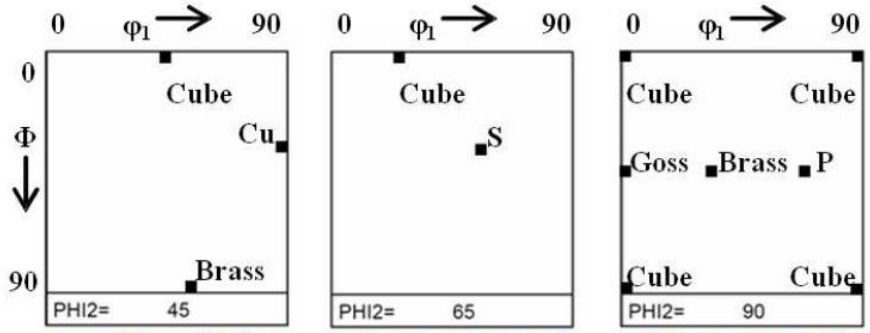

Figure 4.8. Most important orientations in FCC materials [155].

Fibres are a source of other information that can be extracted from an ODF. In FCC materials, the most important orientation fibres are the α *and* β fibres. The α fibre runs from the Goss orientation to the Bs orientation, with {011}// RD observed at low deformation degrees. If the degree of deformation is high, then the β fibre appears, which runs from the Cu orientation through the S orientation to the Bs orientation, where it meets the α fibre.

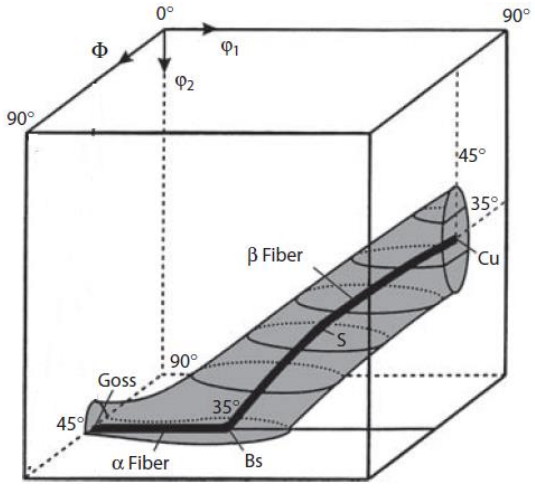

Figure 4.9. Positions of the α and β fibres, including texture components (FCC) [151].

In steel alloys, the texture components can be found primarily in the $\varphi_2 = 45^{\circ}$ section. Steel grades tend to form fibre textures, which comprise different texture components. The most observed fibres, which are α and γ, are shown schematically in Figure **4.10**.

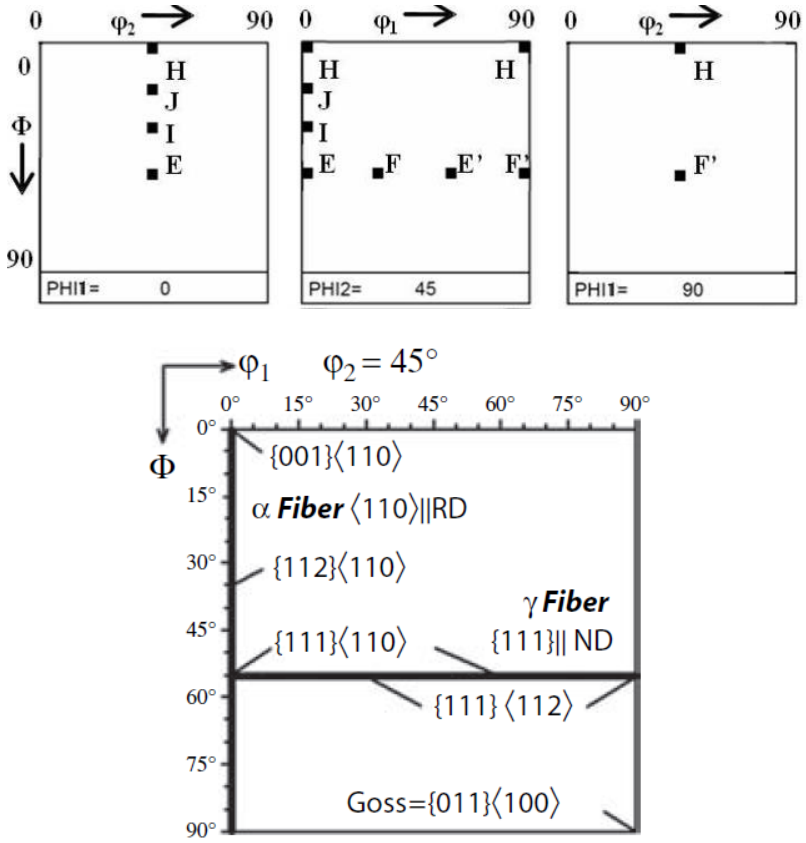

Figure 4.10. Positions of the α and γ fibres, including texture components (BCC) [151,155].

The designation, Miller indices, and Euler angle of the most common components for BCC materials are provided in Table **4.4**.

Table 4.4. The most important orientations of BCC alloys after rolling and recrystallization.

Designation	Miller indices {hkl}<uvw>	Euler angles $\varphi_1, \Phi, \varphi_2$.
H	{001}<110>	0^o; 0^o; 45^o
J	{114}<110>	0^o; 19.5^o; 45^o
I	{112}<110>	0^o; 35^o; 45^o
E	{111}<110>	0^o; 54.7^o; 45^o
F	{111}<112>	30^o; 54.7^o; 45^o
E’	{111}<110>	60^o,54.7^o,45
F’	{111}<112>	90^o,54.7^o,45^o

4.8 Taylor-Bishop-Hill

Taylor [128] and Bishop-Hill [37,119] are theoretical models that are used to calculate yield locus from the texture or to predict the texture evolution. These models describe the plastic behaviour (deformation) of a polycrystalline material from the plastic properties of the single crystals of which it is constructed [156]. With a known texture and plastic strain rate tensor that describes the macroscopic deformation of the material, these theories [157] can used to calculate the following quantities for each crystal grain individually:

- Active slip systems
- Local plastic stress state
- Local plastic work rate
- Slip rates on the individual glide systems
- New orientation of the grain

The previous quantities would be calculated to determine the average behaviour of a polycrystal material.

4.8.1 Full constraint Taylor model (TF)

It was demonstrated that Taylor and Bishop-Hill theories are equivalent theories but with different methods to identify the active slip systems [157]. Therefore, any of the two

mentioned theories can be referred to as Taylor-Bishop-Hill (TBH), Taylor, or Full constraint model (FC). The TBH theory is the classical statistical model, and it is also the simplest model [37,119,128].

4.8.1.1 *Basic assumptions*

These theories assume that the strain rate tensors are identical for all crystallites, which requires at least five slip systems to be activated to achieve this prescribed strain [129]. In other words, the TBH model assumes that the plastic deformation is homogeneous (i.e. a homogeneous distribution of plastic velocity gradient). This assumption provides a qualitative prediction as well as an upper bound solution [24]. In other words, the plastic flow occurs by crystallographic slip on a given slip system within each crystal [7]. This induces a homogeneous plastic strain rate distribution (i.e. each crystal experiences the same macroscopic strain/deformation) [24]:

$$L^{macro} = L^{micro} \rightarrow \dot{\varepsilon}^{macro} = \dot{\varepsilon}^{micro} \tag{4.3}$$

Several different combinations of sets of five slip systems can be identified, but according to [128], the set that will be active is the one that requires the minimum energy (i.e. minimum sum of slip shears) [158]. However, [37,119] use, instead, the maximum work principle to find the stress states that could activate at least five slip systems. Further details can be found in [159]. However, the equilibrium at grain boundaries will be violated by such an assumption. Also, plastic deformation cannot be homogeneous because the orientations of each crystallite are different [7].

4.8.2 The Pancake model (TP)

The previous strict assumption in the FC model is dropped by relaxing the shear components through the thickness [24] (i.e. the strain rate components $\dot{\varepsilon}_{13}$ and $\dot{\varepsilon}_{23}$ are relaxed and 'left free'). Thus, these components are not equal for all grains [129]. Figure 4.11 shows these components. [129] designed this model for pancake-shaped grains ($l \approx b \geq d$).

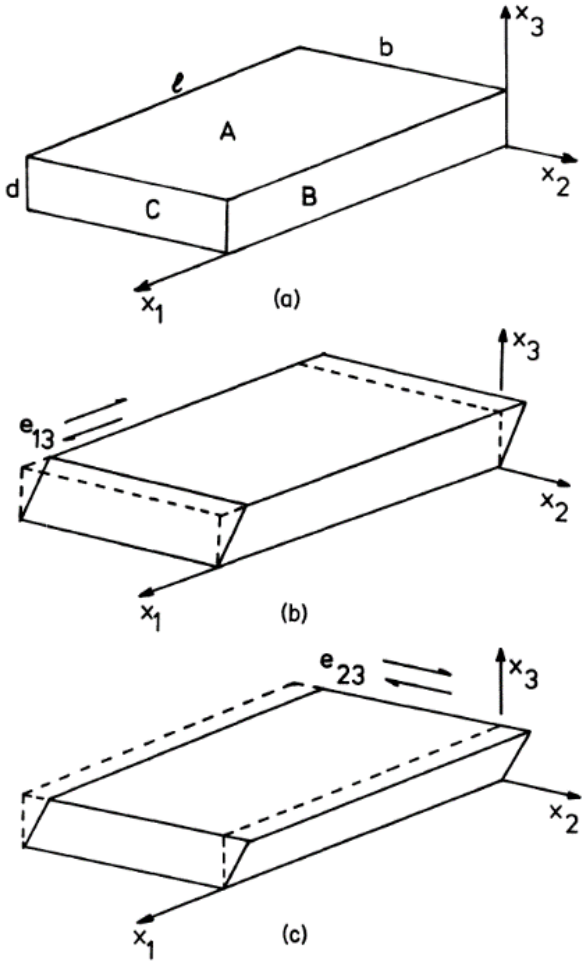

Figure 4.11. Flat grain cold-rolled sheet representation – x1 is the RD, x2 is TD, and x3 is the normal to the sheet surface. a Schematic representation of a flat grain in a cold rolled sheet b Simple shear stress $\dot{\varepsilon}_{13}$ c Simple shear stress $\dot{\varepsilon}_{23}$ [129].

4.9 Calculation of the yield locus of textured polycrystals using Taylor and the relaxed Taylor theory

A yield locus describes the plastic anisotropy of a material. The stress states when the plastic yielding of the material takes place are represented geometrically by a yield locus. In these models, it is assumed that the crystallographic texture of the sample is the main cause of the anisotropy of the material.

According to [129], the description of the yield loci calculation method is made up of finding a set of hyper-planes that is tangent to the yield locus. Each hyper-plane corresponds to a certain strain mode, described by a strain rate tensor $\dot{E}_{ij}$. The FC or RC models can be used to compute the Taylor Factor for a crystal with orientation g with

respect to the specimen coordinate system (RD, TD, and ND). The Taylor factor (M), which is the sum of glide shears [158], can be seen as the amount of energy required to deform a grain with a particular orientation. Taylor factor is a geometrical factor that depends on the axial ratio of one component to another and the orientation g. The Taylor factor is given by:

$$M_T = \left(\sum_{s=1}^{z} \left| \dot{\gamma}_s \right| \right) \Big/ \dot{E}_{eq} \tag{4.4}$$

where $\dot{\gamma}_s$ is the rate of slip on slip system s, and z is the total slip number; $\dot{E}_{eq}$, which is the equivalent strain rate of the macroscopic strain and is identified by the von Mises convention, would be:

$$\dot{E}_{eq} = \left((2/3) \dot{E}_{ij} \, \dot{E}_{ij} \right)^{1/2} \tag{4.5}$$

Then, the plastic work rate per unit volume for that crystal is determined by the following relationship:

$$\dot{W} = \tau^c M_T \, \dot{E}_{eq} \tag{4.6}$$

where τ^c is the critical resolved shear stress of the crystal, which is assumed to be equal on all the slip systems.

Then the plastic work rate equation is averaged on the entire polycrystal

$$\overline{\dot{W}} = \tau^c \overline{M} \, \dot{E}_{eq} \tag{4.7}$$

with

$$\overline{M} = \oint M(g) f(g) dg \tag{4.8}$$

The average Taylor factor $\overline{M}$ is a function of the measured crystal orientation distribution function $f(g)$ and the strain mode $\dot{E}_{ij}$. The M_T values for all possible crystal orientations g are computed using any of the Taylor model codes for a given strain mode to identify the series expansion of M_T itself:

$$M(g) \approx \sum_{l}^{L} \sum_{\mu}^{N_1(l)} \sum_{\nu}^{N_2(l)} m_l^{\mu\nu} \dot{\dot{T}}_l^{\mu\nu}(g) \tag{4.9}$$

where, $\dot{\dot{T}}_l^{\mu\nu}(g)$ are symmetrical generalised spherical harmonics of order $l, \mu, and\ \upsilon$, and $m_l^{\mu\nu}$ are the corresponding coefficients which describe the function $M(g)$ and do not depend on the texture. These coefficients depend on the degree of the series expansion L. These sets of coefficients are stored once and for all for different strain modes.

The averaging procedure is now identified by the following:

$$\overline{M} = \sum_{l} \sum_{\mu} \sum_{\nu} \frac{m_l^{\mu\nu} C_l^{\mu\nu}}{2l+1} \tag{4.10}$$

where $C_l^{\mu\nu}$ are the series expansion coefficients of the material texture which must be measured.

Now, the average work rate per unit volume can be given by another relationship:

$$\dot{\overline{W}} = \tau^c \overline{M}\, \dot{E}_{eq} = \dot{E}_{ij}\, S_{ij} \tag{4.11}$$

S_{ij} is a matrix representing a tensor S which describes the stress states when the material begins to yield plastically.

Equation (4.11), which is independent of the convention for $\dot{E}_{eq}$, is found by using equation (4.4), and then

$$\dot{E}_{ij}\, S_{ij} = \tau^c \sum_{s=1}^{n} \left| \dot{\gamma}_s \right| \tag{4.12}$$

Thus, for a given strain mode $\dot{E}_{ij}$, the $\overline{M}$ can be computed using equation (4.10). Equation (4.11) becomes a linear equation for unknown stress components S_{ij}. This in the stress space represents a hyper-plane. One point of this hyper-plane represents one point of the yield locus. By constructing many hyper-planes, an envelope to the yield locus can be identified, as shown in Figure **4.12**.

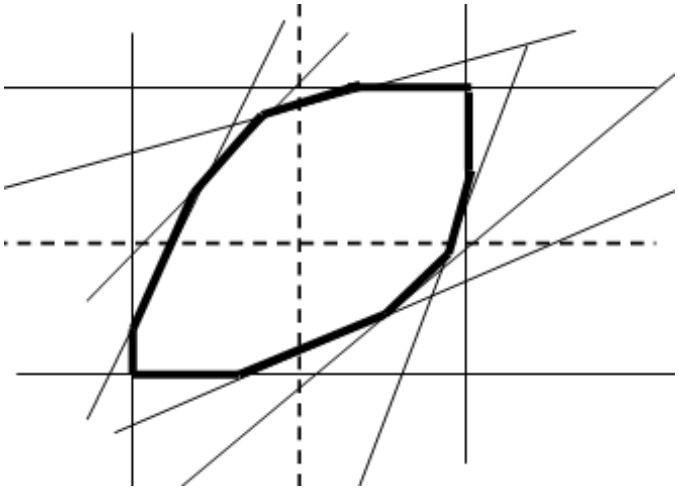

Figure 4.12. Yield locus development (Adopted from: [129]).

4.10 CTFP model (steel grades)

A correlation between the calculated texture-based yield loci and those measured from mechanical tests to define advanced yield functions efficiently and effectively for different steel grades was investigated by An et al. [7]. More specifically, a comparison of the Taylor full constraint and pancake models with experimental points and Hill' 48 yield function, fitted with plastic anisotropy *R*-values and fitted with yield stresses, shows that the full constraint model (TF) captures generally the shape of the measured yield loci except in the stretching region (first quarter of the yield locus). It was observed that the TF model underestimates the stress factors in the stretch regime, while the TP model overestimates the stress factors at the same region. It has also been noticed that the measured biaxial points are between those calculated from the two Taylor models. Based on the two texture-based yield loci calculated from the Taylor models, An et al. proposed a new combined model referred to as CTFP [7]. The model is based on calculation of the stress factors which are ratios of the principal stresses over the equivalent stress. The equivalent stress is defined as the uniaxial yield stress in the rolling direction. The CTFP model is utilised for steel grades and is used as a deployment tool to fit advanced phenomenological yield functions (e.g. Yld2000/BBC2005 with the help of simply a uniaxial tensile test in three directions). It is a qualified alternative for the biaxial test, such as the hydraulic bulge test which is required to identify the biaxial yield stress. Therefore, the high cost associated with the determination of the experimental yield loci can be minimised using the CTFP model. Consequently, complex analytical yield functions for stamping simulations can be used more frequently.

Before expressing the CTFP model mathematically, the meaning of the stress factors must be clarified geometrically. As shown in Figure **4.13**, the stress factor components of a point (P) that lies on a yield locus is the x and y coordinates of that point. The x and y axes, which are denoted as S_1 and S_2, are the ratios of the principal stresses over the uniaxial yield stress in the rolling direction. The principal stresses are obtained using the texture-based Taylor models, while the uniaxial yield stress in the rolling direction is obtained with aid of a uniaxial tensile test.

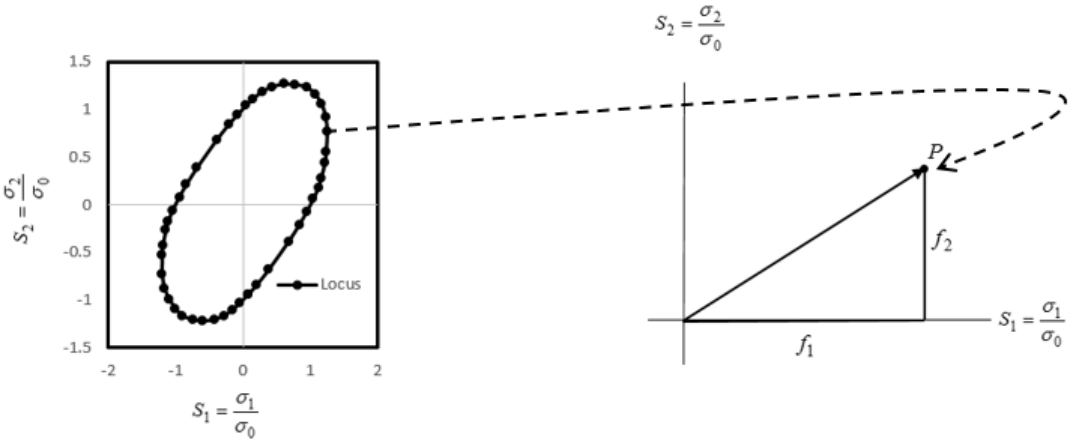

Figure 4.13. Geometrical representation of the stress factors.

The CTFP model keeps the shape of the yield loci calculated from the TF model, but the size in the first quadrant of the yield locus is scaled using the averaged biaxial points of each model, as shown in Figure **4.14**.

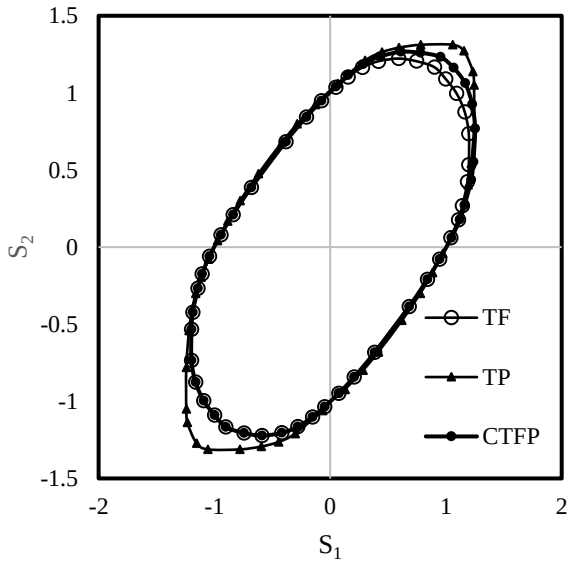

Figure 4.14. Illustration of the CTFP, TF, and TP models.

First, the biaxial point of the CTFP must be defined as follows:

$$f_b = \frac{1}{2}(f_b^{TF} + f_b^{TP}) \tag{4.13}$$

$$f_{b1} = f_b \tag{4.14}$$

$$f_{b2} = f_b \tag{4.15}$$

where f_b, f_b^{TF} and f_b^{TP} refer to the balanced biaxial stress factor on the yield loci for the CTFP model, the TF model, and the TP model, respectively; and f_{b1} and f_{b2} are the two stress factor components for the biaxial point.

Mathematically, the stress factors f_1 and f_2 in the stretching regime of the CTFP are expressed as follows:

$$f_1 = f_1^{TF} + (f_b - f_b^{TF}).\frac{f_2^{TF}}{f_b^{TF}} \tag{4.16}$$

$$f_2 = \beta^{TF}.f \tag{4.17}$$

$$\beta^{TF} = f_2^{TF} \Big/ f_1^{TF} \tag{4.18}$$

where the f_1^{TF} and f_2^{TF} are the components of the stress factor on the yield loci derived from the TF model. The parameter β^{TF} is the stress ratio for each point on the TF model. The stress ratio for each point on the CTFP model is the same as that on the TF model except in the stretching regime.

4.11 CTF (aluminium grades)

This section is devoted to the simple and efficient yield locus description. Following broadly the principle of the CTFP model described in the previous section, a similar model for the aluminium alloys is proposed. It is referred to as the CTF model. The CTF model might be used to skip a biaxial test such as the hydraulic bulge test, which can be used to identify the biaxial yield stress that is used as input for advanced yield functions such as BBC2005. A carful comparison between the TF model and measured yield locus (BBC2005) for two aluminium grades indicates that the TF are more elongated in the stretching regions.

Let’s describe some of the features of the CTF model that form the basis of the model. If we take any point lying on any locus, then this point has major and minor components, which are the stress factors.

To clarify the idea, say that we have P_1 and P_2, which are two points that lie on the loci of the CTF and TF models, respectively, as shown in Figure **4.15**. The coordinates of any point lying on any model are the major and minor components of the stress factors. The radial coordinate of a point is the **hypotenuse.**

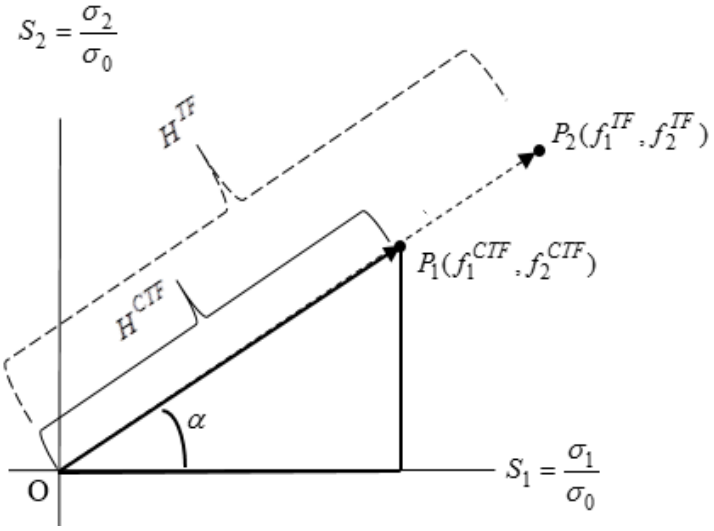

Figure 4.15. Illustration of the CTFP model and the TF model (O is the origin (0,0)).

First, the **hypotenuse** of the biaxial point of the TF (H_b^{TF}) must be defined as follows:

$$H_b^{TF} = \sqrt{(f_b^{TF})^2 + (f_b^{TF})^2} \tag{4.19}$$

where f_b^{CTF} and f_b^{TF} refer to the balanced biaxial stress factor on the yield loci for the CTF model and the TF model, respectively.

From that it is assumed that the **hypotenuse** of the biaxial point of the CTF (H_b^{CTF}) is expressed as follows:

$$H_b^{CTF} = 0.95 * H_b^{TF} \tag{4.20}$$

Then the biaxial stress factor of the CTF model can be calculated:

$$f_{b1}^{CTF} = f_{b2}^{CTF} = f_b^{CTF} = \cos(\alpha) * H_b^{CTF} = \sin(\alpha) * H_b^{CTF} \tag{4.21}$$

where f_{b1}^{CTF} and f_{b2}^{CTF} are the two stress factor components for the biaxial point of the CTF. The α is the angle where the stress factor is measured i.e. it is the angel between the radial coordinate and the x-axis.

For any point between the uniaxial stress mode in the rolling direction and the balanced biaxial point, the **hypotenuse** of any point of the CTF is expressed as

$$H_1^{CTF} = H^{TF} - [(H_b^{TF} - H_b^{CTF}) * (f_2^{TF} / f_1^{TF})] \quad (4.22)$$

For any point between the balanced biaxial point and the uniaxial stress mode in the transverse direction, the **hypotenuse** of any point of the CTF is expressed as

$$H_2^{CTF} = H^{TF} - [(H_b^{TF} - H_b^{CTF}) * (f_1^{TF} / f_2^{TF})] \quad (4.23)$$

Mathematically, the major and minor stress factors f_1^{CTF} and f_2^{CTF} in the stretching regime of the CTF are expressed as follows:

$$f_1^{CTF} = \cos(\alpha) * H^{CTF} \quad (4.24)$$

$$f_2^{CTF} = \sin(\alpha) * H^{CTF} \quad (4.25)$$

Note that the stress, f_2^{CTF}, can be expressed in terms of the stress ratio on the Taylor full constraint model, TF, as follows:

$$f_2^{CTF} = \beta^{TF} . f_1^{CTF} \quad (4.26)$$

$$\beta^{TF} = f_2^{TF} \Big/ f_1^{TF} \quad (4.27)$$

where the f_1^{TF} and f_2^{TF} are the major and minor components of the stress factor on the yield loci derived from the TF model. The parameter β^{TF} is the stress ratio for each point on the TF model. The stress ratio for each point on the CTF model is the same as that on the TF model (i.e. the CTF model keeps the shape of the yield loci calculated from the TF model in the shear regions). The scaling procedure involved in the CTF model is applied in the first and third quadrants, because the CTF is a symmetric model.

4.12 Summary

In this chapter, the polycrystal plasticity, which is the second approach for describing the behaviour of polycrystalline material, was presented. The relation between texture and anisotropy was identified. A brief review of the various polycrystalline plasticity models was provided. It was shown that the phenomenological approach requires a significant number of mechanical tests when the advanced yield function is utilised, while the polycrystal plasticity approach demands huge processing power. Several efforts that

combine the strengths of the two approaches, with different phenomenological yield functions and polycrystalline plasticity models and various metallic sheets, were presented briefly.

Texture definition and its representation tools were discussed. The FC and TP models were described. The FC-Taylor model forms the basis of the newly proposed model referred to as CTF, which was designed for aluminium alloys under this study. The CTF model is similar in nature to the CTFP model that was proposed for the steel alloys.

Chapter 5

Biaxial Flow Curve

5.1 Introduction

This chapter presents a new simple methodology to determine a biaxial flow curve from the hydraulic bulge test in the absence of an optical measurement system. In practice, sheet metals generally are assumed to harden isotropically [65], as illustrated in Figure **5.1**. In other words, the size of the yield locus would expand uniformly, as shown in the figure. Isotropic hardening describes the evolution of the material's anisotropy and was proved to be an effective method when coupled with an accurate yield function [160].

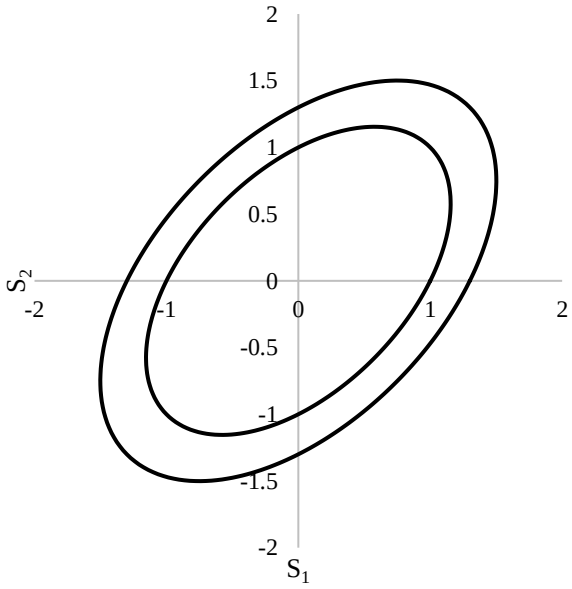

Figure 5.1. Concept of isotropic hardening.

Various isotropic hardening laws, such as Voce [161] and Holloman [162], can be used to fit a uniaxial flow curve in the rolling direction or to fit a biaxial hardening curve. This representative flow curve eventually can be used as input for FE simulations.

In this chapter, the concept of the hardening curve obtained from the hydraulic bulge test for sheet metals is explained briefly. In section 5.2, a general background for the determination of the plastic hardening curve and yield locus of metallic sheets is given. Section 5.3 presents a selection of approaches to obtain the biaxial flow curve. In section

5.4, a new method to determine the biaxial yield curve is suggested. In section 5.6, the methods of calculating the biaxial yield stress are discussed. Finally, a summary of the chapter is given in section 5.7.

5.2 General background

5.2.1 Hardening curve

Numerical simulation of sheet metal forming processes such as the stamping process is crucial in the design phase [6]. The reliability of such simulation depends on the accuracy of the mechanical characterizations of the materials [4]. One of the most important items in the material characterizations that has a major influence on the quality of the forming simulations is the plastic hardening curve [163,164]. This curve, which describes the work hardening behaviour of the metallic sheet, is an essential input for FE simulation [165]. To obtain stress-strain curves, various mechanical tests such as tensile, compression, and hydraulic bulge can be used [33]. In the field of sheet metal forming, the uniaxial tensile test is most commonly used. It provides flow curves up to the point of diffuse necking at very low levels of plastic strain. However, in sheet forming processes, the level of the plastic strains can be higher. Therefore, it is more appropriate to use biaxial stress state tests such as the hydraulic bulge test, which can reach higher plastic strain levels before necking and fracture occur [166]. Another advantage of using the hydraulic bulge test is the fact that the dominant deformation mode in sheet forming processes is the biaxial mode; thus, it is more appropriate to use such a test for obtaining the flow curves [33]. Finally, the hydraulic bulge test has the advantage of providing one of the material parameters, namely the biaxial yield stress, which is required to define most advanced yield functions [18].

The hydraulic bulge test in combination with a digital image correlation (DIC) system is the state of the art for the determination of biaxial stress-strain curves [29–31]. However, in the absence of continuous and in-line thickness measurement systems, such as the DIC system, researchers use simple analytical methods to determine the biaxial flow curves [30,32]. Furthermore, the usefulness of these analytical methodologies becomes apparent when deformation is recorded at high temperature [32,33]. It was reported by Koc et al. [33] that the results obtained with optical systems are inaccurate due to vapour and smoke resulting during deformation at high temperature conditions. These methods are concerned with identifying the bulge radius as well as the thickness at the dome apex.

One of the earliest models was developed by Hill [167], who created an analysis method for calculating the bulge radius. Panknin [168] later improved on the model by accounting for the curvature of the sheet material around the tooling fillet radius, as this significantly affects the bulge of the sheet.

Hill also introduced another analytical model for the determination of the thickness at the pole of the bulge. Chakrabarty and Alexander [169] proposed an analytical model for the polar thickness evaluation that improved the accuracy of the formula developed by Hill [167] by considering material hardening. Kruglov [170] developed a simple analysis method for dome apex thickness. In the assessment of analysis methods, Koc et al. [33] concluded that Kruglov's thickness determination approach coupled with Panknin's polar radius method is the best combination [33]. Lăzărescu et al. [30,171] have since made improvements to the overall accuracy of this method. The accuracy was improved by incorporating a correction factor relating to the polar thickness to account for the non-uniformity of the strain distribution on the dome apex. The accuracy of their methodology was observed at the final stages of the bulging experiment.

5.2.2 Yield locus

The other ingredient in the material characterizations is the yield function, which was the topic of chapter 3. It has a vital impact on the accuracy of the numerical results such as thinning and splitting [17,21–23]. Regarding this ingredient, many researchers have proposed several advanced criteria such as the Banabic–Balan–Comsa (BBC) yield criteria [48,49,57,84] and the Barlat yield criteria [16,19], which can describe the plastic behaviour of the materials accurately because they incorporate a large number of parameters. These advanced criteria account for the biaxial stretching regime that is the dominant regime in sheet metal forming [33,42]. It has been proved that these advanced models can overcome inaccuracies of classical models such as Hill'48 [47] by improving the description of the plastic behaviour of the metallic materials. Recently, Banabic et al. presented a review of the most recent yield criteria [4] for describing the anisotropic plastic behaviour.

5.3 Biaxial flow curve determination

Membrane theory is a common approach used for the determination of biaxial flow curves [168,172]. The flow curves are determined based on the analysis of measurable variables from the bulge test [29] when the sheet is clamped between the die and blank holder, as illustrated in Figure **5.2**. The theory is only valid when the ratio of the sheet thickness to

the bulge diameter is small [172]. The ratio of the sheet thickness to the radius of the die cavity is typically lower than 0.02 [173]. This theory assumes that the through-thickness stress σ_3 is zero, and a relationship can be established using Laplace's formula

$$\frac{\sigma_1}{\rho_1}+\frac{\sigma_2}{\rho_2}=\frac{p}{t} \tag{5.1}$$

where σ_1 and σ_2 are the principal stresses on the material surface, ρ_1 and ρ_2 are the curvature radii, p is the hydraulic pressure, and t is the sheet thickness at the dome apex. However, the bulge test is considered as an axisymmetric case; therefore, the principal stress can be assumed to be equivalent and equal to the membrane stress; i.e. $\sigma_1=\sigma_2=\sigma_b$. The same conclusion for the curvature radii can be drawn; i.e. $\rho_1=\rho_2=\rho$. Under these simplifications, the current biaxial stress or membrane stress σ_b is defined as

$$\sigma_b=\frac{p\rho}{2t} \tag{5.2}$$

For strain calculation, the constant volume condition of Eq. (5.3) is used. This assumption is based on the fact that the plastic deformation in metals and alloys occurs without any appreciable change in volume [3].

$$\varepsilon_{11}+\varepsilon_{22}=-\varepsilon_{33} \tag{5.3}$$

Therefore, the thickness strain or the biaxial strain ε_b can be evaluated as follows:

$$\varepsilon_b=-\varepsilon_{33}=\ln\frac{t_o}{t} \tag{5.4}$$

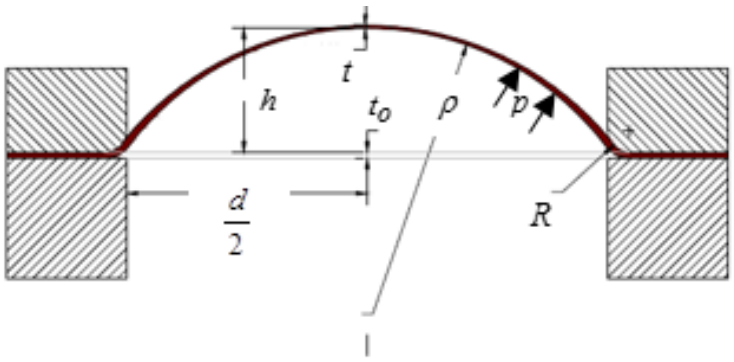

Figure 5.2. Geometry of the bulge test.

5.3.1 Experimental and analytical methods

It can be observed that the calculation of the pressure p, polar radius ρ, and current thickness at the dome apex t are required to determine the biaxial stress-strain data using Eqs. (5.2) and (5.4). The current pressure p can be recorded using a sensor attached to the hydraulic chamber. However, the other variables are not measured in a direct manner. They are derived from other experimental data, namely the polar height h.

5.3.1.1 *Polar radius*

Hill [167] developed an analysis method for bulge radius without considering the effect of the die fillet radius R. To improve the accuracy of this variable, Panknin [168] developed the analytical formula given in Eq. (5.5) for the evaluation of the polar radius that includes the effect of the fillet radius.

$$\rho = \frac{1}{2h}\left(\frac{d}{2} + R\right)^2 + \frac{h}{2} - R \tag{5.5}$$

where d is the diameter of the die cavity, R is the die fillet radius, and h is the dome height. The parameters d and R are constants related to the experimental device, while the parameter h is a variable that is measured using a displacement sensor such as a Linear Voltage Displacement Transducer (LVDT) or a DIC system [30,33].

5.3.1.2 *Polar thickness*

The data of dome apex thickness evolution can be derived experimentally using data measured by a DIC system or calculated using different approaches. Hill [167] predicted the current value of the polar thickness at the pole t using the following relationship:

$$t = t_o\left[\frac{1}{1 + (h/(d/2))^2}\right]^2 \tag{5.6}$$

Chakrabarty and Alexander [169] modified Hill's equation by considering the hardening effect to improve the accuracy. An unknown parameter λ is introduced into Hill's formula, which is a function of the strain hardening exponent of the material [169]:

$$\lambda = 1 - n \tag{5.7}$$

For all realistic cases, λ must lie between 0 and 1 to ensure that the rate of plastic work is to be positive. Chakrabarty and Alexander proposed that the polar (compressive) thickness strain rate is obtained as

$$\frac{d\varepsilon_b}{dh} = (1+\lambda)\frac{2h}{(d/2)^2 + h^2} \tag{5.8}$$

Eq. (5.8) is integrated to obtain the polar thickness strain ε_b as

$$\varepsilon_b = (2-n)\ln(1+\frac{h^2}{(d/2)^2}) \tag{5.9}$$

Since Eq. (5.9) equals Eq. (5.4),

$$\varepsilon_b = -\varepsilon_3 = \ln\frac{t_o}{t} = (2-n)\ln(1+\frac{h^2}{(d/2)^2}) \tag{5.10}$$

Then the thickness at the dome apex is defined as

$$t = t_o[\frac{1}{1+(h/(d/2))^2}]^{2-n} \tag{5.11}$$

Eq. (5.11) reduces to Eq. (5.6) when $\lambda = 1$. Moreover, the Ross and Prager assumptions [174] are obtained if $\lambda = 0$ [169].

Kruglov et al. [170] developed a simple analysis method for dome apex thickness. The formula is based on the assumption that the meridian stresses are uniformly distributed along the surface thickness [170]. The thickness at the dome apex proposed by Kruglov is obtained as

$$t = t_o[\frac{(d/2)/\rho}{\sin^{-1}((d/2)/\rho)}]^2 \tag{5.12}$$

5.4 The new methodology

This section details the method that was developed for an accurate determination of the biaxial flow curve for various aluminium and steel alloys when a continuous and in-line thickness measurement system, such as the digital image correlation (DIC) system, is absent.

Based on the constant volume assumption, the principal strains generated during a biaxial test can be related to compressive thickness strain. It is known that the biaxial strain deformation is sensitive to the plastic anisotropy [172]. It is proposed that the accuracy of the polar thickness prediction by Chakrabarty and Alexander [169] can be improved by considering the effect of the plastic strain ratios instead of the hardening effect.

Here we assume that λ is a function of the normal plastic anisotropy. Because the *R*-values for the range of materials tested here range from 0.5 to 2, we make the following assumptions of the relationship between $\bar{R}$ and λ:

$$\lambda = \begin{cases} 2\bar{R} - 1 & for \;\; 0.5 \le \bar{R} \le 1 \\ 2 - \bar{R} & for \;\; 1.0 \le \bar{R} \le 2 \end{cases} \tag{5.13}$$

where $\bar{R}$ is the coefficient of the normal anisotropy that is computed as

$$\bar{R} = \frac{R_0 + 2R_{45} + R_{90}}{4} \tag{5.14}$$

The term *normal* refers to the direction perpendicular to the sheet. The variation of the plastic properties along the thickness of the sheet is characterized by the $\bar{R}$ parameter [35]. Eq. (5.15) ensures that the rate of the plastic work condition is not violated.

$$0 \le \lambda(\bar{R}) \le 1 \tag{5.15}$$

For most of the aluminium alloys, the corresponding values of the $\bar{R}$ lie within the limit $0.5 \le \bar{R} \le 1$. Thus**,** the through-thickness logarithmic strain and current value of the polar thickness at the pole can be calculated using the following relationships:

$$\varepsilon_b = (2\bar{R}) \ln(1 + \frac{h^2}{(d/2)^2}) \tag{5.16}$$

$$t = t_o [\frac{1}{1 + (h/(d/2))^2}]^{2\bar{R}} \tag{5.17}$$

For most steel alloys, the assumption of λ is different than the one for aluminium grades. Generally, the normal anisotropy parameter for steels lies in the range of 1 to 2. Therefore, the polar strain and thickness are calculated using the following expressions:

$$\varepsilon_b = (3 - \bar{R}) \ln(1 + \frac{h^2}{(d/2)^2}) \tag{5.18}$$

$$t = t_o [\frac{1}{1 + (h/(d/2))^2}]^{3-\bar{R}} \tag{5.19}$$

For $\lambda = 2\overline{R} - 1$, it can be seen that the upper and lower bounds of the proposed methodology correspond to Hill's approach [175] and Ross and Prager's assumption [174], respectively. When $\lambda = 2 - \overline{R}$, the opposite condition holds.

5.5 Determination of the biaxial yield stress

The method of the 0.2% offset for the initial biaxial yield stress is not reliable [176] because the biaxial stress-strain data at a low level of plastic strain involve a significant amount of error [163]; therefore, the principle of the equivalent plastic work is used to obtain an average initial biaxial yield stress [31,163,176]. The principle of the equivalent plastic work can be written for the uniaxial and biaxial stress states as

$$W_u = \int \sigma_u d\varepsilon_u = W_b = \int \sigma_b d\varepsilon_b \tag{5.20}$$

where W_u, W_b are the plastic work per unit volume in the case of uniaxial and biaxial loading, respectively; σ_u, σ_b are the uniaxial and biaxial stress, respectively; and $d\varepsilon_u$, $d\varepsilon_b$ are the uniaxial and biaxial plastic strain increment, respectively. If equality prevails, then the yield stresses of the same material for the different stress states are identical [31,163]. Then the average ratio is calculated. One of the methods for determining this ratio is the approach used by Lee et al. [176]. For certain strain ranges or plastic work ranges, the ratio between σ_b and σ_u is evaluated; then the average ratio is calculated [163,176]. This average ratio times the uniaxial yield stress is the biaxial yield stress. Theoretically, the average ratio should be independent of the selected range of the plastic work; however, such value affects the resulting average ratio [163]. Alternatively, the ratio between σ_b and σ_u can be evaluated at a point that corresponds to the maximum data of the stress and strain in the uniaxial tensile test. Other methods exists and are discussed by Sigvant et al. [163].

5.6 Summary

In this chapter, the method and approaches used to determine the biaxial flow curve are presented. This chapter provided a new analytical approach to the determination of the polar thickness of a bulged sheet. The new method is based on a modified version of the Chakrabarty and Alexander equation. The proposed method considers the effect of the normal plastic anisotropy of the sheet. In the absence of a continuous and in-line thickness measurement system, the proposed method, coupled with the Panknin method, will be

tested to determine the biaxial flow curve and hence the biaxial yield stress, as presented in chapter 9.

Chapter 6

Methodology

6.1 Introduction

In light of the thesis objectives, the broad research area of this manuscript falls under the following three blocks:

- Yield locus description for aluminium alloys
- Parameter identification strategies of the phenomenological constitutive models for aluminium and steel alloys
- Biaxial flow curve determination for aluminium and steel alloys

Therefore, the broad outline of the project's experimental plan can be summarised as follows:

- Samples should be prepared in order to conduct particular experiments – mainly, tensile test, biaxial test, compression test, and texture measurement. Materials can be characterised in these tests by extracting their mechanical properties at different strain paths.
- Some of the phenomenological models, such as von Mises, Hill '48, YLD2000-2D, BBC2003 and BBC2005, will be calculated using data obtained from the experimental work.
- The respective textures of the two aluminium alloys (AA6111-T4 and AC600) and two of the steel grades (DX54D+Z120 and H220BD+Z120) must be measured using X-ray diffraction by converting diffraction data into pole figures, and then into the Orientation Distribution Function (ODF) using MTM-FHM software developed by van Houtte [154].
- Based on measured texture data, yield loci of the materials will be calculated using polycrystalline plasticity models – mainly, the Taylor full-constraint model and the relaxed pancake model – using MTM-FHM software
- From the Taylor models, the CTFP will be computed
- The CTFP then must be validated for different aluminium grades. The validation process will be easily carried out by using data points of the combined model (CTFP)

directly in the BBC2005 model, and comparing it with the one measured via the experimental work

- Finally, if the new combined model (CTFP) is not valid, another new model will be proposed
- A comparison will be carried out between phenomenological and micro–macro approaches, in terms of accuracy

This chapter describes the methodology followed in order to reach the goals of this thesis. Section 6.2 presents the materials used in this study and the reasons behind their choice. In section 6.3, mechanical tests used to define phenomenological yield functions are described. In section 6.4, phenomenological macroscopic models used in this study, and the justification of their usage, are presented. Section 6.5 explains the methodology used to identify plastic anisotropy parameters of different phenomenological yield criteria for various metallic sheets. Finally, section 6.6 is dedicated to texture measurement and polycrystalline plasticity models used in this thesis.

6.2 Materials

This thesis has three main objectives. These objectives, as well as the materials used to achieve them, are illustrated in Figure 6.1. The new yield locus description, based on the simple FC-Taylor model, was validated using two aluminium alloys (Al-Mg-Si alloys): AA6111-T4 and AC600. The comparison of line-search and trust-region strategies for the identification of the plastic anisotropy parameters of BBC2003 and Yld2000-2d yield criteria were performed for five materials: AA6111-T4, AC600, AA2090-T3, DX54D+Z, and H220BD+Z. Biaxial flow curves were determined using four materials: AA6111-T4, AC600, DX54D+Z, and H220BD+Z.

Objectives	1. Yield locus description	AA6111-T4
		AC600
	2. Parameter identification	AA6111-T4
		AC600
		AA2090-T3
		DX54D+Z
		HC220BD+Z
	3. Biaxial flow curve determination	AA6111-T4
		AC600
		DX54D+Z
		HC220BD+Z

Figure 6.1. Materials used in the study.

The automotive materials used were AC600, AA6111-T4, DX54D+Z120, and H220BD+Z100 cut from 0.9, 0.92, 0.74, and 0.69-mm-thick sheets, respectively.

The aluminium alloys contained in the 6xxx series are amongst those most frequently used as auto body panels, since they have excellent formability and corrosion resistance [12,177]. The 6xxx series has allowed companies such as Jaguar to reduce material thickness from 1.5 to 1.1 mm with no loss in strength, resulting in a significant weight reduction and less dependency on high-strength steel sheets [178].

DX54D is a continuously annealed interstitial-free metallic-coated forming steel that is used for complex components such as door inner parts, wheel arches, body sides, and tailgates [179]. The HC220BD is a bake-hardening high-strength steel used for bonnets, roofs and doors. The steel grades were utilised as a baseline in order to regenerate the CTFP model [7].

The other aluminium grade used in this study is AA2090-T3, particularly employed for parameter identification strategy studies. This material is used for aerospace applications [19]. It is strongly textured and therefore exhibits a high level of anisotropy [48]. Material properties are adopted from Barlat et al. [19], and automotive materials' chemical compositions are obtained from [19,180].

Aluminium and steel sheets were provided by Jaguar Land Rover and Tata Steel, respectively. Chemical composition limits and values, given in weight percentages

where possible, are illustrated in Table **6.1** and Table **6.2** for aluminium alloys and steel grades, respectively.

Table 6.1. Chemical composition limits in wt. % for the three aluminium alloys.

Material		Cu	Fe	Mg	Mn	Si	Ti	Cr	Zn	Li	Zr
AA6111-T4	Max.	0.90	0.40	1.00	0.45	1.10	0.10	0.10	0.15	-	-
	Min.	0.50	-	0.50	0.10	0.60	-	-	-	-	-
	Value	0.75	0.25	0.74	0.19	0.64	0.03	0.01	-	-	-
AC600	Max.	0.25	0.35	0.85	0.15	0.95	-	0.05	0.15	-	-
	Min.	-	-	0.40	-	0.30	-	-	-	-	-
	Value	0.08	0.22	0.67	0.08	0.88	-	0.01	0.02	-	-
AA2090-T3	Max.	3.00	0.12	0.25	0.05	0.10	0.15	0.05	0.10	2.6	0.15
	Min.	2.40	-	-	-	-	-		-	1.9	0.08
	Value	2.70	-	-	-	-	-	-	-	2.2	0.12

Table 6.2. Chemical composition limits in wt. % for the two steel alloys [179].

Material		C	Mn	P	S	Al	N	Ti	Si	Nb
DX54D+Z120	Max	0.120	0.60	0.10	0.045	-	-	0.30	-	-
H220BD+Z120	Max	0.1	0.7	0.8	0.025	0.1	0.05	0.12	0.5	0.09

Experimental data were collected from tensile, bulge and compression tests. The automotive materials used were AC600, AA6111-T4, DX54D+Z120, and H220BD+Z120 cut from 0.9, 0.92, 0.74 and 0.69-mm-thick sheets, respectively. Experimental procedures will be discussed in the next section.

6.3 Mechanical tests

6.3.1 Tensile test

The tensile test is one of the most widely used to define the mechanical properties of metallic materials at ambient temperature. Uniaxial stress–strain curves, uniaxial yield stresses, *R*-values, and n-values of the materials being studied are obtained using the following standards: EN 10002-1, ISO 10113, and ISO 10275 [181–183]. The uniaxial tensile tests equipped with two extensometers were performed at 0°, 45° and 90° at an equivalent strain rate of $0.001\,s^{-1}$. One of the extensometers is used to identify the true plastic strain in the longitudinal direction of the sample, whilst the other identifies the

true plastic strain in the transverse direction of the sheet. Uniaxial yield stresses or proof strengths of tested sheets were determined at 0.2% of the plastic extension – i.e. at 0.002 true plastic strain. To ensure reproducibility of the data, these tests were repeated five times at most. Data obtained from tensile tests are the uniaxial flow curves, yield stresses, *R*-values, and n-values.

Uniaxial data are used for calculating biaxial yield stresses, yield loci and determination of the uniaxial flow curve to be compared with the biaxial flow curve, as will be demonstrated in the results section.

Average mechanical properties of the first four sheets – AC600, AA6111-T4, DX54D+Z120, and H220BD+Z120 – as shown in Table **6.3**, were determined using a Zwick/Roell testing machine of 150 kN at the laboratory of the Technical University of Cluj-Napoca (by Professor Banabic team), whilst properties of the AA2090-T3, as mentioned previously, were adopted from Barlat et al. [19].

Table 6.3. The average mechanical properties of the metallic sheets.

Material	t_0 **[mm]**	YS_0 **[MPa]**	YS_{45} **[MPa]**	YS_{90} **[MPa]**	R_0 **[-]**	R_{45} **[-]**	R_{90} **[-]**	$\overline{R}$ **[-]**	n **[-]**
AA6111-T4	0.92	1	0.927	0.913	0.699	0.539	0.509	0.572	0.282
AC600	0.90	1	0.979	0.986	0.615	0.399	0.658	0.518	0.246
DX54D+Z	0.74	1	1.037	1.018	2.007	1.699	2.370	1.944	0.247
H220BD+Z	0.69	1	1.048	1.044	1.666	1.544	2.107	1.715	0.169
AA2090-T3	1.6	1	0.811	0.910	0.21	1.58	0.69	-	-

(t_0 : initial thickness; YS_0, YS_{45} and YS_{90} : yield stresses at 0°, 45° and 90°; R_0, R_{45} and R_{90} : R-values at 0°, 45° and 90°; $\overline{R}$: coefficient of normal anisotropy ; n : hardening exponent determined from sheet oriented 0° to the RD)

6.3.2 Hydraulic Bulge test

Under biaxial stress conditions, a biaxial tensile test, stack compression test, or hydraulic bulge test can be used to determine the plastic flow curve. The biaxial tensile test can be advantageously employed to generate data for any combination of tensile stresses [184]. However, this test uses a cruciform specimen that is complicated to manufacture [31]. Other major disadvantages of the test are its associated costs, and complexity of the machine [31].

The other valuable and acceptable test for characterising material properties at the equibiaxial strain path is the compression test of stacked metallic sheets [184]. This through-thickness compression test is a simple method; however, one disadvantage is that stress and strain data must be corrected due to the friction effect between sample and platen [185]. Therefore, it is difficult to measure the reliable hardening curve [186].

Alternatively, the hydraulic bulge test is most commonly used [186]. In contrast to the previously discussed tests, the hydraulic bulge test provides hardening data to very high strain levels [184,186]. Other valuable features of this test are its simplicity and cost-effectiveness [31]. However, the test is limited for the equibiaxial stress state loading condition [186].

In this thesis, as described in the following subsections, the hydraulic bulge test is used to determine:

- Biaxial yield stress
- Biaxial flow curve "plastic hardening curve"

6.3.2.1 *Biaxial yield stress*

In order to be computed, most advanced and complex yield functions require biaxial yield stress, which is an essential input used to define them. Determining a biaxial yield stress requires that the following data first be prepared:

- Uniaxial flow curve in the rolling direction
- Biaxial flow curve

Thereafter, the work per unit volume in the two cases must be calculated. To do so, an approximation of the area under the curve, as illustrated in Figure 6.2, has to be calculated using the trapezoidal rule, as follows:

$$Area_{total} = \left[\frac{(\sigma_i + \sigma_{i-1})}{2} \cdot \Delta x_k \right] + Area_{k-1} \tag{6.1}$$

where k=1,2, ...m are the number of areas to be calculated; i=0,1,2 …n are the stresses at the y-axis; σ is the true stress; and Δx is the x-axis interval.

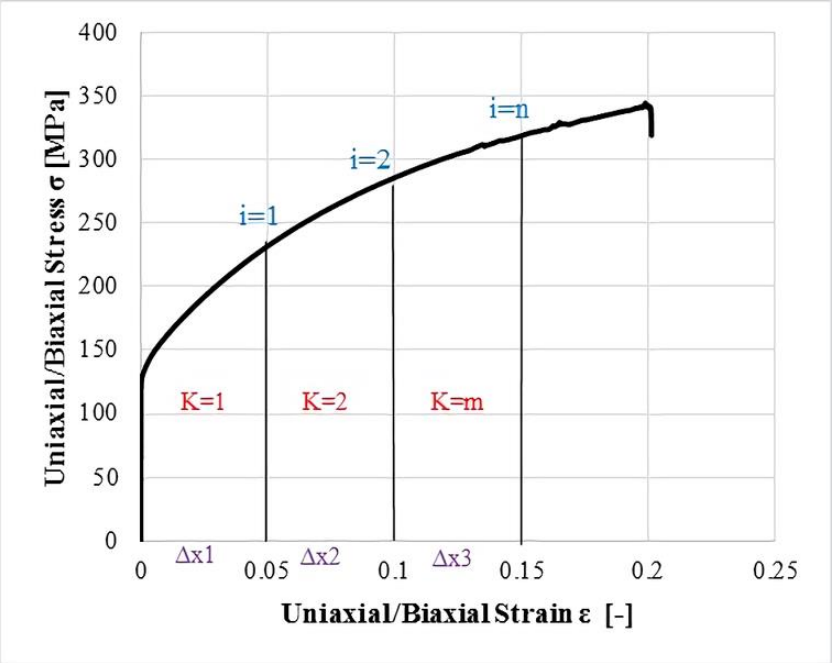

Figure 6.2. Determination of the area under the curve.

Stress–work data is then tabulated for both uniaxial and biaxial stress states. Since the intervals of the x and y-axis of both flow curves are not equal, a linear interpolation method is used in order to determine any untabulated stress or strain values. The stress–work data for both tests are illustrated in Figure 6.3.

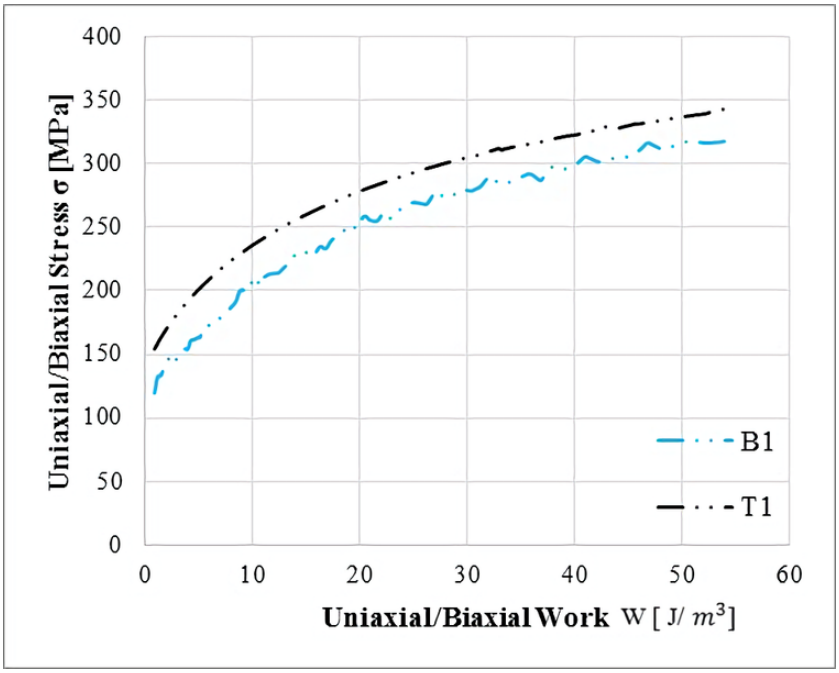

Figure 6.3. The uniaxial and biaxial flow curves as a function of plastic work for AA6111-T4 (T1: Tensile test No. 1; B1: Bulge test No. 1).

From both data illustrated in Figure **6.3**, the ratio of biaxial to uniaxial stresses over a range of plastic work is obtained, as depicted in Figure **6.4**.

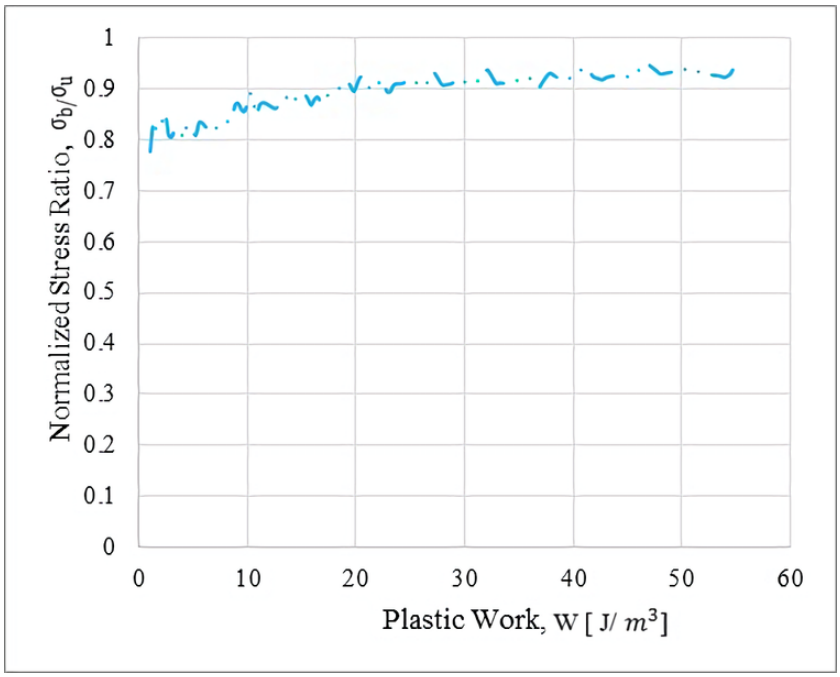

Figure 6.4. The σ_b/σ_u ratio as a function of plastic work for AA6111-T4 using DIC data.

These ratios should be constant over the chosen range. However, this is not the case in practice, as shown in Figure 6.4. Therefore, different methods for the practical computation of this ratio exist, as discussed by [163]:

- Evaluating the ratio at maximum values of stress and strain in the uniaxial test
- Evaluating the ratio at any value in the range of plastic work from 0 to maximum work performed in the uniaxial test
- Evaluating the ratios for many points, then calculating the average of these ratios (i.e. $ratio = \frac{1}{n}\sum_{i=1}^{n}\frac{\sigma_{bi}}{\sigma_{ui}}$) [176]
- Scaling the bulge test data such that the last point of the uniaxial data must be continued by bulge test data

Notably, these methods tend to vary by ±1% around their mean [163]. Therefore, the first and third methods will be used in this thesis.

Higher precision of biaxial data can be attained when the ratio of the current pressure to maximum pressure measured during the test is greater than or equal to 20% [187], and the ratio of the height of the bulge to radius of the bulging orifice is less than or equal to

0.56 [33,164]. Therefore when method three, mentioned previously, is in use, these limits are considered.

Once the ratio, irrespective of the method used, is determined, then the biaxial yield stress equals that ratio multiplied by the uniaxial yield stress.

6.3.2.2 *Plastic hardening curves*

The biaxial flow curve is currently determined using the hydraulic bulge test, in combination with a digital image correlation (DIC) system.

In the absence of continuous and in-line thickness measurement systems, such as the DIC system, accurate description of the biaxial flow curve, which is the second goal of this thesis, must be reached.

The determination of biaxial flow curves requires the instantaneous measurement or calculation of specific variables. The experimental method and combinations of different analytical approaches were used in this study. Pressure is measured using a sensor, and Polar radius determined with the DIC system and calculated analytically using Panknin's approach. The thickness at the dome apex was determined with the DIC system and calculated analytically with Chakrabarty and Alexander's method [169], its proposed modification, and the Kruglov [170] method. The continuous hydraulic bulging experiments were performed in order to validate the proposed methodology. The approach of Chakrabarty and Alexander is used for comparative purposes, as is the approach of Kruglov. Biaxial flow curves were determined using four materials: AA6111-T4, AC600, DX54D+Z, and H220BD+Z. A summary of the approaches used in this study to determine the biaxial stress–strain curves is shown in Figure **6.5**.

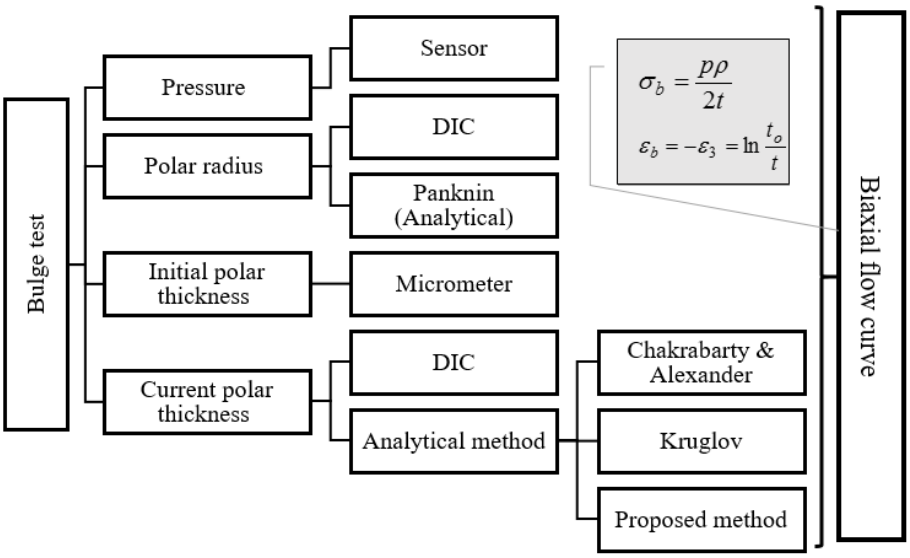

Figure 6.5. Methodologies used in the study for biaxial flow curve determination.

Bulge tests were performed on samples with diameters of 180 mm at an equivalent strain rate of 0.02 s^{-1}. The equipment is based at the laboratory of the Technical University of Cluj-Napoca. The tests were carried out by Banabic's team. As illustrated in Figure 6.6, it consists mainly of the following:

- CCD cameras
- ARAMIS strain-measurement system
- Hydraulic device

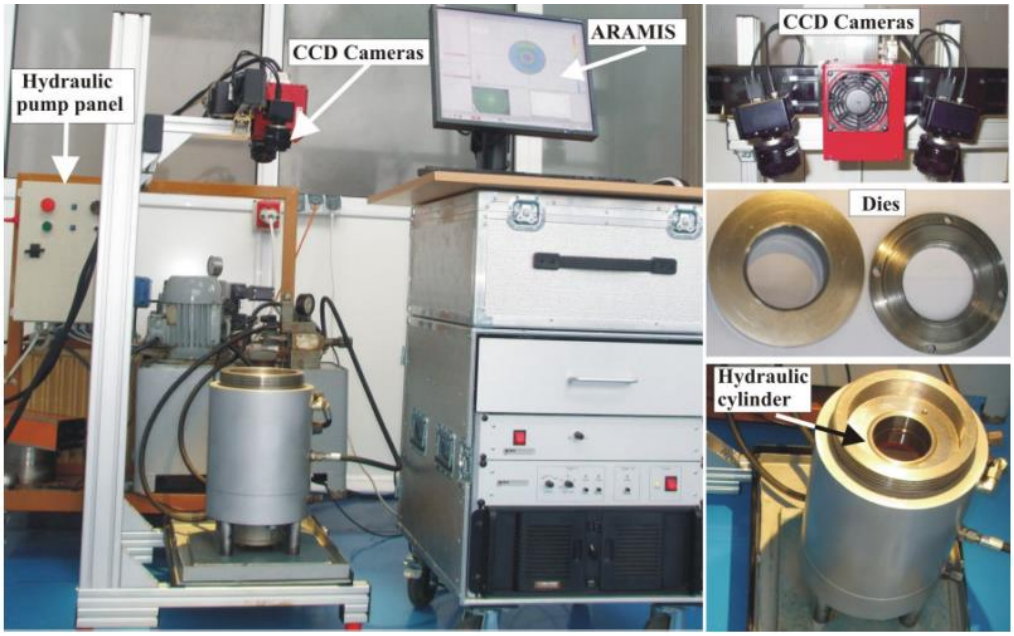

Figure 6.6. Bulge test [30].

In summary, the main two goals of the bulge test are:

- Proposing a new methodology to determine biaxial strain
- Determining biaxial yield stress

6.3.3 Through-thickness disk compression test

Advanced yield functions such those utilised in this thesis (e.g. Yld2000, BBC20003, and BBC2005) require an important material parameter to be defined. This is the equibiaxial *R*-value, denoted as R_b, which was introduced by Barlat et al. [19]. The equation $R_b = \varepsilon_{TD}/\varepsilon_{RD}$ describes the slope of the tangent to the yield surface at the point of the balanced biaxial stress state [102]. The importance of this parameter is its ability to control the shape of the yield locus, which, in turn, affects the predicted forming limit curves [188].

This parameter can be determined as follows:

- Experimentally using the procedure explained by [19]
- Estimated theoretically, using either the polycrystalline plasticity model if the crystallographic texture measurement is available [36]
- Evaluated using different yield functions such as Yld96 [80], as described by [36], Hill [47] and Tong [189]

Compression tests were performed on samples with diameters of 10 mm at an equivalent strain rate of 0.001 s^{-1}. Sheep Suet, provided by Erichsen GmbH & Co. KG, Germany, was used as a lubricant in the compression tests. The compression test of the disks was realized using a tensile-compression machine Instron of 250 kN. The tests were conducted at the laboratory of the Technical University of Cluj-Napoca (by Professor Banabic team).

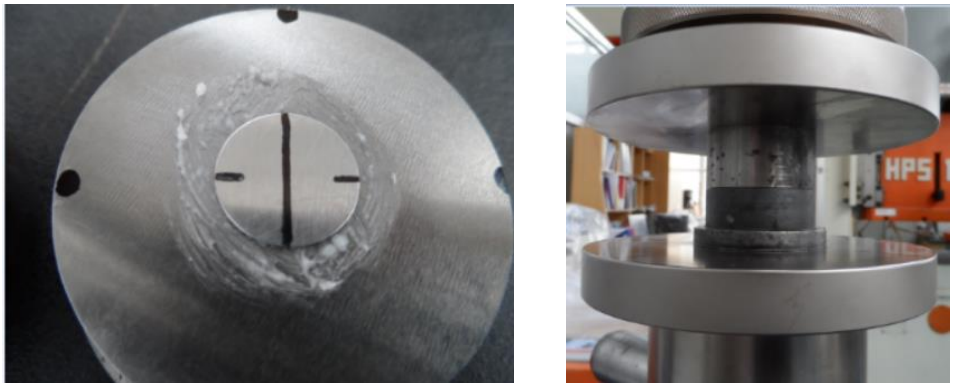

Figure 6.7. Sample before deformation (left) and holders of the machine (right).

Each of the disks is compressed through its normal direction to a specific applied force that causes deformation. Then, strains in the rolling and transverse directions are

measured. A linear relationship, as demonstrated by [36], is developed between the strains, the slope of which is equivalent to the equibiaxial anisotropy parameter R_b. The tests are repeated five times for each material.

6.3.3.1 *Determination of the* R_b

The deformed (large circle) and undeformed (small circle) states of the specimen are depicted in Figure **6.8**. The a_0 is the original diameter of the specimen parallel to the rolling direction, a_1 is the diameter of the specimen after deformation parallel to the rolling direction of the sheet, b_0 is the original diameter of the specimen perpendicular to the rolling direction of the sheet, b_1 is the diameter of the specimen after deformation perpendicular to the rolling direction, ε_{RD} is the true strain parallel to the rolling direction of the sheet, and ε_{TD} is the true strain perpendicular to the rolling direction of the sheet.

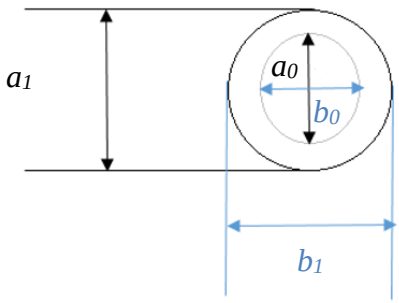

Figure 6.8. Deformed and undeformed disks.

The dimensions of the undeformed sample (a_0 and b_0) are determined first. After applying a specific amount of force on the disk, dimensions of the deformed samples (a_1 and b_1) are then measured. Next, the true strains in the rolling direction [$\varepsilon_{RD}=\ln(a_1/a_0)$] and in the transverse direction [$\varepsilon_{TD}=\ln(b_1/b_0)$] are calculated. Finally, the slope [$R_b=\varepsilon_{TD}/\varepsilon_{RD}$] equals R_b. The equibiaxial *R*-values of all materials are summarised in Table **6.4** Details of experimental data used to compute the biaxial anisotropy parameter are presented in Table 6.5, Table 6.6, Table 6.7 and Table 6.8 for AC600, AA6111-T4, DX54D+Z120, and H220BD+Z100, respectively.

Table 6.4. A summary of the biaxial anisotropy parameter.

Material	R_b **[-]**
AA6111-T4	1.299
AC600	0.962
AA2090-T3*	0.33
DX54D+Z120	0.902
H220BD+Z100	0.871

**The equibiaxial R-value was calculated following the process outlined by Barlat et al.* [36]

Table 6.5. Biaxial anisotropy coefficient – Compression test – AC600.

Material	Test No.	a_0	b_0	a_1	b_1	$\varepsilon_{RD}=\ln(a_1/a_0)$	$\varepsilon_{TD}=\ln(b_1/b_0)$	$R_b=\varepsilon_{TD}/\varepsilon_{RD}$
AC600	1	10.010	10.000	12.480	12.360	0.22054277	0.211880359	0.96072231
	2	10.000	10.005	12.310	12.340	0.207826847	0.20976105	1.009306802
	3	10.000	10.000	12.465	12.255	0.220339624	0.203348924	0.922888586
	4	9.995	10.000	11.335	11.340	0.125810316	0.125751205	0.99953016
	5	10.000	10.000	11.525	11.395	0.141933496	0.13058957	0.920075764
							Average	**0.9625047243**

Table 6.6. Biaxial anisotropy coefficient – Compression test – AA6111-T4.

Material	Test No.	a_0	b_0	a_1	b_1	$\varepsilon_{RD}=\ln(a_1/a_0)$	$\varepsilon_{TD}=\ln(b_1/b_0)$	$R_b=\varepsilon_{TD}/\varepsilon_{RD}$
AA6111-T4	1	9.990	10.005	11.630	12.150	0.152003374	0.194244202	1.277894015
	2	10.000	10.005	11.690	12.380	0.156148682	0.212997299	1.36406722
	3	9.990	10.000	11.480	12.080	0.139021798	0.1889661	1.359255181
	4	9.995	10.000	11.535	12.130	0.143300924	0.19309663	1.347490477
	5	9.995	10.000	11.785	12.085	0.164742568	0.189379921	1.149550617
							Average	**1.2996515019**

Table 6.7. Biaxial anisotropy coefficient – Compression test – DX54D+Z120.

Material	Test No.	a_0	b_0	a_1	b_1	$\varepsilon_{RD}=\ln(a_1/a_0)$	$\varepsilon_{TD}=\ln(b_1/b_0)$	$R_b=\varepsilon_{TD}/\varepsilon_{RD}$
DX54D	1	10.180	10.165	11.615	11.485	0.131872355	0.122091389	0.92583005
	2	10.160	10.165	11.580	11.485	0.13082103	0.122091389	0.933270355
	3	10.150	10.170	11.660	11.475	0.138690475	0.120728546	0.870489091
	4	10.150	10.160	11.595	11.425	0.133100265	0.117345495	0.881632313
	5	10.155	10.170	11.590	11.455	0.132176462	0.118984106	0.900191333
							Average	**0.902282628**

Table 6.8. Biaxial anisotropy coefficient – Compression test – H220BD+Z100.

Material	Test No.	a_0	b_0	a_1	b_1	$\varepsilon_{RD}=\ln(a_1/a_0)$	$\varepsilon_{TD}=\ln(b_1/b_0)$	$R_b=\varepsilon_{TD}/\varepsilon_{RD}$
H220BD	1	10.150	10.165	11.050	11.030	0.084956722	0.081668386	0.961293984
	2	10.150	10.160	11.475	11.245	0.12269705	0.101465143	0.826956662
	3	10.150	10.170	11.845	11.535	0.154432132	0.125943682	0.8155277
	4	10.140	10.160	11.725	11.520	0.145235316	0.125626213	0.86498392
	5	10.150	10.160	11.725	11.550	0.144249609	0.128226995	0.888924385
							Average	**0.87153733**

6.4 Phenomenological yield functions

The analytical yield functions used in this study are von Mises, *R*-based Hill ‘48, BBC2003, YLD2000, and BBC2005. The von Mises is the only isotopic yield criterion used in this thesis for the purpose of comparison.

Hill ‘48 is commonly used in the industry due to its simplicity; therefore, it will be utilised in this thesis. Anisotropy is introduced analytically into the von Mises formulation. Its parameters are calibrated using the *R*-values.

The other yield functions utilised in this study – mainly, BBC2003, YLD2000, and BBC2005 – are advanced models and are chosen because it was established that any yield function that employs at least eight material parameters can predict the earing profile accurately [63,64].

Experimental observations showed that most of these advanced yield surfaces accurately describe the biaxial stretching region, which is the dominant deformation mode in sheet metal forming. Numerous researchers explored the validity of these yield criteria. For instance, Mattiasson and Sigvant [18] proved that the advanced yield criteria, referred to as Yld2000, are suitable for industrial sheet forming applications. Researchers [65] established that Yld2000 could capture the earing profile (number of ears as well as overall shape) of particular aluminium alloys. Both Banabic et al. [49] and Paraianu and Banabic [87] demonstrated that BBC2005 and BBC2003 can both describe the effects of the plastic anisotropy of metallic sheets (aluminium and steel) subjected to forming processes, such as bulging and cross-deep drawing.

Researchers in [16] found that BBC2003 and Yld2000-2d are the same, yet appear in different forms [6,48]. In order to formulate an anisotropic yield function, the authors of BBC2003/BBC2005 included new coefficients into Hershey’s formulation, whereas the authors of Yld2000-2d used a linear transformation method.

6.5 Parameter identification

After determining mechanical inputs of the yield functions (BBC2003, Yld2000), different algorithms (two line search and one trust region search solution methods) were tested to identify the plastic anisotropy parameters associated with them. However, these parameters for BBC2005 were determined using a Newton solver.

To examine and identify the issues and sources of difficulty that can occur during the coefficients identification methods, this study employs three different algorithms to calculate the material coefficients of the Yld2000 and BBC2003 yield functions for different sheets of aluminium and steel alloys, used in the automotive and aerospace industries. All of the applied algorithms are gradient-based, yet have different search strategies (line search or trust region). We apply the trust region dogleg (TRD) algorithm, which is a modified version of the Powell dogleg method [106] with a certain similarity to the algorithm implemented in MINPACK [190]. We also apply the Levenberg (L) [107] and Levenberg–Marquardt (LM) [108] minimisation algorithms. We demonstrate that all these algorithms can circumvent the difficulties encountered when using the NR method. These algorithms are implemented through the fsolve function in the MATLAB Toolbox. Experimental results are gathered from tension, bulge and compression tests. The BBC2003 [48] and Yld2000-2d [19] yield criteria are considered.

6.5.1 Implementation

The yield functions BBC2003 and Yld2000-2d, and their systems of eight nonlinear equations, were written in MATLAB in order to verify the ability of the TRD, L and LM algorithms to solve issues encountered with the NR method. These algorithms were implemented using a built-in function from the Optimization Toolbox in MATLAB: fsolve. This function finds the roots of a system of nonlinear equations. The TRD algorithm is available in fsolve, implemented in a function termed trustnleqn. The Levenberg-Marquardt function implements both L and LM algorithms. In these two versions, the initial damping parameter was first set to 0.1 and then 100. The function fsolve uses finite differencing to approximate the Jacobian of the system. Only the forward finite difference method was used because it is faster than the central finite difference method, owing to the smaller total number of function evaluations. In our experience, the accuracy gained by the latter method is not required for the calculation of plastic anisotropy coefficients involved in the yield functions of this study.

To examine the sensitivity of the yield functions to the initial guess, solution method and material, a set of 100 random variables were used as initial guesses for testing both yield criteria with the applied algorithms. These random variables were generated using a uniform distribution, returning real numbers between zero and one.

A suitable algorithm should be robust, efficient and accurate [98]. Therefore, we will discuss these properties regarding the applied algorithms.

6.6 Polycrystalline plasticity approach

This section describes procedures used to determine the full constraint of the Taylor model, and its relaxed version.

6.6.1 Materials preparation

The polycrystalline plasticity models consider texture as the main source of anisotropy. Therefore, the initial texture must be measured in the form of an ODF, by conducting a texture goniometer measurement. However, before proceeding with the measurement, such material must be prepared.

Through-thickness texture gradient is assumed to be negligible [118,143,155,191] – i.e. the texture in the mid-thickness layer is the same as that in the outer surface of the sample. However, to ensure a representative texture, the sample must be etched to its centreline layer. Deriving the texture at the mid-thickness layer has the advantage of avoiding those layers where processing rolls contact the specimen; thus, potential surface heterogeneities are eliminated [192].

To measure the material's texture at the mid-thickness layer, a square sample of 10×10 mm is obtained. The surface of the sample needs to be grinded and polished using grinding papers (700, 1200, 4000 [~7μm]), diamond pastes (3 μm and 1 μm), and a final stage with an oxide polishing system with SiO2 (0.25 μm), to avoid any deformed material.

6.6.2 X-ray (Texture, pole figures, ODF)

6.6.2.1 *X-ray experiment*

The X-ray technique is used to measure macro-texture with the so-called Schultz reflection method [151]. This method allows a pole figure to be obtained. However, some useful texture information may be lost, and to overcome this uncertainty an ODF is used [147]. Using an X-ray pole figure goniometer is more rapid than other techniques and easily automated, as well as being inexpensive in acquisition and maintenance [145].

Texture or preferred orientation of crystallites is an intrinsic aspect of metals, and the physical properties of the materials, such as strength, toughness, etc., will be affected by the texture, particularly in the anisotropy of these properties [145].

One conventional technique used to measure macro-texture – averaged orientation data from many grains – of the material is the X-ray technique, which is much easier in terms

of access than neutron sources [151]. Also, it is a reliable and accurate measurement for measuring Taylor models, as many studies have demonstrated – e.g. [7,61,125,141,193].

The number of grains sampled by the X-ray technique is larger than those able to be sampled using the EBSD method, which is based on an electron source [194]. However, it has been established that the EBSD is also an alternative for the X-ray technique when deriving a macro-texture result [194]. Thus, for the purpose of the thesis, the ability to sample more grains would characterise the sheet more efficiently. This measurement can also be made via neutron diffraction, which is an alternative means for measuring macro-texture of the materials. However, the X-ray machine will be able to produce a reliable result for the purposes of this thesis.

Measurements were conducted on a Siemens D500 X-ray goniometer at the Department of Materials Engineering, University of Leuven. The goniometer is equipped with a copper anode – with a wavelength of 1.54051 A^o – operating at 40 kV and 40 mA.

Under such operating conditions, for AA6111-T4 and AC600, four incomplete pole figures {111}, {200}, {220} and {311} were measured, while for the BCC metals DX54D and H220BD+Z, pole figures {110}, {200}, {211} and {103} were measured.

Powder samples of 99% pure aluminium and 99% pure iron with particle sizes of 10 microns must be measured for background and defocusing correction procedures. The small sizes were chosen in order to ensure the absence of texture – i.e. random texture.

6.6.2.2 *Corrections*

Defocusing and background correction procedures for the raw data or pole figures measured by the D500 X-ray goniometer must be performed using MTM-FHM software developed by Van Houtte [154]. This is used to process incomplete pole figures measured with the X-ray diffraction technique using the back reflection method employing a texture goniometer, in order to produce an ODF using Euler angles. This system can be used for materials with cubic crystal structure and orthorhombic sample symmetry, as is the case for cold-rolled aluminium and steel sheets. Another feature of this software is its ability to calculate yield loci derived from the full-constraint Taylor model and its relaxed version, both of which were described in Chapter 4.

The background and defocusing are due to incoherent scattering and fluorescence in the sample, and increasing sample tilt, respectively [151]. Another error intrinsic to the experiment is that computed ODFs contain truncation and ghost errors that require

correction [146,151]. There is a need to truncate the series expansion of pole figure as well as the ODF, which leads to a broadening of texture peaks and a minimising of some intensities near strong texture components. Missing or wrong intensities that appear are termed negative or positive ghosts, respectively [151]. Such errors must be corrected by the MTM-FHM software.

6.6.2.3 *ODF*

After obtaining corrected measurements of the pole figures, the texture is presented by an ODF. For FCC metals, the ODF is measured from four pole figures {111}, {200}, {220} and {311}, while for BCC metals, it is measured from pole figures {110}, {200}, {211} and {103}.

To retrieve an ODF from the pole figure, various methods can be used [144–146,151], such as the WIMV method developed by Williams, Imhof, Matthies, and Vinel, the vector method, and the maximum entropy method, which function in direct space and use tomography algorithms. In contrast, other methods such as the most well-established technique – namely, the harmonic method introduced by Bunge (1965) – work in Fourier space. The MTM-FHM calculates the ODF based on the harmonic method. It is important to note that all of these methods yield similar results [145]. Although the direct methods implicitly address some of the problems associated with measurement, such as ghost errors, the harmonic method is more rapid and is considered reliable [145,151]. Also, some texture-related properties – e.g. plastic anisotropy – can be calculated using C-coefficients. Moreover, using the harmonic method yields an easier normalisation procedure of the pole figures [151].

6.6.2.4 *Yield loci*

Based on measured texture data (ODF), yield loci of the materials will be calculated using the polycrystalline plasticity models: the Taylor full-constraint model and the relaxed pancake model. These models are implemented in the MTM-FHM software. Both Taylor models are required to compute the CTFP model, whilst the full-constraint Taylor is the only model used for the development of the new model, referred to as the CTF.

From the Taylor models, the CTFP is computed. Then, the CTFP must be validated for different aluminium grades. This process is easily carried out by using data points of the combined model (CTFP), with the assistance of a uniaxial tensile test directly in the BBC2005 model, and a comparison of this with the one measured via the experimental work – involving all three basic mechanical tests: tensile, bulge, and compression.

6.6.3 Comparison between the two approaches

Another objective of this thesis is to carry out a comparison between the two approaches – the phenomenological approach (BBC2005 – von Mises – Hill ‘48) and the polycrystalline plasticity approach (FC, RC, CTFP, and CTF) – in terms of accuracy. This comparison is outlined in Chapter 7.

Chapter 7

Polycrystalline Model Combined With Phenomenological Model (Results and Discussion)

7.1 Introduction

This chapter presents the experimental procedures used to validate the CTFP model, presented in chapter 4, section 4.10, for the considered aluminium alloys. In addition, the chapter addresses the process used to validate the new model, known as the CTF model, which was described in chapter 4, section 4.11.

Once these models are validated, they will be deployed to fit other flexible yield functions such as the BBC2005. This will be accomplished by extracting, if possible, points of the different stress states from the models with the help of the data from tensile tests.

Section 7.2 presents the scan measurements. Section 7.3 shows the texture measurements, including the measurement of the pole figures and calculation of the orientation distribution function. In section 7.4, calculation of the yield loci with the polycrystalline approach for the materials in the study is presented and compared with the phenomenological models. Finally, a summary of the main findings is shown in section 7.5.

7.2 Scan measurement

Four square samples of 10×10 mm were grinded and polished to the mid-thickness layer of the sample. Figure 7.1 shows the principle for identification of the Bragg angle. As illustrated in Figure 7.1, each sample was mounted on the sample stage in a way that the rolling direction (RD) was parallel to the incident beam. The tension and current of the generator, which is the X-ray source, were set to 40 kV and 40 mA, respectively. The goniometer was equipped with a copper anode which generates rays with a wavelength (λ_w) of 1.54051 Aº. A nickel filter was used to reduce the intensity of unnecessary radiation such as the characteristic line Kβ and background intensities.

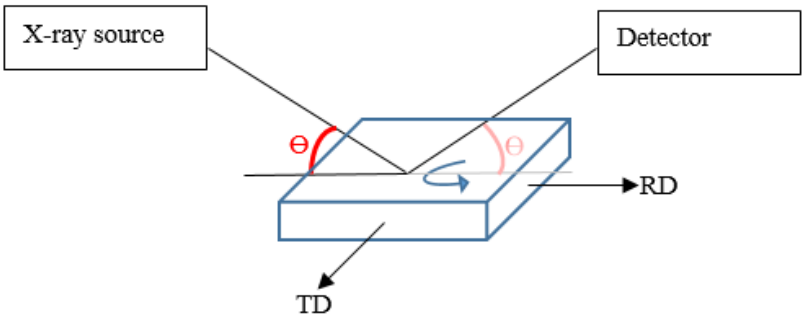

Figure 7.1. Identification of the diffraction angle 2Θ.

The diffraction angle, or Bragg angle, 2Θ, of any set of planes (h k l) can be obtained by scanning the sheet metals or powders over certain ranges. These ranges, which can be seen in Figure 7.2, are 30 to 80 and 40 to 120 for aluminium and steel samples, respectively. Scanning within these limits with a Cu kα radiation source will identify the reflections or peaks for the different families of planes that satisfy the Bragg law condition (λ_w=2 d sin Θ, where d is the interplanar spacing). In other words, for aluminium materials, the Bragg angles of the {111}, {200}, {220}, and {311} family of planes will be identified, while for the steel grades, the Bragg angles of the {110}, {200}, {211}, and {103} family of planes will be defined, as illustrated in Figure 7.2.

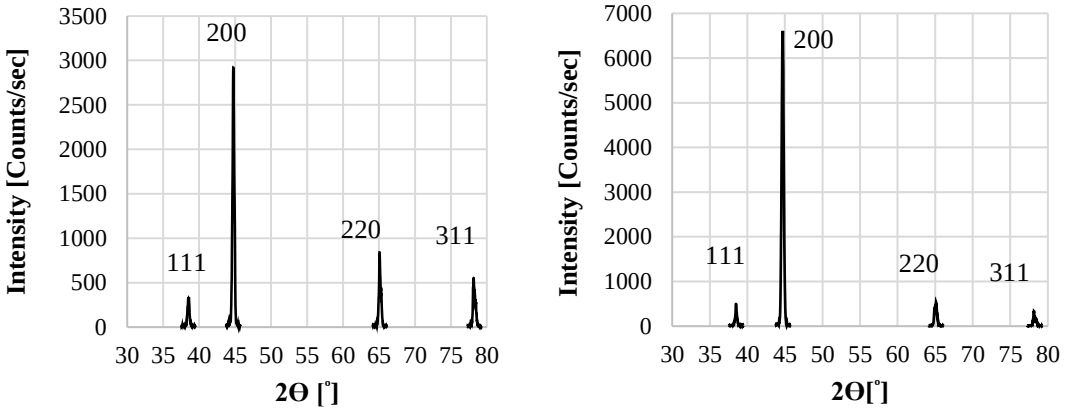

(a) (b)

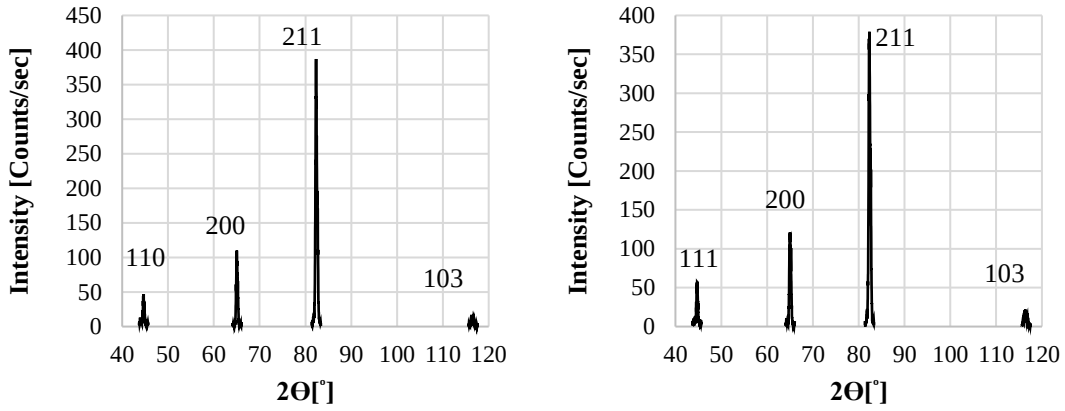

(c) (d)

Figure 7.2. Scan measurements: **a** AA6111-T4, **b** AC600, **c** DX54D+Z, **d** H220BD+Z.

The scan measurements were taken for the specimen of each sheet, as illustrated in Figure 7.2. The scan measurements were also conducted on two powder samples. Two powder samples of 99% pure aluminium and 99% pure iron were employed to identify the 2Θ of the same sets of planes used to identify the Bragg angles of the sheets.

These families of planes and the corresponding Bragg angles for the sheet and powder samples, and the angles where the background measurements for the sheet and powder samples were taken, are tabulated in Table 7.1, Table 7.2, Table 7.3 and Table 7.4 for AA6111-T4, AC600, DX54D+Z, and H220BD+Z, respectively.

Table 7.1. Bragg and background angles related to AA6111-T4 and aluminium powder.

hkl	2 Θ [°]		Background [°]
	Sheet	Powder	
111	38.516	38.442	34
200	44.746	44.706	50
220	65.08	65.096	60
311	78.152	78.222	74

Table 7.2. Bragg and background angles related to AC600 and aluminium powder.

hkl	2 Θ [°]		Background [°]
	Sheet	Powder	
111	38.5	38.442	34
200	44.704	44.706	50
220	65.11	65.096	60
311	78.126	78.222	74

Table 7.3. Bragg and background angles related to DX54D+Z and iron powder.

hkl	2 Θ [°]		Background [°]
	Sheet	Powder	
110	44.638	44.66	50
200	64.998	65	60
211	82.308	82.31	90
310	116.388	116.348	110

Table 7.4. Bragg and background angles related to H220BD+Z and iron powder.

hkl	2 Θ [°]		Background [°]
	Sheet	Powder	
110	44.716	44.66	50
200	64.994	65	60
211	82.308	82.31	90
310	116.316	116.348	110

7.3 Texture

The textures of the considered materials are represented by pole figures and the orientation distribution function (ODF).

7.3.1 Raw and corrected pole figures

The purpose of measuring pole figures is to calculate an orientation distribution function. This function is the primary input for the polycrystalline plastic models used in this study.

From the XRD measurements, two files, which were used as inputs for the MTM-FHM software, were constructed. The two files are

1. Pole figure file
2. Powder file

The measurements followed to construct these files are described in the following sections.

7.3.1.1 *Sheet sample (pole figure file)*

The pole figure file consists of the raw data of the four measured pole figures and the four background values at the centres of the considered poles.

To measure a pole figure of a certain family of planes:

1. The sample was mounted on the three-axis cradle, "the Eulerian cradle", or specimen stage) in a way that the rolling direction (RD) was parallel to the incident beam.
2. The goniometer was set at the 2Θ that corresponded to that set of planes. For example, to measure the {111} pole figure of AA6111-T4, the X-ray source was set at 2Θ = 38.516º, as illustrated in Table **7.1**.

To clarify the principle of measuring any pole figure, the following information is required.

- The pole figure consists of circles starting at the centre, as depicted at the right-hand side of Figure 7.3. Each circle is characterized by different ϕ. The sample is horizontal at ϕ = 0 and at the centre of the pole figure. The other circles are obtained by tilting the sample in anticlockwise direction around the rolling direction axis (see the left-hand side of Figure **7.3**) in steps of 5º. The maximum inclination is set to 80º. Therefore, each pole figure has 17 values or circles. The inclination starts from ϕ =0º to 80º in steps of 5º.
- Each circle consists of many data points, "segments", or "readings" that represent the intensities of the reflections of the specific set of planes. For each circle, the stage rotates the sample in anticlockwise direction around the sample's normal. The rotation goes from α= 0º to 360º in steps of 4º. This method of rotation results in 90 "readings" (intensities) per circle.

The total number of readings is 17× (360º/4º) (i.e. 1530 intensities per pole figure). This process takes roughly about half an hour for a complete pole figure to be measured with a counting time of one second per data point.

Beside these values, the background intensity for the specific pole figure at the centre of the pole is required for the case of the sheet sample to be measured. The measurements of such intensities for the different sets of planes are taken by offsetting their 2Θ angles forward or backward by a few degrees.

This set of measurements is repeated for each reflection (i.e. in the case of aluminium alloys, the measurements are done for the {111}, {200}, {220}, and {311} reflections). A portion of the pole figures file of the AA6111-T4 measurements is given in appendix A.1.

7.3.1.2 *Powder sample (powder file)*

Aluminium and iron powder samples were prepared carefully to ensure that each sample had as random a texture as possible. The powder sample was measured precisely, following the same procedures that were set for the measurement of the pole figure. The powder file was constructed for the purposes of background and defocusing corrections. The powder file contains the average background values and the unit intensity values for the considered circles (i.e. in our study for both powder samples, measurements are taken for 17 average background values and 17 unit intensities). The unit intensity equals the average intensity on a specific circle minus the background intensity on the same circle. The powder file of the aluminium data is illustrated in appendix A.2.

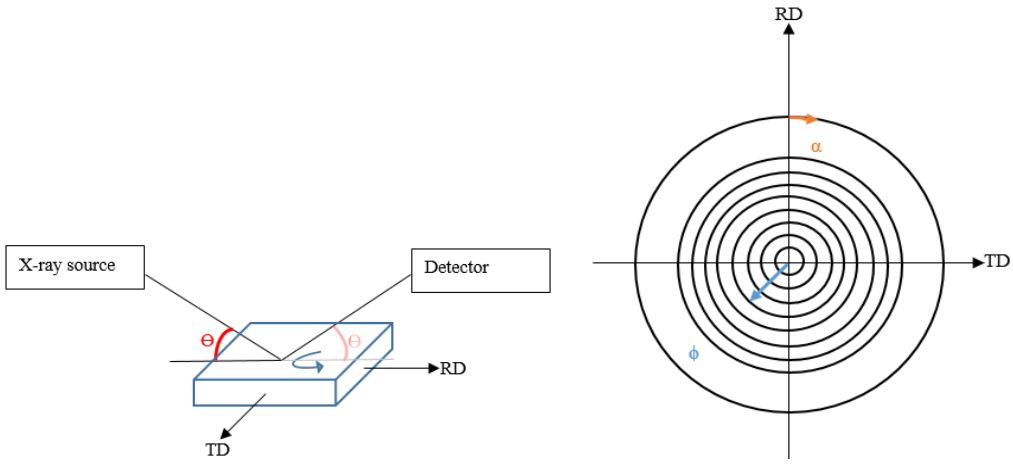

Figure 7.3. Pole figure measurement.

7.3.1.3 *Corrected pole figures*

Now the two input files were ready to be used to perform defocusing and background corrections by running a batch file called the RAWTRO1.BAT in the MTM-FHM software, as shown in appendix A.3. However, because the tilting angle ϕ was limited to 80º, the resulting corrected pole figures, typically denoted as PLF type files, were

incomplete. These corrected incomplete pole figures were used to calculate the orientation distribution functions of the materials under this study. A portion of the PLF file for AA6111-T4 is given in appendix A.4

7.3.2 Orientation distribution function (ODF) and recalculated pole figures

Analysis of the textures of the materials was limited to ODF because it reveals more details of the pole figures. Calculation of the ODF was done by taking the PLF-type file created by RAWTRO1, which contains four corrected pole figures, as input for the batch procedure denoted as S_ODF1.BAT, which is built into the MTM-FHM software (see appendix A.5). The series expansion method was used to fit the ODF $f(g)$. The spherical harmonic functions were used for fitting purposes. In the analysis, the Bunge notation using Euler angles was used.

During the ODF calculation, the following errors were encountered [151]:

- Truncation error: as a result, the texture's peaks were broadened
- Ghost error: intensities could be missing (negative ghosts) or incorrect (positive ghosts)

To minimise the impact of the truncation error, the maximal degree of the series expansion L_h for our materials was chosen to be 22 for steel and aluminium alloys [151,154], except if the resulting ODF was quite sharp (i.e. $f(g)_{\max} > 20$ [195]); then, the maximal degree was chosen to be 32. The AC600 alloy has a very sharp texture because the $f(g)_{\max}$ is greater than 20. Therefore, the harmonic coefficients were calculated for L_h=32. Next, the ghost correction procedure was done using the exponential method described in [196].

To run the S_ODF procedure, the following parameter files had to be prepared:

- PDPPOLE which controls the transformation of the PLF-type file into a PHAT-type file which is a suitable file for the purpose of the analysis
- ODF_A which controls the analysis of the incomplete pole figures
- ODF_Q which controls the ghost correction
- ODF_O which controls the ODF plot
- ODF_P which controls the recalculated pole figures plots

Examples of the setups of the files used for the ODF of the AA6111-T4 alloys are presented in appendices A.6 to A.10.

Then, the numerical values of the ODF were generated in the AODF file type. These values on a grid of Euler space using the Bunge convention were formulated. The distance between the grid points was 5º; therefore, nineteen values were used for each of the Euler angles, which resulted in 19*19*19 points for the ODF in total. An example of the AODF is shown in appendix A.11.

The ODFs of the four considered materials and the locations of the most common texture components are displayed in Figures 7.4 (a), 7.5 (a), 7.6 (a), and 7.7 (a). Complete pole figures are derived from the ODF. The recalculated pole figures for each material considered in this study are illustrated in Figures 7.4 (b), 7.5 (b), 7.6 (b), and 7.7 (b).

The AA6111-T4 grade, as illustrated in Figure **7.4**, has a weak α-fibre which consists of the Goss (0.63) and the Brass (1.94) components. A moderate β-fibre which runs from the Brass (1.94) through S (1.6) to Cu (1.69) also can be seen. However, the material consists of two main components: a strong dominant cube component with intensity of 5.68 and P component with a relatively medium intensity of 2.34. A minor R component with intensity of 1.0 is also present.

The AC600 alloys, as shown in Figure **7.5**, exhibit a relatively moderate α-fibre which consists of the Goss (5.3) and the Brass (0.55) components. A weak β-fibre which runs from the Brass (0.55) through S (1.65) to Cu (1.44) is prevailed. A minor P component with a low intensity of 1.48 is present.

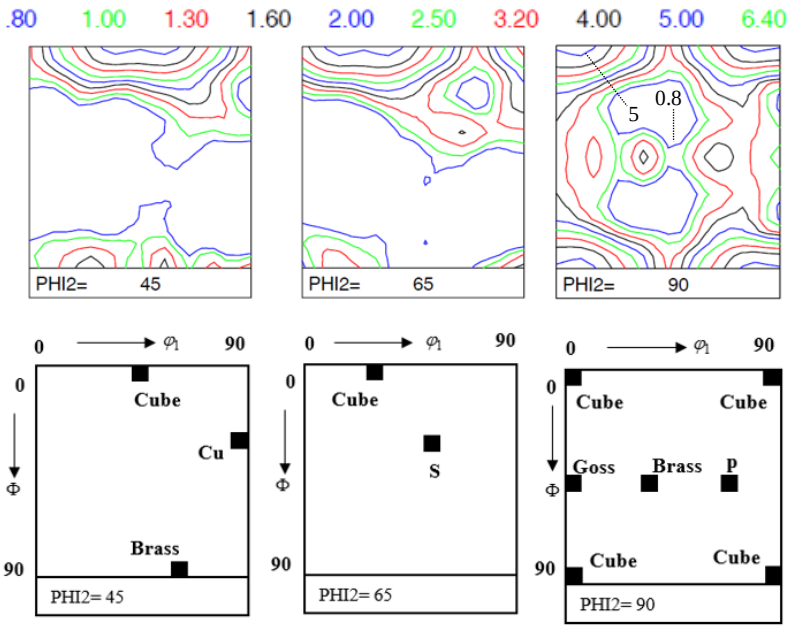

(a)

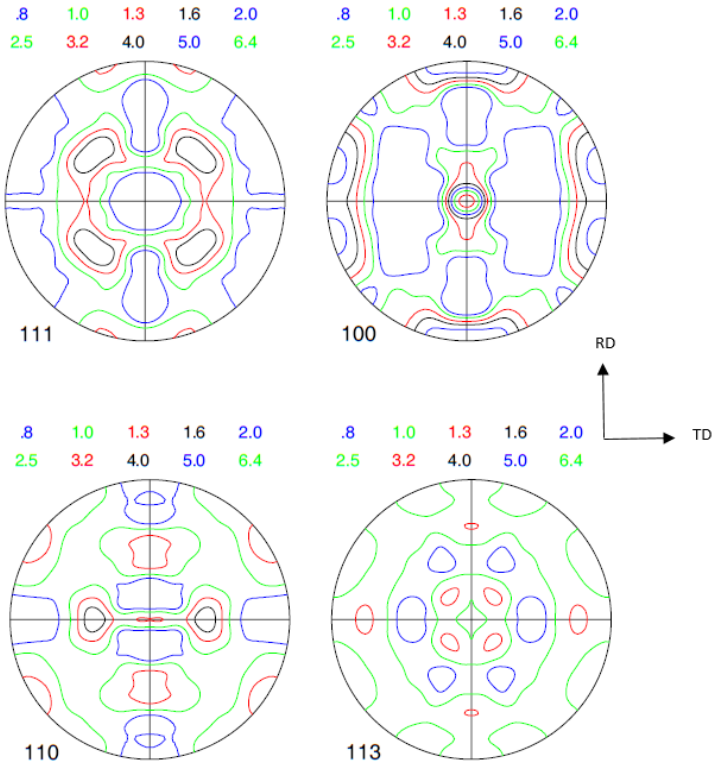

(b)

Figure 7.4. ODF and recalculated pole figures for AA6111-T4. (Maximum value of ODF:5.72).

However, an extremely strong, well-defined cube component, which is the typical recrystallization component, is present. It has an intensity of 52.88. A minor recrystallization R component with intensity of 2.0 is also noticed.

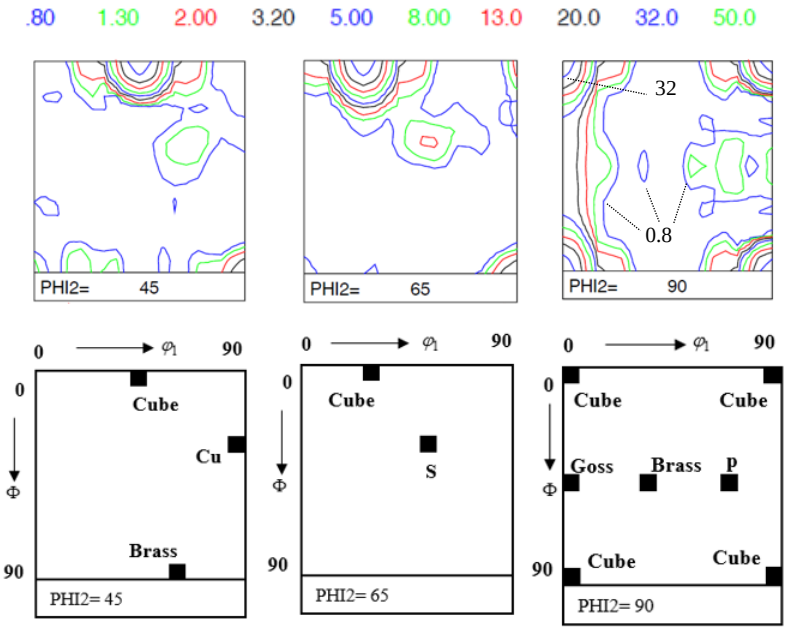

(a)

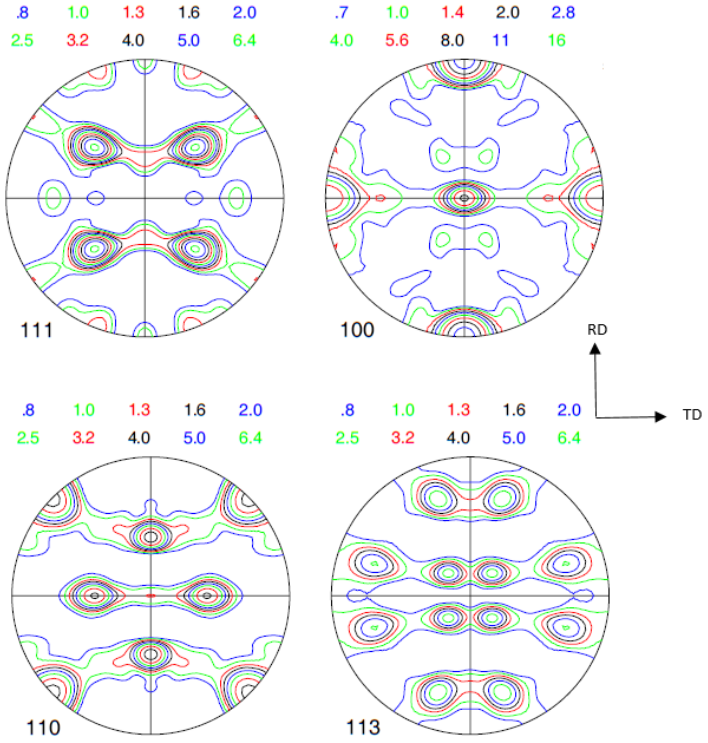

(b)

Figure 7.5. ODF and recalculated pole figures for AC600 (Maximum value of ODF:52.88).

The DX54 alloy, as depicted in Figure **7.6**, consists of a very weak α-fibre that runs from the H (0.77) to J (1.71) to I (3.4) to E (12.18) components. However, this alloy has a very strong γ-fibre which consists of the F (12.43), E' (12.18), and F' (12.43) components.

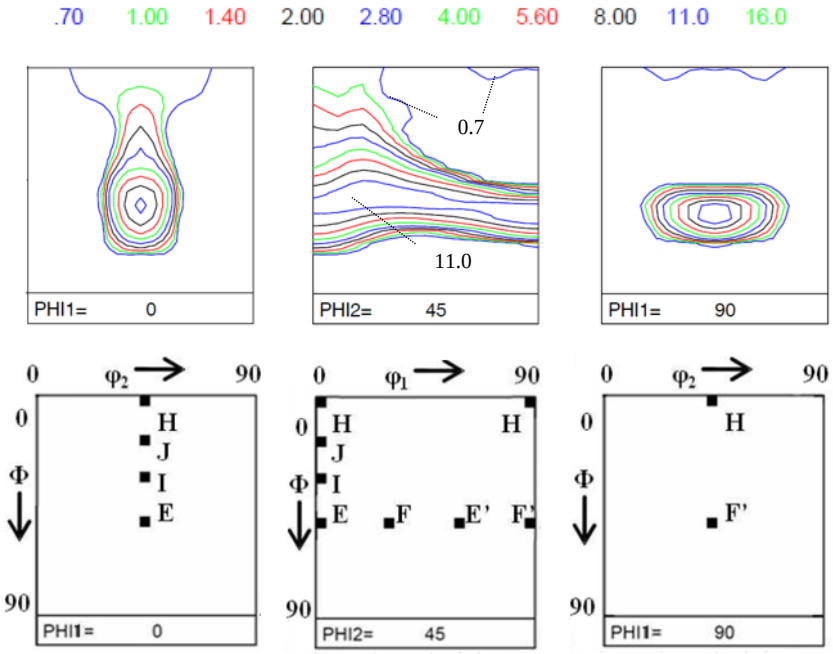

(a)

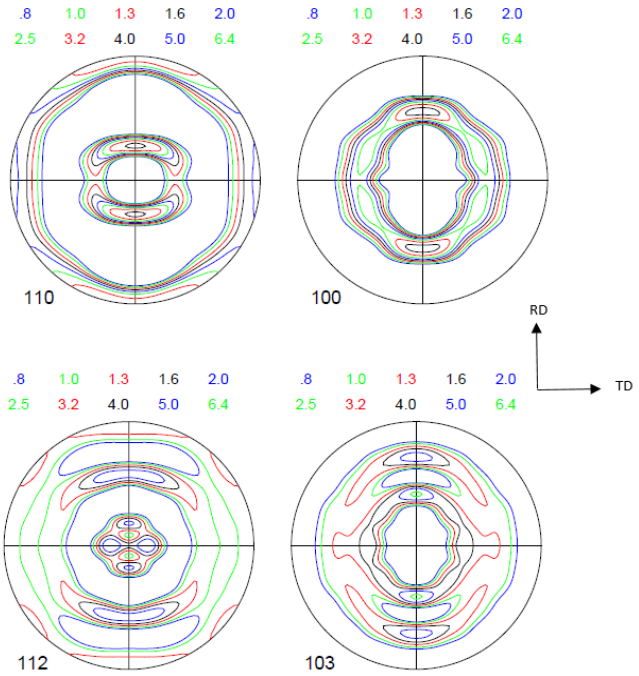

(b)

Figure 7.6. ODF and recalculated pole figures for DX54D+Z (Maximum value of ODF:15.06).

The H220BD alloy, as displayed in Figure **7.7**, consists of a very weak α-fibre that runs from the H (0.82) to J (1.93) to I (1.71) to E (7.06) components. This alloy also has a strong γ-fibre which consists of the F (10.0), E' (7.06), and F' (10.0) components.

The homogeneity and uniformity of the strong γ-fibre present in the forming steel (DX54) led to a higher plastic anisotropy (cf. [7]). Consequently, a material with such properties has a high drawability (cf. [155]). However, moderate planar anisotropy is expected to be exhibited by the considered steel materials. This is due to the inhomogeneous γ-fibre and the presence of the α-fibre.

In this study, the analysis of the texture will not be taken further. For instance, studying the relationship between texture and anisotropic properties, such as planar variation in yield stresses and *R*-values or exploring the effect of the texture on earing profile, is not part of the scope of this research.

The main source of anisotropy assumed in this study is texture. Texture, which is the primary input for the polycrystalline plasticity models (Taylor's models), was measured

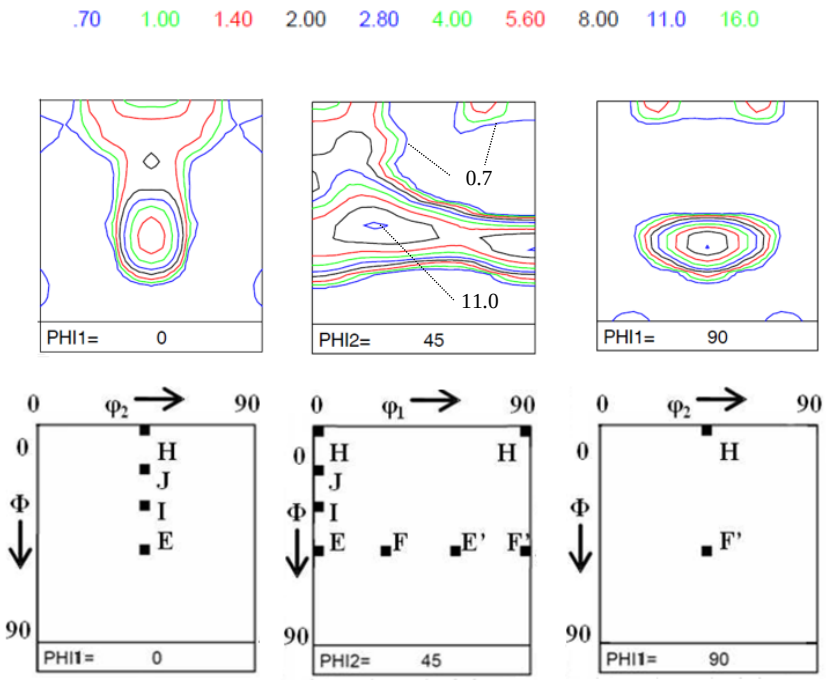

(a)

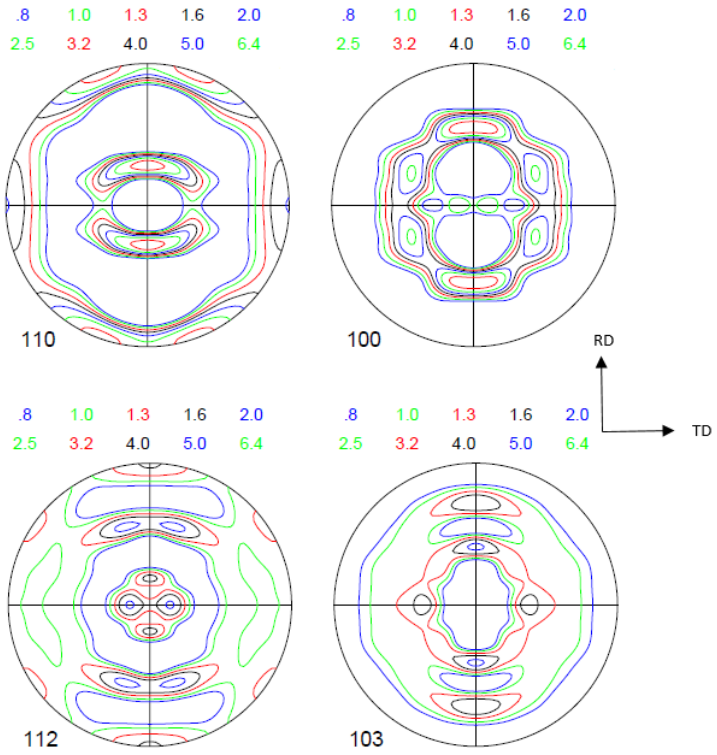

(b)

Figure 7.7. ODF and recalculated pole figures for H220BD+Z (Maximum value of ODF:11.88).

and presented. The following section provides the measured and calculated yield loci obtained with phenomenological and polycrystalline plasticity approaches, respectively.

7.4 Yield loci

In this study, the yield locus generated by the BBC2005 yield function is considered to be the most accurate; therefore, the validation processes of the CTFP and CTF models are done by benchmarking them against the BBC2005. The comparison is simplified by normalizing the yield loci using the yield stresses of the materials in the rolling directions.

7.4.1 Validation of the CTFP model

7.4.1.1 *BBC2005 vs. Taylor's models (steel and aluminium alloys)*

The CTFP model is described in detail in chapter 4 (section 4.10). To derive the CTFP model, the Taylor models, namely the full constraint (TF) and relaxed constraint "pancake" (TP), must be calculated first. The Taylor's models and BBC2005 for different materials were compared, as illustrated in Figure **7.8**. The S_1 and S_2 represents the normalized yield stresses (i.e. principal stresses over yield stress in the uniaxial tension in the rolling direction). The plastic anisotropy coefficients of the BBC2005 for both steel materials were determined with the Newton solver. The resulting anisotropy parameters are tabulated in Table **7.5**.

Table 7.5. Anisotropy coefficients for the steel alloys DX54D+Z and H220BD+Z for BBC2005.

Approach	Material constants							
	a_{B5}	b	L	M	N	P	Q	R_{B5}
DX54D+Z	0.43183	0.48905	0.46389	0.43353	0.50155	0.49870	0.54710	0.53948
H220BD+Z	0.36863	0.44704	0.49426	0.44379	0.50894	0.50631	0.54828	0.51238

For steel grades, advanced or complex yield criteria such as Yld2000, BBC2005, or Vegter lie between the Taylor's models (cf. the derived yield loci in [7]). Major differences are always present between the full constraint model and the pancake model in which the pancake model overestimates the stress factors in the stretching regime while the TF model underestimates the stress factors in the same regime (cf. the Taylor models derived for different steel grades in [7,132]). Figure **7.8** (a) and (b) confirmed that this is the case for the considered steel alloys.

However, this is not the case when the Taylor's models are compared with the BBC2005 for the considered aluminium alloys. As shown in Figure **7.8** (c) and (d), both of the resulting polycrystalline plasticity models overestimate the stress factors in the stretching quadrant. Moreover, minor deviation between the TF and TP models is noticed. Accordingly, if the CTFP model was derived, it still would be overestimating the stress factor in the stretching regime. Therefore, this study concludes that the CTFP model is inapplicable for the aluminium alloys considered in this study.

7.4.1.2 *BBC2005 vs. CTFP (steel alloys)*

For the considered steel alloys, the CTFP model is derived and compared to the BBC2005 as illustrated in Figure 7.9 (a) and (b). This study confirms the suitability of the CTFP to derive the biaxial yield stress as well as uniaxial yield stress in the transverse direction of the sheets. However, for the H220BD alloy, it is important to note that the CTFP model underestimates slightly the biaxial yield stress when compared with the experimental biaxial yield stresses "experimental points in red" calculated from the bulge tests. The CTFP model was validated in the study done by An et al. [7] by benchmarking it against different advanced models such as Vegter, BBC2005, and Yld2000 which were fitted with biaxial yield stress calculated from compression tests.

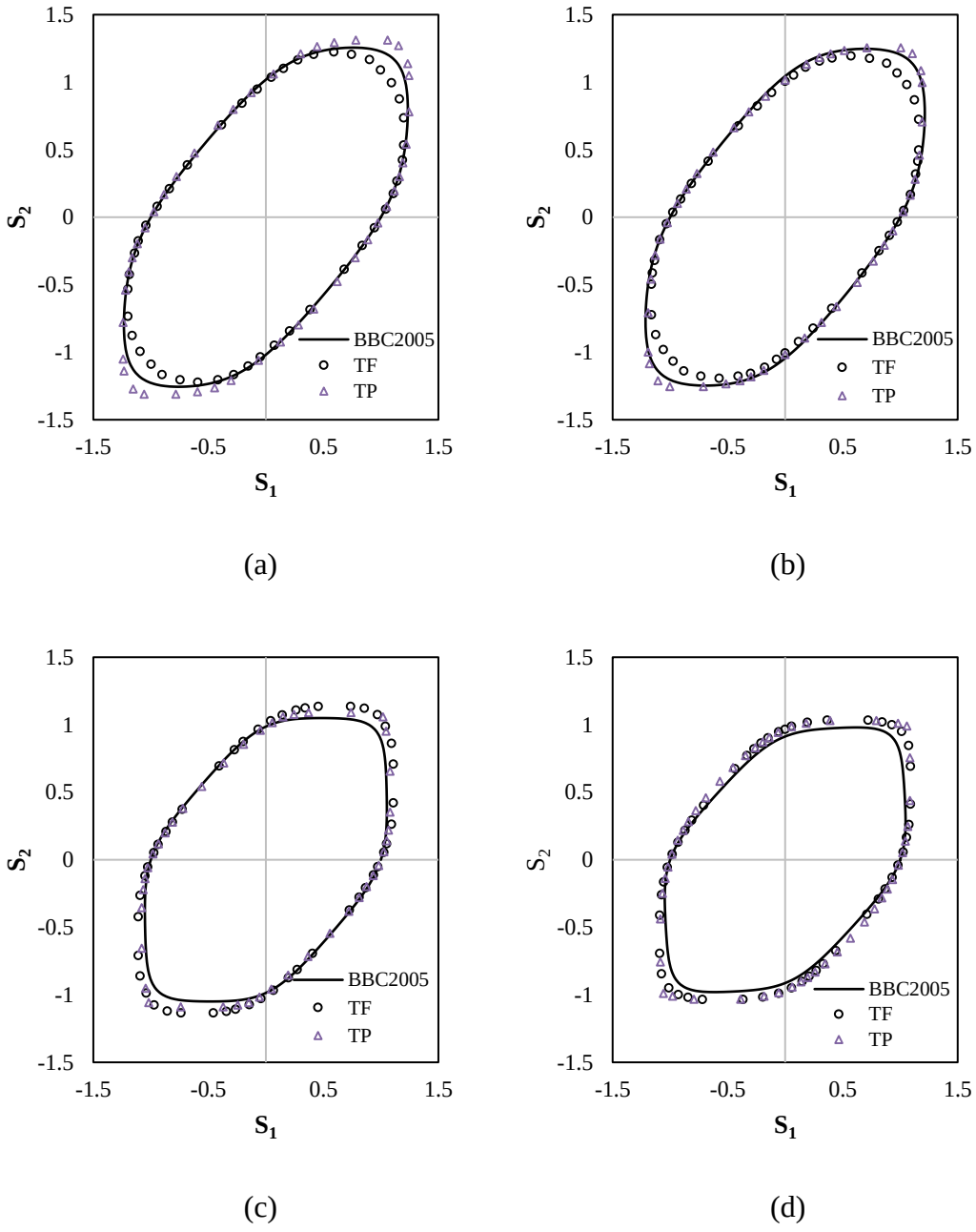

Figure 7.8. BBC2005 vs. Taylor's models: **a** DX54D+Z, **b** H220BD+Z, **c** AC600, **d** AA6111-T4.

The author of this research believes this might be the reason for the slight inaccuracy of the CTFP model in predicting the biaxial point.

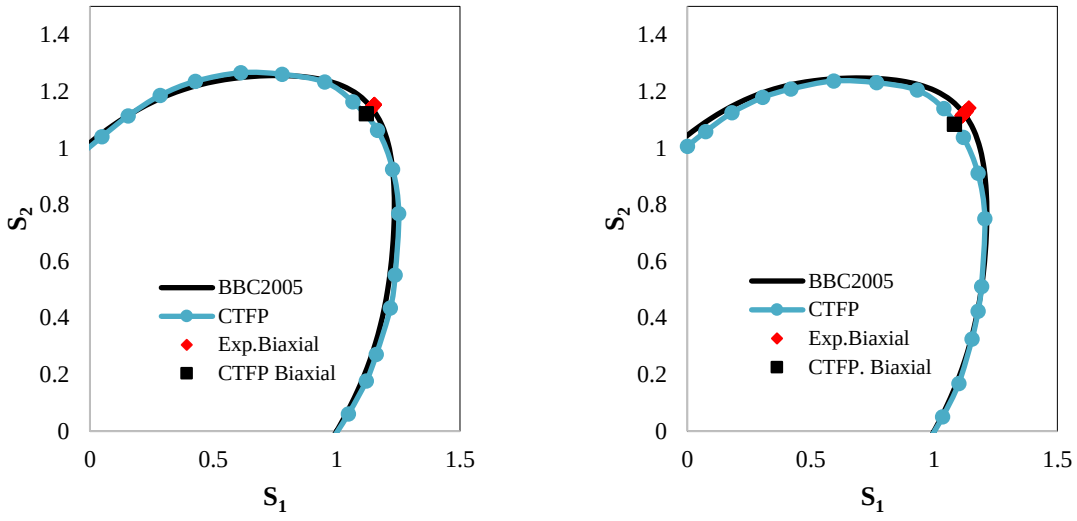

(a) (b)

Figure 7.9. BBC2005 vs. CTFP: a DX54D+Z, b H220BD+Z.

7.4.1.3 *Polycrystalline plasticity vs. phenomenological models (steel alloys)*

For the considered steel grades, isotropic (von Mises) and anisotropic (Hill'48, BBC2005) phenomenological yield functions will be compared with polycrystalline plasticity models (TF and TP) and the combined model (CTFP). The comparison of these models for the DX54 and H220BD steel alloys is provided in Figure 7.10 (a) and (b), respectively.

For both steel alloys, it can be seen in the stretching regime that von Mises and Hill'48 deviate remarkably from the experimentally measured yield function: the BBC2005. The isotropic von Mises isotropic yield function underestimates the biaxial stress states, while the Hill'48 greatly overpredicts the biaxial state. Therefore, an accurate biaxial point cannot be predicted by these two yield functions. The TF model predicts the biaxial state better than the von Mises, while the TP model estimates the biaxial stress state better than the Hill'48.

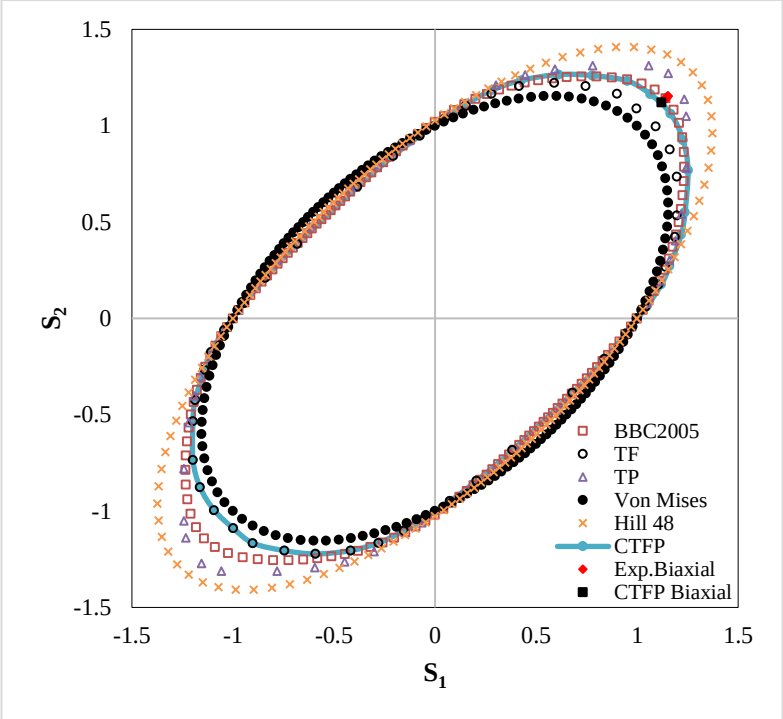

(a)

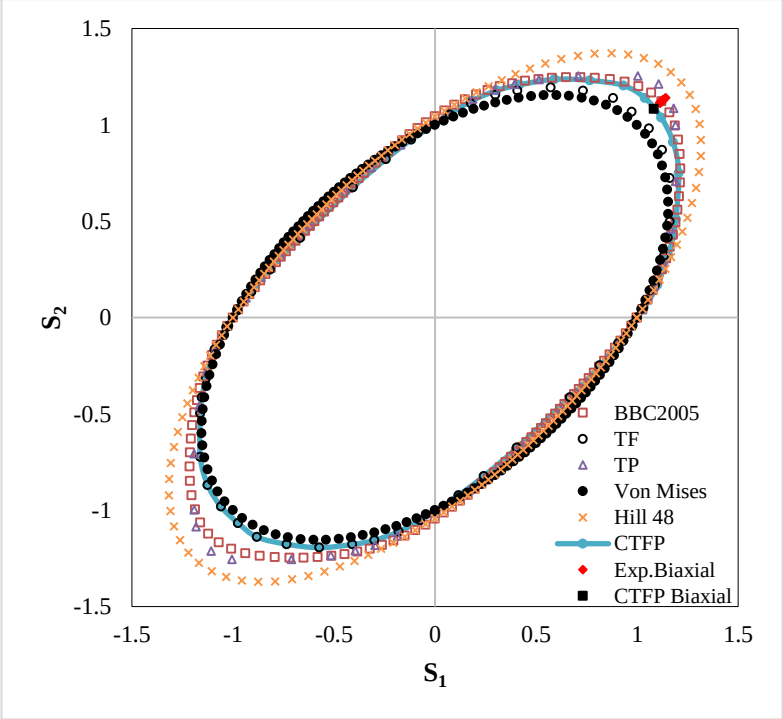

(b)

Figure 7.10. Polycrystalline plasticity models vs. phenomenological models for steel grades: **a** DX54D+Z, **b** H220BD+Z.

To conclude, the CTFP model predicts the biaxial points as well as other strain state points such as uniaxial yield stress in the transverse direction very well for the considered steel alloys. In general, it performs better than the other utilised yield loci in this study.

7.4.2 Validation of the CTF model

This section is devoted to the CFT model which was described in detail in chapter 4 (section 4.11). The CTF model is a texture-based model which is based on the full-constraint Taylor's model referred to as TF. Therefore, as a starting point, the TF models for the two considered aluminium alloys were derived using the MTM-FHM software. The main inputs for the TF model were the texture in terms of the c-coefficients and the slip system (i.e. making the assumption that slipping occurs on {111} crystallographic planes in <110> directions for the considered aluminium grades). The full constraint models for the two aluminium alloys were derived and compared with the BBC2005, as shown in Figure **7.8** (c) and (d). It is clear that the full-constraint (TF) model for both materials does overestimates the biaxial strain state. However, the TF model predicts well the other strain states.

7.4.2.1 *Deriving the CTF*

Based on the TF model, the following quantities must be identified to derive or define the proposed CTF model:

- Balanced stress factor f_b^{TF} on the TF model for the AC600 and AA6111-T4 are derived from the data of the TF models.
- **Hypotenuse "radial coordinate"** of the biaxial point of the TF model (H_b^{TF}) is defined using equation 4.19 ($H_b^{TF} = \sqrt{(f_b^{TF})^2 + (f_b^{TF})^2}$).
- **Hypotenuse** of the biaxial point of the CTF model (H_b^{CTF}) is calculated using equation 4.20 (i.e. $H_b^{CTF} = 0.95 * H_b^{TF}$).
- Now the biaxial stress factor of the CTF model is calculated using equation 4.21 (i.e. $f_{b1}^{CTF} = f_{b2}^{CTF} = f_b^{CTF} = \cos(\alpha) * H_b^{CTF} = \sin(\alpha) * H_b^{CTF}$). The $\alpha = 45$ is the angle where the biaxial stress factor is measured. In other words, it is the angle between the radial coordinate at the balanced biaxial point and the rolling direction (x-axis).

Table **7.6** summarises the mentioned quantities and their values that are required to derive the CTF model.

Table 7.6. Quantities required to derive the CTF model.

Material	f_b^{TF}	H_b^{TF}	H_b^{CTF}	f_b^{CTF}
AC600	1.016918	1.43814	1.366233	0.966073
AA6111-T4	0.972968	1.37598	1.307185	0.924319

Now for the points between the uniaxial stress mode in the rolling direction and the balanced biaxial point, their **hypotenuses** are calculated using equation 4.22 (i.e. $H_1^{CTF} = H^{TF} - [(H_b^{TF} - H_b^{CTF}) * (f_2^{TF} / f_1^{TF})]$). However, for the points between the balanced biaxial point and the uniaxial stress mode in the transverse direction, their **hypotenuses** can be obtained using equation 4.23 (i.e. $H_2^{CTF} = H^{TF} - [(H_b^{TF} - H_b^{CTF}) * (f_1^{TF} / f_2^{TF})]$).

Finally, the major and minor stress factors f_1^{CTF} and f_2^{CTF} in the stretching regime of the CTF are calculated using equations 4.24 and 4.25, respectively (i.e. $f_1^{CTF} = \cos(\alpha) * H^{CTF}$, $f_2^{CTF} = \sin(\alpha) * H^{CTF}$). Figure 7.11 (a) and (b) illustrate the CTF models in comparison with TF and BBC2005 for the two considered aluminium alloys.

Two aspects have to be considered when calculating the CTF model:

- The scaling procedure involved in the CTF model is applied in the first and third quadrants (i.e. the CTF is a symmetric model, with no strength differential effect).
- The CTF model keeps the shape of the yield loci calculated from the TF model in the shear regime (i.e. in the shear regime the stress ratio for each point on the CTF model is the same as that on the TF model).

The CTF data for the two considered aluminium alloys are plotted in Figure 7.11 (a) and (b). For both of the aluminium alloys, the biaxial stress state of the CTF model is less elongated than that of the TF model.

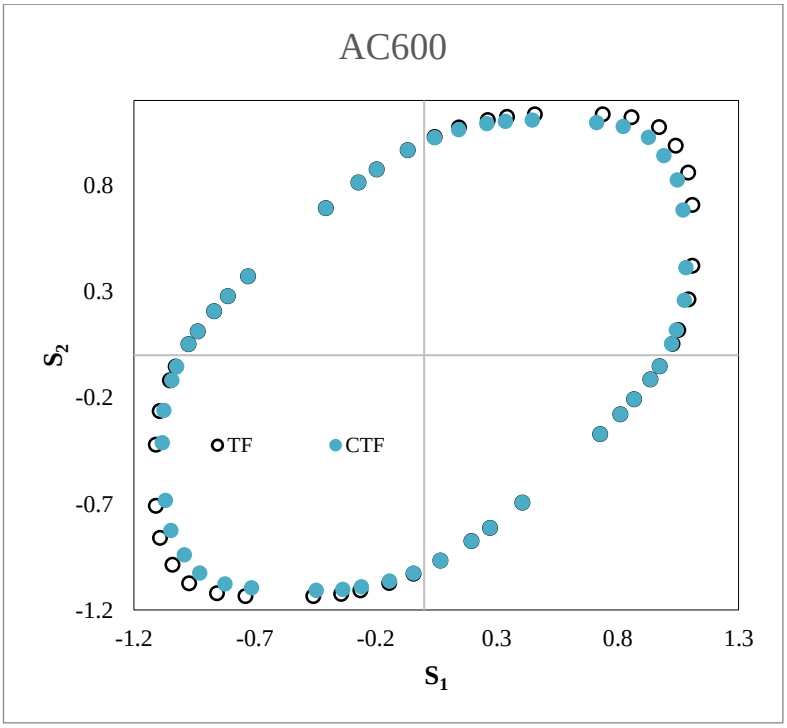

(a)

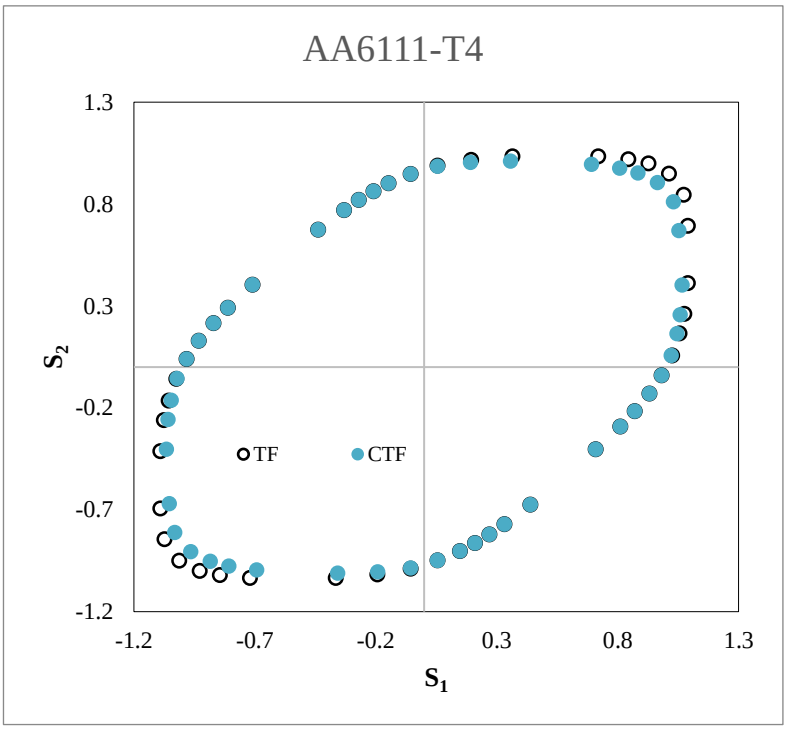

(b)

Figure 7.11. TF vs. CTF models for aluminium grades: **a** AC600, **b** AA6111-T4.

7.4.2.2 *BBC2005 vs. CTF*

The resulting yield loci derived using the CTF model were validated first by comparing its prediction with the performance of the BBC2005 macroscopic yield function. The comparison between the two models is depicted in Figure 7.11 (a) and (b) for AC600 and AA6111-T4, respectively.

The BBC2005 yield function, which was experientially fitted with data obtained from mechanical tests, was used to measure the yield loci of the considered aluminium alloys.

The eight mechanical inputs that are required to define fully the BBC2005 were experimentally determined and include:

- Three uniaxial yield stresses (YS_0, YS_{45}, YS_{90}) performed on sheets oriented 0°,45°,90° to the rolling direction. From the three uniaxial tension tests, the *R*-values (R_0, R_{45}, R_{90}) were also obtained.
- Biaxial yield stress Y_b was calculated from the bulge test data.
- Equibiaxial strain ratio R_b obtained from the compression test.

For the sake of clarity, the procedure that was followed to define the BBC2005 with the eight previously mentioned inputs will be denoted as **Method I**. This method is compared with a suggested procedure denoted as **Method II** that will be discussed in more detail in 7.4.2.3.

It can be observed, as shown in Figure 7.12 for the considered aluminium alloys, that the proposed CTF model is able to predict well both the equibiaxial yield stress YS_b and uniaxial yield stress in the transverse direction YS_{90}. In terms of accuracy, the CTF model predicts an equibiaxial yield stress (CTF Biaxial) corresponding exactly with the measured experimentally balanced points (Exp. Biaxial) (experimental Biaxial) for both of the considered aluminium alloys. The CTF model overestimates the biaxial points for both materials by 1% at the most. Moreover, the CTF model gives an accurate prediction and overestimates the uniaxial yield stress in the transverse direction YS_{90} for the AC600 alloy by less than 2%. However, the prediction for the yield stress in the transverse direction YS_{90} for the AA6111-T4 material is less accurate. The model overpredicted the YS_{90} by approximately 6%, which is about 7 MPa.

The error (e) for a strain mode is defined as {[e = (Prediction by the CTF -Experimental data) / Experimental data] *100}. All the estimated errors are shown in Figure 7.12.

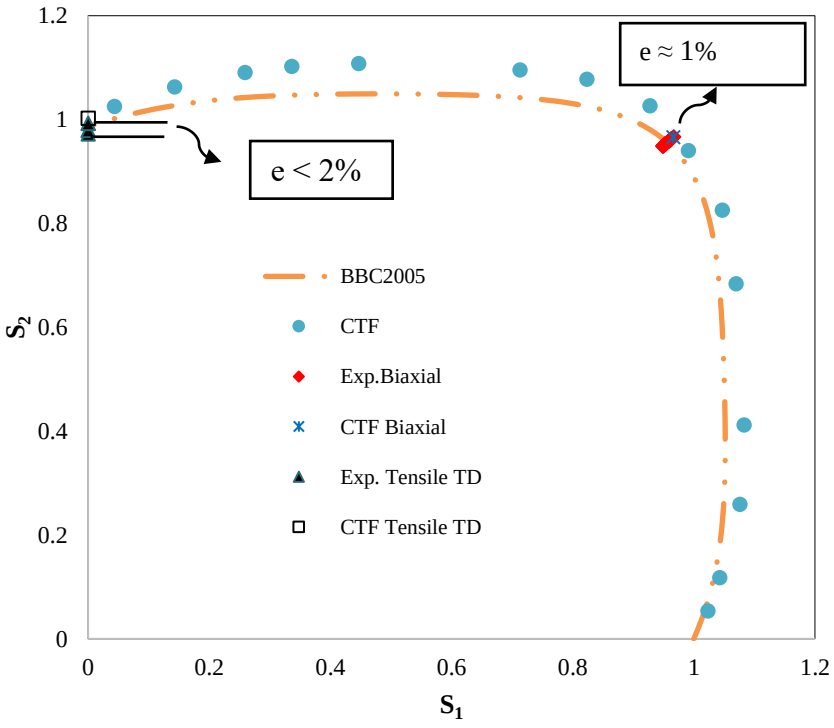

(a)

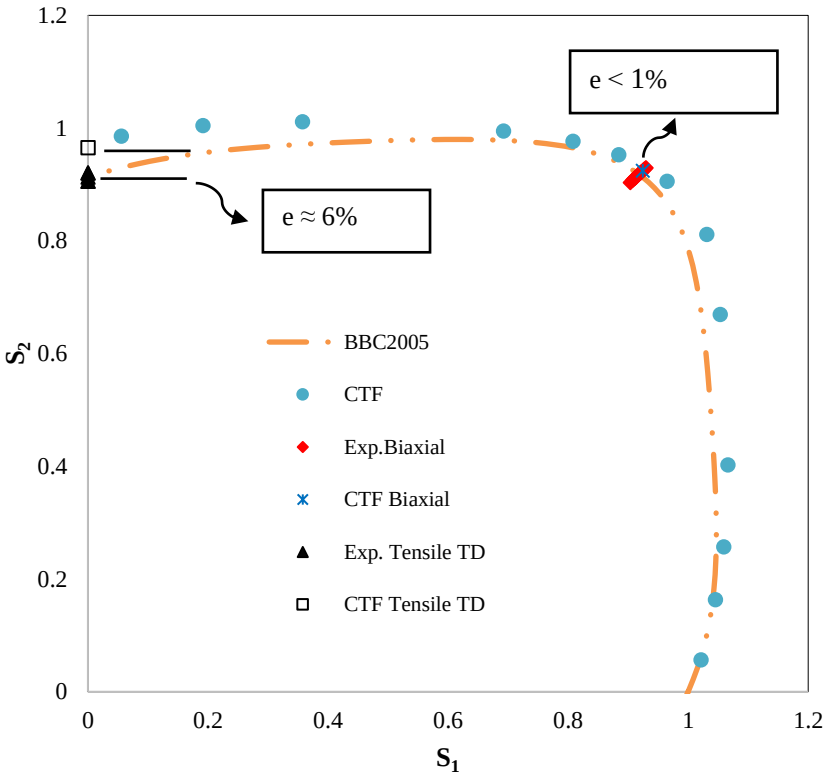

(b)

Figure 7.12. BBC2005 vs. CTF models for aluminium grades: **a** AC600, **b** AA6111-T4.

Table **7.7** summarises the values of the yield stresses for different stress states, either predicted by the CTF model or experimentally determined, and the errors that could be produced by the estimation of the CTF model.

Table 7.7. Error in the predicted yield stresses by the CTF model.

Material		**Experimental** YS_{90}	**Prediction** YS_{90}	**Experimental** YS_b	**Prediction** YS_b
AC600	Value [MPa]	142	144.34	137.68	139.11
	Error (e) %	< 2%		≈ 1%	
AA6111-T4	Value [MPa]	126	133.69	126.68	127.56
	Error (e) %	6%		< 1%	

7.4.2.3 *Deployment of the CTF*

As discussed previously in chapters 3 and 4, the most common approach to describe the yielding behaviour of anisotropic materials is the phenomenological approach. This approach uses mathematical expressions that are fitted with experimental data obtained

from mechanical tests. Many advanced mathematical descriptions, known as yield functions, have been proposed over the past decade, including the ones proposed by [19,48,49] . However, the major downside of this type of approach is the fact that these advanced yield functions are costly to be determined since they require a significant number of mechanical tests which consume time and effort. For instance, the BBC2005 yield function in the current study requires five mechanical tests to be conducted which are repeated at least four times. A summary of the number of experimental work conducted to define fully the BBC2005 for the material considered is shown in .

Table 7.8. The average mechanical properties of the considered materials are summarised in Table **7.9**.

Table 7.8. A summary of the total experimental work conducted to define the BBC2005.

Material	YS_0 **[MPa]** + R_0 **[-]**	YS_{45} **[MPa]** + R_{45} **[-]**	YS_{90} **[MPa]** + R_{90} **[-]**	YS_b **[MPa]**	R_b **[-]**	**Total work**
AA6111-T4	5 Tensile	5 Tensile	5 Tensile	5 Bulge	5 Compression	25
AC600	5 Tensile	5 Tensile	5 Tensile	5 Bulge	5 Compression	25
DX54D+Z	4 Tensile	4 Tensile	5 Tensile	5 Bulge	5 Compression	23
H220BD+Z	5 Tensile	5 Tensile	5 Tensile	4 Bulge	5 Compression	24

Table 7.9. The average mechanical properties of the metallic sheets.

Material	t_0 **[mm]**	YS_0 **[MPa]**	YS_{45} **[MPa]**	YS_{90} **[MPa]**	Y_b **[-]**	R_0 **[-]**	R_{45} **[-]**	R_{90} **[-]**	R_b **[-]**
AA6111-T4	0.92	138	128	126	126.68	0.699	0.539	0.509	1.299
AC600	0.90	144	141	142	137.68	0.615	0.399	0.658	0.962
DX54D+Z	0.74	162	168	165	184.97	2.007	1.699	2.370	0.902
H220BD+Z	0.69	248	260	259	278.15	1.666	1.544	2.107	0.871

These average mechanical properties are provided for either the set of equations associated with Hill'48 or the system of nonlinear equations associated with BBC2005 to determine the plastic anisotropy coefficients. After the plastic anisotropy parameters are identified, the yield locus of the specific material can be calculated.

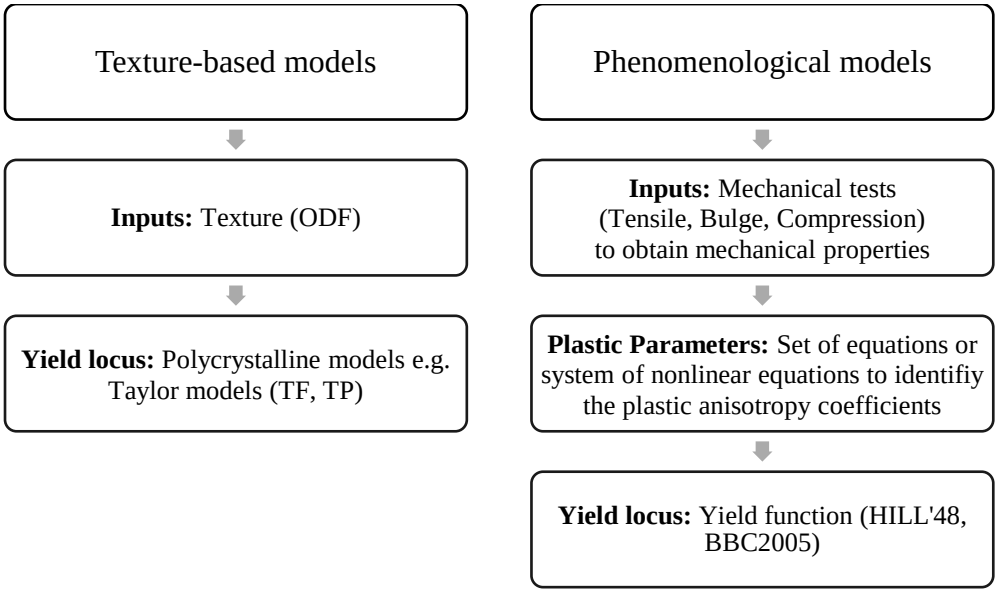

Figure 7.13. Polycrystalline plasticity vs. phenomenological approaches.

Conversely, texture-based models are quicker but less accurate compared to advanced and complex phenomenological models. Texture is the main input for polycrystalline plasticity models such as the Taylor models. A brief outline of the two mentioned approaches is depicted in Figure **7.13**.

It was demonstrated in the previous section that the proposed texture-based model, referred to as the CTF model, can predict the yield stresses for the two different stress states, namely the YS_b and YS_{90}, accurately, but its accuracy could not be guaranteed in other strain states. Therefore, the CTF model will be deployed to fit the advanced yield criterion denoted as BBC2005.

A method, denoted as **Method II**, is suggested. The method combines strengths of the polycrystalline plasticity approach and phenomenological approach that are outlined in Figure **7.13**. **Method II** combines the data obtained from the CTF model, experimental work, and Backofen [197] description for the balanced biaxial strain ratio.

In this suggested method, the same experimental data presented in **Method I** are used except for the following quantities:

- Uniaxial yield stress perpendicular to the rolling direction (YS_{90}) will be predicted from the newly proposed model known as CTF.
- Biaxial yield stress Y_b will be extracted from the CTF model.
- The *R*-value in the transverse direction R_{90} will be estimated using the Backofen equation [197], which is ($R_b=R_0/R_{90}$) (i.e. the R_{90} will be a function of the R_0 obtained

experimentally from uniaxial tensile tests performed in the rolling direction and R_b obtained experimentally from the compression test).

To summarise (see Table 7.10), the eight mechanical inputs required to define fully the BBC2005 are determined either experimentally (**Method I**) or using the combined procedure (**Method II)**.

Table 7.10. Method I vs. Method II.

	YS_0 **[MPa]**	YS_{45} **[MPa]**	YS_{90} **[MPa]**	YS_b **[MP]**	R_0 **[-]**	R_{45} **[-]**	R_{90} **[-]**	R_b **[-]**
Method I	Tensile	Tensile	Tensile	Bulge	Tensile	Tensile	Tensile	Compression
Method II	Tensile	Tensile	CTF	CTF	Tensile	Tensile	Backofen	Compression

Table **7.11** and Table **7.12** present the eight mechanical properties/inputs using either Method I or Method II, which are required to fully define the BBC2005 yield function. The resulting yield loci for both aluminium alloys are plotted in Figure 7.14. The plastic anisotropy coefficients from both methods for AC600 and AA6111-T4 were determined with a Newton solver and are tabulated in Table **7.13** and Table **7.14**. From Figure **7.14** it can be observed that the new suggested method (Method II: BBC2005 fitted with CTF), for both of the considered aluminium alloys, outperforms the other yielding descriptions.

Table 7.11. Mechanical properties obtained using **a** Method I (Experiments), **b** Method II (Experiments + CTF+ Backofen) for AC600.

Material	YS_0 **[MPa]**	YS_{45} **[MPa]**	YS_{90} **[MPa]**	YS_b **[MP]**	R_0 **[-]**	R_{45} **[-]**	R_{90} **[-]**	R_b **[-]**	$\overline{R}$ **[-]**
Experiments	144	141	142	137.68	0.615	0.399	0.658	0.962	0.518
Experiments + CTF +Backofen	144	141	144.34	139.11	0.615	0.399	0.639	0.962	0.513

Table 7.12. Mechanical properties obtained using **a** Method I (Experiments), **b** Method II (Experiments + CTF+ Backofen) for AA6111-T4.

Material	YS_0 **[MPa]**	YS_{45} **[MPa]**	YS_{90} **[MPa]**	YS_b **[MPa]**	R_0 **[-]**	R_{45} **[-]**	R_{90} **[-]**	R_b **[-]**	$\overline{R}$ **[-]**
Experiments	138	128	126	126.68	0.699	0.539	0.509	1.299	0.572
Experiments + CTF +Backofen	138	128	133.21	127.56	0.699	0.539	0.538	1.299	0.579

As shown, the R_{90} value using the Backofen equation deviates approximately by -3% and 6% for AC600 and AA6111-T4. However, the effect of this difference on the shape of the yield loci and the calculated normal plastic anisotropy $\overline{R}$ of the two materials is negligible.

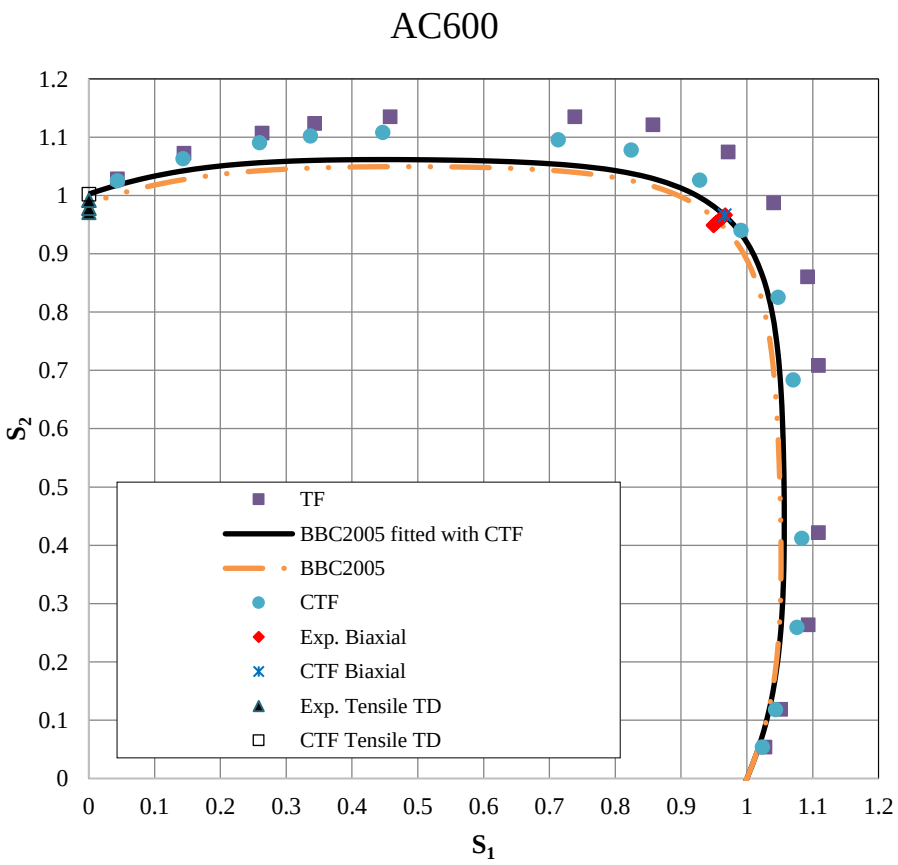

(a)

AA6111-T4

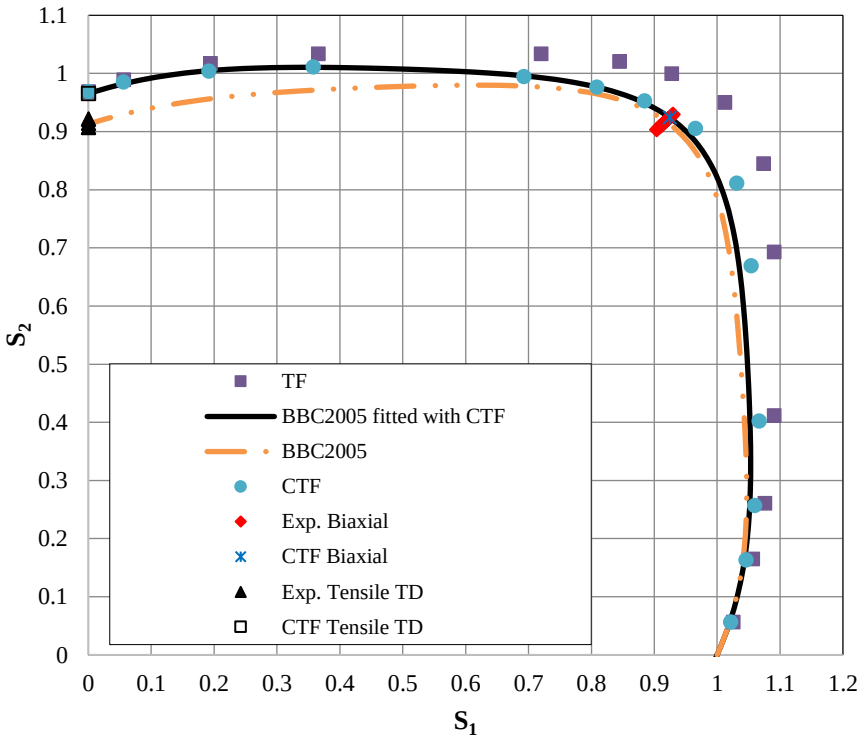

(b)

Figure 7.14. Yield loci of the TF, BBC2005 (Method **I)**, and BBC2005 fitted with CTF (Method II) for **a** AC600 and **b** AA6111-T4.

The description of the BBC20005 when fitted with the CTF model improves the yield function performance: specifically, at the plane strain states in the rolling and transverse directions. Consequently, the uncertainties of yielding behaviour in the plane strain states are minimised when the new suggested model (Method II) is used. The new procedure gives almost identical yield locus as the method identified fully with experimental work.

Table 7.13. Anisotropy coefficients for the aluminium alloy AC600 for BBC2005 and BBC2005 fitted with CTF.

Approach	**Material constants**							
	a_{B5}	**b**	**L**	**M**	**N**	**P**	**Q**	**R_{B5}**
BBC2005	1.04373	0.31688	0.46989	0.48401	0.46554	0.46074	0.56014	0.58580
Method II	1.15458	0.30681	0.46683	0.46547	0.45689	0.45445	0.57287	0.57570

Table 7.14. Anisotropy coefficients for the aluminium alloy AA6111-T4 for BBC2005 and BBC2005 fitted with CTF.

Approach	Material constants							
	a_{B5}	b	L	M	N	P	Q	R_{B5}
BBC2005	1.48078	0.60691	0.42602	0.52503	0.46284	0.46645	0.49302	0.54926
Method II	1.60015	0.59790	0.45363	0.48100	0.42530	0.43993	0.53432	0.53763

7.4.2.4 *Polycrystalline plasticity vs. phenomenological models (aluminium alloys)*

For the considered aluminium alloys, isotropic (von Mises) and anisotropic (Hill'48, BBC2005) phenomenological yield functions were compared with polycrystalline plasticity models (TF and TP), the proposed model (CTF), and the suggested method (Method II). The comparison of these models for the AC600 and AA6111-T4 aluminium grades is illustrated in Figure **7.15** (a) and (b), respectively.

For both aluminium sheets, it can be seen in the stretching regime that von Mises deviates remarkably from the experimentally fitted yield function: the BBC2005 (i.e. using **Method I)**. From Figure **7.15**, it is observed for the two materials that the Hill'48 yield function is unable to predict the biaxial stress states, which indicate the dominant deformation mode in sheet metal forming. The isotropic von Mises isotropic yield function overestimates the biaxial stress states, while the Hill'48 greatly underpredicts the biaxial state. Therefore, an accurate biaxial point cannot be extracted by these two yield criteria.

The full-constraint Taylor model gives a similar accuracy as von Mises in predicting the biaxial state, while the pancake model is considered the worst model in estimating the balanced biaxial stress points when compared to the measured points.

The proposed CTF model predicts the biaxial points as well as other strain state points such as uniaxial yield stress in the transverse direction very well for the considered aluminium alloys. In general, the CTF model outperforms the performances of the other utilised yield loci in this study.

Therefore, the CTF model was used as a deployment tool to extract virtual data points, namely the YS_b and YS_{90}, which were used as inputs in the new suggested procedure denoted as **Method** II, which was described in 7.4.2.3. Method II **(**see Figure **7.15**, BBC2005 fitted with CTF), gives the best yielding description among the current utilised models in this study when compared to the BBC2005 fitted fully with mechanical testing procedure denoted as **Method I** (see Figure **7.15**, BBC2005).

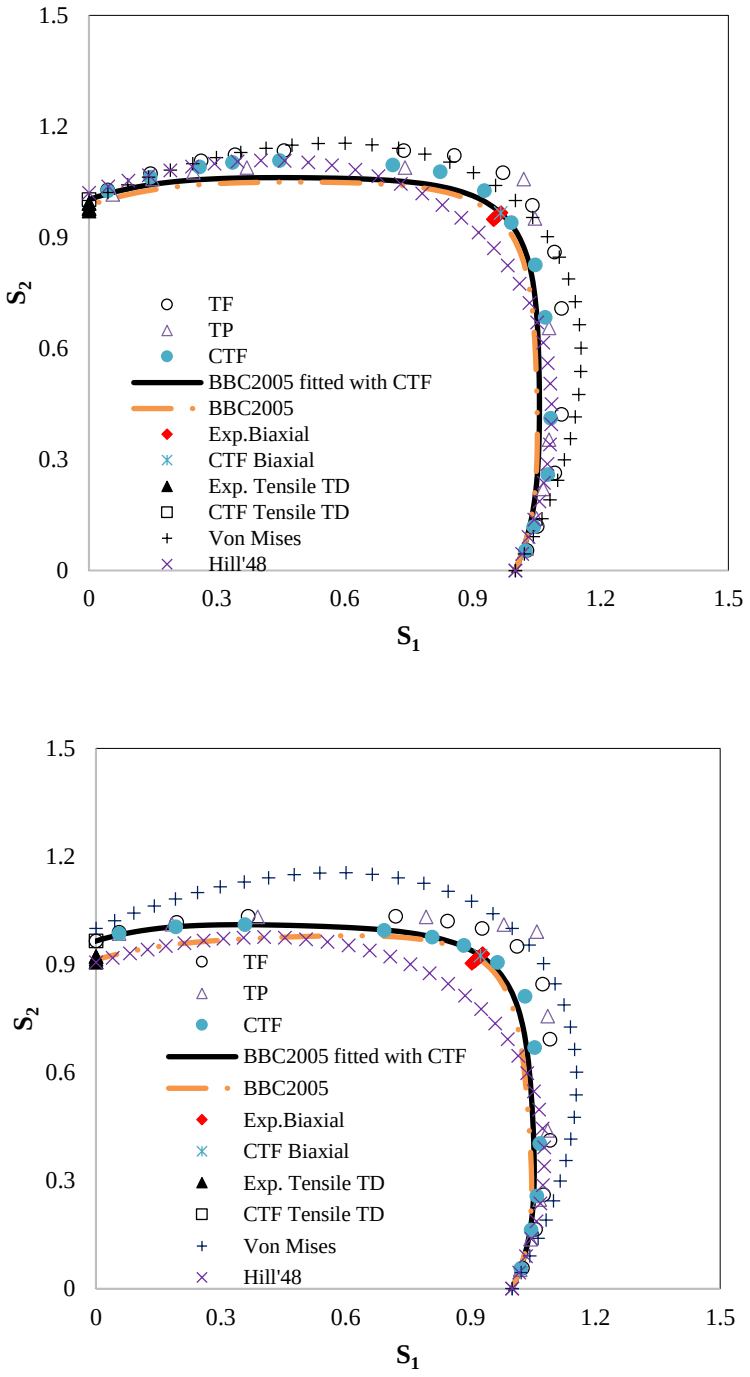

Figure 7.15. Stretching regime descriptions – Polycrystalline plasticity models vs. phenomenological models for aluminium grades: **a** AC600, **b** AA6111-T4.

Figure **7.16** (a) and (b) show different models that describe the yielding behaviour in the shear regime for AC600 and AA6111-T4, respectively. In general, it can be concluded that the new procedure **(Method II)** gives the best description for both materials.

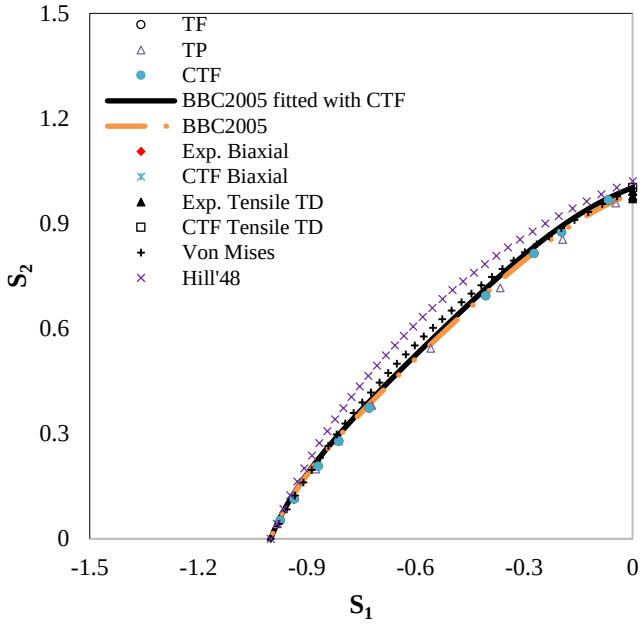

(a)

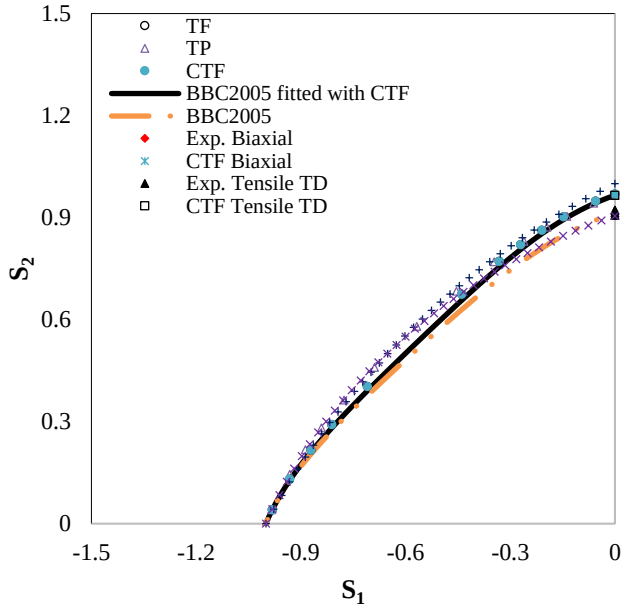

(b)

Figure 7.16. Shear regime descriptions - Polycrystalline plasticity models vs. phenomenological models for aluminium grades: **a** AC600, **b** AA6111-T4.

7.5 Conclusion

In this chapter, the experimental work involved to calculate the ODF, which is the main source of anisotropy and primary input for the utilised texture-based yield loci, was presented. Two texture-based models, which are the Taylor models, were then calculated.

Based on the Taylor models, the CTFP model was derived and proved to be inapplicable for the considered aluminium alloys. A new simple model, denoted as CTF, was validated for the considered aluminium grades. It was shown that the CTF model, for both aluminium materials, can predict accurately the balanced biaxial stress point as well as the uniaxial yield stress in the transverse direction. Moreover, a new method referred to as **Method II** was suggested. This new procedure deploys the CTF model with the help of a certain number of mechanical tests and the Backofen equation to fit the advanced yield function—the BBC2005. The capability of the new suggested procedure **(Method II)** was demonstrated with the two considered aluminium alloys.

In the sheet metal forming industry, for the considered 6xxx materials, the CTF model deployment will facilitate the use of the more-accurate advanced phenomenological yield functions. This will be accomplished by eliminating the main drawbacks, which are the greater time consumption and expensive material characterization process, of using the advanced models.

Chapter 8

Identification Strategies (Results and Discussion)

8.1 Introduction

The aim of this chapter is to present and analyse the reviewed solution methods: the TRD algorithm, Levenberg algorithm, and Levenberg-Marquardt algorithm. A discussion was devoted to these numerical methods in chapter 3. Specifically, sections 3.6.2 and 3.6.3 detail the methods.

These algorithms are sufficiently accurate and robust to identify the plastic anisotropy parameters of the BBC2003 and Yld2000-2d yield functions for different aluminium and steel alloys with various levels of anisotropy without applying constraints on the models' parameters or modifying the initial guesses. With the line-search-based algorithms (i.e. Levenberg (L) and Levenberg-Marquardt (LM) algorithms) the parameter λ_s was set to different values to examine its effect on the behaviours of the algorithms for different materials and yield functions. In these two versions, the initial damping parameter first was set to 0.1, and then to 100.

The sensitivity of the yield functions to the initial guesses for different solution methods and materials is firstly examined. Next, the robustness and effectiveness of the solution methods for the considered models and materials are investigated. Finally, the performances of the yield functions with the suggested identification procedures for different materials are compared. Therefore, the correlation between materials, solution methods, and yield functions used in this study will be associated. Figure **8.1** is a schematic of the categorical variables that must be correlated.

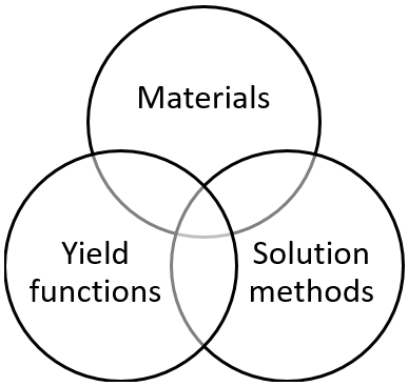

Figure 8.1. Schematic of the categorical variables.

The remainder of the chapter is structured as follows. Section 8.2 first examines th sensitivity of the systems of nonlinear equations associated with Yld2000-2d and BBC2003 to the initial guesses and materials used. Then, the results of the algorithms in terms of their convergence and cumulative number of iterations are discussed in section 8.3. In section 8.4, a comparison of the performance of the two yield functions with the applied identification procedures for different materials is made. Finally, the computed plastic anisotropy coefficients of the Yld2000-2d and BBC2003 yield functions as well as the resulting yield loci are presented in section 8.5. Conclusions are given in section 8.6.

8.2 Sensitivity of the nonlinear equation systems

The sensitivity of the yield criteria to the initial guesses for the different materials and applied algorithms was examined first. A set of 100 random initial guesses was tested for both yield functions, namely BBC2003 and Yld2000-2d, for different aluminium and steels alloys using the TRD, L, and LM algorithms.

8.2.1 Yld2000-2d

The bar chart in Figure **8.2** illustrates the percentage of successful initial guesses for various algorithms and materials with the Yld2000-2d yield function. The TRD algorithm, for all the materials, is uniformly sensitive to the initial guess. Approximately 40–50% of the 100 random initial guesses were successful. However, with the other solution methods, a notable variation occurs in the successful initial guess percentages for all materials. Specifically, the TRD algorithm is the least sensitive to the initial guess for aluminium grades, whereas the LM algorithm is the most sensitive. In contrast, the LM algorithm, for both lambda parameters, is the least sensitive algorithm for the steel alloys considered. In this study, the steel alloys are generally less sensitive to the initial

guesses than the aluminium alloys for all solution methods used in this study. Finally, the initial value of the lambda parameter does not significantly influence the fraction of successful initial guesses.

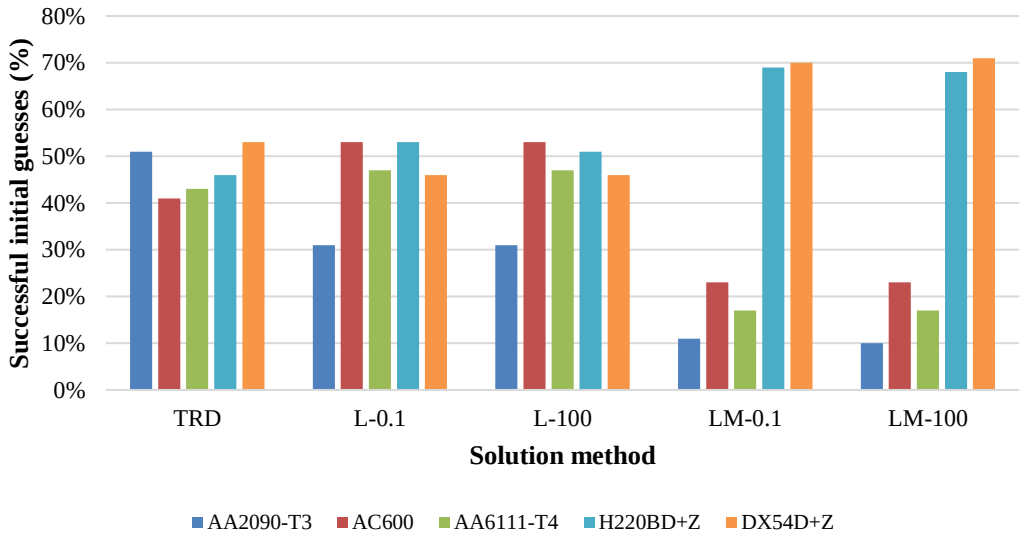

Figure 8.2. Sensitivity of Yld2000-2d to the initial guess for different solution methods and alloys.

8.2.2 BBC2003

The bar chart in Figure **8.3** illustrates the percentage of the successful initial guesses for different algorithms and materials with the BBC2003 yield function. In general, the TRD algorithm is the most sensitive algorithm to the initial guess, especially for the aluminium grades considered. In addition, it can be observed that the L algorithm, for both lambda values, is the least sensitive algorithm to the initial guess, especially for the steel alloys considered. Finally, the initial value of the lambda parameter again has little influence on the sensitivity of the LM algorithms to the initial guess.

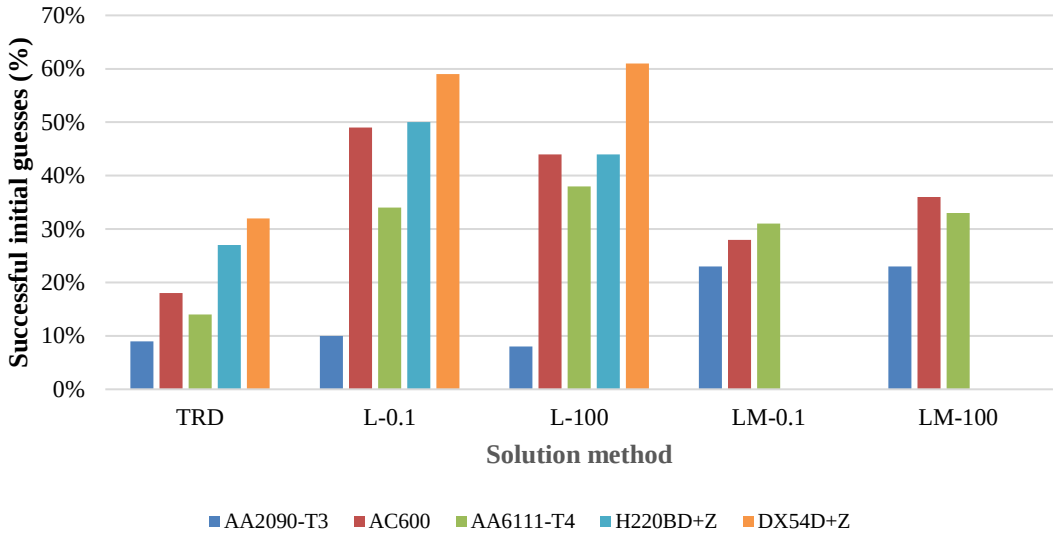

Figure 8.3. Sensitivity of BBC2003 to the initial guess for different solution methods and alloys.

8.3 Investigating the robustness and the effectiveness of the solution methods

8.3.1 Yld2000-2d

To investigate the robustness and the effectiveness of the solution methods for the yield criteria and materials used, the TRD, L, and LM algorithms were first verified for the Yld2000-2d model for different aluminium and steel alloys. The convergence of each solution method and the number of function evaluations that occurred during the identification procedure were examined for all the materials considered in this study.

Figure 8.4 depicts the evolution of the identification error with each iteration for all of the solution methods considered. The y-axis, $f(x)$, gives the function value at each step. As shown in this figure, all of the applied routines converge to a global minimum for all materials. For all the materials except for the highly anisotropic AA2090-T3, both the L and LM routines require fewer iterations to converge than the TRD algorithm. Yet again, the initial lambda value does not significantly affect the convergence rate for the Yld2000-2d model for all materials. Additionally, the TRD routine is the slowest algorithm, except in the case of AA2090-T3, for which it is the fastest routine. Furthermore, the L routine performs better than the slowest routine by only a few iterations (2–5 iterations) for most of the materials in this study. Overall, all of the applied algorithms were robust for all the materials examined. In addition, all the routines had approximately the same level of effectiveness.

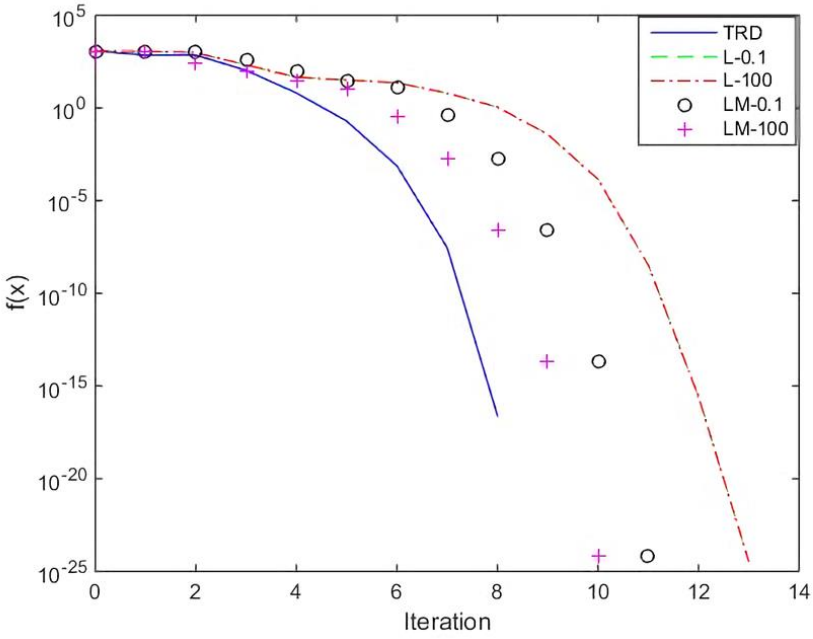
TRD
L-0.1
L-100
LM-0.1
LM-100
f(x)
Iteration

(a)

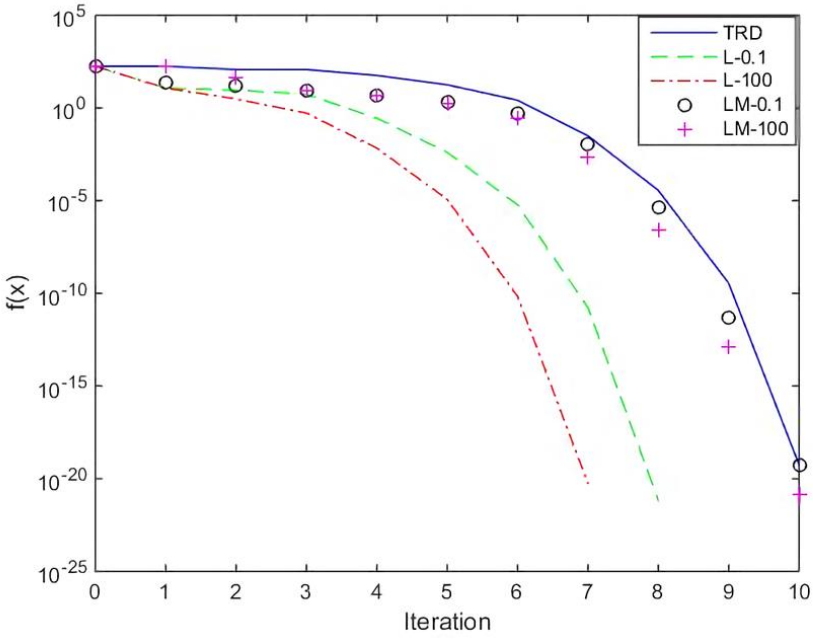
TRD
L-0.1
L-100
LM-0.1
LM-100
f(x)
Iteration

(b)

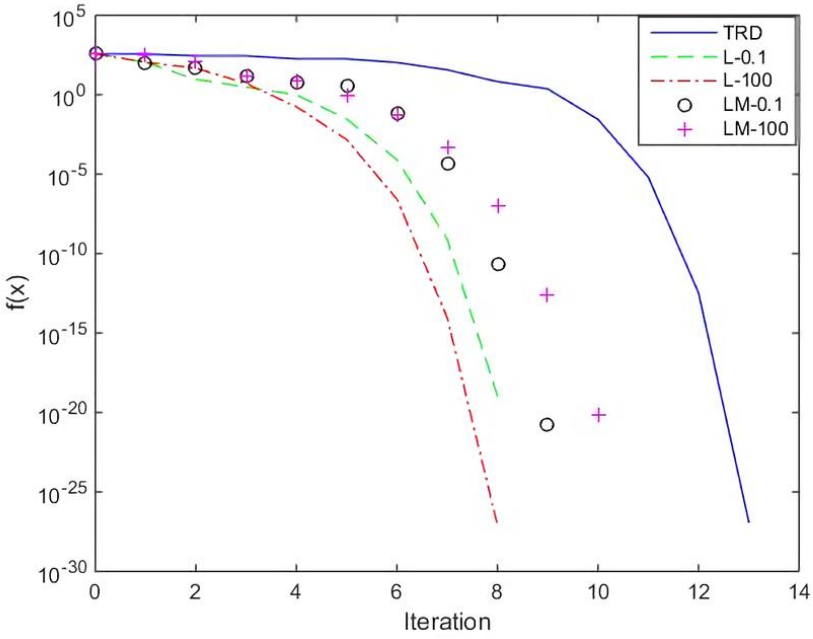
TRD
L-0.1
L-100
LM-0.1
LM-100
f(x)
Iteration

(c)

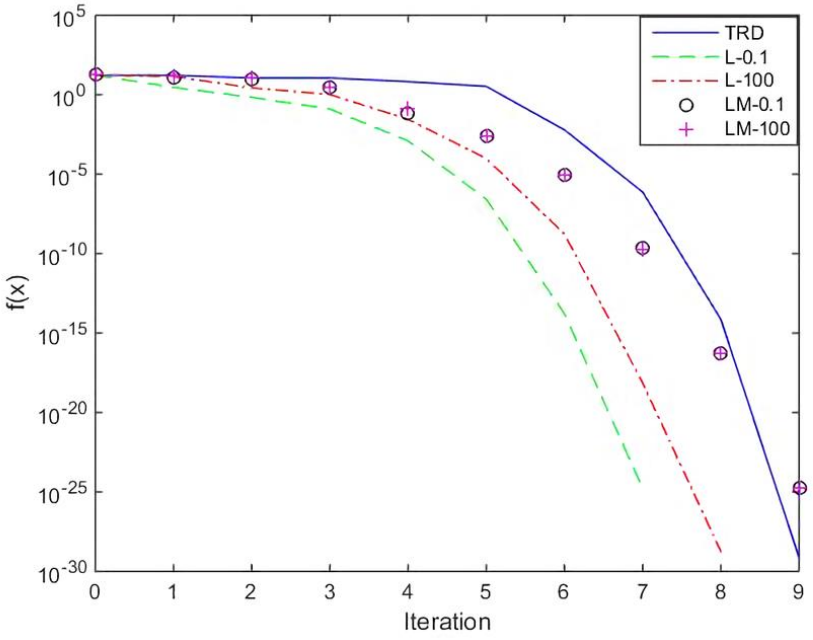
TRD
L-0.1
L-100
LM-0.1
LM-100
f(x)
Iteration

(d)

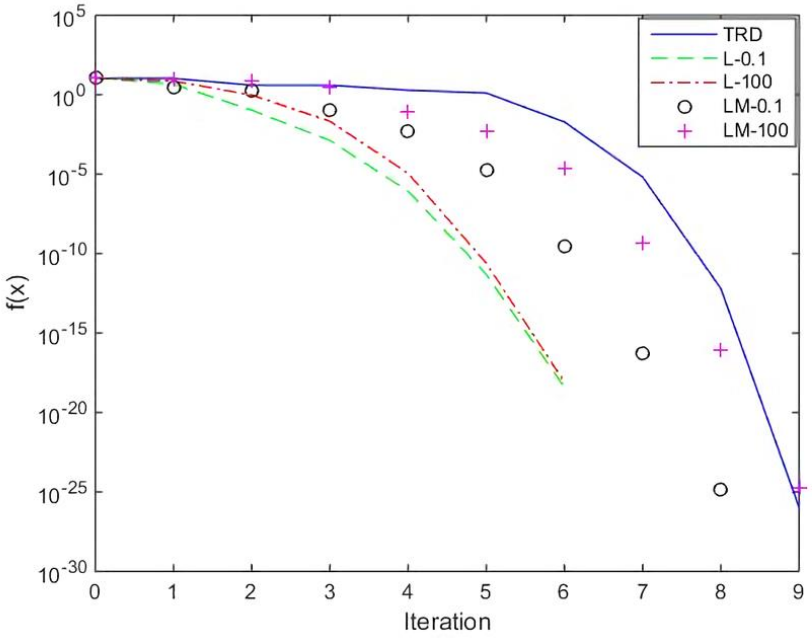

(e)

Figure 8.4. Convergence of the solution methods for Yld2000-2d: **a** AA2090-T3, **b** AC600, **c** AA6111-T4, **d** DX54D+Z, **e** H220BD+Z.

Figure **8.5** presents the number of function evaluations that occurred during the identification procedures for all of the solution methods considered. F-count accounts for the cumulative number of times the objective function was evaluated during the iterations. It was noted by Powell [99] that the TRD method economises the number of function evaluations when the Jacobian is approximated numerically.

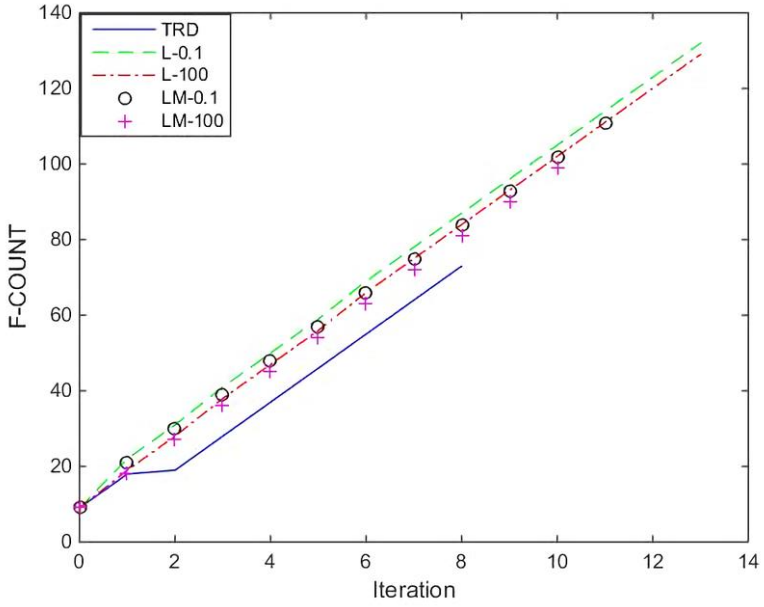

(a)

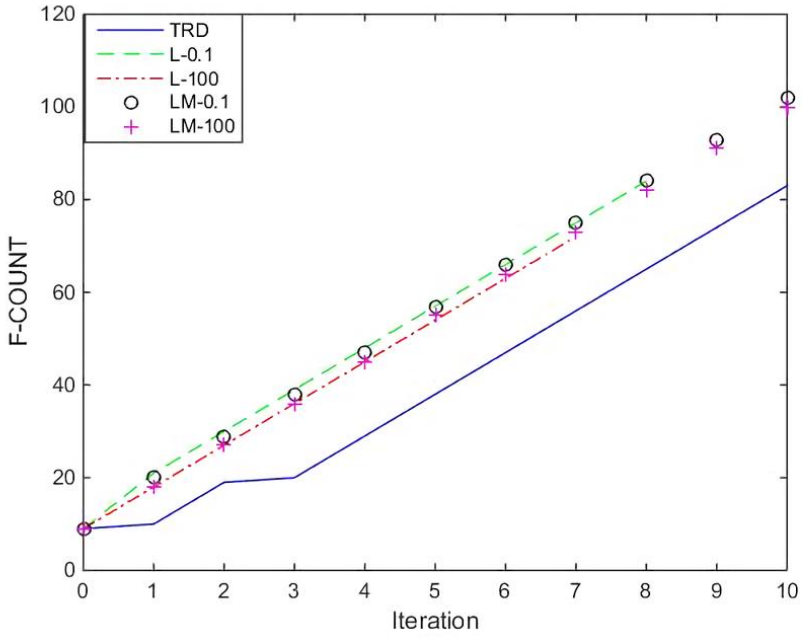
TRD
L-0.1
L-100
LM-0.1
LM-100
F-COUNT
Iteration
0
20
40
60
80
100
120
0
1
2
3
4
5
6
7
8
9
10

(b)

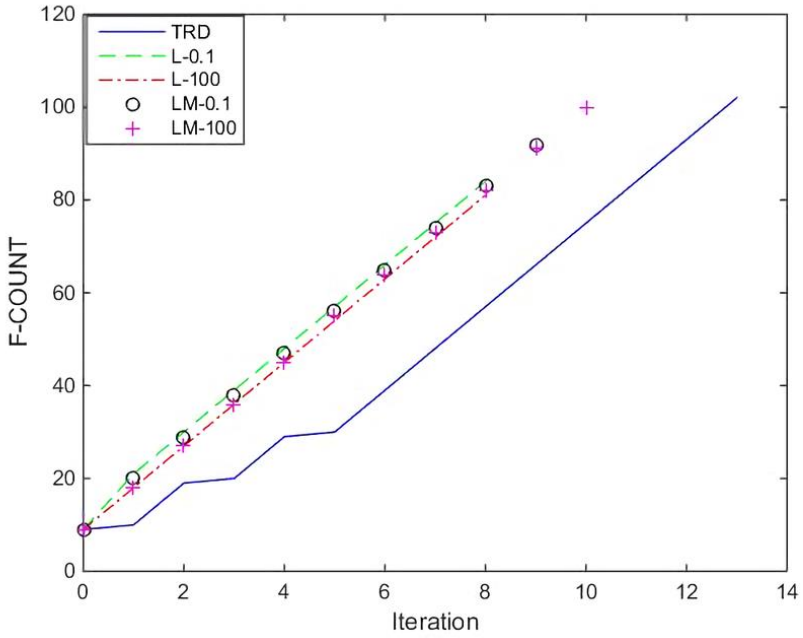
TRD
L-0.1
L-100
LM-0.1
LM-100
F-COUNT
Iteration
0
20
40
60
80
100
120
0
2
4
6
8
10
12
14

(c)

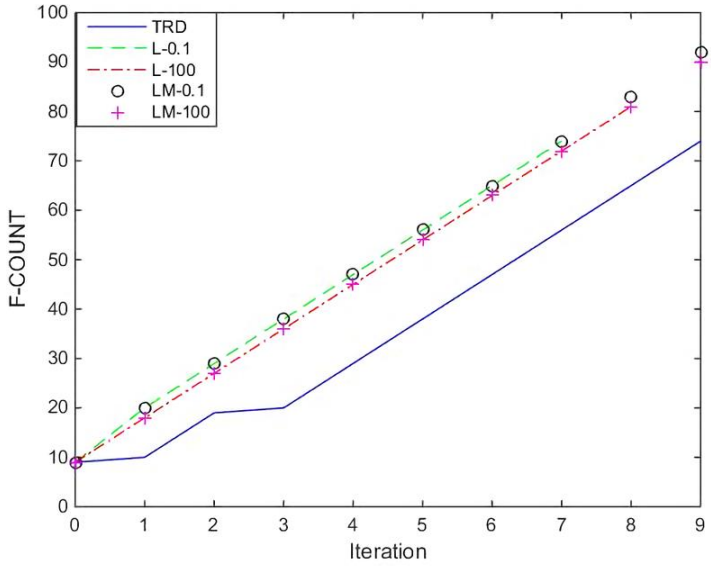

(d)

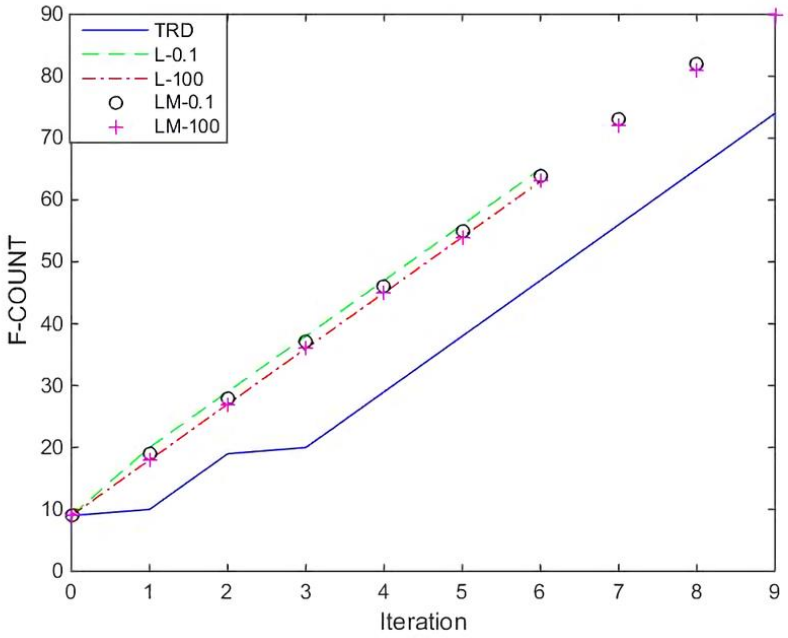

(e)

Figure 8.5. Number of function evaluations that occurred during the identification procedures for Yld2000-2d: **a** AA2090-T3, **b** AC600, **c** AA6111-T4, **d** DX54D+Z, **e** H220BD+Z.

This aspect is noticeable in Figure **8.5**. After any number of iterations, the TRD method requires fewer function evaluations than any permutation of the L & LM algorithms for the same number of iterations.

8.3.2 BBC2003

The BBC2003 yield criterion was examined in the same manner as was done for Yld2000-2d in the preceding section. Figure **8.6** depicts the evolution of the identification error with each iteration, for all of the algorithms considered. This figure reveals that the TRD method shows much better convergence than the other algorithms for most of the materials considered in the analysis. The L routine with $\lambda_S = 0.1$ converges at the same rate as the TRD routine for all of the aluminium alloys except AA2090-T3; however, this is not the case for the steel alloys. Additionally, the LM routine failed in finding the roots of the system of nonlinear equations for the steel grades. Furthermore, the lambda value noticeably affects the convergence of the BBC2003 model for most of the materials. In particular, the L algorithm converges faster with the small lambda than with the large value.

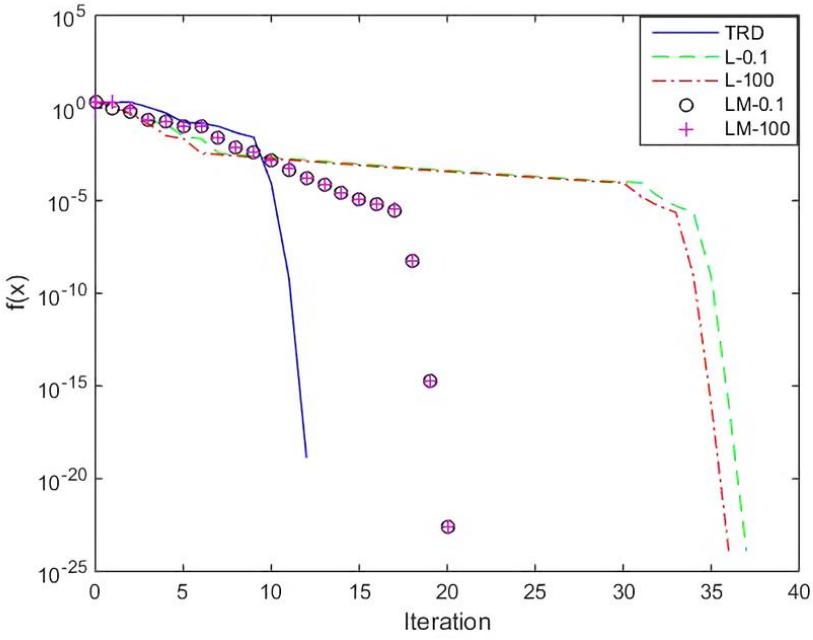

(a)

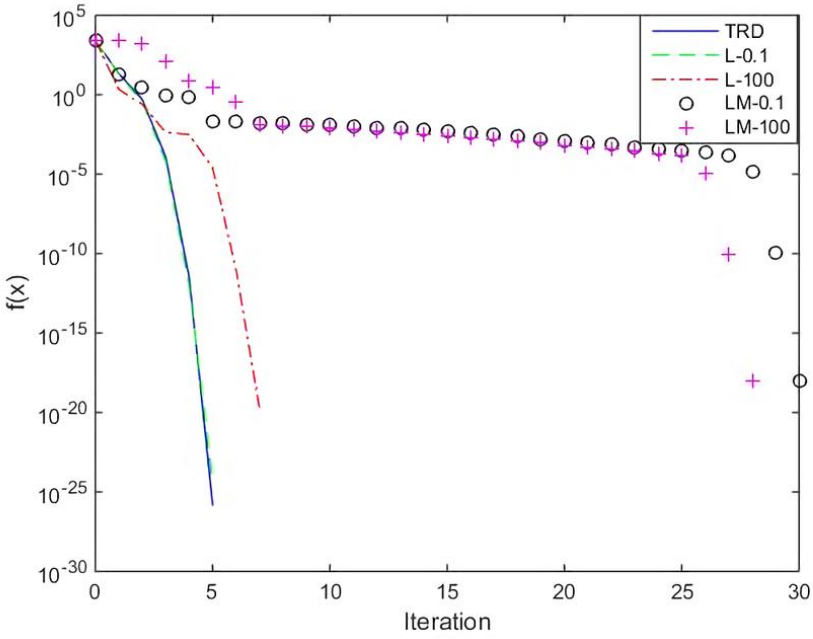
TRD
L-0.1
L-100
LM-0.1
LM-100
f(x)
Iteration

(b)

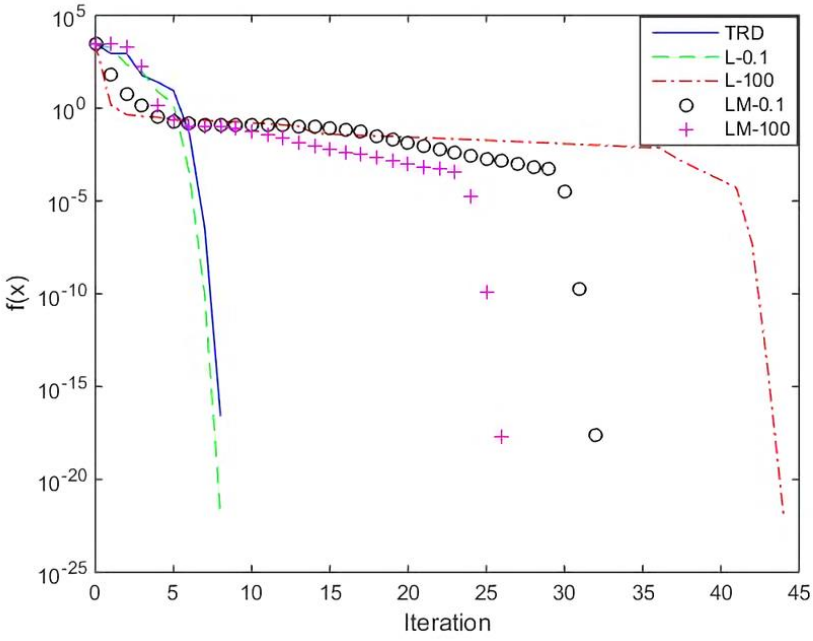
TRD
L-0.1
L-100
LM-0.1
LM-100
f(x)
Iteration

(c)

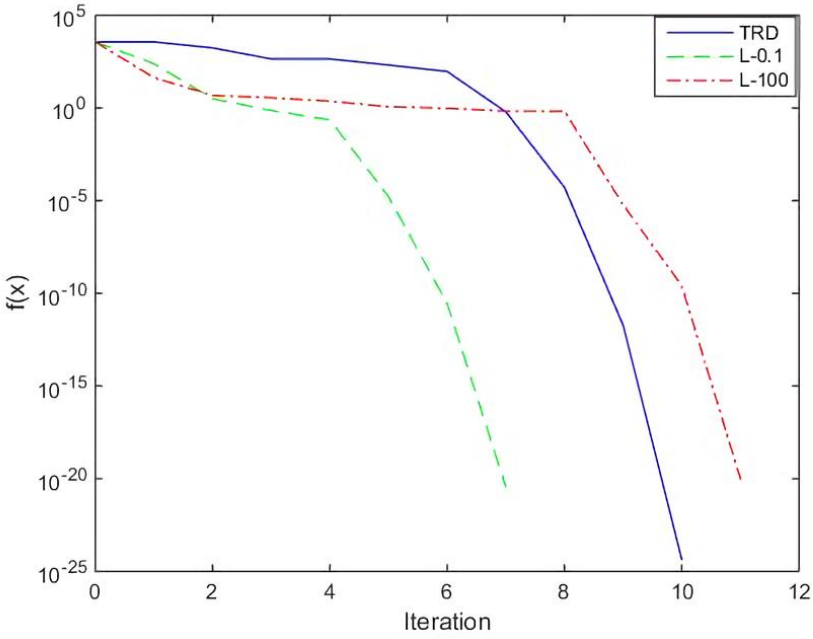

(d)

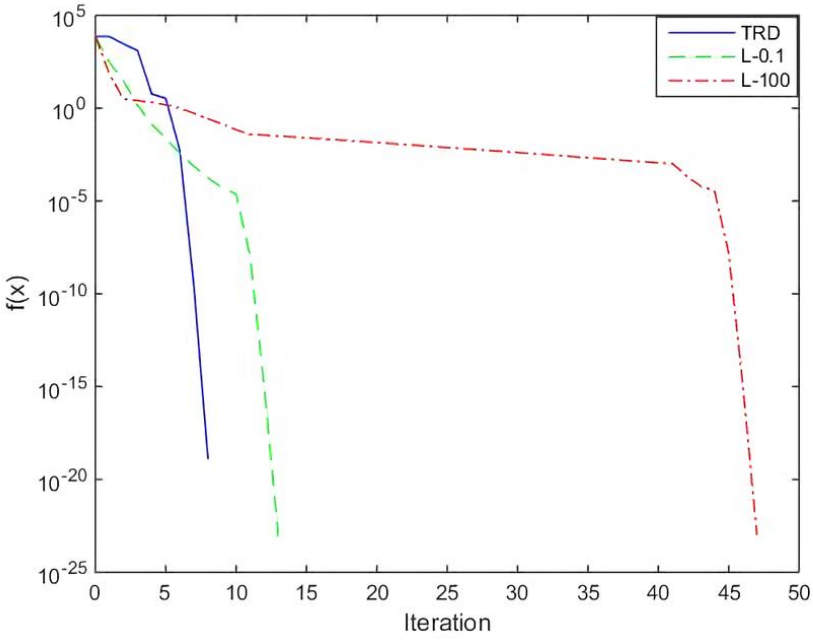

(e)

Figure 8.6. Convergence of the solution methods for BBC2003: **a** AA2090-T3, **b** AC600 **c** AA6111-T4, **d** DX54D+Z, **e** H220BD+Z.

Figure 8.7 depicts the number of function evaluations that occurred during the identification procedures for all of solution methods considered. Figure 8.7 demonstrates again that the TRD routine economises the number of function evaluations when the Jacobian is approximated for all of the materials considered in this study. Overall, all of

the applied algorithms were robust for all of the aluminium alloys considered in this study. Moreover, the LM algorithm failed to converge for the steel alloys considered. In addition, the level of effectiveness of these routines varied greatly for the different materials.

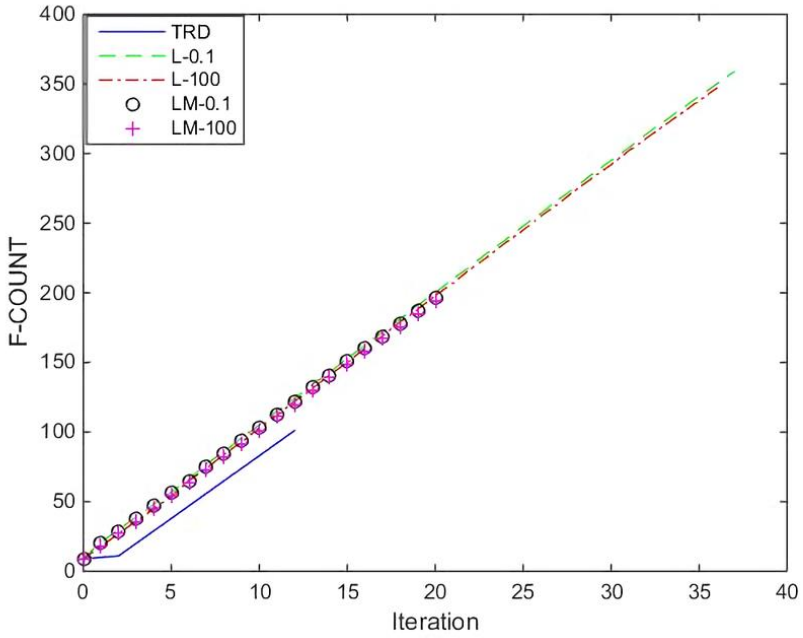

(a)

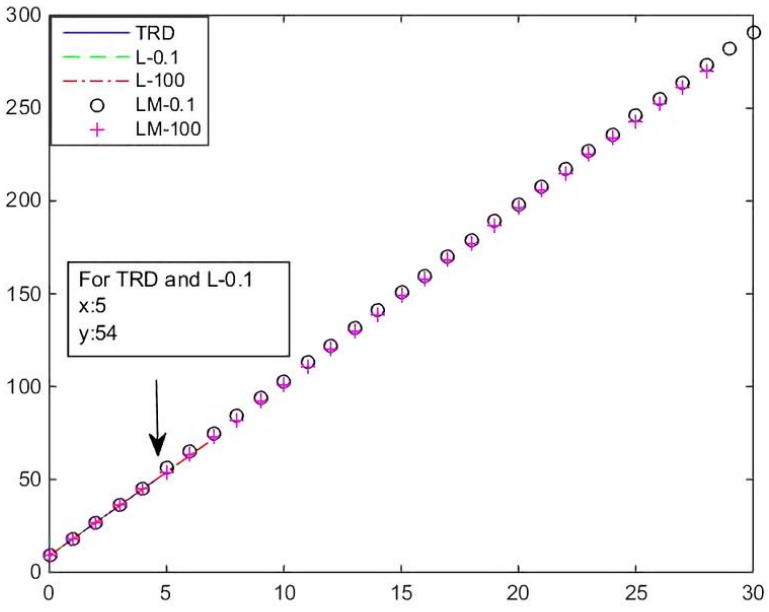

(b)

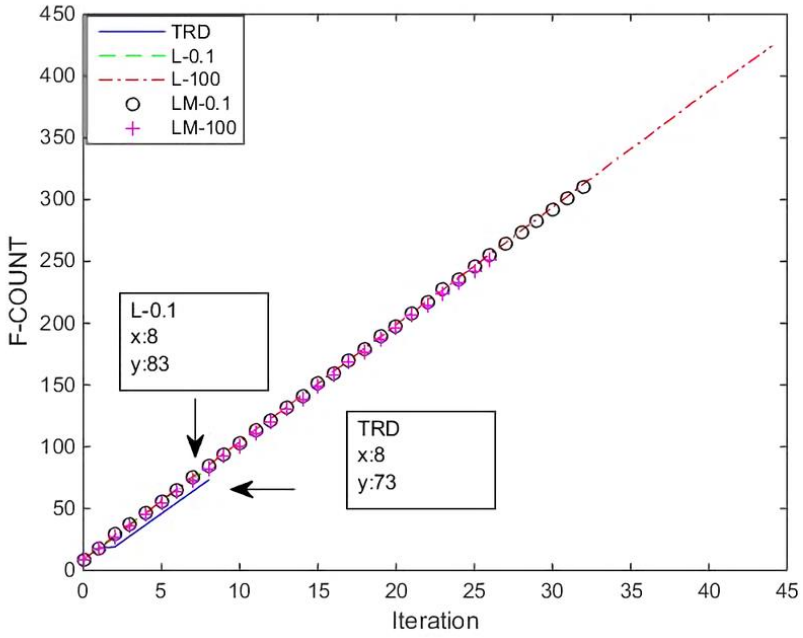
TRD
L-0.1
L-100
LM-0.1
LM-100
L-0.1
x:8
y:83
TRD
x:8
y:73
F-COUNT
Iteration

(c)

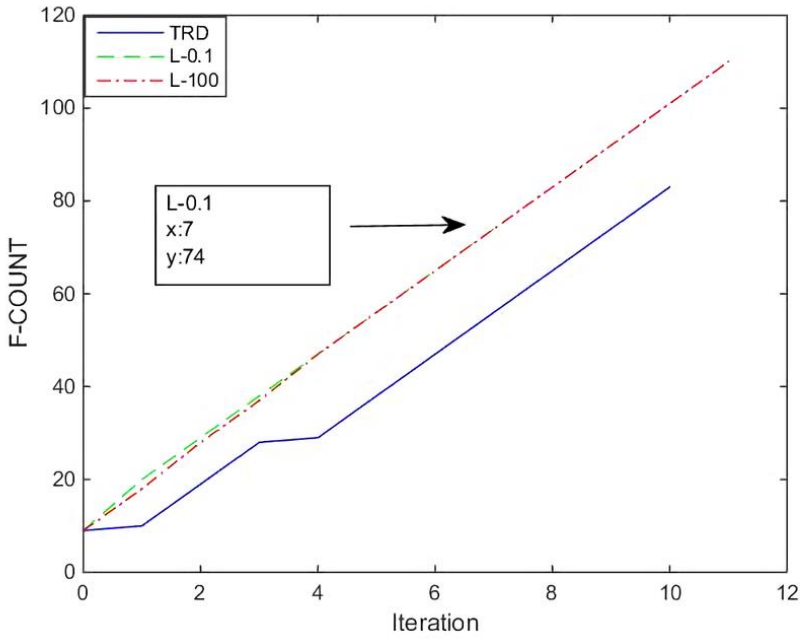
TRD
L-0.1
L-100
L-0.1
x:7
y:74
F-COUNT
Iteration

(d)

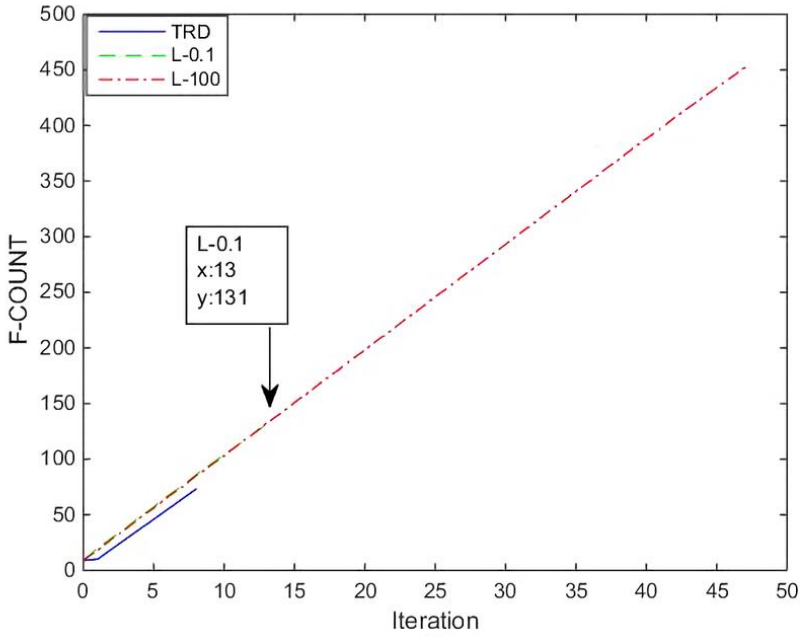

(e)

Figure 8.7. Number of function evaluations that occurred during the identification procedures for BBC2003: **a** AA2090-T3, **b** AC600, **c** AA6111-T4, **d** DX54D+Z, **e** H220BD+Z.

8.4 Comparison of Yld2000-2d and BBC2003

In terms of sensitivity to the initial guesses, with the TRD routine, Yld2000-2d is less sensitive to the initial guess than BBC2003. For the other applied algorithms, both yield criteria have almost the same level of sensitivity to the initial guess. In addition, when the algorithms converge to a solution with both yield functions, the steels grades are generally less sensitive to the initial guess than the aluminium alloys.

In terms of robustness, with the Yld2000-2d, all of the applied algorithms were able to identify the plastic anisotropy parameters for all of the materials considered in this study, whereas with BBC2003, the LM method failed to converge to solutions for two of the materials, one of which could not be solved with any of the methods considered. Thus, Yld2000-2d is a more flexible yield criterion than BBC2003with respect to different solution methods and alloys.

Finally, in terms of effectiveness, all of the applied algorithms converge to solutions in a smaller number of iterations with Yld2000-2d than with BBC2003. Consequently, the total number of function evaluations that occurred during all of the iterations for all of the

materials considered in this study and for all solution methods was less with Yld2000-2d than with BBC2003.

8.5 Yield loci

For all of the materials considered in this study, the three applied algorithms were used to compute the plastic anisotropy coefficients of the Yld2000-2d and BBC2003 yield functions; the results are shown in Table **8.1** and Table **8.2**, respectively. Coincidentally, all of the methods produced the same solution. Since the shapes of the yield loci derived by the BBC2003 and Yld2000-2d are identical, the yield loci were derived using Yld2000-2d for all of the materials considered in this study, and they are shown in Figure **8.8**. The acceptable roots (i.e., parameters) were constrained to real, positive numbers.

The considered algorithms worked efficiently if the randomly selected initial guesses were generated using a uniform distribution returning real numbers between 0.65 and 0.85 for both yield criteria for all the materials considered in the analysis. Therefore, all of the parameters were identified by using initial guesses that lie in this range.

Table 8.1. Plastic anisotropy parameters of Yld2000-2d for different materials.

Material	α_1	α_2	α_3	α_4	α_5	α_6	α_7	α_8
AA2090-T3	0.6035	1.2497	0.6004	1.0085	1.0487	0.9664	1.2309	1.5123
AA6111-T4	0.9180	1.1017	1.0503	1.1143	1.0514	1.1514	1.0246	1.1461
AC600	0.9498	1.0089	1.0522	1.0395	1.0398	1.0837	0.9458	1.0922
H220BD+Z	1.0755	0.9620	0.8748	0.8960	0.9237	0.8343	0.9815	0.9510
DX54D+Z	1.0554	1.0240	0.8382	0.8917	0.9107	0.8171	0.9965	0.9745

Table 8.2. Plastic anisotropy parameters of the BBC2003 for different materials.

Material	a_B	M_B	N_B	P_B	Q_B	R_B	S_B	T_B
AA2090-T3	0.0873	1.3552	1.6766	1.4916	1.8809	0.7595	0.9593	1.1417
AA6111-T4	0.4097	1.2326	1.0875	1.0960	1.1750	0.9591	1.0191	1.0035
AC600	0.6511	1.0301	0.9837	0.9734	1.0567	1.0141	1.0347	0.9893
H220BD+Z	0.3436	0.8978	1.0301	1.0248	1.0124	0.9916	0.9555	0.9380
DX54D+Z	0.2770	0.9348	1.0787	1.0725	1.0753	0.9826	0.9728	0.9370

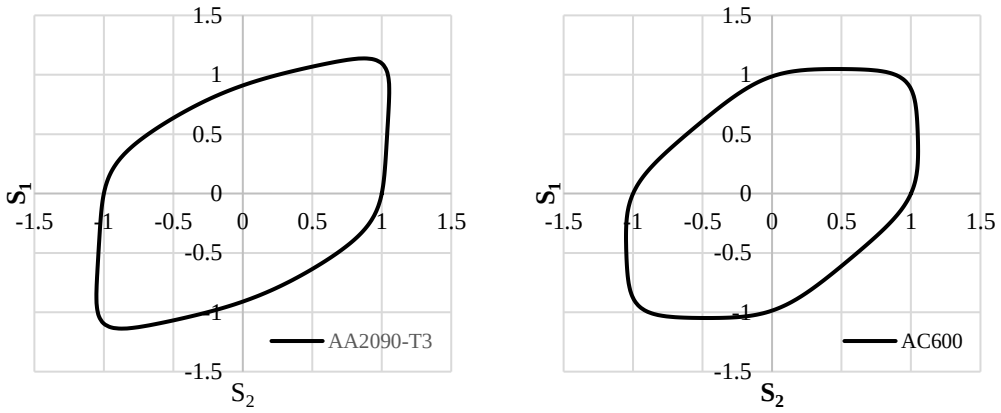

(a)

(b)

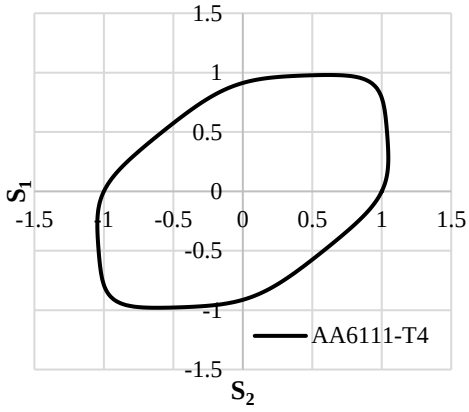

(a)

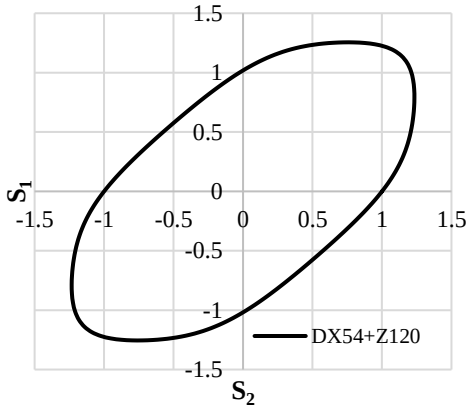

(b)

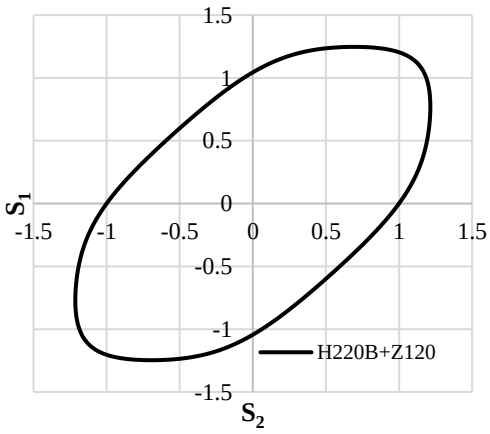

(e)

Figure 8.8. Yield loci derived for Yld2000-2d: **a** AA2090-T3, **b** AC600, **c** AA6111-T4, **d** DX54D+Z, **e** H220BD+Z.

8.6 Conclusion

This chapter presented a comparison of line-search based algorithms and a trust-region based algorithm and demonstrated their ability in overcoming the difficulties encountered by the NR procedure. These applied optimization strategies were used to identify the plastic anisotropy parameters associated with different yield functions for various aluminium and steel alloys. Tensile, bulge, and compression tests were performed to obtain the data for these materials. The phenomenological models denoted as Yld2000-2d and BBC2003 were used to describe the material behaviour.

For Yld2000-2d, all of the applied algorithms were robust for all the materials in this study. Additionally, all of these routines were relatively equivalent in effectiveness. In addition, for all of the materials, the number of function evaluations invoked by the TRD routine was lower than all permutations of the LM algorithms for the same number of iterates.

For BBC2003, the L routine was less sensitive to the initial guess than the other routines. In addition, all of the applied algorithms were robust for all of the aluminium alloys considered in this study. Furthermore, the TRD routine was the most robust algorithm. Unfortunately, the LM routine failed to converge for steels. Moreover, the variation in the level of effectiveness of these routines varied greatly for the different materials.

Finally, Yld2000-2d was less sensitive to the initial guess than BBC2003 and was more flexible with different solution methods for various alloys than BBC2003. Additionally, all of the algorithms for all of the materials converged faster with Yld2000-2d than with BBC2003, which will in turn economize the number of computer evaluations when the Jacobian is approximated numerically.

Chapter 9

Biaxial Flow Curve Determination (Results and Discussion)

9.1 Introduction

This chapter has three purposes. First, the methodology proposed to determine the biaxial flow curves using hydraulic bulge tests with circular dies must be validated. The methodology modifies the correction factor used in Chakrabarty and Alexander's formula. Instead of being based on an *n*-value, the modification proposes that the correction factor should be based on normal plastic anisotropy. Continuous hydraulic bulge experiments were performed to validate this methodology. Second, the research compares the results obtained by the proposed method with the approaches of Chakrabarty and Alexander, and Kruglov. The comparison looks at the following:

- Relation between polar thickness and dome height (section 9.2.1)
- Relation between the applied pressure and polar strain (section 9.2.2)
- Resulting biaxial flow curves (section 9.3)

Finally, the study investigates the effects of using the three analytical approaches on the resulting shape of the BBC2005 yield locus for four sheet alloys. In section 9.4, the predicted shape of the yield locus is compared to a yield locus, which is derived using biaxial stress that is determined from measured DIC data. The conclusion is presented in section 9.5.

9.2 Validation of the method

9.2.1 Polar thickness vs. dome height

The polar thickness was measured using the DIC software and compared with the predictions of Chakrabarty and Alexander, Kruglov, and modified Chakrabarty and Alexander equations, i.e. Eq. (5.11), Eq. (5.12), Eq. (5.17), and Eq. (5.19). Figure **9.1** illustrates polar thickness as a function of the dome height for different materials. The conclusion that can be drawn is that the proposed method (P-C-M) predicted accurately the polar thickness data measured by the DIC system for all of the materials investigated in this study. It can be seen that Kruglov's approach also leads to the same conclusion except for the H220BD+Z. For the mentioned material, Kruglov's prediction gradually

diverges with increasing dome height. The magnitude tends to be higher than that of the experimental data. In contrast, Chakrabarty and Alexander's method gradually diverges with increasing apex height. The magnitude tends to be lower than that of the experimental data.

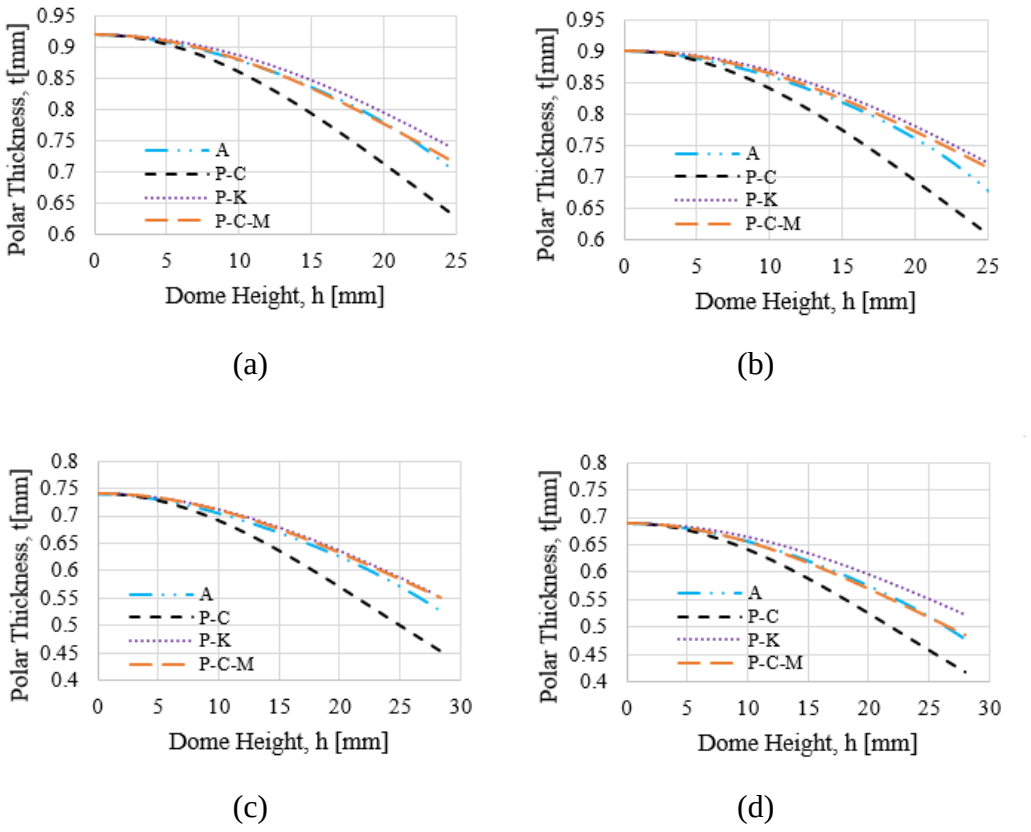

Figure 9.1. Variation of polar thickness with dome height for **a** AA6111-T4, **b** AC600, **c** DX54D+Z, and **d** H220BD+Z. (A: ARAMIS, P-C: Panknin-Chakrabarty & Alexander, P-K: Panknin-Kruglov, and P-C-M: Proposed model).

It should be noted that the height measurements up to 24 mm and 28 mm were used in the calculations of the polar thickness for the aluminium and steel alloys, respectively.

9.2.2 Pressure vs. polar strain

The relation between the polar strain and the pressure is illustrated in Figure **9.2**. The strain is calculated by Eq. (5.4) using the thickness data measured by ARAMIS software. The resulting strain from the continuous bulging experiment was compared with calculated strain using the Chakrabarty and Alexander method (Eq. 9), Kruglov method (Eq. 5.4, Eq. 5.12), and modified Chakrabarty and Alexander methods (Eq. 5.16, Eq. 5.18).

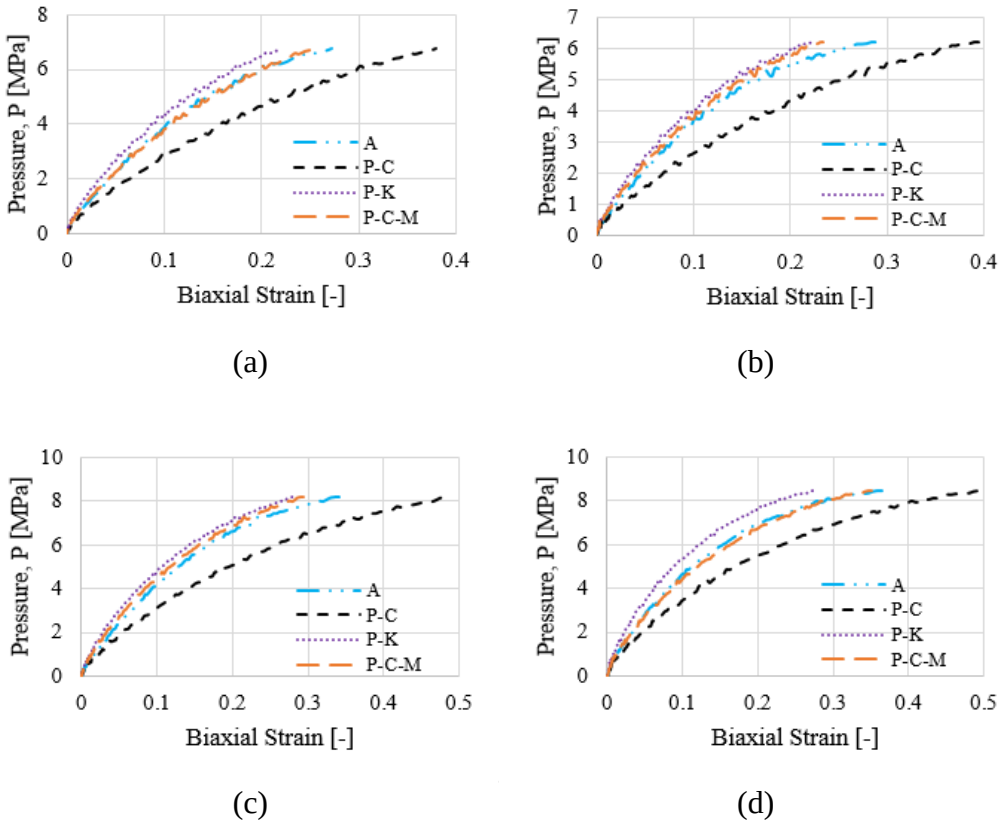

Figure 9.2. Variation of oil pressure with polar strain for **a** AA6111-T4, **b** AC600, **c** DX54D+Z, and **d** H220BD+Z. (A: ARAMIS, P-C: Panknin-Chakrabarty & Alexander, P-K: Panknin-Kruglov, and P-C-M: Proposed model).

The P-C model under-predicted the data, while the P-K overestimated the data. Conversely, the modified method (P-C-M) generally captured the magnitude and trend of the experimental data.

9.3 Biaxial flow curves

Finally, the biaxial stress-strain curves were calculated and compared with the measured flow curves provided by the DIC system. The results are plotted in Figure **9.3** a, b, c, and d for AA6111-T4, AC600, DX54D+Z, and H220BD+Z, respectively. Overall, the prediction of the proposed methodology (P-C-M) captures the trends and magnitudes of the experimental data. In contrast, the P-C model approximates the magnitude of the data but does not predict the trend as well as the PCM model does. It can be observed that the prediction of the P-K method is accurate for the steel grades. The plotted data for the aluminium alloys and steel grades are approximated using Voce and power law type equations, respectively. One bulge test for each material was used and fitted. The tensile tests for all of the materials are included in Figure **9.3**.

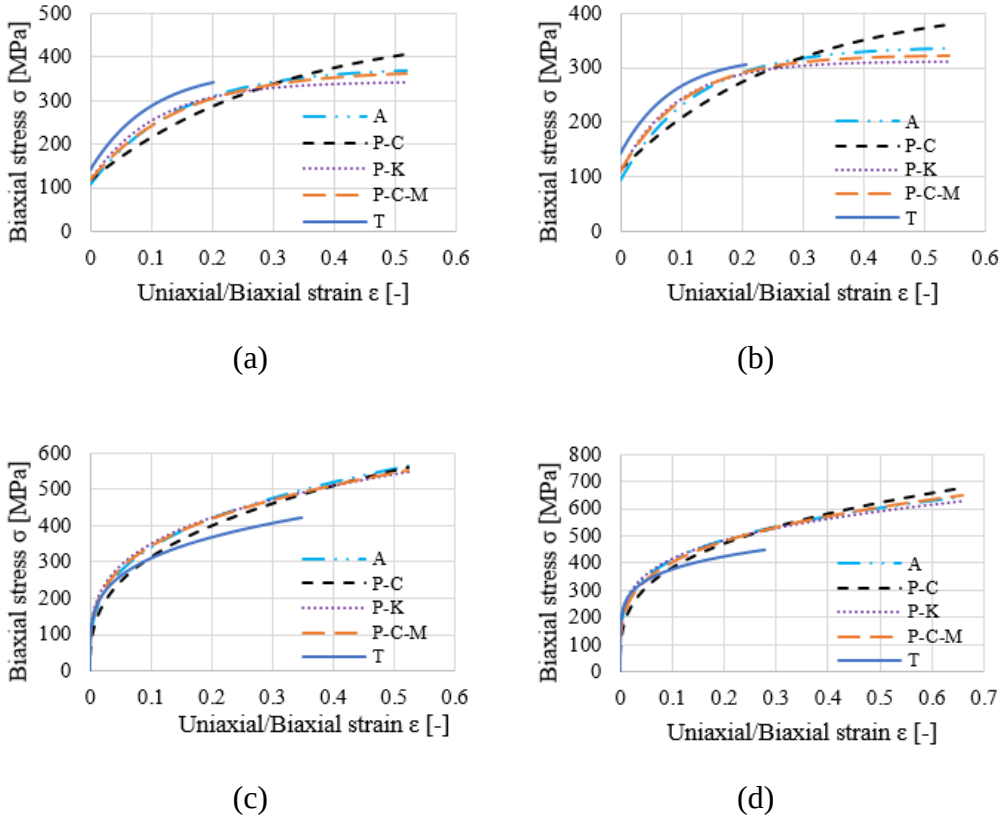

Figure 9.3. The uniaxial curve vs. biaxial flow curves obtained with different methodologies: **a** AA6111-T4, **b** AC600, **c** DX54D+Z, and **d** H220BD+Z. (A: ARAMIS, P-C: Panknin-Chakrabarty, P-K: Panknin-Kruglov, P-C-M: Proposed model, and T: Rolling direction flow curve).

The flow stress curves of aluminium alloys given in Figure **9.3** were fitted into Voce's equation [161] form. The obtained hardening constants (A, B, and C) are tabulated in Table 9.1.

Table 9.1. Hardening parameters for Voce type hardening equation ($\sigma = A - Be^{(-c\varepsilon)}$).

Approach	AA6111-T4			AC600		
	A	**B**	**C**	**A**	**B**	**C**
DIC	376.1	269.3	6.99	338.3	243.7	8.145
P-C	470.5	352.1	3.233	421.6	309.8	3.685
P-K	342	223	9.217	312.6	200.9	10.69
P-C-M	369	251.4	6.803	322.3	212.3	9.312
T	372	231.9	10.04	320.3	177.5	11.72

However, the flow stress curves of steel alloys given in Figure **9.3** were fitted into Hollomon's [162] equation form. Strength coefficient (K) and strain hardening exponent (n) values are tabulated in Table **9.2**. The fitting into these forms was done for eventual use in finite element analyses.

Table 9.2. Hardening coefficients in Hollomon's equation ($\sigma = K\varepsilon^n$).

Approach	DX54D+Z		H220BD+Z	
	K	***n***	***K***	***n***
DIC	688.9	0.3066	713	0.2367
P-C	705.4	0.3504	770.5	0.3018
P-K	651.3	0.2707	688.8	0.219
P-C-M	663.7	0.2865	719.7	0.2524
T	546.21	0.2466	560	0.169

9.4 Effect of using the analytical approaches on the shape of the BBC2005

9.4.1 Stress ratios

For each material, the biaxial flow curves from hydraulic bulge tests were measured using the DIC data (A) and calculated by the predictions of the Chakrabarty and Alexander (P-C), Kruglov (P-K), and modified Chakrabarty and Alexander (P-C-M) methods. Therefore, for each material, generally four different biaxial flow curves are obtained. The number of the specimens used in the hydraulic bulge and uniaxial tests that were employed to derive the stress ratios are shown in Figure 9.4. For instance, for the AA6111-T4 alloy, three uniaxial flow curves and five biaxial flow curves measured with the DIC were used to obtain 15 variations of the σ_b / σ_u ratio. For certain strain ranges or plastic work ranges, as shown in Figure 9.4, the average of the variations between σ_b and σ_u is evaluated for each methodology; then, the average ratio is calculated (σ_b / σ_u Avg.). This ratio at the average ratio times the uniaxial yield stress YS_0 is the biaxial yield stress YS_b, as summarized in Table **9.3** and Table **9.4**

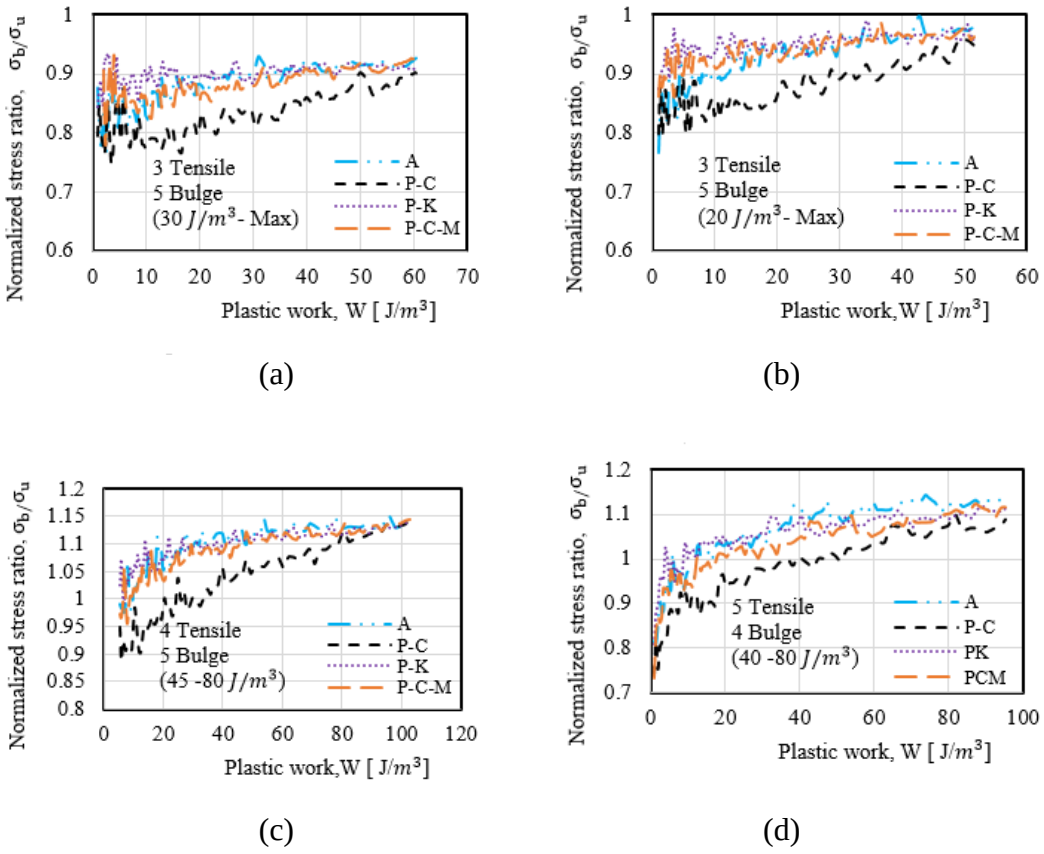

Figure 9.4. The σ_b/σ_u ratio as a function of plastic strain for different methodologies **a** AA6111-T4, **b** AC600, **c** DX54D+Z, and **d** H220BD+Z. (A: ARAMIS, P-C: Panknin-Chakrabarty and Alexander, P-K: Panknin-Kruglov, and P-C-M: Proposed model).

Table 9.3. The average ratios (σ_b/σ_u Avg.) and uniaxial yield stresses (YS_0) for different materials with various approaches.

Approach	Materials							
	AA6111-T4		AC600		DX54D+Z		H220BD+Z	
	σ_b/σ_u Avg.	YS_0 [MPa]	σ_b/σ_u Avg.	YS_0 [MPa]	σ_b/σ_u Avg.	YS_0 [MPa]	σ_b/σ_u Avg.	YS_0 [MPa]
A	0.918	138	0.956	144	1.143	162	1.116	248
P-C	0.865		0.903		1.063		1.047	
P-K	0.9115		0.954		1.120		1.105	
P-C-M	0.906		0.951		1.117		1.093	

Table 9.4. The biaxial yield stresses (YS_b) for all the materials determined by various methods.

Approach	Materials			
	YS_b −AA6111-T4 [MPa]	YS_b −AC600 [MPa]	YS_b −DX54D+Z [MPa]	YS_b −H220BD+Z [MPa]
A	126.68	137.68	184.97	278.15
P-C	119.41	130.10	172.33	259.71
P-K	125.79	137.47	182.52	273.60
P-C-M	125.06	137.03	182.04	271.11

9.4.2 Yield loci

To study the effect of using the proposed approach and other developed approaches of the biaxial stress-strain curve determination on the shape of the BBC2005 yield locus using four different sheet alloys, the flow curves for the considered materials were first determined. This was accomplished by using three combinations of analytical models that determine the dome apex thickness and polar curvature at the dome apex. The flow curves were used to compute the biaxial yield stresses for the different employed approaches for all of the materials considered in this study with the aid of the approach proposed by Lee et al. [176] that is based on the principle of the equivalent plastic work. Figure **9.5** illustrates yield loci for the materials under this study. The results are plotted in Figure **9.5** a, b, c, and d for AA6111-T4, AC600, DX54D+Z, and H220BD+Z, respectively. Overall, the prediction of the proposed methodology (P-C-M) captures the magnitude of the experimental biaxial yield stress. In contrast, the P-C model underestimated the

magnitude of the biaxial yield stress. Alternatively, it can be seen that the biaxial yield stress obtained by the P-K method is of similar accuracy to the P-C-M for all the material grades.

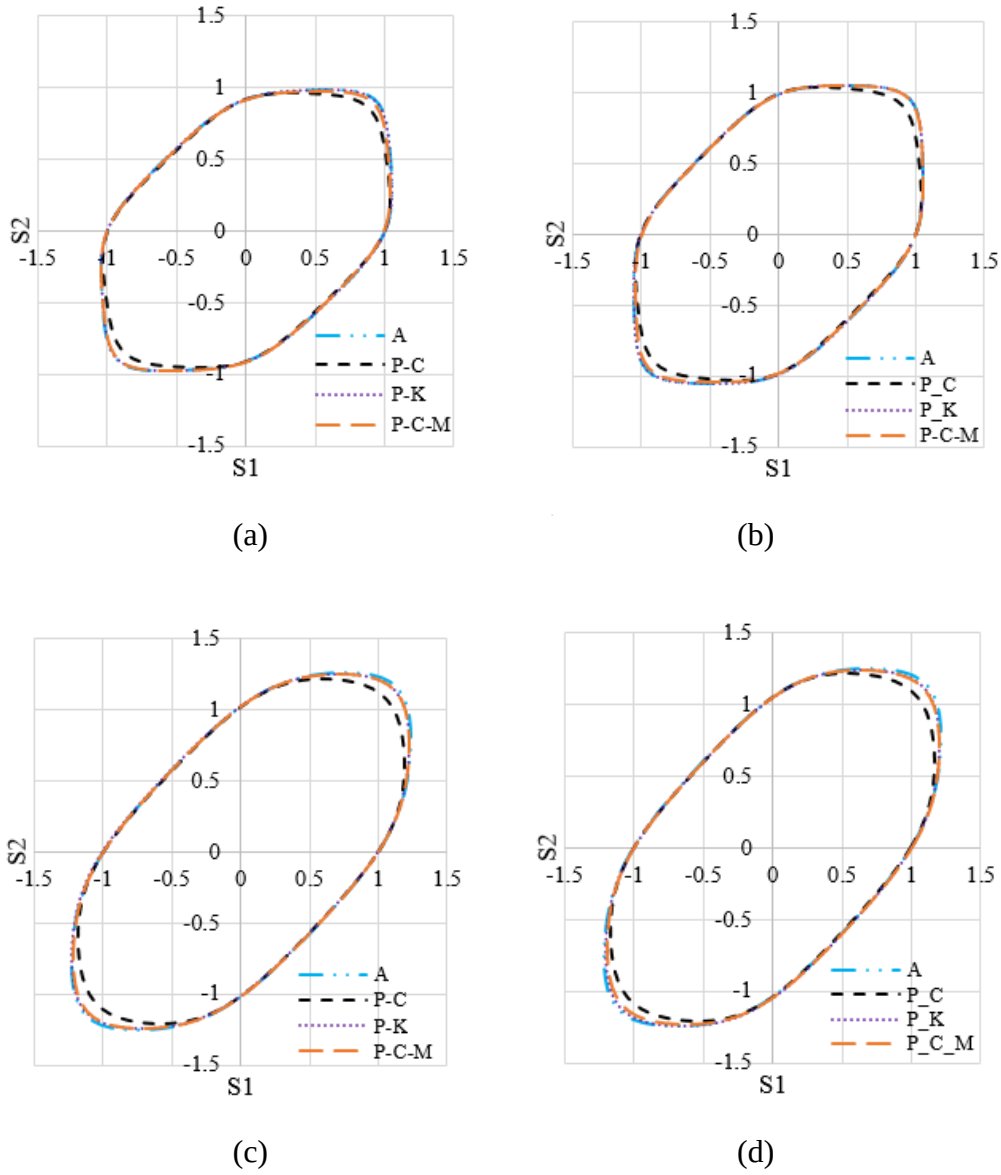

Figure 9.5. Yield loci obtained with different methodologies: **a** AA6111-T4, **b** AC600, **c** DX54D+Z, and **d** H220BD+Z.

Table **9.5**, Table **9.6**, Table **9.7** and Table **9.8** present the material coefficients a_{B5}, b, L, M, N, P, Q, and R_{B5} calculated by means of a Newton solver for the materials examined in this study.

Table 9.5. BBC2005 anisotropy coefficients for the aluminium alloy AA6111-T4.

Approach	Material constants							
	a_{B5}	b	L	M	N	P	Q	R_{B5}
A	1.48078	0.60691	0.42602	0.52503	0.46284	0.46645	0.49302	0.54926
P-C	0.79824	0.68538	0.49554	0.59428	0.45853	0.46578	0.49075	0.55332
P-K	1.38070	0.61656	0.43359	0.5326	0.4624	0.46636	0.49256	0.54983
P-C-M	1.30319	0.62438	0.43990	0.53889	0.46202	0.46629	0.49223	0.55028

Table 9.6. BBC2005 anisotropy coefficients for the aluminium alloy AC600.

Approach	Material constants							
	a_{B5}	b	L	M	N	P	Q	R_{B5}
A	1.04374	0.31688	0.46989	0.48401	0.46554	0.46074	0.56014	0.58580
P-C	0.57751	0.37110	0.53531	0.55164	0.46380	0.45749	0.55377	0.57977
P-K	1.02812	0.31839	0.47149	0.48566	0.46549	0.46066	0.55992	0.58559
P-C-M	0.99628	0.32152	0.47485	0.48912	0.46540	0.46050	0.55949	0.58516

Table 9.7. BBC2005 anisotropy coefficients for the aluminium alloy DX54D+Z.

Approach	Material constants							
	a_{B5}	b	L	M	N	P	Q	R_{B5}
A	0.43183	0.48905	0.46389	0.43353	0.50155	0.49870	0.54710	0.53948
P-C	0.24119	0.51469	0.54388	0.51754	0.50318	0.49716	0.54489	0.53779
P-K	0.38927	0.49406	0.47753	0.44783	0.50179	0.49847	0.54675	0.53905
P-C-M	0.38127	0.49504	0.48029	0.45072	0.50185	0.49842	0.54668	0.53897

Table 9.8. BBC2005 anisotropy coefficients for the aluminium alloy H220BD+Z.

Approach	Material constants							
	a_{B5}	b	L	M	N	P	Q	R_{B5}
A	0.36863	0.44704	0.49426	0.44379	0.50894	0.50631	0.54828	0.51238
P-C	0.20526	0.47114	0.57665	0.53091	0.51155	0.50487	0.54602	0.51083
P-K	0.32259	0.45302	0.51229	0.46280	0.50946	0.50605	0.54787	0.51186
P-C-M	0.29911	0.45627	0.52269	0.47378	0.50977	0.50589	0.54761	0.51161

9.5 Conclusion

This chapter presents a new analytical approach to determine the polar thickness of the bulged sheet. The new methodology is based on a modified version of the Chakrabarty and Alexander equation. The proposed method considers the effect of the normal plastic anisotropy of the sheet. In the absence of a continuous and in-line thickness measurement system, the proposed method coupled with the Panknin method is found to be a reliable combination to determine the biaxial flow curve and hence the biaxial yield stress. For an accurate definition of the yield surface, it is crucial to provide an accurate material parameter, namely the biaxial yield stress material using biaxial loading tests such as the hydraulic bulge test. Therefore, the proposed method predicted very well the biaxial yield stresses compared to the DIC data for all of the materials considered in this study.

Chapter 10

Conclusions and Recommendations

In this chapter, the main findings of the work in this thesis are summarised, and recommendations for future work are outlined.

10.1 Accurate and cost-effective description of the yield locus

One of the essential elements that is required to be specified to describe the plastic deformation involved with sheet forming processes is the yield locus. This element predicts the onset of yielding at different stress states. It is a central ingredient of the material characterisation process involved in sheet metal forming simulation processes. The yield locus is a primary simulation input that is critical in the accurate prediction of forming defects, such as thinning and splitting.

This essential concept of classical plasticity can be treated numerically through two approaches. The first approach, the phenomenological approach, is a modelling of the macroscopic plasticity in which the average behaviour of all the grains is determined, generally with experimental and mechanical tests. The second approach, the polycrystalline plasticity approach, is based on the crystal behaviour and averaging scheme used to determine the behaviour of the polycrystalline material.

The phenomenological approach is the only realistic approach to define the yield criteria [18,25,26,141]. However, some of the advanced models have a high number of parameters which must be computed by conducting more experimental work. Such mechanical tests that are involved in the identification process are costly and time consuming and must be conducted with care [7,27]; therefore, they are unrealistic for the sheet forming industry.

Of note, the main downside of the polycrystalline plasticity approach is the fact that the computational costs are still quite high. This hinders their applicability for industrial applications. However, the question remains whether models under this approach can replace experimental tests.

To meet the demands of the sheet forming industry, different aspects such as accuracy, simplicity, and efficiency must be considered at the phase of proposing a new description for the anisotropic yielding behaviour. Such aspects were examined in the current study.

The trend in recent years is to combine the strengths of the physics-based models and phenomenological yield criteria. In this manner, the severity associated with the extensive and difficult tests that are required for calibrating advanced flexible yield functions can be reduced. The previous mentioned issues can be solved to some extent by combining the strengths of the polycrystalline and phenomenological approaches (i.e. the possible accuracy of the polycrystal plasticity models and the computational efficiency of the phenomenological models) [25]. Crystal plasticity models can provide data points or "virtual points or experiments" that can be employed, in addition to experimental data, to calibrate advanced macroscopic yield functions. In other words, they can identify the anisotropy coefficients of the macroscopic yield functions [28].

The process of improving texture-based models and documenting knowledge about the performances of different polycrystalline models, as well as their performances in fitting advanced yield functions for different metallic sheets, is still in progress.

10.1.1 Yield locus for aluminium alloys

10.1.1.1 *CTFP*

Pioneering previous work in the area of combining the strengths of the two approaches showed that the simple Taylor models, namely the full-constraint model and its relaxed version, were able to be useful tools to describe the behaviour of different considered steel alloys [7]. In the work of An et al., the correlation between the calculated texture-based yield loci and those measured from mechanical tests to define advanced yield functions efficiently and effectively for different steel grades was investigated. Based on the two texture-based yield loci calculated from the Taylor models, An et al. proposed a new combined model referred to as CTFP [7]. The CTFP model is utilised for steel grades and is used as a deployment tool to fit advanced phenomenological yield functions (e.g. Yld2000/BBC2005) with the help of a simple uniaxial tensile test in three directions. It is a qualified alternative for biaxial tests such as the hydraulic bulge test, which is required to identify the biaxial yield stress. Therefore, the high cost associated with determination of the experimental yield loci can be minimised using the CTFP model. Consequently, with this method, complex analytical yield functions for stamping simulations can be used more frequently.

The applicability of the CTFP model was examined for the considered aluminium alloys. It was proved that both of the resulting polycrystalline plasticity models overestimate the stress factors in the stretching quadrant when the Taylor's models were compared with the BBC2005 for the considered aluminium alloys. Accordingly, if the CTFP model was derived, it would still overestimate the stress factors in the stretching regime. Therefore, this study concludes that the CTFP model is inapplicable for the aluminium alloys considered in this study.

10.1.1.2 *CTF and its deployment (Method II)*

Following a similar methodology to the CTFP model, a new yield loci description based on the simple FC-Taylor model was proposed; it is compared with different macroscopic yield functions in chapter 7. The new methodology focuses on calibrating the initial yield loci of the BBC2005 for two aluminium alloys (Al-Mg-Si alloys). Simplicity and efficiency are the main intrinsic features of the proposed model.

The CTF model is a texture-based model which is based on the full-constraint Taylor's model referred to as TF. Therefore, as a starting point, the TF models for the two considered aluminium alloys were derived using the MTM-FHM software. The main inputs for the TF model were the texture in terms of the c-coefficients and the slip system (i.e. making the assumption that slipping occurs on {111} crystallographic planes in <110> directions for the considered aluminium grades). The full-constraint models for the two aluminium alloys were derived and compared with the BBC2005. It is clear that the full-constraint (TF) model when applied on both materials does overestimate the stretching regimes (i.e. first quadrants of the yield loci). However, the TF model is a good predictor of the other strain states.

The CTF model might be used to skip the biaxial test and uniaxial test in the transverse direction, which can be used to identify the biaxial yield stress YS_b and the uniaxial yield stress in the transverse direction YS_{90} that are used as inputs for advanced yield functions such as BBC2005. A careful comparison between the TF model and measured yield locus (BBC2005) for two aluminium grades indicates that the TF are more elongated in the stretching regions.

First, the resulting yield loci derived using the CTF model was validated by comparing its prediction with the performance of the BBC2005 macroscopic yield function. The BBC2005 yield function, which was experientially fitted with data obtained from mechanical tests, was used to measure the yield loci of the considered aluminium alloys.

It was observed for the considered aluminium alloys that the proposed CTF model could predict well both the equibiaxial yield stress YS_b and uniaxial yield stress in the transverse direction YS_{90}. In terms of accuracy, the CTF model predicted an equibiaxial yield stress (CTF Biaxial) corresponding exactly with the measured experimentally balanced points (Experimental Biaxial) for both of the considered aluminium alloys. The CTF model overestimated the biaxial points for both materials by 1% at the most, which was negligible. Moreover, the CTF model gave an accurate prediction and overestimated the uniaxial yield stress in the transverse direction YS_{90} for the AC600 alloy by less than 2%, with a value of approximately 2 MPa. However, the prediction for the yield stress in the transverse direction YS_{90} for the AA6111-T4 material was less accurate. The model over-predicted the YS_{90} by about 6%, with a value of approximately 7 MPa.

It was demonstrated that the proposed texture-based model, referred to as the CTF model, could predict the yield stresses for the two different stress states, namely the Y_b and Y_{90}, accurately, but its accuracy could not be guaranteed in other strain states. Therefore, the CTF model will be deployed to fit the advanced yield criterion denoted as BBC2005.

A method, denoted as **Method II**, was suggested. The method combines strengths of the polycrystalline plasticity approach and the phenomenological approach. **Method II** combines the data obtained from the CTF model, experimental work, and Backofen [197] description for the balanced biaxial strain ratio.

In this suggested method, the same experimental data presented to derive fully the BBC2005 yield function with mechanical testing that is referred to as **Method I** were used, except for the following quantities:

- Uniaxial yield stress perpendicular to the rolling direction (YS_{90}) were predicted from the newly proposed model known as CTF.
- Biaxial yield stress Y_b was extracted from the CTF model.
- The R-value in the transverse direction R_{90} was estimated using the Backofen equation [197], which is ($R_b=R_0/R_{90}$) (i.e. the R_{90} was a function of the R_0 obtained experimentally from uniaxial tensile tests performed in the rolling direction and R_b obtained experimentally from the compression test).

To summarise (see Table 10.1), the eight mechanical inputs required to define fully the BBC2005 were determined either experimentally (**Method I**) or using the combined procedure, denoted as **Method II**.

Table 10.1. Method I vs. Method II.

	YS_0 **[MPa]**	YS_{45} **[MPa]**	YS_{90} **[MPa]**	YS_b **[MP]**	R_0 **[-]**	R_{45} **[-]**	R_{90} **[-]**	R_b **[-]**
Method I	Tensile	Tensile	Tensile	Bulge	Tensile	Tensile	Tensile	Compression
Method II	Tensile	Tensile	CTF	CTF	Tensile	Tensile	Backofen	Compression

It was observed that the new suggested method (Method II: BBC2005 fitted with CTF), for both of the considered aluminium alloys, performed better than the other yielding descriptions.

It was seen that the R_{90} value using the Backofen equation deviated by -3% and +6% for AC600 and AA6111-T4. However, the effect of such discrepancy on the shape of the yield loci and the calculated normal plastic anisotropy $\overline{R}$ of the two materials was negligible.

The BBC20005 when fitted with the CTF model improved the yield function performance more specifically at the plane strain states in the rolling and transverse directions. Consequently, the uncertainties of yielding behaviour in the plane strain states were minimised when the new suggested model (Method II) was used. The new procedure gave almost identical yield locus as the one identified fully with experimental work.

To conclude, the practical use of texture-based yield loci can be summarised as

- Currently stamping simulation cannot accept texture-based yield loci.
- For a 6xxx material, the following steps will enable its use in stamping simulation:
  - Carry out texture measurement using X-ray machine.
  - Obtain texture-based yield locus derived by the full-constraint Taylor model (TF).
  - Scale the TF model following the scheme described in chapter 4 in section 4.11.
  - Extract the biaxial yield stress YS_b and uniaxial yield stress in the transverse direction YS_{90}.
  - Carry out two tensile tests in the (0°,45°).
  - Estimate the *R*-value in the transverse direction R_{90} using the Backofen equation [197], which is a function of the R_0 obtained experimentally from uniaxial tensile tests performed in the rolling direction and R_b obtained experimentally from the compression test.
  - Define an advanced phenomenological model such as BBC2005.

- Input to simulation.

- Therefore, to enable current simulation to accept texture-based yield locus, a hybrid solution **(Method II)** is suggested.

The key intrinsic features of this hybrid method that are looked for at the proposing phase are

- Good accuracy
- Simplicity
- Efficiency

10.1.2 Optimization of the phenomenological constitutive models parameters

This thesis presentes a comparison of line search based algorithms and a trust region based algorithm and demonstrates their ability in overcoming the difficulties encountered by the NR procedure. These applied optimization strategies were utilised to identify the plastic anisotropy parameters associated with different yield functions for various aluminium and steel alloys. Tensile, bulge, and compression tests were performed to obtain the data for these materials. The phenomenological models denoted as Yld2000-2d and BBC2003 were used to describe the material behaviour.

For Yld2000-2d, all of the applied algorithms were robust for all the materials under this study. Additionally, all of these routines were approximately equal in effectiveness. Furthermore, for all of the materials, the number of function evaluations invoked by the TRD routine was less than all permutations of the LM algorithms for the same number of iterates.

For BBC2003, the L routine was less sensitive to the initial guess than the other routines. In addition, all of the applied algorithms were robust for all of the aluminium alloys considered in this study. Furthermore, the TRD routine was the most robust algorithm. Unfortunately, the LM routine failed to converge for steels. Moreover, there was a large variation in the level of effectiveness of these routines for the different materials.

Finally, Yld2000-2d was less sensitive to the initial guess than BBC2003 and was more flexible with different solution methods for the different alloys than BBC2003. Additionally, all of the algorithms for all of the materials converged faster with Yld2000-2d than with BBC2003, which will in turn economize the number of computer evaluations when the Jacobian is approximated numerically.

10.2 Accurate and cost-effective description of the biaxial flow curve

This thesis presentes a new analytical approach for determination of the polar thickness of the bulged sheet. The new methodology is based on a modified version of the Chakrabarty and Alexander equation. The proposed method considers the effect of the normal plastic anisotropy of the sheet. In the absence of a continuous and in-line thickness measurement system, the proposed method coupled with the Panknin method is found to be a reliable combination for the determination of the biaxial flow curve and hence the biaxial yield stress. For an accurate prediction of the yield locus, it is very important to provide an accurate material parameter, namely the biaxial yield stress of the material using biaxial stress state tests such as the hydraulic bulge test. Therefore, as found in this research, the proposed method predictes very well the biaxial yield stresses compared to the DIC data for all of the materials considered in this study.

10.3 Limitations and future work

10.3.1 CTF

It should be noted that the capability of the CTF model to extract other stress state points was not examined. Therefore, the model must be tested on shear and plane strain states. Once the model is validated, and its applicability in extracting other stress state data is proved, then it can be used as a deployment tool to fit more complex yield loci such as Vegter and Boograard model [53].

The new proposed model, denoted as CTF, must be validated on different aluminium materials. Because materials such as those in the temper state will have a different texture (recrystallization texture), which is assumed to be the main input for the utilised polycrystalline plasticity models, validating the CTF model on different aluminium alloys is a potential extension to this work.

Formability of sheets in the industry of sheet forming is evaluated with FLD. The performance or capability of the theoretical model (CTF) in predicting the FLD must be assessed.

A similar scheme to the one used in the CTF development can be applied on magnesium alloy sheets which deform by slip and twining. The twining phenomenon is an active deformation mechanism at the compression mode for metals with hexagonal close-packed crystal structure.

10.3.2 Identification strategy

The main drawback of the applied trust region approach used in this study is its ability to solve only square nonlinear systems of equations (i.e. the number of equations equals the number of unknowns). The next step is to see if there is a potential trust region method that works with a non-square system of nonlinear equations.

10.3.3 Biaxial flow curve

The proposed methodology denoted as P-C-M must be examined for other aluminium and steel alloys that have different levels of normal anisotropy from the alloys that were considered in this thesis.

A potential future extension of the P-C-M model is to include the effect of the plastic anisotropy in the description of the flow curve for magnesium alloys.

Chapter 11

References

[1] T. Altan, A.E. Tekkaya, Sheet Metal Forming Fundamentals, 1st ed., ASM International, 2012.

[2] P. Hu, N. Ma, L. Liu, Z. Yi-guo, Theories, Methods and Numerical Technology of Sheet Metal Cold and Hot Forming Analysis, Simulation and Engineering Applications, Springer-Verlag London, 2013.

[3] Z. Marciniak, J. Duncan, S. Hu, Mechanics of Sheet, Second, 2002.

[4] D. Banabic, F. Barlat, O. Cazacu, T. Kuwabara, Advances in anisotropy and formability, Int. J. Mater. Form. 3 (2010) 165–189.

[5] A.E. Tekkaya, State-of-the-art of simulation of sheet metal forming, J. Mater. Process. Technol. 103 (2000) 14–22.

[6] D. Banabic, Sheet Metal Forming Processes, 2010.

[7] Y.G. An, H. Vegter, L. Carless, M. Lambriks, A novel yield locus description by combining the Taylor and the relaxed Taylor theory for sheet steels, Int. J. Plast. 27 (2011) 1758–1780.

[8] A. Makinouchi, C. Teodosiu, T. Nakagawa, Advance in FEM Simulation and its Related Technologies in Sheet Metal Forming, CIRP Ann. - Manuf. Technol. 47 (1998) 641–649.

[9] M. Tisza, Numerical modelling and simulation in sheet metal forming, J. Mater. Process. Technol. 151 (2004) 58–62. doi:10.1016/j.jmatprotec.2004.04.009.

[10] Y.G. An, H. Vegter, L. Carless, A new description of yield loci based on polycrystal plasticity for high strength steels, 410–411 (2009) 543–553.

[11] N. Uema, M. Asano, Characteristics of the aluminum alloy sheets for forming and application examples, 670 (2013) 667–670.

[12] O. Engler, J. Hirsch, Texture control by thermomechanical processing of {AA6xxx} Al–Mg–Si sheet alloys for automotive applications—a review, Mater. Sci. Eng. A. 336 (2002) 249–262.

[13] A.G. Leacock, The Future of Sheet Metal Forming Research, Mater. Manuf. Process. 27 (2012) 366–369.

[14] S.K. Ghosh, Metal forming: Mechanics and metallurgy, 1985. doi:10.1016/0378-3804(85)90124-X.

[15] M.J. Michno, W.N. Findley, An historical perspective of yield surface investigations for metals, Int. J. Non. Linear. Mech. 11 (1976) 59–82.

[16] F. Barlat, J.W. Yoon, O. Cazacu, On linear transformations of stress tensors for the description of plastic anisotropy, Int. J. Plast. 23 (2007) 876–896.

[17] K. Mattiasson, On The Influence Of The Yield Locus Shape In The Simulation Of Sheet Stretch Forming, AIP Conf. Proc. 778 (2005) 395–400.

[18] K. Mattiasson, M. Sigvant, An evaluation of some recent yield criteria for industrial

simulations of sheet forming processes, Int. J. Mech. Sci. 50 (2008) 774–787.

[19] F. Barlat, J.C. Brem, J.W. Yoon, K. Chung, R.E. Dick, D.J. Lege, et al., Plane stress yield function for aluminum alloy sheets—part 1: theory, Int. J. Plast. 19 (2003) 1297–1319.

[20] D.S. Comsa, D. Banabic, Plane-stress yield criterion for highly-anisotropic sheet metals, in: Numisheet 2008, 2008: pp. 43–48.

[21] S.T. H. Laurent, R. Grèze, P. Y. Manach, Influence of constitutive model in springback prediction using the split-ring test, Int. J. Mech. Sci. 51 (2009) 233–245.

[22] D. Banabic, M. Sester, Influence of Material Models on the Accuracy of the Sheet Forming Simulation, Mater. Manuf. Process. 27 (2012) 273–277.

[23] T. Beier, J. Gerlach, L. Kessler, and M. Linnepe, A discussion of benefits and challenges by using multiparameter yield locus models in FEM-simulation, in: Int. Deep Draw. Res. Gr., 2010: pp. 679–686.

[24] A.M. Habraken, Modelling the Plastic Anisotropy of Metals, 11 (2004) 3–96.

[25] H. Zhang, M. Diehl, F. Roters, D. Raabe, A virtual laboratory using high resolution crystal plasticity simulations to determine the initial yield surface for sheet metal forming operations, Elsevier Ltd, 2016.

[26] K. Zhang, B. Holmedal, O.S. Hopperstad, S. Dumoulin, J. Gawad, A. Van Bael, et al., Multi-level Modelling of Mechanical Anisotropy of Commercial Pure Aluminium Plate: Crystal Plasticity Models, Advanced Yield Functions and Parameter Identification, Int. J. Plast. (2014).

[27] S. Bruschi, T. Altan, D. Banabic, P.F. Bariani, A. Brosius, J. Cao, et al., Testing and modelling of material behaviour and formability in sheet metal forming, CIRP Ann. - Manuf. Technol. 63 (2014) 727–749.

[28] A. Saai, S. Dumoulin, O.S. Hopperstad, O.-G. Lademo, Simulation of yield surfaces for aluminium sheets with rolling and recrystallization textures, Comput. Mater. Sci. 67 (2013) 424–433.

[29] H. Campos, A. Santos, B. Martins, K. Ito, N. Mori, F. Barlat, Hydraulic bulge test for stress-strain curve determination and damage calibration for Ito-Goya model, in: 11th World Congr. Comput. Mech. (WCCM XI), Barcelona, 2014.

[30] L. Lăzărescu, Dan Sorin Comşa, and D. Banabic., Analytical and experimental evaluation of the stress-strain curves of sheet metals by hydraulic bulge tests, Key Eng. Mater. Vol. 473. (2011).

[31] L. Lăzărescu, I. Nicodim, I. Ciobanu, D.S. Comşa, D. Banabic, Determination of Material Parameters of Sheet Metals Using the Hydraulic Bulge Test, Acta Metall. Slovaca. 19 (2013) 4–12.

[32] Billur, Eren, M. Koç, A comparative study on hydraulic bulge testing and analysis methods, in: Int. Manuf. Sci. Eng. Conf., American Society of Mechanical Engineers, Evanston, IL, USA., 2008: pp. 59–65.

[33] M. Koç, E. Billur, Ö.N. Cora, An experimental study on the comparative assessment of hydraulic bulge test analysis methods, Mater. Des. 32 (2011) 272–281.

[34] R. Hill, The mathematical theory of plasticity, Oxford university press, 1998.

[35] R.H. Wagoner, J.-L. Chenot, Fundamentals of Metal Forming, John Wiley & Sons, Inc., 1996.

[36] F. Barlat, H. Aretz, J.W. Yoon, M.E. Karabin, J.C. Brem, R.E. Dick, Linear transfomation-based anisotropic yield functions, Int. J. Plast. 21 (2005) 1009–1039.

[37] J.F.W. Bishop, R. Hill, XLVI. A theory of the plastic distortion of a polycrystalline aggregate under combined stresses., Philos. Mag. Ser. 7. 42 (1951) 414–427.

[38] M. Safaei, Constitutive Modelling of Anisotropic Sheet Metals Based on a Non-Associated Flow Rule Mohsen Safaei, 2013.

[39] H. Aretz, A less hypothetical perspective on rate-independent continuum theory of metal plasticity, Mech. Res. Commun. 33 (2006) 734–738.

[40] D.C. Drucker, A definition of stable inelastic material., 1957.

[41] T.B. Stoughton, J.W. Yoon, Review of Drucker's postulate and the issue of plastic stability in metal forming, Int. J. Plast. 22 (2006) 391–433.

[42] H. Aretz, F. Barlat, New convex yield functions for orthotropic metal plasticity, Int. J. Non. Linear. Mech. 51 (2013) 97–111.

[43] M. Safaei, S.L. Zang, M.G. Lee, W. De Waele, Evaluation of anisotropic constitutive models: Mixed anisotropic hardening and non-associated flow rule approach, Int. J. Mech. Sci. 73 (2013) 53–68.

[44] F. Barlat, O. Cazacu, M. Życzkowski, D. Banabic, J.W. Yoon, Yield Surface Plasticity and Anisotropy, in: Contin. Scale Simul. Eng. Mater., Wiley-VCH Verlag GmbH & Co. KGaA, 2005: pp. 145–183.

[45] R. von Mises, Mechanik der plastischen Formänderung bei Kristallen, J. Appl. Math. Mech. Angew. Math. Mech. 8 (3) (1928) 161–185.

[46] S. Soare, F. Barlat, Convex polynomial yield functions, J. Mech. Phys. Solids. 58 (2010) 1804–1818.

[47] R. Hill, A Theory of the Yielding and Plastic Flow of Anisotropic Metals, Proc. R. Soc. A Math. Phys. Eng. Sci. 193 (1948) 281–297.

[48] D. Banabic, An improved analytical description of orthotropy in metallic sheets, Int. J. Plast. 21 (2005) 493–512.

[49] D. Banabic, D. Sorin Comsa, M. Sester, M. Seilg, W. Kubli, K. Mattiasson, et al., Influence of constitutive equations on the accuracy of prediction in sheet metal forming simulation, in: Numisheet, 2008.

[50] Hershey, The plasticity of an isotropic aggregate of anisotropic face centred cubic crystals., J. Appl. Mech. (1954) 241–249.

[51] F. Barlat, D.J. Lege, J.C. Brem, A six-component yield function for anisotropic materials, Int. J. Plast. 7 (1991) 693–712.

[52] A.P. Karafillis, M.C. Boyce, A general anisotropic yield criterion using bounds and a transformation weighting tensor, J. Mech. Phys. Solids. 41 (1993) 1859–1886.

[53] H. Vegter, A.H. van den Boogaard, A plane stress yield function for anisotropic sheet material by interpolation of biaxial stress states, Int. J. Plast. 22 (2006) 557–580.

[54] O. Cazacu, F. Barlat, Generalization of drucker's yield criterion to orthotropy, Math. Mech. Solids. 6 (2001) 613–630.

[55] F. Barlat, J. Lian, Plastic behaviour and strechability of sheet metals. Part 1: A yield function for orthotropic sheets under plane stress conditions, Int. J. Plast. 5 (1989) 51–66.

[56] R. Hill, Constitutive Modeling of Orthotropic Plasticity in Sheet Metals, J. Mech. Phys. Solids. 38 (1990) 405–417.

[57] D. Banabic, T. Balan, D.S. Comsa, A new yield criterion for orthotropic sheet metals

under plane stress conditions, in: 7th Cold Met. Form. Conf., 2000: pp. 217–224.

[58] B.M. Chaparro, J.L. Alves, L.F. Menezes, J. V Fernandes, Optimization of the phenomenological constitutive models parameters using genetic algorithms, in: Adv. Methods Mater. Form. SE - 3, Springer Berlin Heidelberg, 2007: pp. 35–54.

[59] W. Hosford, R. Caddell, Metal forming:Mechanics and metallurgy, 3rd ed., Cambridge, 2007.

[60] L.F. Simões, V. M., Coër, J., Laurent, H., Oliveira, M. C., Alves, J. L., Manach, P. Y., & Menezes, Influence of the yield criteria in the numerical simulation of an AA5745-O cylindrical cup, in: Congr. Métodos Numéricos En Ing., 2013.

[61] P. Flores, L. Duchene, C. Bouffioux, T. Lelotte, C. Henrard, N. Pernin, et al., Model identification and FE simulations: Effect of different yield loci and hardening laws in sheet forming, Int. J. Plast. 23 (2007) 420–449.

[62] Z. Tourki, A. Zeghloul, G. Ferron, Sheet metal forming simulations using a new model for orthotropic plasticity, Comput. Mater. Sci. 5 (1996) 255–262.

[63] M. Vrh, M. Halilovič, B. Starman, B. Štok, D.-S. Comsa, D. Banabic, Capability of the BBC2008 yield criterion in predicting the earing profile in cup deep drawing simulations, Eur. J. Mech. - A/Solids. 45 (2014) 59–74.

[64] S. Soare, D. Banabic, About the mechanical data required to describe the anisotropy of thin sheets to correctly predict the earing of deep-drawn cups, Int. J. Mater. Form. 1 (2008) 285–288.

[65] J.H. Yoon, O. Cazacu, J. Whan Yoon, R.E. Dick, Earing predictions for strongly textured aluminum sheets, Int. J. Mech. Sci. 52 (2010) 1563–1578.

[66] J.W. Yoon, F. Barlat, R. Dick, M. Karabin, Prediction of six or eight ears in a drawn cup based on a new anisotropic yield function, Int. J. Plast. 22 (2006) 174–193.

[67] D. Banabic, Effect of the Constitutive Laws on the Accuracy of Sheet Metal Simulation, Key Eng. Mater. 535–536 (2013) 279–283.

[68] H. Vegter, C.H.L.J. ten Horn, Y. An, E.H. Atzema, H.H. Piljman, A.H. van den Boogaard, et al., Characterisation and modelling of the plastic material behaviour and its application in sheet metal forming simulation, in: E. Oñate, D.R.J. Owen (Eds.), VII Int. Conf. Comput. Plast. COMPLAS VII, 2003: pp. 1–20.

[69] L. Lăzărescu, I. Ciobanu, I.P. Nicodim, D.S. Comșa, D. Banabic, Effect of the Mechanical Parameters Used as Input Data in the Yield Criteria on the Accuracy of the Finite Element Simulation of Sheet Metal Forming Processes, Key Eng. Mater. 554–557 (2013) 204–209.

[70] C.H.L.J. Horn, H. Vegter, M. El Mouatassim, Increased accuracy in forming simulation of complex renault part through Corus-Vegter material model, in: E. Oñate, D. R. J. Owen (Eds.), VIII Int. Conf. Comput. Plast., 2005: pp. 2–5.

[71] J. Lubliner, Plasticity theory, Courier Corporation, 2008.

[72] J.W. Yoon, Y. Lou, J. Yoon, M. V. Glazoff, Asymmetric yield function based on the stress invariants for pressure sensitive metals, Int. J. Plast. 56 (2014) 184–202.

[73] H. Tresca, On the yield of solids at high pressures, Comptes Rendus Acad. Des Sci. 59 (1864) 754 (in French).

[74] Hosford, W.F., A Generalized Isotropic Yield Criterion., J. Appl. Mech. 39 (1972) 607–609.

[75] D.C. Drucker, “Relation of experiments to mathematical theories of plasticity.,” J. Appl. Mech. ASME. 16 (1949) 349–357.

[76] M. Yu, Advances in strength theories for materials under complex stress state in the 20th Century, Appl. Mech. Rev. 55 (2002) 169.

[77] R. Hibbeler, Mechanics of materials, 6th ed., Pearson Hall Inc, Singapore, 2005.

[78] R. Hill, Theoretical plasticity of textured aggregates, Math. Proc. Cambridge Philos. Soc. 85 (1979) 179.

[79] R. Hill, A user-friendly theory of orthotropic plasticity in sheet metals, Int. J. Mech. Sci. 35 (1993) 19–25.

[80] F. Barlat, Y. Maeda, K. Chung, M. Yanagawa, J.C. Brem, Y. Hayashida, et al., Yield function development for aluminum alloy sheets, J. Mech. Phys. Solids. 45 (1997) 1727–1763.

[81] M. Gotoh, A theory of plastic anisotropy based on a yield function of fourth order., Int. J. Mech. Sci. 19 (1977) 505–520.

[82] Budiansky B, Anisotropic plasticity of plane-isotropic sheets., in: Dvorak GJ, Shield RT (Eds.), Mech. Mater. Behav., Elsevier, Amsterdam, 1984: pp. 15–29.

[83] G. Ferron, R. Makkouk, J. Morreale, A parametric description of orthotrpic plasticity in metal sheets, 10 (1994) 431–449.

[84] D. Banabic, T. Kuwabara, T. Balan, D.S. Comsa, D. Julean, Non-quadratic yield criterion for orthotropic sheet metals under plane-stress conditions, Int. J. Mech. Sci. 45 (2003) 797–811.

[85] B. Plunkett, O. Cazacu, F. Barlat, Orthotropic yield criteria for description of the anisotropy in tension and compression of sheet metals, Int. J. Plast. 24 (2008) 847–866.

[86] S. Soare, J.W. Yoon, O. Cazacu, On the use of homogeneous polynomials to develop anisotropic yield functions with applications to sheet forming, Int. J. Plast. 24 (2008) 915–944.

[87] L. Paraianu, D. Banabic, Predictive accuracy of different yield criteria, in: SISOM 2006, Bucharest, 2006: pp. 17–19.

[88] M.C. Butuc, D. Banabic, A. Barata da Rocha, J.J. Gracio, J. Ferreira Duarte, P. Jurco, et al., The performance of Yld96 and BBC2000 yield functions in forming limit prediction, J. Mater. Process. Technol. 125–126 (2002) 281–286.

[89] A.E. Tekkaya, W. Homberg, A. Brosius, 60 Excellent inventions in metal forming, 2015.

[90] M. Vaz, P.A. Munoz Rojas, E.L. Cardoso, M. Tomiyama, Considerations on parameter identification and material response for Gurson-type and Lemaitre-type constitutive models, Int. J. Mech. Sci. 106 (2016) 254–265.

[91] B.M. Chaparro, S. Thuillier, L.F. Menezes, P.Y. Manach, J.V. Fernandes, Material parameters identification: Gradient-based, genetic and hybrid optimization algorithms, Comput. Mater. Sci. 44 (2008) 339–346.

[92] M.C. Butuc, C. Teodosiu, F. Barlat, J.J. Gracio, Analysis of sheet metal formability through isotropic and kinematic hardening models, Eur. J. Mech. - A/Solids. 30 (2011) 532–546.

[93] T. Ypma, Historical Development of the Newton-Raphson Method, SIAM Rev. 37 (1995) 531–551.

[94] R. Idema, D.J.P. Lahaye, Computational Methods in Power System Analysis, Atlantis Press, Paris, 2014.

[95] O. Cazacu, F. Barlat, Application of the theory of representation to describe yielding of

anisotropic aluminum alloys, Int. J. Eng. Sci. 41 (2003) 1367–1385.

[96] Mathworks, Optimization Toolbox: User's Guide R2014 b, 2014.

[97] D.G. Luenberger, Linear and Nonlinear Programming, Springer, 2008.

[98] J. Nocedal, S.J. Wright, Numerical Optimization, Second, 2006.

[99] M.J.D. Powell, A hybrid method for non-linear equations, in: P. Rabinowitz, (Ed.) (Eds.), Numer. Methods Nonlinear Algebr. Equations, 1970: p. 87–114.

[100] A. Shterenlikht, N. a. Alexander, Levenberg–Marquardt vs Powell's dogleg method for Gurson–Tvergaard–Needleman plasticity model, Comput. Methods Appl. Mech. Eng. 237–240 (2012) 1–9.

[101] H. Aretz, A non-quadratic plane stress yield function for orthotropic sheet metals, J. Mater. Process. Technol. 168 (2005) 1–9.

[102] H. Aretz, O.S. Hopperstad, O.G. Lademo, Yield function calibration for orthotropic sheet metals based on uniaxial and plane strain tensile tests, J. Mater. Process. Technol. 186 (2007) 221–235.

[103] F. Bron, J. Besson, A yield function for anisotropic materials Application to aluminum alloys, Int. J. Plast. 20 (2004) 937–963.

[104] N. Gould, An introduction to algorithms for continuous optimization, 2006. http://www.numerical.rl.ac.uk/people/nimg/course/lectures/paper/paper.pdf.

[105] W. Sun, Y. Yuan, "Trust-Region Methods and Conic Model Methods.," in: Optim. Theory Methods Nonlinear Program., Society for Industrial and Applied Mathematics, 2006: p. 303–351.

[106] M.J.. Powell, A Fortran Subroutine for Solving Systems of Nonlinear Algebraic Equations, in: P. Rabinowitz (Ed.), Numer. Methods Nonlinear Algebr. Equations, 1970.

[107] K. Levenberg, A method for the solution of certain problems in least squares, Q. Appl. Math. 2 (1944) 164–168.

[108] D.W. Marquardt, An Algorithm for Least Squares Estimation of Nonlinear Parameters, J. Soc. Ind. Appl. Math. 11 (1963) 431–441.

[109] J.J. More, The Levenberg-Marquardt algorithm: Implementation and theory, in: G. A. Watson (Ed.), Numer. Anal., Springer Berlin Heidelberg, 1978: pp. 105–116.

[110] H.P. Gavin, The Levenberg Marquardt method for nonlinear least squares curve fitting problems, Dep. Civ. Environ. Eng. (2011) 1–15.

[111] A. Ranganathan, The Levenberg Marquardt Algorithm, Tutoral LM Algorithm. (2004) 1–5.

[112] J. Gawad, D. Banabic, A. Van Bael, D.S. Comsa, M. Gologanu, P. Eyckens, et al., An evolving plane stress yield criterion based on crystal plasticity virtual experiments, Int. J. Plast. (2015) 1–29.

[113] W. Hosford, Influence of Textures on Sheet Forming, (2000).

[114] L. Duchêne, A.M. Habraken, Multiscale Approaches, in: F. Chinesta, E. Cueto (Eds.), Adv. Mater. Form. Esaform 10 Years, Springer Paris, 2007: pp. 125–141.

[115] Q. Xie, P. Eyckens, H. Vegter, J. Moerman, A. Van Bael, P. Van Houtte, Polycrystal plasticity models based on crystallographic and morphologic texture: Evaluation of predictions of plastic anisotropy and deformation texture, Mater. Sci. Eng. A. 581 (2013) 66–72.

[116] P. Eyckens, H. Mulder, J. Gawad, H. Vegter, D. Roose, T. Van Den Boogaard, et al., The prediction of differential hardening behaviour of steels by multi-scale crystal plasticity modelling, Int. J. Plast. 73 (2015) 119–141.

[117] F. Barlat, Constitutive Modeling for Metals, in: Prof. Dorel Banabic (Ed.), Adv. Methods Mater. Form., Springer Berlin Heidelberg, 2007: p. pp 1-18.

[118] L. Duchêne, FEM Study of Metal Sheets with a Texture based , Local Description of the Yield Locus, Université de Liège, 2002.

[119] J.F.W. Bishop, R. Hill, CXXVIII. A theoretical derivation of the plastic properties of a polycrystalline face-centred metal, London, Edinburgh, Dublin Philos. Mag. J. Sci. 42 (1951) 1298–1307.

[120] H.J. Bunge, M. Schulze, D. Grzesik, The yield locus and plastic anisotropy of polycrystalline materials, Int. J. Eng. Sci. 19 (1981) 737–745.

[121] S. M'Guil, S. Ahzi, F. Barlat, J.J. Gracio, Microstructural effects on yield surface evolution in cubic metals using the viscoplastic ϕ-model, Int. J. Plast. 27 (2011) 102–120.

[122] J. Gawad, D. Banabic, D.S. Comsa, M. Gologanu, A. Van Bael, P. Eyckens, et al., Evolving texture-informed anisotropic yield criterion for sheet forming, 355 (2013) 350–355.

[123] J. Gawad, A. Van Bael, P. Eyckens, G. Samaey, P. Van Houtte, D. Roose, Hierarchical multi-scale modeling of texture induced plastic anisotropy in sheet forming, Comput. Mater. Sci. 66 (2013) 65–83.

[124] L. Duchêne, A.M. Habraken, Analysis of the sensitivity of FEM predictions to numerical parameters in deep drawing simulations, Eur. J. Mech. - A/Solids. 24 (2005) 614–629.

[125] M. Kraska, M. Doig, D. Tikhomirov, D. Raabe, F. Roters, Virtual material testing for stamping simulations based on polycrystal plasticity, Comput. Mater. Sci. 46 (2009) 383–392.

[126] A. Prakash, R. a Lebensohn, Simulation of micromechanical behavior of polycrystals: finite elements versus fast Fourier transforms, Model. Simul. Mater. Sci. Eng. 17 (2009) 64010.

[127] R.A. Lebensohn, A.D. Rollett, P. Suquet, Fast fourier transform-based modeling for the determination of micromechanical fields in polycrystals, J. Polycrystal Model. 63 (2011) 13–18.

[128] G.I. Taylor, Plastic strain in metals., J. Inst. Met. 62 (1938) 307–324.

[129] P. Van Houtte, Calculation of the yield locus of textured polycrystals using the Taylor and the Relaxed Taylor theory, Texture Microstruct. 7 (1987) 29–72.

[130] Y.G. An, H. Vegter, L. Elliott, Bottema, I. Jumiden, A comparison of yield loci derived from different approaches for aluminium alloys, (2004) 674–679.

[131] K. Zhang, B. Holmedal, T. Manik, Q. Zhao, Crystal Plasticity Calculations of Mechanical Anisotropy of Aluminium Compared To Experiments and To Yield Criterion Fittings, in: H. Weiland, A.D. Rollett, W. A. (Eds.), 13th Int. Conf. Alum. Alloy., 2012: pp. 915–920.

[132] T. Kuwabara, A. Van Bael, E. Iizuka, Measurement and analysis of yield locus and work hardening characteristics of steel sheets wtih different r-values, Acta Mater. 50 (2002) 3717–3729.

[133] P. Van Houtte, S. Li, M. Seefeldt, L. Delannay, Deformation texture prediction: From the Taylor model to the advanced Lamel model, 2005.

[134] K. Zhang, B. Holmedal, O.S. Hopperstad, S. Dumoulin, Modelling the plastic anisotropy

of aluminum alloy 3103 sheets by polycrystal plasticity, Model. Simul. Mater. Sci. Eng. 22 (2014) 75015.

[135] T. Mánik, B. Holmedal, Additional relaxations in the Alamel texture model, Mater. Sci. Eng. A. 580 (2013) 349–354. doi:10.1016/j.msea.2013.05.071.

[136] R.A. Lebensohn, C.N. Tomé, A self-consistent anisotropic approach for the simulation of plastic deformation and texture development of polycrystals: Application to zirconium alloys, Acta Metall. Mater. 41 (1993) 2611–2624.

[137] O. Engler, Y. An, Correlation of Texture and Plastic Anisotropy in the Al-Mg Alloy AA5005, Sloid State Phenom. 105 (2005) 277–284.

[138] K. Zhang, O.S. Hopperstad, B. Holmedal, S. Dumoulin, A robust and efficient substepping scheme for the explicit numerical integration of a rate-dependent crystal plasticity model, Int. J. Numer. Methods Eng. I. 99 (2014) 239–262.

[139] F. Barlat, O. Cazacu, D. Banabic, Anisotropy in sheet metals Numisheet 2002, Numerical Simulation of 3D Sheet Forming Processes., in: Des. Innov. Through Virtual Manuf., 2002: pp. 515–524.

[140] F. Grytten, B. Holmedal, O.S. Hopperstad, T. Børvik, Evaluation of identification methods for YLD2004-18p, Int. J. Plast. 24 (2008) 2248–2277.

[141] K. Zhang, B. Holmedal, O.S. Hopperstad, S. Dumoulin, Modelling the plastic anisotropy of aluminum alloy 3103 sheets by polycrystal plasticity, Model. Simul. Mater. Sci. Eng. 22 (2014) 75015.

[142] F. Pourboghrat, Y. Guan, F. Barlat, Finite Element analysis of aluminum tube hydroforming based on non-quadratic yield function, Int. J. Manuf. Technol. Manag. 14 (2008) 84.

[143] K. Inal, R.K. Mishra, O. Cazacu, Forming simulation of aluminum sheets using an anisotropic yield function coupled with crystal plasticity theory, Int. J. Solids Struct. 47 (2010) 2223–2233.

[144] U.F. Kocks, C. Tome, H.-R. Wenk, Texture and anisotropy: Preferred Orientations in Polycrstals and their Effect on Materials Properties, 1st ed., 1998.

[145] H.-R. Wenk, P. Van Houtte, Texture and anisotropy, Reports Prog. Phys. 67 (2004) 1367–1428.

[146] H.J. Bunge, Texture Analysis in Materials Science: mathematical methods., Butterworth & Co, 1982.

[147] B. Cullity, S. Stock, Elements of x-ray diffraction, 3rd ed., Prentice Hall, 2001.

[148] C. Noyan, H. Schaeban, C. Murray, Texture measurment and analysis, in: D. MacKenzie, G. Totten (Eds.), Anal. Charact. Aluminum, Steel, Superalloys, Taylor & Francis Group, 2006: pp. 575–604.

[149] R.K.R. Satyam Suwas, Crystallographic Texture of Materials, 2014.

[150] aluMATTER, Steriogaphic projection definition, (2010). http://aluminium.matter.org.uk/content/html/eng/0210-0010-swf.htm (accessed September 2, 2013).

[151] O. Engler, V. Randle, Introduction to texture analysis Macrotexture, Microtexture, and Orientation mapping, second, 2010.

[152] S. Suwas, N.P. Gurao, Crystallographic texture in Materials., J. Indian Inst. Sci. 88 (2012) 151–177.

[153] aluMATTER, How do we Represent Textures?, (2010). http://aluminium.matter.org.uk/content/html/eng/default.asp?catid=100&pageid=1039432491 (accessed May 31, 2016).

[154] P. Van Houtte, The " MTM-FHM " software system Version 2 Manual, 1994.

[155] P. Eyckens, Formability in incremental sheet forming : Generalization of the Marciniak-Kuczynski model, Katholieke Universiteit Leuven, 2010.

[156] P. Van Houtte, On the Equivalence of the Relaxed Taylor Theory and the Bishop-Hill Theory for Partially Constrained Plastic Deformation of Crystals, Mater. Sci. Eng. 55 (1982) 69–77.

[157] P. Van Houtte, A Comprehensive Mathematical Formulation of an Extended Taylor–Bishop–Hill Model Featuring Relaxed Constraints, the Renouard–Wintenberger Theory and a Strain Rate Sensitivity Model, Textures Microstruct. 8 (1988) 313–350.

[158] H.J. Bunge, Some applications of the Taylor theory of polycrystal plasticity, Krist. Und Tech. 5 (1970) 145–175.

[159] H.R. Piehler, Crystal-Plasticity Fundamentals, in: S.. Furrer, D.U.; Semiatin (Ed.), ASM Handbook, Vol. 22A - Fundam. Model. Met. Process., ASM International, 2009: p. 232.

[160] P. Flores, L. Duchêne, C. Bouffioux, T. Lelotte, C. Henrard, N. Pernin, et al., Model identification and FE simulations: Effect of different yield loci and hardening laws in sheet forming, Int. J. Plast. 23 (2007) 420–449.

[161] E. Voce, A practical strain-hardening function, Metallurgia. 51 (1955) 219–226.

[162] J.H. Hollomon, Tensile deformation, AIME TRANS. 12 (1945).

[163] M. Sigvant, K. Mattiasson, H. Vegter, P. Thilderkvist, A viscous pressure bulge test for the determination of a plastic hardening curve and equibiaxial material data, Int. J. Mater. Form. 2 (2009) 235–242.

[164] G. Gutscher, H.-C. Wu, G. Ngaile, T. Altan, Determination of flow stress for sheet metal forming using the viscous pressure bulge (VPB) test, J. Mater. Process. Technol. 146 (2004) 1–7.

[165] S. Keller, W. Hotz, H. Friebe, Yield curve determination using the bulge test combined with optical measurement, in: Proc. IDDRG 2009 - Int. Deep Draw. Res. Gr. Conf. Golden, Color. USA., Golden, Colorado, USA., 2009: p. 319–330.

[166] T. Altan, H. Palaniswamy, P. Bortot, W. Heidl, A. Bechtold, Determination of sheet material properties using biaxial bulge tests, in: 2nd Int. Conf. Accuracy Form. Technol., 2006: pp. 79–92.

[167] R. Hill, A theory of the plastic bulging of a metal diaphragm by lateral pressure, London, Edinburgh, Dublin Philos. Mag. J. Sci. 41 (1950) 1133–1142.

[168] W. Panknin, The hydraulic bulge test and the determination of the flow stress curves., University of Stuttgart, 1959.

[169] J. Chakrabarty, J.M. Alexander, Hydrostatic bulging of circular diaphragms, J. Strain Anal. Eng. Des. 5 (1970) 155–161.

[170] A.. Kruglov, F.U. Enikeev, R.Y. Lutfullin, Superplastic forming of a spherical shell out a welded envelope, Mater. Sci. Eng. A. 323 (2002) 416–426.

[171] L. Lăzărescu, D.S. Coms¸a, I. Nicodim, I. Ciobanu, D. Banabic, Investigation of bulge radius variation and its effect on the flow stress in the hydraulic bulge test., in: Proc. 14th Int. Conf. Met. Form., Krakow, 2012: p. 395–398.

[172] M. Atkinson, Accurate determination of biaxial stress—strain relationships from hydraulic bulging tests of sheet metals, Int. J. Mech. Sci. 39 (1997) 761–769.

[173] L.C. Reis, M.C. Oliveira, A.D. Santos, J. V. Fernandes, On the determination of the work hardening curve using the bulge test, Int. J. Mech. Sci. 105 (2016) 158–181.

[174] E.W. Ross Jr, W. Prager., On the Theory of the Bulge Test., 1953.

[175] R. Hill, A theory of the plastic bulging of a metal diaphragm by lateral pressure, London, Edinburgh, Dublin Philos. Mag. J. Sci. 41 (1950) 1133–1142.

[176] M.-G. Lee, D. Kim, C. Kim, M.L. Wenner, R.H. Wagoner, K. Chung, Spring-back evaluation of automotive sheets based on isotropic-kinematic hardening laws and non-quadratic anisotropic yield functions, Int. J. Plast. 21 (2005) 883–914.

[177] H. Inoue, Formability of Aluminum Alloys, in: B. Cantor, P. Grant, C. Johnston (Eds.), Automot. Eng. Light. Funct. Nov. Mater., 2008: pp. 97–108.

[178] Institution of Mechanical Engineers, Sustainable Vehicle Technologies: Driving the Green Agenda, revised, Elsevier, 2012.

[179] Tata Steel Europe Limited, Automotive - Metallic coated - Steel for forming, (2016).

[180] K. Chung, D. Kim, T. Park, Analytical derivation of earing in circular cup drawing based on simple tension properties, Eur. J. Mech. A/Solids. 30 (2011) 275–280.

[181] DIN EN 10002-1:2001, Metallic materials - Tensile testing - Part 1: Method of testing at ambient temperature, DIN, 2001.

[182] ISO 10113-2006, Metallic materials - Sheet and strip - Determination of plastic strain ratio, BSI Stand. Publ. 3 (2006) 10.

[183] ISO 10275-2007, Metallic materials — Sheet and strip — Determination of tensile strain hardening exponent, 2007.

[184] J. Mulder, H. Vegter, J. Ha, a. H. van den Boogaard, Determination of Flow curves under equibiaxial stress conditions, Key Eng. Mater. 504–506 (2012) 53–58.

[185] Y.G. An, H. Vegter, Analytical and experimental study of frictional behavior in through-thickness compression test, J. Mater. Process. Technol. 160 (2005) 148–155.

[186] T. Kuwabara, F. Sugawara, Multiaxial tube expansion test method for measurement of sheet metal deformation behavior under biaxial tension for a large strain range, Int. J. Plast. 45 (2013) 103–118.

[187] DIN EN ISO 16808:2014-11 (E), Metallic materials - sheet and strip - determination of biaxial stress-strain curve by means of bulge test with optical measuring systems, BSI, 2014.

[188] H. Aretz, Impact of the equibiaxial plastic strain ratio on FLD prediction, in: Proc. 9th ESAFORM Int. Conf. Mater. Form., 2006: pp. 311–314.

[189] W. Tong, A plane stress anisotropic plastic flow theory for orthotropic sheet metals, Int. J. Plast. 22 (2006) 497–535.

[190] J.J. Moré, B.S. Garbow, K.E. Hillstrom, User Guide for MINPACK-1, 1980.

[191] K.J. Kozaczek, C.O. Ruud, J. Hirsch, J.C. Conway, C.J. Yu, Crystallography-based prediction of plastic anisotropy of polycrystalline materials, J. Nondestruct. Eval. 12 (1993) 97–107.

[192] G. Charca Ramos, M. Stout, R.E. Bolmaro, J.W. Signorelli, P. Turner, Study of a drawing-quality sheet steel. I: Stress/strain behaviors and Lankford coefficients by

experiments and micromechanical simulations, Int. J. Solids Struct. 47 (2010) 2285–2293.

[193] S. Dumoulin, O. Engler, O.S. Hopperstad, O.G. Lademo, Description of plastic anisotropy in AA6063-T6 using the crystal plasticity finite element method, Model. Simul. Mater. Sci. Eng. 20 (2012) 55008.

[194] O. Engler, Comparison of X-ray and electron backscatter diffraction textures for back-annealed Al–Mg alloys, J. Appl. Crystallogr. 42 (2009) 1147–1157.

[195] O. Engler, A simulation of recrystallization textures of Al-alloys with consideration of the probabilities of nucleation and growth, Textures Microstruct. 32 (1999) 197–219.

[196] P. Van Houtte, A method for the generation of various algorithms-the example of the positivity method and the exponential method, Textures Microstruct. 13 (1991) 199–212.

[197] W.A. Backofen, Deformation Processing, (1972) 1–59.